

DEVELOPMENTS
IN
APPLIED
SPECTROSCOPY

Volume 7A

DEVELOPMENTS IN APPLIED SPECTROSCOPY

Selected papers from the Annual Mid-America Spectroscopy Symposia

- 1962: Volume 1 — Twelfth Annual Symposium, 1961
Edited by W. D. Ashby
- 1963: Volume 2 — Thirteenth Annual Symposium, 1962
Edited by J. Ziomek and J. R. Ferraro
- 1964: Volume 3 — Fourteenth Annual Symposium, 1963
Edited by J. E. Forrette and E. Lanterman
- 1965: Volume 4 — Fifteenth Annual Symposium, 1964
Edited by E. N. Davis
- 1966: Volume 5 — Sixteenth Annual Symposium, 1965
Edited by L. R. Pearson and E. L. Grove
- 1968: Volume 6 — Eighteenth Annual Symposium, 1967
Edited by W. K. Baer, A. J. Perkins, and E. L. Grove
- 1969: Volume 7A } Nineteenth Annual Symposium, with the
Volume 7B } Seventh National Meeting of the SAS, 1968
Edited by E. L. Grove and A. J. Perkins

A Publication of the Chicago Section of the Society for Applied Spectroscopy

DEVELOPMENTS
IN
APPLIED
SPECTROSCOPY
Volume 7A

edited by

E. L. Grove Illinois Institute of Technology Research Laboratories Chicago, Illinois	Alfred J. Perkins University of Illinois College of Pharmacy Chicago, Illinois
---	---

Selected papers from the Seventh National Meeting of the Society for
Applied Spectroscopy (Nineteenth Annual Mid-America Spectroscopy Symposium)
Held in Chicago, Illinois, May 13-17, 1968



PLENUM PRESS • NEW YORK – LONDON • 1969

ISBN 978-1-4684-8702-2 ISBN 978-1-4684-8700-8 (eBook)
DOI 10.1007/978-1-4684-8700-8

Library of Congress Catalog Card No. 61-17720

*Plenum Press, New York
A Division of Plenum Publishing Corporation
227 West 17 Street, New York, N.Y. 10011*

*United Kingdom edition published by Plenum Press, London
A Division of Plenum Publishing Company, Ltd.
Donington House, 30 Norfolk Street, London W.C. 2, England*

© 1969 *Chicago Section of the Society for Applied Spectroscopy*
Softcover reprint of the hardcover 1st edition 1969

All rights reserved

*No part of this publication may be reproduced in any
form without written permission from the publisher*

Preface

Volume 7 of *Developments in Applied Spectroscopy* is a collection of forty-two papers selected from those that were presented at the 7th National Meeting of the Society of Applied Spectroscopy, held (in place of the 19th Mid-America Symposium on Spectroscopy) in Chicago, May 13-17, 1968. These papers, selected by the editors and reviewed by persons knowledgeable in the field, are those of the symposium type and not those pertaining to specific research topics that one would expect to be submitted to a journal. It is the opinion of the committee that this type of publication has an important place in the literature.

The relatively large number of papers would result in quite a sizable volume if bound in one set of covers. For this reason, and to present the material in areas of more specific interest, Volume 7 was divided into two parts, Part A, Physical-Inorganic, and Part B, Physical-Organic Developments.

The 7th National Meeting was sponsored by the Chicago Section as host in cooperation with the St. Louis, New England, Penn York, Niagara-Frontier, Cincinnati, Ohio Valley, New York, Baltimore-Washington, North Texas, Rocky Mountain, and Southeastern Sections of the Society for Applied Spectroscopy and the Chicago Gas Chromatography Group.

The editors wish to express their appreciation to the authors and to those who helped with the reviewing. The latter include Dr. Elma Lanterman, Mr. John E. Forrette, Dr. Carl Moore, Dr. B. Jaselskis, Mr. H. G. Zelinski, Mr. D. J. Rokop, Mr. N. R. Stalica, Dr. Charles Reagan, Dr. Morris A. Wahlgren, and Dr. David Edgington.

Thanks should also be extended to the exhibitors for their part in the Symposium and the exhibitor seminars.

E. L. Grove
A. J. Perkins

Contents

X-RAY SPECTROSCOPY

Dispersive and Nondispersive X-Ray Fluorescence Methods for the Measurement of the Thicknesses of Films of Cadmium Sulfide and Other II-VI Compounds	3
Frank L. Chan	
Applications of X-Ray Topography in the Characterization of Semiconductor Surface Layers	31
P. Wang and F. X. Pink	
High-Energy Electron-Diffraction and X-Ray Emission Analysis of Surfaces and Their Reaction Products	61
P. B. Sewell, D. F. Mitchell, and M. Cohen	
Surface Analysis with the Electron Probe	80
Gudrun A. Hutchins	
Experience with a Computer-Coupled X-Ray Spectrometer	97
F. Bernstein	
Use of Total Reflection at the Critical Angle for Dispersion of Ultrasoft X-Rays	108
Heribert K. Herglotz	
The Shift in Wavelength with Voltage of Certain X-Ray Lines	121
A. F. Burr and R. J. Liefeld	

EMISSION, FLAME, AND ATOMIC ABSORPTION SPECTROSCOPY

Spectroscopy Study of Hot Gases	133
Firouz Shahrokhi	
Analysis of Plant-Ash Solutions by Spark-Emission Spectroscopy	152
J. Benton Jones, Jr., and Myron H. Warner	

Routine Industrial Analysis of Stainless Steels	161
Robert L. Chapple and Charles A. Spellman	
Some Difficult Working Areas in Atomic-Absorption Flame Photometry	169
Juan Ramírez-Muñoz	
A New Look at Calcium Flame Interferences	189
R. E. Popham and W. G. Schrenk	
Some Experimental Considerations in Atomic Absorption	201
F. I. Grunder and E. A. Boettner	
An Experimental Device for Atomic-Absorption Spectroscopy	215
J. D. Johnson, G. K. Yamasaki, and J. C. Burger	
Indirect Atomic-Absorption Spectrometric Methods of Analysis	222
David F. Boltz	
Atomic-Absorption Spectrophotometry in Mineral and Trace-Element Studies in Man	227
Dace Osis, Kathryn Royston, Joseph Samachson, and Herta Spencer	

MASS SPECTROMETRY

Investigation of Solids by Means of an Ion-Bombardment Mass Spectrometer	239
H. W. Werner	
Application of Mass Spectrometry to Forensic Toxicology. I. Acidic and Neutral Drugs	267
Paritosh K. De and Charles J. Umberger	
Identification and Determination of Oxidation Inhibitors in Synthetic Lube Oils by Ultraviolet and Mass Spectrometry	274
John F. Kinder and James Neel	
Spectroscopy in Space – An Introduction and Overview	286
R. E. Ruckman	
A Computer-Controlled System for Automatically Scanning and Interpreting Photographic Spectra	294
C. A. Bailey, R. D. Carver, R. A. Thomas, and R. J. Dupzyk	

NUCLEAR PARTICLE SPECTROSCOPY

Nuclear Applications of Liquid Scintillation Systems	303
Donald L. Horrocks	

INSTRUMENTAL PARAMETERS

A Comparison of the Function of the Slit in Light-Absorption Studies Using Tungsten and Laser Sources	329
Martin J. Houle, Marvin O. Fretwell, and William J. Romig	
Index	339

X-Ray Spectroscopy

Dispersive and Nondispersing X-Ray Fluorescence Methods for the Measurement of the Thicknesses of Films of Cadmium Sulfide and Other II-VI Compounds

Frank L. Chan

*Chemistry Research Laboratory
Aerospace Research Laboratories
Wright-Patterson Air Force Base, Ohio*

Cadmium sulfide and other II-VI compounds have been deposited on various substrates by the vacuum technique using a setup consisting of a mechanical pump and a diffusion pump. Attempts are being made to employ a high-speed turbo-molecular pump to produce the necessary vacuum. Such pumps have been claimed to produce higher vacuum than those of earlier types. The use of x-ray fluorescence seems to be the best method for the determination of thicknesses of films of these compounds. By using this method the determination can be carried out both rapidly and nondestructively, so that the samples can be used for further experimentation or preserved for future reference. Both the vacuum and air-path spectrometers were employed with the dispersive (conventional) x-ray fluorescence method, depending on the x-ray spectra used and the film thickness to be determined. The vacuum spectrometer described earlier has been modified to improve the intensity of the secondary x-ray. The modified setup with low-Z kit has been changed to accommodate four analyzing crystals in the vacuum chamber. The radioisotopes dysprosium-159, iodine-125, and others were used with the nondispersing x-ray fluorescence method. Recent instruments based on the dispersive and nondispersing systems are described here. Some of these instruments have been used to measure the thicknesses of films of II-VI compounds.

INTRODUCTION

Since the discovery of the photovoltaic effect of cadmium sulfide and other II-VI compounds by the Aerospace Research Laboratories some fourteen years ago^{1,2} a great deal of work has been done on the use of these materials for the fabrication of solar cells for aerospace application, as well as on theoretical studies of the solid-state phenomena involved.

While single crystals are required for the fabrication of cells with such materials as silicon and germanium, cadmium sulfide need not be in this form.³ Films of the II-VI compounds can be and are being used for the fabrication of solar cells. In some respects the use of cadmium sulfide for the fabrication of solar cells has advantages over the use of the conventional materials. In spite of the conversion efficiency of 5.4%, pound for pound on the basis of material cadmium sulfide in the form of thin film is more efficient than thin films of silicon and germanium. Cells with thin film when properly fabricated can be made into rolls and these rolls can be spread out in space for energy conversion. In the present state of the art of the fabrication of cadmium sulfide solar cells certain film thicknesses are required. Normally, these cells have a nominal thickness of 18–20 μ . The overall thickness of a cell, including substrate and overlay, amounts to four mils.

In the 1950's much interest was centered on the use of the x-ray fluorescence method for determining the thickness of metallic films. Not only were thicknesses of tin, iron, and steel determined by this method nondestructively, but film thicknesses were also monitored using this principle.⁴

In the present study cadmium sulfide films were prepared by the vacuum technique on a number of substrates. Many difficulties were experienced and overcome in order to obtain the yellow cadmium sulfide with no apparent decomposition or contamination when using this high-vacuum technique. The sublimation temperature and the location of the substrate within the vacuum chamber appear to be critical for the optimum deposition. Two different devices have been worked out for the deposition of the film on the substrate. In the earlier preparation of films of cadmium sulfide and other II-VI compounds a commercially available vacuum evaporator consisting of a mechanical pump and a diffusion pump was used. However, in recent studies on zinc sulfide platelets the presence of oxygen in this compound causes a marked shift of the band gap. Therefore for the preparation of films of II-VI compounds every effort is being made to obtain as high a vacuum as possible. The presence of oxygen in the II-VI compounds is being investigated by the use of various chemical methods such as conversion from sulfide to sulfate and the use of such instruments as the electron probe as well as the more recent Betaprobe.

For the determination of film thickness for II-VI compounds both the dispersive and nondispersive x-ray fluorescence systems were used. In the dispersive system the primary x-ray from a target tube impinges on the sample located on its path, which produces the characteristic fluorescence x-ray. After passing through the collimator the fluorescence x-ray is directed toward an analyzing crystal and the diffracted beam is detected by a detector mounted on a goniometer. A setup of this type has certain disadvantages; however, for certain spectral regions it has been pointed out⁵ that the resolution for the dispersive system is far superior to that of the nondispersive system. For instance, in the soft x-ray region (less than 5 keV) the use of crystal diffraction gives resolution 50–100 times superior to either the use of the “balance filter” or pulse-amplitude discrimination using flow-proportional counters. Between 5 and 20 keV (medium-energy x-rays) the use of crystal diffraction

TABLE I
Gamma-Ray, K-Capture, Internal-Conversion Sources

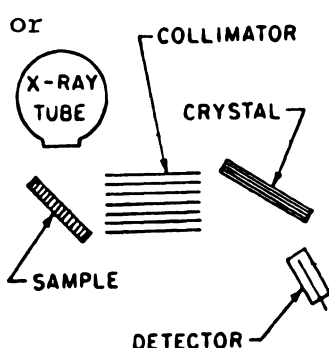
Radioisotope	Half-life	Type of decay; particle energy (keV); abundance	γ energy (keV); abundance	Internal conversion factor (%)	X-ray energy (keV)
⁵⁵ Fe	2.7 years	E.C. (100%)	-	-	5.9
¹⁰⁹ Cd	470 days	E.C. (100%)	88 (4%)	96	22
¹²⁵ I	57.4 days	E.C. (100%)	35.4 (7%)	93	27
²⁴¹ Am	470 years	α 5.44 MeV (13%) 5.48 MeV (85%)	27 (2.8%) 33 (0.2%) 60 (40%) Others	-	11–22
¹⁵³ Gd	236 days	E.C. (100%)	70 (2%) 97 (21%) 103 (25%)	9 8 35	41
¹⁷⁰ Tm	127 days	β^- 880 (22%) 970 (78%)	84 (3%) -	19 -	52 (4%) 7 (3%)
¹⁵⁵ Eu	1.7 years	β^- 154 (80%) 243 (20%) Others	87 105 Others, weaker	- - -	43
⁵⁷ Co	270 days	E.C. (100%)	14 (6%) 122 (88%) 136 (10%)	83 1 1	- 6.4 -
¹⁵⁹ Dy	144.4 days	E.C. (100%)	0.058 (26%) Others	83	(Tby x rays)

gives resolution 2–20 times superior to the use of lithium-drifted silicon detection.

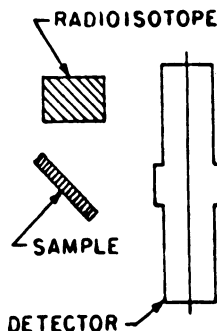
For the nondispersive method a radioisotope such as dysprosium-159, having a half-life of 144.4 days, or iodine-125, having a half-life of 57.4 days (see Table I) is used to excite the samples under investigation. Other radioisotopes are also available.^{5–8} The choice of the radioisotope is dependent upon the elements being investigated. The fluorescence x-ray from the sample is detected by a lithium-drifted silicon semiconductor in conjunction with the associated electronic circuitry, which comprises preamplifier, amplifier, pulse-height selector, recorder, and printer.⁶ It has been pointed out^{5,8,9} that the introduction of lithium-drifted silicon and germanium detectors represents a significant advance in x-ray spectrography. Because of the improvement in resolving power nuclear researchers can presently accomplish in one day what previously required a year.

One of the purposes of this chapter is to present a study of the rapid thickness measurement of films of II–VI compounds by the x-ray fluorescence methods, using the most up-to-date instruments. The methods used were the dispersive (conventional) system and the nondispersive method using radioisotope sources. In the dispersive system the secondary x-ray may be produced by the primary x-ray from an x-ray tube or by the bombardment of low-energy electrons on the sample by an electron gun in the Betaprobe setup. In the nondispersive system a radioisotope x-ray source is used. The detector in such a system is the proportional counter with a suitable filter or lithium-drifted silicon semiconductor. Both systems are shown in Fig. 1.

Electron Gun or



DISPERSIVE SYSTEM



NONDISPERSIVE SYSTEM

Fig. 1. Comparison of the dispersive (conventional) and the nondispersive x-ray fluorescence methods for the determination of the thickness of films of II–VI compounds.^{5,18}

INSTRUMENTATION

Conventional X-Ray Spectrometer

The spectrometer is part of the XRD 6 installation made by the General Electric X-Ray Department. This installation in its initial setup has been described.^{10,11} Since that time many modifications have been made. Essentially, it has an up-to-date x-ray generator capable of operating at 75 kVp and 60 mA for the tungsten target and at 75 kVp and 50 mA for the chromium target. The detector is an SPG-4 and is connected to two up-to-date spectrometers with dual targets (tungsten and chromium), a vacuum emission spectrometer SPG 6 VS, and an air-path or helium-path emission spectrometer SPG 6 S having a molybdenum target specially designed for the determination of film thickness for II-VI compounds. Detailed descriptions of this installation have previously been published.¹⁰⁻¹⁴ Further modifications of the instrument have been made in order to improve the count rate for measurements on II-VI compounds which contain sulfur. These modifications include the low-Z kit for increasing the count rate of the low atomic number, the installation of the four-crystal changer with remote-control mechanism, and the shortening of the gap between the sample and the target tube. The No. 7 flow-proportional counter will soon be replaced by a No. 9 counter in order to improve the counting statistics.

The rapid determination of film thickness for the II-VI compounds has been supplemented by other related studies, and therefore a number of other x-ray instruments have been made available, such as the XRD 6 D/F for film work and for diffraction work employing a diffractometer. Two Norelco x-ray units have also been installed with two different target materials.

The Betaprobe

In recent months the Betaprobe, developed in England (by Telsec), has been introduced into the United States for the quantitative measurement of light elements as well as for other research applications. It is based on a principle similar to the electron probe, with the exception that in the Betaprobe the electron beam is defocused to a $\frac{1}{2}$ in.² area. The vacuum of the system can be quickly reestablished after changing samples. For rapid analysis of samples six to eight channels are provided with each instrument. It also provides a scanning head when measurement of 20 angles is required. As in the conventional method, the optical arrangement is made up of solar slit, analyzing crystal, secondary solar slit, and x-ray detector. The suitable wave-

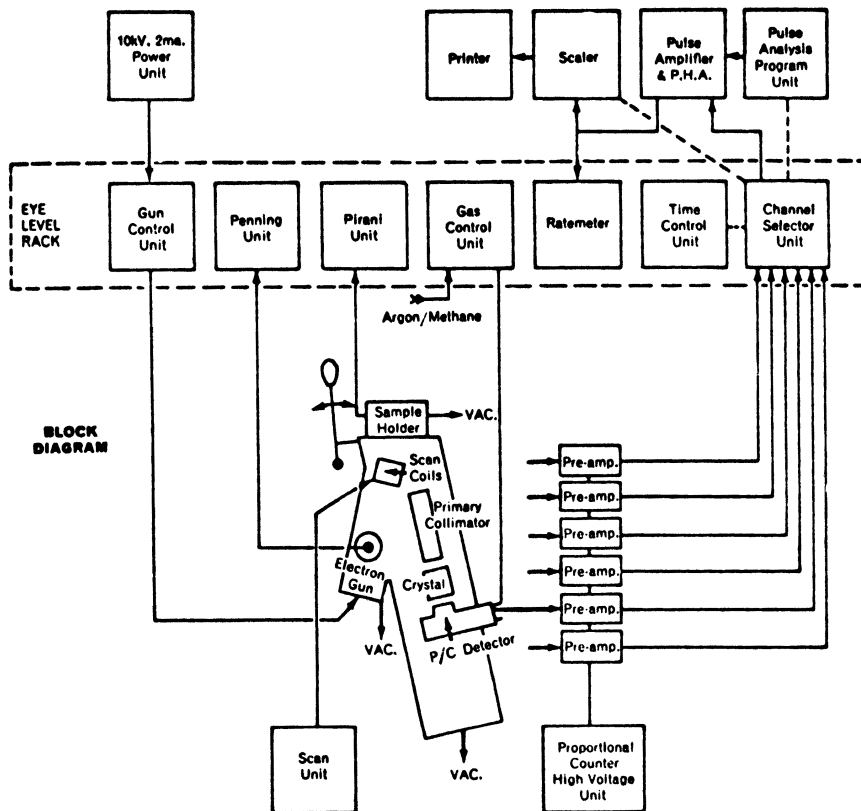


Fig. 2. Diagram of Betaprobe made by Telsec, England.

length range for this probe is between 3.2 \AA and 100 \AA . The overall system is shown in Fig. 2.

Nondispersive System

The instrument used in the present film measurements on the II-VI compounds is shown schematically in Fig. 3.

The Use of Balance Filters and the Sealed Proportional Counter. A battery-operated x-ray spectrometer using a radioisotope source was used to analyze cadmium and zinc selenides. It is based on the central-source geometry illustrated in Fig. 3. The secondary x-ray produced from the after-excited sample is directed to two filters placed above the sealed proportional counters. Some suitable filters for the II-VI compounds are listed in Table II. Opera-

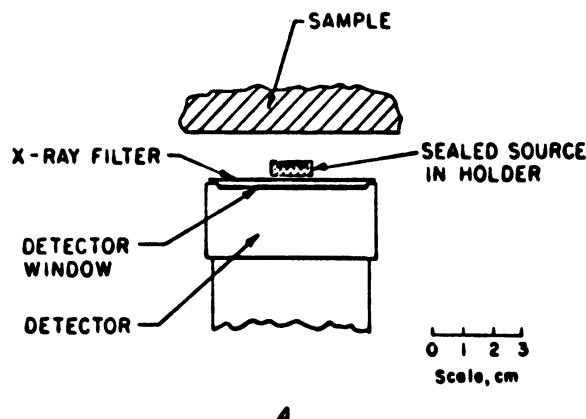
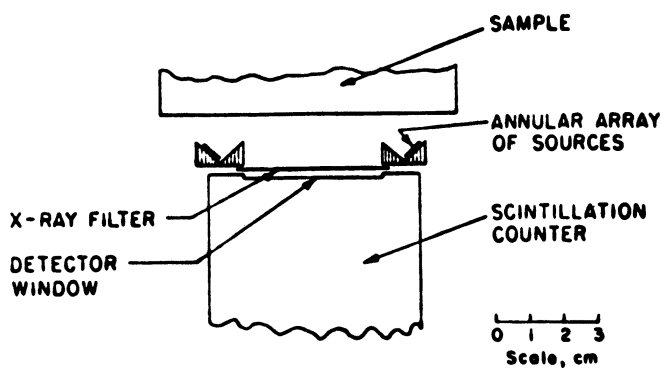
**A****B**

Fig. 3. Central (A) and annular source (B) geometries for the nondispersive system.^{5,8}

TABLE II
Some Suitable Filters for the Measurement of Films of
II-VI Compounds by the Fluorescence Method

<i>K_a</i> spectra	Filter pair	<i>L_{a1}</i> spectra	Filter pair
Zn	Cu, Ni	Cd	Pd, Ru
S	S, P	Te	In, Sn
Se	As, Ge	Hg	Au, Pt

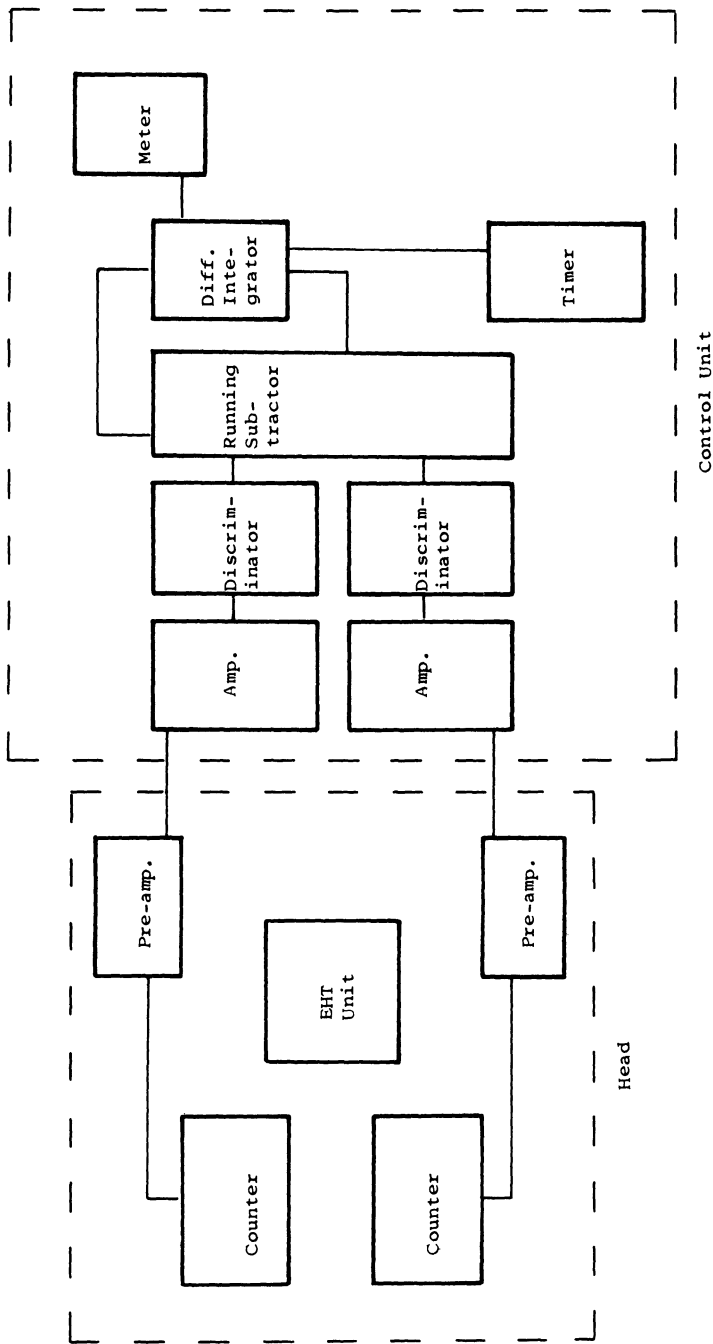


Fig. 4. Diagram of portable x-ray spectrometer (Telsc, England).

ting the proportional counters is accomplished by the use of either ordinary electric circuit or with 20 batteries of 1.5 V connected in parallel with ten cells in series. The unit with two proportional counters (filter and sample are not shown) is shown schematically in Fig. 4.

The twin sealed proportional counters receive x-rays from the sample, which has been excited by the γ -radioactive source. These x-rays pass through the balance filter. One of these filters allows the background and the signal to pass; the other filter allows only the background to pass. The counts are subtracted to obtain a differential count rate which is proportional to the thickness of the film in question. For thickness measurement the thickest film is set at the maximum scale and the intensity taken. Intermediate thicknesses are then determined and plotted. A calibration curve, consisting of the linear portion of the scale reading versus film thickness curve, can be obtained for each compound. Figure 4 shows the flow chart of a portable x-ray spectrometer (made by Telsec, England).

The Use of the Lithium-Drifted Silicon Semiconductor. This is shown schematically in Fig. 5. The use of this semiconductor represents a breakthrough in x-ray spectrography.⁵ It has been pointed out that for Ag $K\alpha$ (22 keV) and Au $K\alpha$ (68 keV) the lithium-drifted silicon detector has a pulse width 2–3 times sharper than a proportional detector and 6–7 times sharper than a scintillation detector. Counting time is usually several minutes.

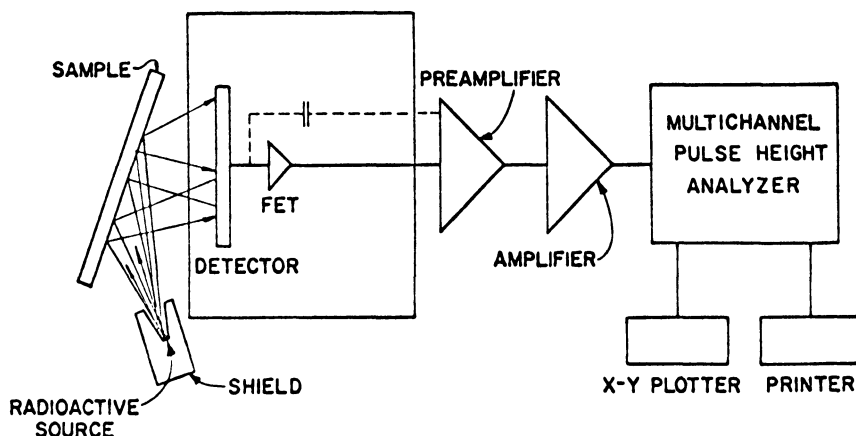


Fig. 5. Diagram of photon spectrometer using lithium-drifted silicon detector (Technical Measurement Corp.).^{6,9}

Vacuum Evaporators and the Preparation of Films

The Use of the Diffusion Pump. Films of II-VI compounds are vacuum deposited on various substrates. The equipment (Model CVC 14 manufactured by the Consolidated Vacuum Corporation) has a diffusion pump, baffle, valve, manifold, base plate, and an ionization gauge. A bell jar 18 in. in diameter with guard and hoist is placed on the base plate, and substrates for deposition are placed inside the bell jar before it is evacuated. The evacuation of the system is carried out in two steps. In the first step most of the air in the jar is removed by a mechanical pump until the chamber pressure is 50–100 mtorr. In the second step the diffusion pump takes over and reduces the pressure to $8\text{--}9 \times 10^{-6}$ torr.

The Use of the Turbo-Molecular Pump. In recent studies on zinc sulfide crystal and platelet the presence of oxygen in this compound caused a marked shift of the band gap, and therefore, for the preparation of films of II-VI compounds, every effort was made to obtain as high a vacuum as possible.

It has been claimed that by the use of the turbo-molecular pump in conjunction with the mechanical pump a vacuum can be obtained as high as 10^{-9} torr. Therefore a turbo-molecular pump was procured from the Welch Scientific Company of Chicago. A complete setup designed by this author is shown in Fig. 6. On top of this pump a specially prepared collar was installed. The purpose of installing this collar is to make the setup more versatile. The collar shown is constructed of a stainless steel pipe $7\frac{1}{2}$ in. in diameter. Holes were driven through the pipe to accommodate the ionization gauge, the thermocouple, the two filament electrodes, the two substrate heater electrodes, and the valve for the admission of inert gases, and one extra hole was driven, making a total of eight holes in all.

The pipe was welded to two flanges so that the lower flange fit tightly to the turbo-molecular pump. The upper flange is attached to a ready-made base plate with the same number of holes provided for the same purposes as described for the collar.

There are three bell jars, one 10 in., one 12 in., and one 18 in. in diameter. Using the fitting described, if a small number of samples or small area is to be experimented upon, the small bell jar is used. When more samples are to be evaporated the 12 in. jar is used, and when a larger area is to be prepared the 18 in. bell jar is used.

The meter that is connected to the system can detect vacuum to 10^{-9} torr. Vacuum evaporation using the 10 in. bell jar requires 2–3 min to reach 10^{-4} torr, 4–5 min to reach 10^{-5} torr, and 45 min or longer to reach 10^{-6} or 10^{-7} torr. For the 10 in. and 12 in. bell jars the electrodes located as shown



Fig. 6. A vacuum evaporator using a turbo-molecular pump.

on the steel collar were used, and for the 18 in. bell jar those located on the base plate were used.

Preparation of Films and Methods Used in the Construction of Calibration Curves. Pure II-VI compounds for which films are to be prepared are

placed in a fused quartz boat or molybdenum boat and are heated electrically by introducing electrical connections through the base plate. An ammeter is connected to the heating circuit and the temperature for heating these compounds is calibrated against the meter reading. A calibration curve, temperature versus ampere reading, was obtained by using a thermometer at lower temperatures and an optical pyrometer at higher temperatures.

To prepare films of desired thickness, the compound is placed in the boat, with substrates properly placed above the boat, within the bell jar. The system is then evacuated, first by a mechanical pump and then by the diffusion pump. Successful preparation of the film depends on the vacuum in the system, the temperature (and therefore the rate of deposition), and the position and distance of the substrates with respect to the compound in the boat. Usually, with a film of 1–2 μ in thickness it is not necessary to heat the substrate. A device for heating the substrate is provided for thicker films. For thin films the substrates are placed inside the chamber in pairs, one film behind the other, so that only one side of each is coated.

With the exception of mercuric selenide, the compounds are resublimed before being used. Each material is provided with a boat for sublimation, to avoid contamination.

Prior to the quantitative determination of the film thicknesses of II–VI compounds by conventional dispersive and nondispersive methods preliminary examination was carried out by visual inspection of the evenness of the film and of the possibility of decomposition. If the film shows fringes, unevenness is the cause. Unevenness can be determined by a method previously described.¹⁴ The greater number of fringes per centimeter the greater the unevenness.

Since neither x-ray fluorescence method is an absolute method, calibration curves are needed. Several methods are used for constructing these curves. The nonspecific method is based on the weighing of substrate of known dimension before and after the deposition of the film. A second method is the chemical analysis of the cation, such as cadmium, by the removal of the sulfide or the selenide by hydrochloric acid in the absence of air. Any insoluble free sulfur or free selenide is removed by filtration. The cadmium is then converted into the sulfate by addition of sulfuric acid, and is cautiously evaporated to remove the excess sulfuric acid. Finally, it is ignited in a platinum crucible up to 400–450°C and weighed as the sulfate.¹⁵ Inert substances such as glass, Pyrex, or polymers, which are not attacked by hydrochloric acid or sulfuric acid, are suitable substrates for this procedure. In a third method sulfides can be oxidized by strong oxidizing agents to the sulfate, precipitated with barium chloride, and weighed as barium sulfate. In a fourth method, selenide is determined volumetrically by oxidizing it to the selenide

with nitric acid. After destroying the nitric oxide by urea the cooled solution is added to potassium iodide in excess. The liberated iodine is then titrated with standard sodium thiosulfate.^{12,14}

Neutron-activation and laser-microprobe methods for checking the thickness of these films have also been used. Results of these findings will appear in a separate publication.

The suitable sample size is 2 in. \times 2 in. for the vacuum spectrograph and $1\frac{3}{4} \times 1\frac{7}{8}$ in. for the air-path spectrograph. Films with substrate can be $\frac{1}{8}$ in. or more in thickness.

For the conventional spectrograph the sample is placed in the holder provided (four samples can be placed in the vacuum spectrograph before evacuation of the spectrograph), the goniometer is turned to the proper setting for the spectra of interest, and the intensities of the spectral lines are recorded. Net count is the difference between the total count and the average of the background counts taken from each side of the peak spectral line, 0.5–3.0 from the peak angle, depending on the element determined.

For the nondispersive method using the radioisotope for exciting the characteristic x-ray fluorescence the sample size (or smaller) cited for the conventional method can also be used. By this method a sample can be placed next to the radioisotope source and analyzed by storing the counts in the pulse-height analyzer. Permanent records for this count are taken by the use of the printer and the *X-Y* recorder.

RESULTS AND COMMENTS

As pointed out earlier, since the x-ray fluorescence method, either dispersive or nondispersive, is not an absolute method, a calibration curve based on the count rate as ordinate and film thickness as abscissa is highly desirable and to a certain extent necessary. Experience in the past two years has shown that a reliable calibration curve for films of II-VI compounds can be obtained, but with much difficulty, especially for thin films up to 1 μ thick, because a number of errors are encountered when obtaining the experimental points on the curve. However, after much experimentation it was found that the count rate of zinc *Ka* for elements with atomic number greater than 30 is not affected by layers of polymers such as Mylar placed over the film. Table III shows that placing as many as eight layers of $\frac{1}{4}$ in. Mylar over the films of II-VI compounds does not affect the counts of *Ka*.¹⁶ It was further shown that these films can be coated on the Mylar several microns in a number of cases. It is therefore possible to construct a calibration curve by placing coated Mylar layers of known film thickness one upon another. Based

TABLE III
Effect of the Presence of Mylar on Thickness Measurements
on Cadmium Selenide Films*

Selenium $K\alpha$ (PHS in)		Cadmium $K\alpha$ (PHS out)	
No Mylar (net. counts per second)	Eight layers Mylar (net counts per second)	No Mylar (net counts per second)	Eight layers Mylar (net counts per second)
60151	60170	38055	38553
60022	60134	37955	38527
60132	60063	37999	38462
60061	60009	38034	38383
60007	60024	38002	38511
av. 60075	60080	38013	38487

*Conditions: Mo target; 60 kVp, 10 mA; analyzing crystal, LiF; scintillation counter.

on this procedure a number of curves were obtained using different II-VI compounds and film thicknesses.

Figure 7 shows a calibration curve for the characteristic x-ray spectrum of CdTe films using the radioisotope dysprosium-159. The four peaks are from 200-channel recorder chart. These peaks are Cd $K\alpha$ on channel 115, Te $K\alpha$ on channel 138, and Cd $K\beta$ on channel 158. The scale on the right is excitation energy in keV. A straight line can then be drawn, and this calibration curve is used for films of CdSe, CdTe, and CdS. The peak positions of Se $K\alpha$ and Se $K\beta$ appear at the positions expected. The same curve for the radioisotope iodine-125 was also calibrated for peak position and used for ZnS and HgSe.

Aluminum-coated CdS films were explored with a Betaprobe, as described under Instrumentation. Calibration curves are shown in Fig. 8. Unknown samples were determined by the use of these curves. Table IV shows the results. Counting errors based on repeated measurements of S $K\alpha$ have also been determined and are shown in Table V.

Figure 9 shows a comparison between the conventional and nondispersive systems for measuring the film thickness of cadmium sulfide. For the conventional method a molybdenum target and a scintillation counter were used, and cadmium $K\alpha$ was used for the determination of film thickness. A straight line can be drawn for count rate versus thickness over the range of the experiment (0-4.4 μ). Similarly, in the nondispersive method a straight line can also be

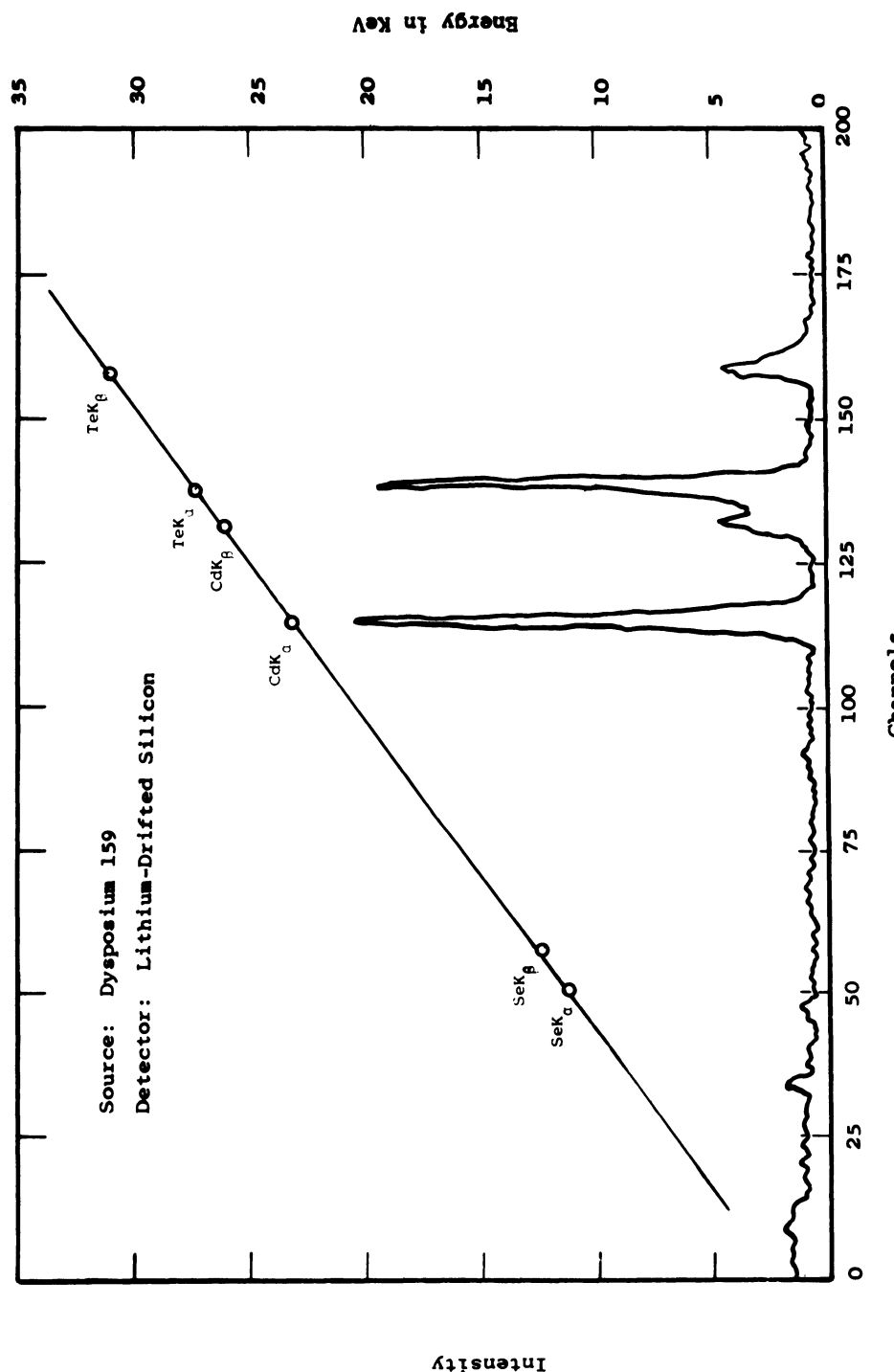


Fig. 7. Characteristic x-ray spectrum of a film of cadmium telluride, used for calibration.

TABLE IV
Thickness Determination of Films of CdS Based on
S Ka and Al Ka (Substrate Peak) with Betaprobe*

S Ka cps	Thickness, μ	Al K	Thickness cps	Difference μ
89,317	0.512	—	—	—
79,144	0.454	50,503	0.428	-0.026
9,272	0.051	76,974	0.050	-0.001
6,683	0.036	76,637	0.053	0.017
6,560	0.035	77,108	0.046	0.011
6,831	0.036	77,374	0.042	0.006
5,864	0.031	77,401	0.045	0.014
20,842	0.118	73,398	0.105	-0.013
13,550	0.075	75,940	0.069	-0.006
4,881	0.024	79,481	0.016	-0.008
91,820	0.526	46,270	0.494	-0.032

*For operating conditions, see Fig. 8.

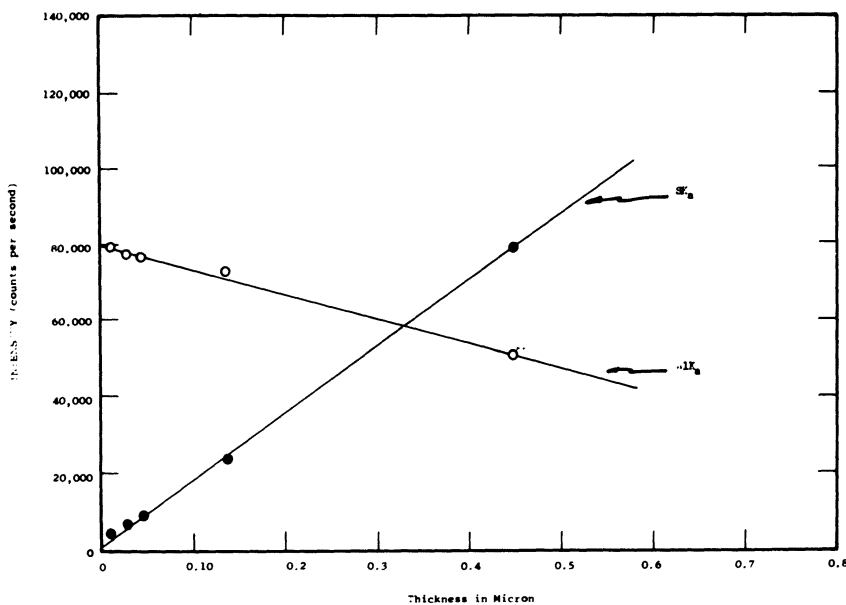


Fig. 8. Calibration curves for the determination of the thickness of CdS on an aluminum substrate with the Betaprobe. Conditions: 10 kV; 0.2 mA; analyzing crystal: NaCl for S Ka, EDDT for Al Ka; collimation, 1° divergence; PHA: $E = 1.0$ V, $\Delta E = 0.4$ V for Al Ka, $E = 1.0$ V, $\Delta E = 0.8$ V for S Ka; 10 seconds counting time; flow-proportional counter with Mylar window with 10% methane and 90% argon.

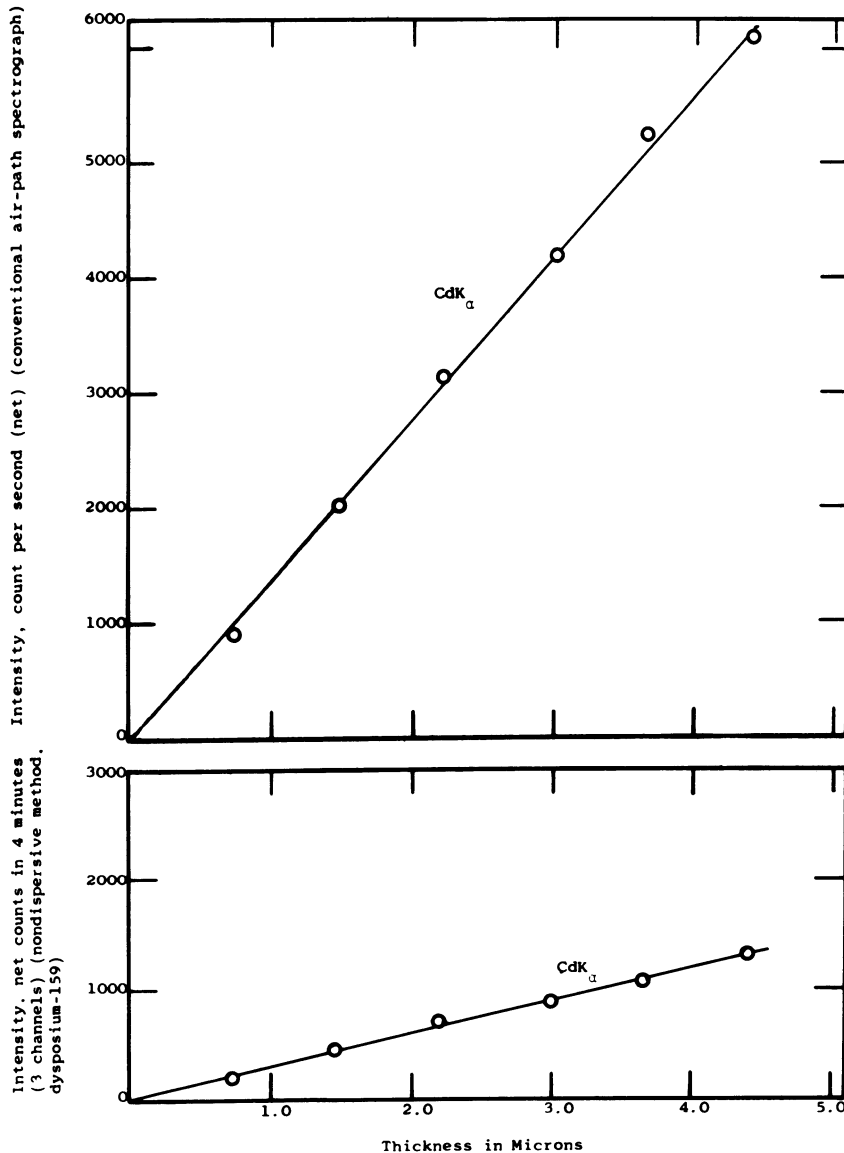


Fig. 9. Comparison of conventional and nondispersive x-ray fluorescence methods for the determination of film thickness for cadmium sulfide. Conditions: Upper graph—Mo target; no PHS; air path; 60 kVp, 10mA; analyzing crystal, LiF; scintillation counter. Lower graph—radioisotope, dysprosium-159; PHA channels, 200; total counting time, 4 min, lithium-drifted silicon detector.

TABLE V
Counting Error Based on Repeated Measurements
of S Ka Using Betaprobe
 $\sigma\% = 100/\sqrt{N}$

	Counts per second*	\sqrt{N}	$100/\sqrt{N}$
1.	77,909	279.12	0.358
2.	78,043	279.36	0.358
3.	77,713	278.77	0.359
4.	77,907	279.12	0.358
5.	77,776	278.88	0.359
6.	77,692	278.73	0.359
7.	77,600	278.57	0.359
8.	77,532	278.45	0.359
9.	77,364	278.14	0.360
10.	77,079	277.63	0.360
11.	77,006	277.50	0.036

* One-tenth of ten-second counts; for other operating conditions, see calibration curves Fig. 8.

obtained by plotting total counts taken from three channels for the Cd *Ka* using a 4 min counting time and a dysprosium-159 radioisotope.

For thicker cadmium sulfide films, ranging between 0 and 18 μ and using Cd *Ka* for the determination of the thickness, three calibration curves were constructed using the conventional, vacuum, and air-path spectrographs and the nondispersive method. These curves are shown in Fig. 10. These curves were used to analyze a number of samples prepared by the Clevite Electronic Research Corporation, Cleveland, Ohio. The thickness of these films on Pyrex was determined by the optical method independently by that establishment and by the Aerospace Research Laboratories. The optical method used is known to have a precision of $\pm 1.0 \mu$ for the cadmium sulfide film deposited by the vacuum technique. Results reported by these organizations are shown in the figures. In spite of the fact that the precision which can be obtained by the x-ray fluorescence method depends on the intensity of the beam, the duration of counting, and the area of sample exposed to the incident beam, cadmium sulfide films can be analyzed, as the results indicate, with greater precision than by the optical or other methods. Film samples can be determined by x-ray fluorescence methods rapidly and nondestructively.

Other experimental results have also been obtained for the analysis of cadmium sulfide films using S *Ka* and Cd *L β_1* . When LiF is the analyzing crystal *La*₁ cannot be used with the available instrument. There are two restrictions to the use of these spectra. First, these spectra are in the soft x-ray region, and attenuation by air is excessive. Therefore an x-ray vacuum

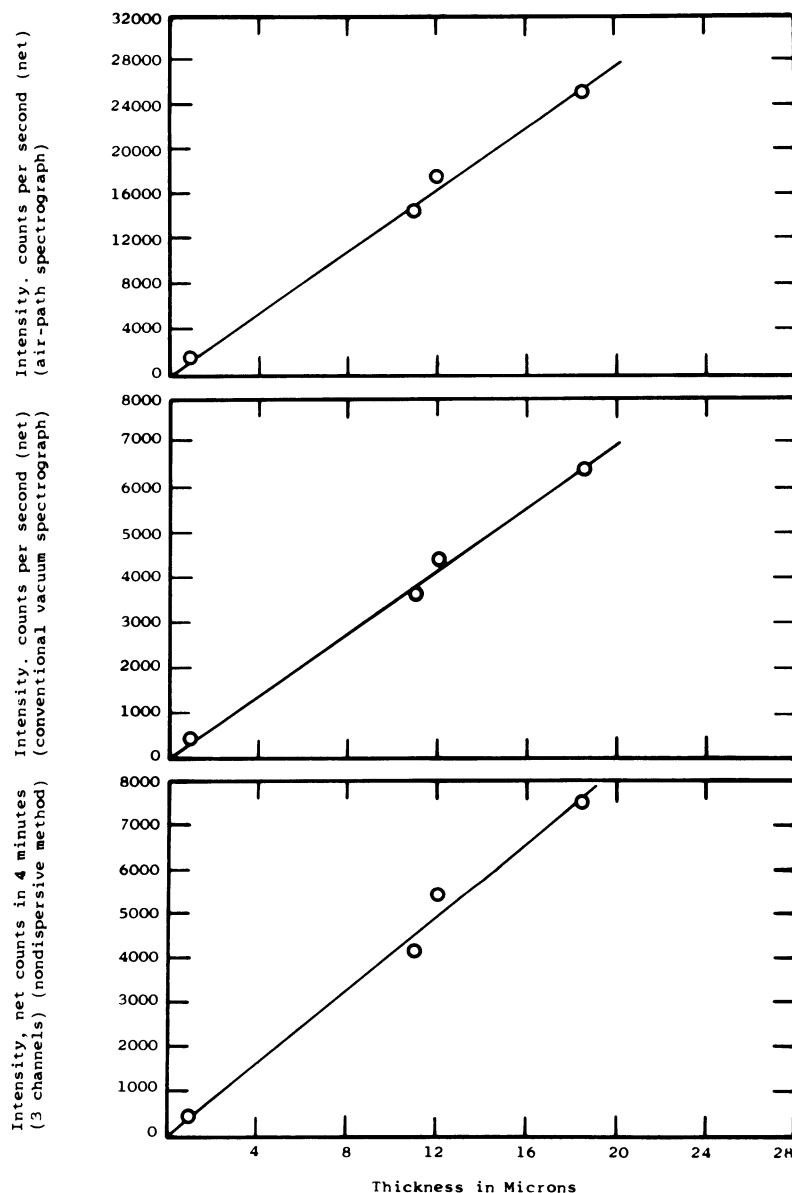


Fig. 10. Determination of film thickness for cadmium sulfide using conventional vacuum (upper graph) and air-path (middle graph) x-ray spectrophotographs, and using the nondispersive x-ray fluorescence spectrometer with the radioisotope dysprosium-159 (lower graph). Conditions: Upper graph—Mo target; no PHS; air path; 60 kVp; 10 mA; analysing crystal, Li; scintillation counter. Middle graph—W target; no PHS; vacuum; 5–10 μ ; 60 kVp; 50 mA; analyzing crystal, LiF; No. 7 proportional counter. Lower graph—Radioisotope, dysprosium-159; PHA channels, 200; total counting time, 4 min; lithium-drifted silicon detector.

spectrograph is required to detect these spectra. Second, only comparatively thin films can be analyzed since the linear region of the count rate versus film thickness curve is in the range 0–1 μ .

Figure 11 shows the intensity of Se Ka and Cd Ka plotted against film thickness up to 7 μ as found by the conventional and the nondispersive systems. For Cd Ka the linear region can be extended to thicknesses of 16 μ .¹⁰ However, for Se Ka and films of cadmium selenide the linear region is about 2 μ . Beyond this region the slope starts to decrease. This is true with both the conventional and the nondispersive methods. The conditions and radioisotope used in this determination are the same as those used for cadmium sulfide.

For the analysis of film thickness using Se Ka it is necessary to use the pulse-height selector because of second-order Cd Ka in the vicinity of the 2 θ angle of Se Ka . Intensity from the second-order Cd Ka can be eliminated by this means.

Analysis of measurements of cadmium telluride films is shown in Fig. 12. As for cadmium selenide, the use of the molybdenum target in the conventional system to excite the Cd Ka resulted in low count rate for this element. For instance, since selenium has lower atomic number, the count rate of Ka for this element under the experimental conditions described is in excess of three times that of Cd Ka , as shown in Fig. 11. The count rate of Te Ka with tellurium having a higher number than cadmium, is even lower than that for Cd Ka . Figure 12 shows that by using the nondispersive system with the dysprosium-159 radioisotope the same low count rate as for Te Ka was found. Straight lines in the intensity versus film thickness curve can be constructed for both Te Ka and Cd Ka as shown in this figure. Films as thick as 20 μ can be determined by both the conventional and nondispersive methods.

Curves for Hg La_1 and Se Ka in films of mercuric selenide are shown in Fig. 13. Since the scintillation counter in the spectrograph has a high efficiency in this spectral region, and since the molybdenum target is used, one would expect a high count rate for both Hg La_1 and Se Ka . The count rate appears higher than for the other selenide shown. Intensities determined by the conventional method, as shown in Figs. 9 to 13, were many times greater than those determined by the nondispersive method using the radioisotopes iodine-125 and dysprosium-159. However, a straight line can be drawn among the experimental points in both cases. Table VI shows a comparison of count rates for several II-VI compounds using the conventional x-ray fluorescence method.

The precision in a determination of a 11.5- μ film thickness for cadmium sulfide on Pyrex by the nondispersive x-ray fluorescence method is shown in Table VII. Successive 4 min. counts on this sample were taken. The total counts (three channels) and the background counts are listed. The method for

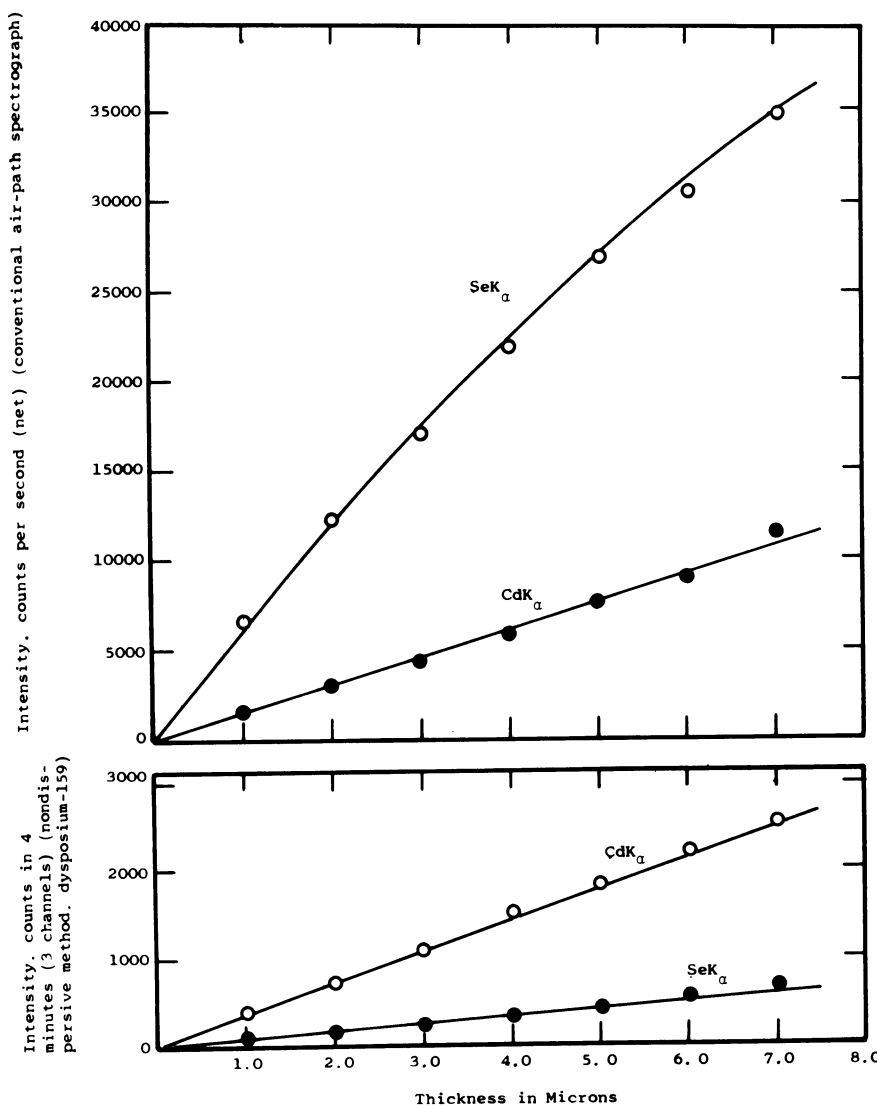


Fig. 11. Comparison of conventional and nondispersive x-ray fluorescence methods for the determination of film thickness for cadmium selenide. Conditions: Upper graph—Mo target; no PHS; air path; 60 kVp, 10 mA; analyzing crystal, LiF; scintillation counter. Lower graph—Radioisotope, dysprosium-159; PHA channels 200; total counting time, 4 min; lithium-drifted silicon detector.

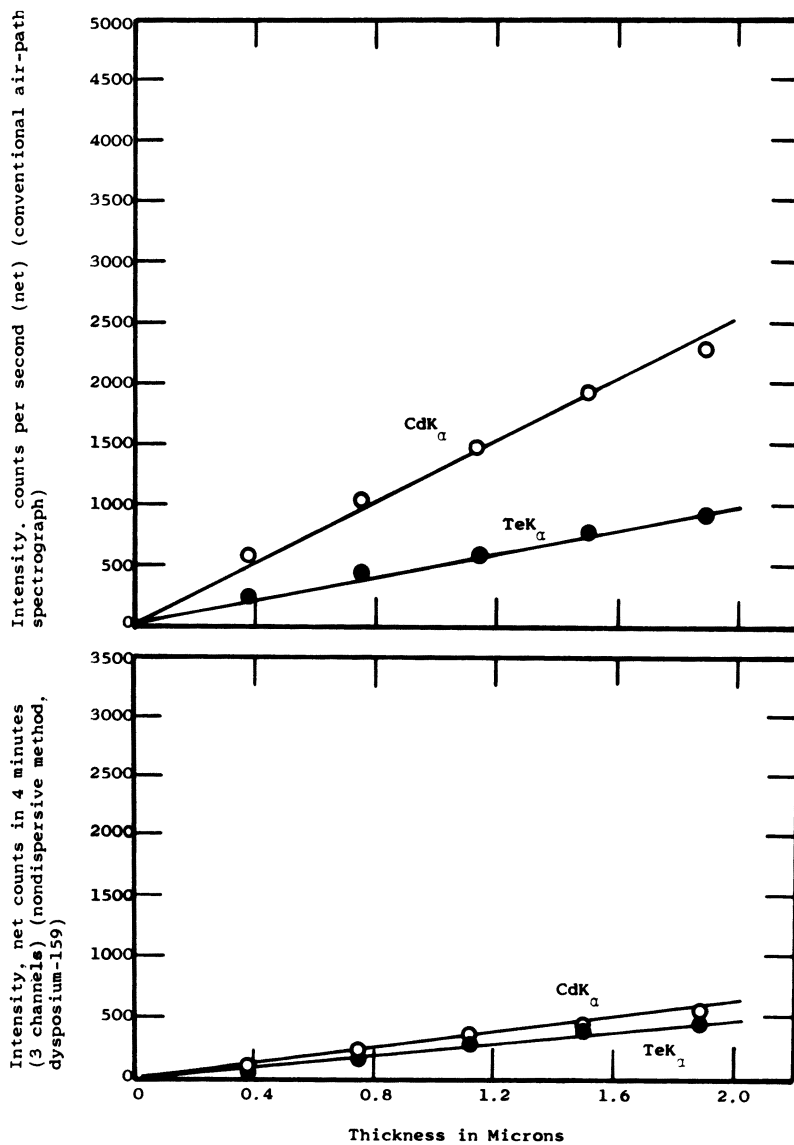


Fig. 12. Comparison of conventional and nondispersive methods for the determination of film thickness for cadmium telluride. Conditions: Upper graph—Mo target; no PHS; air path; 60 kVp, 10 mA; analyzing crystal, LiF; scintillation counter. Lower graph—Radioisotope, dysprosium-159; PHA channels, 200; total counting time, 4 min; lithium-drifted silicon detector.

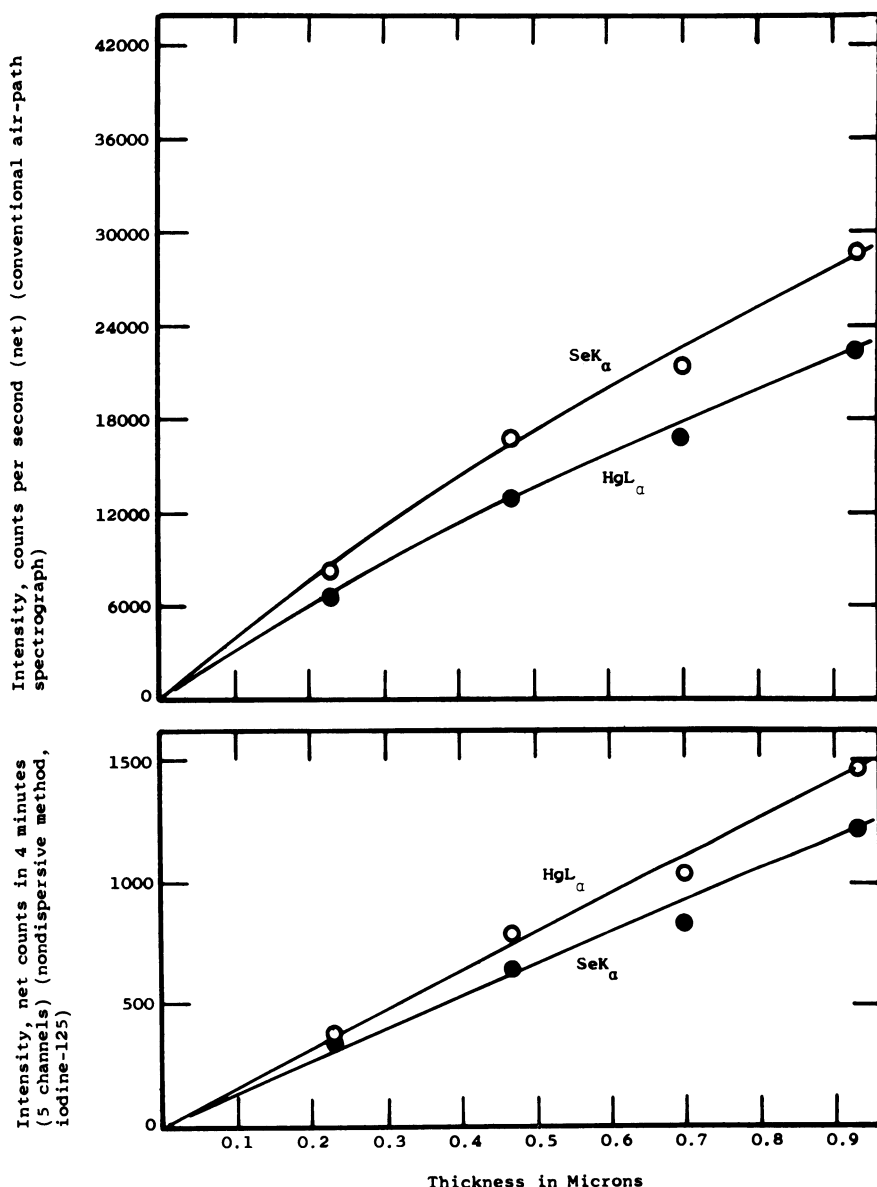


Fig. 13. Comparison of conventional and nondispersive methods for the determination of film thickness for mercuric selenide. Conditions: Upper graph—Mo target; no PHS; air path; 60 kVp, 10 mA; analyzing crystal, LiF; scintillation counter. Lower graph—Radioisotope, iodine-125; PHA channels, 200; total counting time, 4 min; lithium-drifted silicon detector.

TABLE VI
Comparisons of Count Rates for Several II-VI Compounds
Using the Conventional X-Ray Fluorescence Method*

Films of II-VI compounds	Spectra used	PHS	Counts per second (net) per μ thickness
ZnSe	Zn $K\alpha$	Out	12,800
	Se $K\alpha$	Out	28,900
CdSe	Cd $K\alpha$	Out	7,400
	Se $K\alpha$	In	28,800
CdTe	Cd $K\alpha$	Out	3,900
	Te $K\alpha$	—	2,000
CdS	Cd $K\alpha$	Out	5,600
	—	—	—
HgSe	Hg $L\alpha$	Out	24,000
	Se $K\alpha$	Out	30,100

*Conditions: Mo target; air path; 60 kVp, 50 mA; analyzing crystal, LiF; scintillation counter.

TABLE VII
Counting Error for Nondispersive X-Ray Fluorescence Method*

	Total counts, N_T	Background counts, N_B	Net counts, $N_T - N_B$	$\sqrt{N_T + N_B}$	Counting error in parts per 100, x^\dagger
1.	4277	90	4186	66.08	1.58
2.	4235	81	4154	65.70	1.58
3.	4213	88	4125	65.58	1.59
4.	4249	92	4157	65.89	1.59
5.	4231	76	4155	65.63	1.58
6.	4200	71	4129	65.35	1.58
7.	4205	65	4140	65.35	1.58
8.	4237	74	4163	65.66	1.58
9.	4146	86	4060	65.05	1.60
10.	4169	57	4112	65.01	1.58
11.	4229	69	4160	65.56	1.58

*Conditions: Four minutes counting time; three-channel counts; dysprosium-159 radioisotope for excitation; lithium-drifted silicon detector.

$$\dagger x = 100 \sqrt{N_T + N_B} / (N_T - N_B)$$

deriving counting error involving background counts has been described.¹⁷ Counting errors in parts per 100 are listed in the last column of Table VII.

Nondispersive and dispersive x-ray fluorescence methods have been compared. Various aspects of these methods are listed in Table VIII.

TABLE VIII
DETERMINATION OF II-VII-COMPOUND FILM
THICKNESS BY NONDISPERSIVE AND DISPERSIVE
X-RAY FLUORESCENCE METHODS

	Nondispersive (radioisotope)	Dispersive (conventional)
Measurement of thickness	Rapid	Rapid
Nondestruction of samples	Yes	Yes
Simultaneous display of spectra	Yes	No
Detector	Lithium-drifted silicon or germanium; proportional or scintillation counter	Proportional and/or scintillation counters
Temperature of detector	Cooled to liquid nitrogen	Room temperature
Instrument setup	Compact	Bulky
Preparation of sample	Simple	Simple
Mobility of instrument	Mobile	Permanently installed in laboratory
Capability of instrument	Elements with atomic number 20 and above can be measured	With special setup boron or carbon can be measured
Excitation of spectra	Depends on radioisotope used; high-energy radioisotope can excite all <i>K</i> spectra	<i>K</i> spectra of heavy elements cannot be excited by ordinary instrument

Thin films of II-VI compounds have been studied from other aspects. For instance, the methods of activating and recrystallizing have been described by Vecht and Apling¹⁹ and by Vecht.²⁰ The mechanisms of the photovoltaic effect in thin-film solar cells have been studied.³

On the subject of nondispersive x-ray fluorescence analysis, Campbell and Brown listed²¹ no less than 120 papers dealing with this subject. There were 53 papers on instrumentation, including such topics as detectors, filters, operating principles, radiation safety, radioisotope sources, and spectral convolution. The remainder of the 120 papers deals with applications.

CONCLUSIONS AND SUMMARY

A new versatile device employing a turbo-molecular pump has been constructed for the efficient vacuum evaporation of films of II-VI compounds. Three compartments of different capacities can be chosen for such evaporation.

Four instruments of dispersive and nondispersive type have been described for the measurement of films of II-VI compounds. The usefulness of each instrument was discussed, as were the merits of each system.

Calibration curves for these compounds can be constructed with precision and are based on a method of measuring multiple layers of thin films of predetermined thickness.

Which spectral lines to use for the determination of film thickness depends on a number of factors, including the thickness and kind of film being measured. For instance, S $K\alpha$ and Cd $L\beta_1$ can be used very well for thin films. Cd $K\alpha$ and Te $K\alpha$ are used for thicker films. The choice also depends on the interference provided by the target material. In any case, by using the x-ray fluorescence method the samples subjected to analysis are not destroyed, and therefore can be used for future references.

A number of substrates for these films have been tried. With the exception of molybdenum and niobium, common substrates such as Pyrex, soft glass, polymers, Al, Cu, etc., do not affect the count rate to any great extent.

Undoubtedly, there will be a very rapid increase in the application of the nondispersive system using radioisotope excitation sources. Some of the advantages of this system are low cost, wide excitation selectivity, and stability. The instrument is portable and simple to operate either using the balance-filter principle or the recently discovered lithium-drifted silicon semiconductor. Such an instrument is well adapted to film-thickness measurement. Many of the difficulties encountered in other methods such as the matrix effect, the question of inhomogeneity, particle size, and many kindred phenomena do not enter here in dealing with film thickness of II-VI compounds.

ACKNOWLEDGMENTS

The author would like to thank Dr. W. Barclay Jones, formerly of the Technical Measurement Corporation and now a Professor at Yale University, for assistance with the measurements using the photon spectrometer. Mr. A. E. Hutching and staff assisted with the measurement using the portable spectrometer, and Dr. Dwight Harris of Cypress Mines is hereby acknowledged for making the Betaprobe available.

REFERENCES

1. D. C. Reynolds, G. Leies, L. L. Antes, and R. E. Marburger, Photovoltaic Effect in Cadmium Sulfide, *Phys. Rev.* **96**, 533 (1954).
2. R. E. Marburger, D. C. Reynolds, L. L. Antes, and R. S. Hogan, Quantum Yield of a Cadmium Sulfide Photovoltaic Cell, *Phys. Rev.* **100**, 978 (1955).
3. L. R. Shiozama, G. A. Sullivan, F. Augustine, and J. M. Jost, Research on the Mechanism of the Photovoltaic Effect in High Efficiency CdS Thin-Film Solar Cells. Contract AF 33(615)-5224, Second Quarterly Progress Report, Sept.-Nov. 1966.
4. H. A. Liebhafsky and P. D. Zemany, Film Thickness by X-Ray Emission Spectrograph, *Anal. Chem.* **28**, 455 (1956).
5. William J. Campbell, Energy Dispersion X-Ray Analysis Using Radioactive Sources, *X-Ray and Electron Methods of Analysis*, H. van Olphen and W. Parish, eds., Plenum Press, New York (1968), pp. 36-54.
6. W. Barclay Jones and Robert A. Carpenter, Nondispersive X-Ray Fluorescent Spectrometer, *Advances in X-Ray Analysis*, Vol. 11, J. B. Newkirk, G. R. Mallett, and H. G. Pfeiffer, eds., Plenum Press, New York (1968), pp. 214-229.
7. Harry R. Bowman, Earl K. Hyde, Stanley G. Thompson, and Richard C. Jared, *Science* **151**, 562-568 (1966).
8. J. R. Rhodes, *Analyst* **96**, 683-699 (1966).
9. W. Barclay Jones and Robert A. Carpenter, Sensitivity of a Nondispersive X-Ray Fluorescent Spectrometer for Multielement Trace Analysis, presented at the Second International Symposium on Nucleonics in Space, Columbus, Ohio, July 1967.
10. Frank L. Chan, A Study of Silicon Determination in Organo-Silicon Compounds by X-Ray Fluorescence with Vacuum Spectrograph, *Analytical Chemistry*, Society of Analytical Chemistry of Great Britain (1965).
11. Frank L. Chan, An Apparatus for the Analysis of Liquid Samples by the X-Ray Fluorescence Method with a Vacuum Spectrograph, *Developments in Applied Spectroscopy*, Vol. 5, L. R. Pearson and E. L. Grove, eds., Plenum Press, New York (1966), pp. 59-75.
12. Frank L. Chan and Donald A. Brooks, A Study of Homogeneity of Solid Solutions of Cadmium Sulfide and Cadmium Selenide by X-Ray Fluorescence, *Advances in X-Ray Analysis*, Vol. 8, W. M. Mueller, G. R. Mallett, and M. J. Fay, eds., Plenum Press, New York (1965), pp. 420-430.
13. Frank L. Chan, Some Observations on the Use of Certain Analyzing Crystals for the Determination of Silicon and Aluminum, *Advances in X-Ray Analysis*, Vol. 9, G. R. Mallett, M. J. Fay, and W. M. Mueller, eds. Plenum Press, New York (1966), pp. 515-527.
14. Frank L. Chan and James T. Carpenter, Solid Solutions of Cadmium Sulfide-Cadmium Selenide Films, *Advances in X-Ray Analysis*, Vol. 12, C. S. Barrett, J. B. Newkirk, and G. R. Mallett, eds., Plenum Press, New York. (1969), pp. 581-600.
15. G. E. F. Lundell, H. A. Bright, and J. I. Hoffman, *Applied Inorganic Analysis*, John Wiley and Sons, New York (1953).
16. Frank L. Chan, A Study of X-Ray Fluorescence Method with Vacuum and Air-Path Spectrographs for the Determination of Film Thickness of II-VI Compounds, *Advances in X-Ray Analysis*, Vol. 11, J. B. Newkirk, G. R. Mallett, and H. G. Pfeiffer, eds., Plenum Press, New York (1968), pp. 191-203.
17. H. A. Liebhafsky, H. G. Pfeiffer, E. H. Winslow, and P. D. Zemany, *X-Ray Absorption and Emission in Analytical Chemistry*, John Wiley and Sons, New York (1960).

18. L. S. Birks, R. J. Labrie, and J. W. Criss, *Anal. Chem.* **38**, 701–707 (1966).
19. A. Vecht and A. Apling, A New Method of Recrystallizing CdS Thin Films, *Physica Status Solidi* **3**, 1238 (1963).
20. A. Vecht, Methods of Activating and Recrystallizing Thin Films of II–VI Compounds, in: *Physics of Thin Films*, Vol. 3, Academic Press, New York (1966).
21. William J. Campbell and James D. Brown, *Annual Reviews, Anal. Chem.* **40**, 346R (1968).

Application of X-Ray Topography to the Characterization of Semiconductor Surface Layers

P. Wang and F. X. Pink

*Sylvania Electric Products, Inc.
Semiconductor Division
Woburn, Massachusetts*

Many of the physical properties of solids depend to a significant extent on the perfection of the surface-layer structure, and x-ray studies provide valuable information about structural perfection both in bulk and at the surface of crystals. X-ray diffraction topography is concerned with variations in the direction and/or intensities of x-rays that have been diffracted by crystals. From these variations the defect structure of the crystal may be examined. X-ray reflection techniques have found very useful applications in studying structural defects introduced in the surface layers by processing, especially by high-temperature treatment. In this chapter, x-ray transmission and reflection topography methods applicable to surface study are described, with emphasis on surface-layer defects in silicon crystals used in the fabrication of microelectronic devices or circuits.

INTRODUCTION

X-ray diffraction topography has been applied to the study of crystal imperfection for over a decade. Many of the physical properties of solids depend to a significant extent on the perfection of the surface-layer structure, and x-ray studies provide valuable information about the structural perfection of the

TABLE I
Perturbations to Structural Perfection in Elemental Single-Crystal Lattice

	Mechanism	Effect	Example
Microscopic perturbation	Substitution	Impurity Desirable Undesirable	Dopant in Si or Ge Traps in Si or Ge
	Omission	Vacancy	Single or double vacancy, vacancy clusters
Addition	Interstitial	Host atom Foreign atoms	Dislocations*
	Distortion	Crystallographic defects*	Frenkl defects, oxygen vacancy in Si
	Combinations of above		
	Formation of new phases	Segregation precipitation*	Cracking, scratches, work damage*
Macroscopic perturbation	Mechanical damage	Distorted surface layer*	Inversion of surface change of chemical and physical properties
	Interaction on surfaces (intentional or unintentional)	Absorption, contamination Formation of surface thin films†	

* Detectable by x-ray topography.

† Discontinuation in oxide films, etc. detectable.

bulk and of the surfaces of crystals. X-ray diffraction topography is concerned with variations in the direction and/or the intensities of x-rays that have been diffracted by crystals. From these variations the defect structure of the crystal may be examined. In many problems it may be applied in a quite straightforward manner as a tool for revealing these defects. However, for a rigorous analysis of dislocation configuration and for correct interpretation in the more refined studies a thorough understanding of the diffraction theory and crystallography is necessary. The present chapter discusses the application of x-ray diffraction topography for characterizing the structural defects in crystal surface layers. For those who have not been engaged in x-ray diffraction topography, the list of suggested references will provide a general background. Several selected technical papers by those who have made important contributions to this field are also listed. X-ray techniques commonly used for surface-layer characterization are described in the following, and applications to semiconductor surfaces are given to illustrate their usefulness. The Berg-Barrett reflection techniques will receive emphasis because of our experience with the application to silicon material used in the fabrication of micro-electronic devices.

The application of x-ray topography in a study of structural imperfection requires specimens with smooth surfaces. We may ask what kinds of crystal defects are easily detected by these techniques. In Table I the types of perturbations to structural perfection in an elemental single crystal lattice and the types of defects detectable are listed. For a chemical compound, even a very simple AB case, the defect structure and the effect on its properties are more complicated. The same is true for a polycrystalline material. However, lattice defects in chemical compounds and polycrystalline material have been studied very successfully and at an earlier date than the study of elemental single crystals. We shall restrict our interest here to single-crystal material because of our familiarity in elemental and compound semiconductors. Although certain types of defects are easily detectable, their identification and origin, the interplay between defects in a crystal and its history, and the relation between defects and the properties of the crystal are sometimes difficult to predict and interpret.

X-RAY TECHNIQUES

Scanning-Transmission Method

The study of crystal surface-layer structure by x-ray topography is based on the extinction-contrast effect. Distorted regions in an otherwise perfect

crystal reduce the primary extinction of x-rays and show up as images of enhanced intensity (dark regions on the emulsion). The scanning-transmission or Lang method has been widely used for the study of crystal bulk defects using hard radiation such as that from Mo or Ag. Table II gives the Bragg angles for Cr, Cu, and Mo $K\alpha_1$ radiation for low-index planes in silicon. The low absorption coefficient and the small Bragg angle of the hard x-rays make these ideal for transmission application. Extensive work has been carried out by x-ray transmission topography in the study of bulk structural defects in metals, ionic compounds, and semiconductors. It is important to note that in the study of surface layers we are concerned with radiation and materials for which the relation $\mu_0 t \leq 1$ is satisfied, where μ_0 is the linear absorption coefficient and t is the sample thickness of effective path length. With respect to dislocations maximum enhanced intensity in the x-ray image is obtained when the latter arises from Bragg reflection against a plane perpendicular to the Burgers vector. If the Burgers vector is parallel to the reflecting net planes, the line image is invisible or only very slightly visible. Modifying the section topography method¹ with a suitable beam-stop in a Lang topograph apparatus, Blech *et al.*² studied dislocations generated by boron or phosphorous diffusion in silicon surface layers. Figure 1 is a schematic diagram of their surface-topography apparatus.

A series of surface topographs of one of the oxidized and diffused wafers is shown in Fig. 2. The depth of the region under examination was estimated at between 25 and 50 μ for the surface of interest, with the incident beam impinging on the back side.

TABLE II
Bragg Angles for Silicon Low-Index Planes

Reflecting planes hkl	d spacing	θ for Cu $K\alpha_1$ radiation	θ for Cr $K\alpha_1$ radiation	θ for Mo $K\alpha_1$ radiation
111	3.138	14°11'	21°23'	6°29'
220	1.920	23°39'	36°36'	10°38'
311	1.638	28°30'	44°20'	12°30'
400	1.357	34°36'	57°31'	15°09'
331	1.246	38°12'	66°45'	16°32'
422	1.1083	44°20'	—	18°24'
(333), (511)	1.0450	47°29'	—	19°50'

Note: Wavelength for Cu $K\alpha_1$: 1.5405 Å; for Cr $K\alpha_1$: 2.2896 Å; for Mo $K\alpha_1$: 0.70926 Å. Lattice spacing for Si: 5.4305 Å.

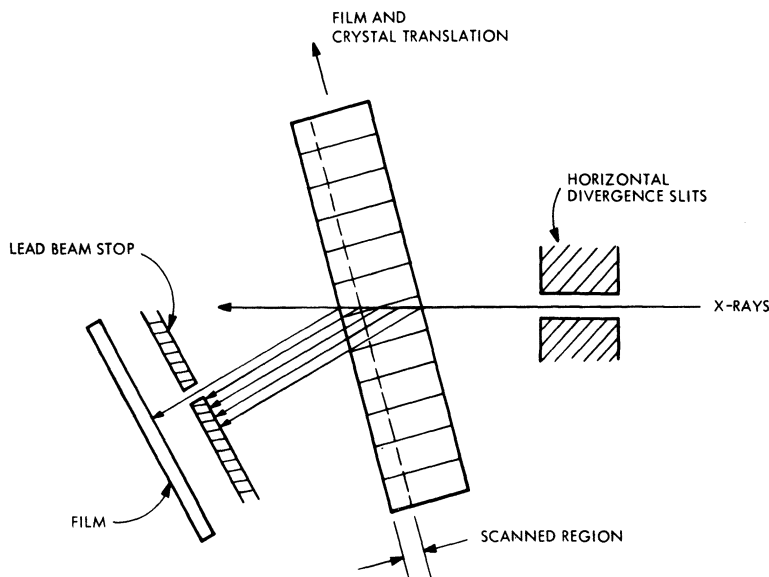


Fig. 1. Schematic diagram of the surface-topography apparatus.

Scanning-Reflection Method

Extinction-contrast micrographs can be obtained in the Bragg geometry using a line x-ray source and scanning. Howard and co-workers^{3,4} used such a reflection technique to study defects in epitaxial Ga (As, P) films on GaAs substrates. The Bragg angle θ is related to the lattice parameters for the (hkl) reflection in a cubic lattice by the expression

$$\theta = \sin^{-1} [\lambda(h^2 + k^2 + l^2)^{1/2}/2a]$$

where λ is the wavelength of the incident beam. A change in lattice parameter a produces a change in the diffraction angle. This technique permits topographs to be obtained as a function of composition for a heteroepitaxial system making it possible to evaluate the perfection of the substrate, the deposit, and the heterojunction or interface. For (440) reflections using Cu $K\alpha$ radiation the following 2θ values were obtained:

GaAs	100.8°
$\text{GaAs}_{0.85}\text{P}_{0.15}$	101.6°
$\text{GaAs}_{0.67}\text{P}_{0.33}$	102.5°

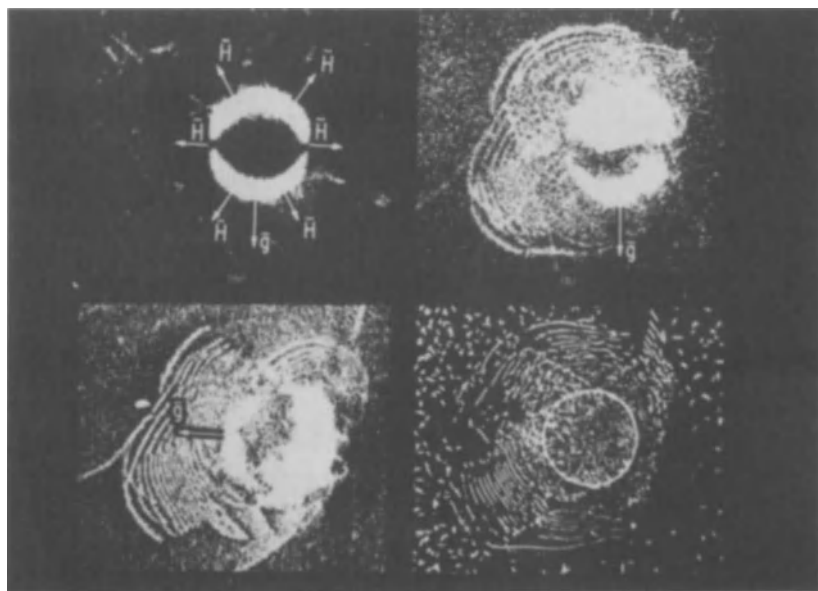


Fig. 2. Surface topograph of oxidized and diffused silicon wafer. (a) [220] micrograph of oxidized silicon surface with a typical 10-mil-diameter window; the strain around the hole is radially symmetrical and elastic in nature. (b) [220] micrograph of the window after boron diffusion and oxide removal, showing dislocation arrays. (c) [111] micrograph of the window after boron diffusion and oxide removal. (d) Optical micrograph of area after copper decoration.

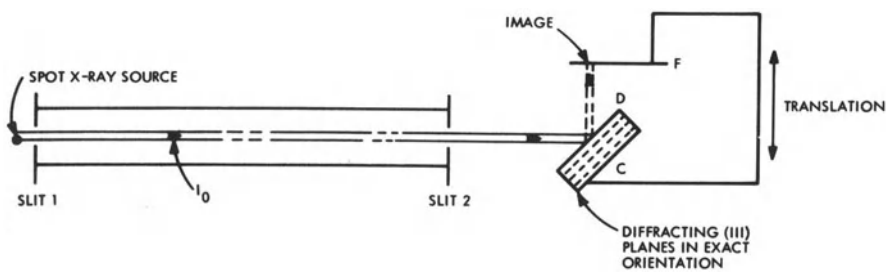


Fig. 3. Geometry used in surface reflection topography (after J. K. Howard *et al.*).

The diffraction angles were then used to align each layer for scanning-reflection topographs.

Figure 3 is a schematic diagram of the x-ray instrumentation for this SRT technique.

Figure 4 is a conceptual diagram for "composition x-ray topography." Each layer can be diffracted separately by utilizing the diffraction angle which corresponds to the lattice parameter of the layer.

Figures 5-7 are reflection topographs of the GaAs substrate, the $\text{GaAs}_{0.67}\text{P}_{0.33}$ layer, and the $\text{GaAs}_{0.33}$ layer, respectively.

In Fig. 5, a (440) topograph of GaAs substrate, the hillocks are revealed as triangular regions on the (111)-B deposit. The white line is a spurious

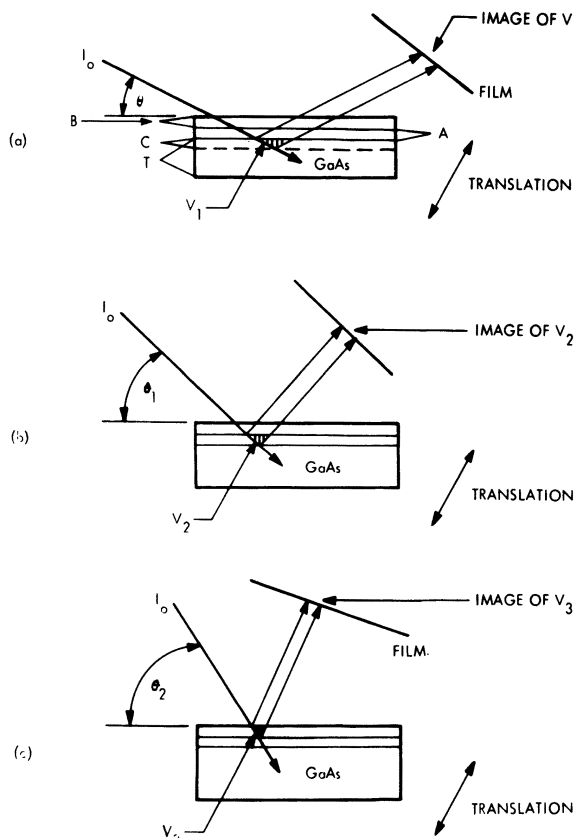


Fig. 4. Schematic diagram showing diffraction positions for different layers in $\text{GaAs}_x\text{P}_{1-x}/\text{GaAs}$ epitaxy.

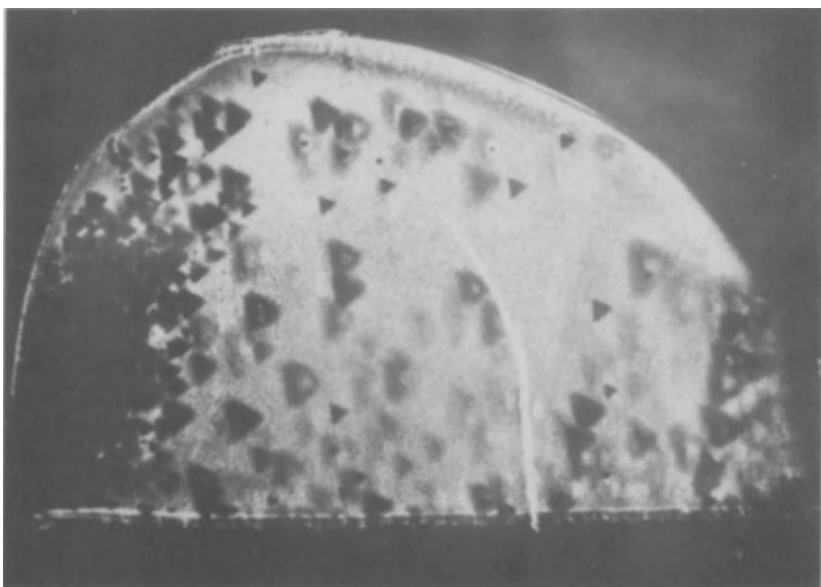


Fig. 5. (440) topograph of the GaAs substrate.

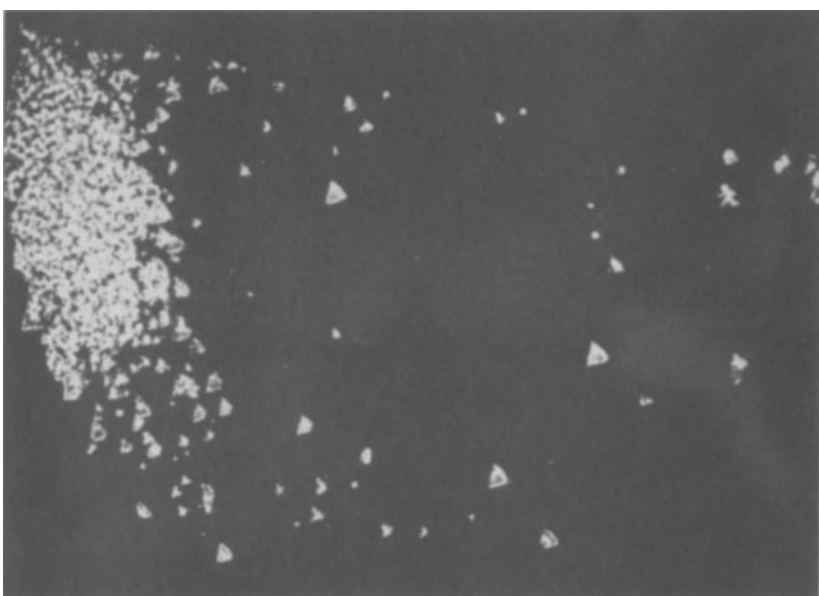


Fig. 6. (440) topograph of the GaAs_{0.85}P_{0.15} layer – only the hillocks are in diffraction position.

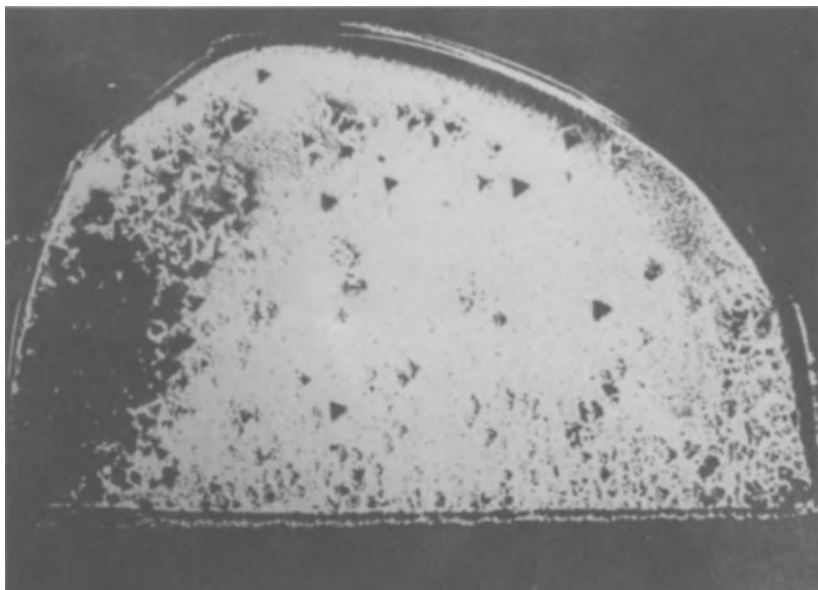


Fig. 7. (440) topograph of the $\text{GaAs}_{0.67}\text{P}_{0.33}$ layer – the dark contrast results from local cracks in the deposit.

reflection. Figure 6 shows the $\text{GaAs}_{0.85}\text{P}_{0.15}$ layer, where only the hillocks are seen, indicating that these defects are of this particular composition. Figure 7 shows the $\text{GaAs}_{0.67}\text{P}_{0.33}$ layer which formed around the hillocks and frequently overgrew these defects.

Meieran⁵ has used a similar scheme for a study of structural defects in GaAs epitaxial films grown on Ge substrates separately using (333) and (440) reflections. In this way the various types of defects appearing in the epitaxial film can be analyzed to show whether or not they were influenced by growth conditions or by substrate preparation. More recently Light *et al.*,⁶ using Berg-Barrett topographs, examined plastic deformation in Ge epitaxial layers grown on semi-insulating GaAs substrates. Figure 8 shows the slip steps on a (111) Ge/GaAs specimen with Ge layer selectively removed in the central region. The arrow indicates the projection of the [333] diffraction vector onto the wafer surface.

Double-Crystal Topography

In this technique x-rays from a line focus source are reflected from a perfect reference crystal, then from the specimen surface, and finally are

recorded on a high-resolution photographic film. In contrast to Lang and Berg-Barrett techniques, a crystal-collimated x-ray beam is used to offer high sensitivity in the detection of strains. This back-reflection equal-crystal topography was first used by Bonse and Kaplan,²¹ who used fine slits to reduce the divergence of the reflected beam to such an extent that it sharply depicted the specimen surface topography on the film. During an exposure the specimen was held in a position where the reflected rays had half-intensity, which corresponded to points on the middle of the two wings of the rocking curve. A modified geometry used by Renninger²² allowed a larger area to be studied.

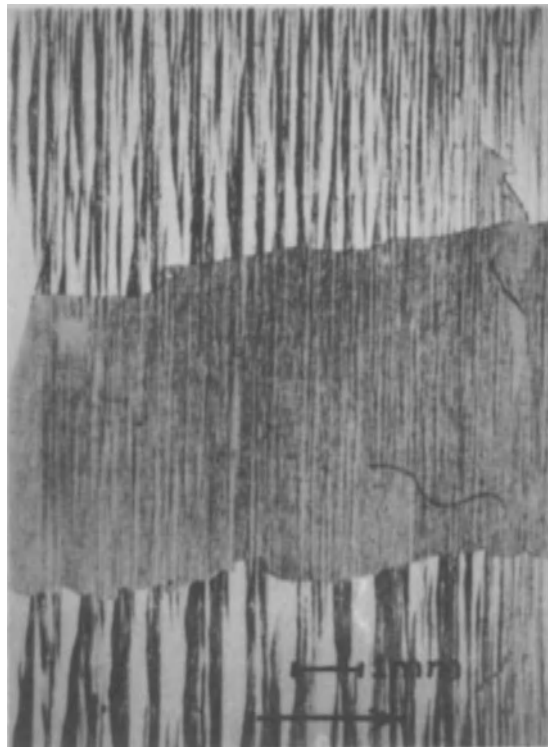


Fig. 8. (333) topograph of (110) Ge/GaAs epitaxial wafer with Ge layer selectively removed in the center region to reveal the GaAs substrate (from Light *et al.*⁶).

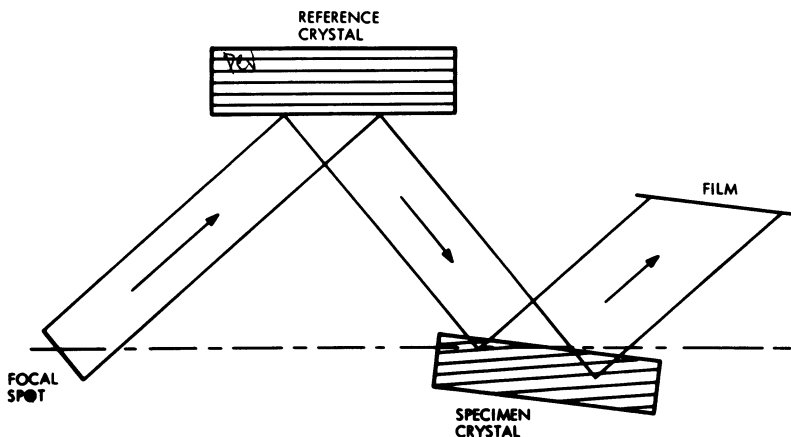


Fig. 9. Mismatched double-crystal geometry used by Deslattes and Paretzkin.⁷

In a more recent work Deslattes and Paretzkin⁷ have shown that a perfect silicon reference crystal can be used to record and determine strains in other materials. They used a mismatched geometry, as shown in Fig. 9. If only a slightly different d -spacing is used, the small amount of increased dispersion that results does not seriously reduce the contrast sensitivity of the method. This simple configuration permits high-quality topographs of large areas to be recorded without scanning. Figure 10 is a topograph of a silicon specimen with dislocation etch-pit density of less than $1000/\text{cm}^2$. The line images are $\langle 111 \rangle$ segments and differ in contrast according to the sign of the Burgers vector.

Modified Berg-Barrett Technique

In the modified Berg-Barrett technique (or Newkirk technique) a collimated beam from a monochromatic x-ray source is diffracted from a specimen surface onto a high-resolution photographic plate. The diffraction conditions are chosen such that the scattering angle is close to $\pi/2$, with the incident beam nearly parallel to the specimen surface. With a large distance between the x-ray source and the specimen very good resolution can be achieved. In our laboratory we use a chromium target x-ray tube for zero-layer reflection and a copper target tube for skew reflection for $\langle 111 \rangle$ oriented silicon. The laboratory facility is shown in Fig. 11.

The $K\alpha$ radiation from the line focus is used and the $K\beta$ radiation is suppressed by an 0.7-mil nickel filter at the exit port. The vertical divergence of

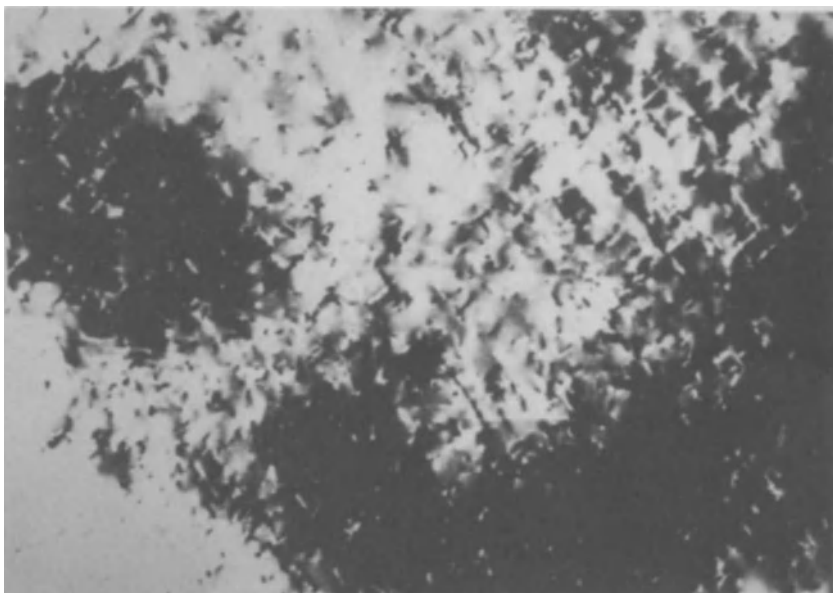


Fig. 10. (440) topograph of a pulled silicon single crystal.

the incident beam is controlled by an adjustable slit system with a maximum aperture of 0.5° and the horizontal divergence is limited to 2.2° by a parallel-slit assembly to reduce background scattering. In operation the sample is mounted on a goniometer head such that the surface to be studied is exposed to the incident beam. Angular rotations are used to position the diffracting planes in exact alignment. The diffracted beam intensity is monitored with a Geiger counter ratemeter circuit. After orientation is completed, the film plate holder is placed in the camera and the topograph recorded.

In our setup the specimen area intercepted by the beam is as large as $1 \times 2.5 \text{ cm}^2$, enough to eliminate the need for scanning. (Scanning the specimen and the camera simultaneously in front of the beam will produce topographs of larger area.) The photographic plate can be placed close enough to the specimen surface to yield satisfactory resolution over most of the recorded image. Nevertheless, the best resolution occurs in the part of the image nearest to the specimen, and uniform resolution is not obtained over the entire surface area under examination. A second disadvantage is that the Ka_1 and Ka_2 are not resolved, resulting in decrease in resolution. A third disadvantage is that the background recorded resulting from incoherent scattering of the incident radiation from the sample is superimposed on the diffracted radiation.

In general, we use Ilford L-4 10- and 25- μ nuclear plates to record Berg-Barrett topographs. Exposure time is usually very short. For instance, in the study of silicon crystals using Cu $K\alpha$ radiation exposure time is between 5 and 10 min. With Cr $K\alpha$ radiation it requires 10 to 20 min. Development of nuclear plates must be carefully controlled by maximum contrast and resolution.¹⁸

*Application of Modified Berg-Barrett Reflection Topography:
Zero-Layer and Skew Reflections*

Previous publications from several laboratories⁸⁻¹¹ reported the application of the Berg-Barrett reflection method to the study of surface strain, mechanical damage, and structural imperfection in materials such as quartz, silicon, diamond, and lithium fluoride, as well as many alloys. Zero-

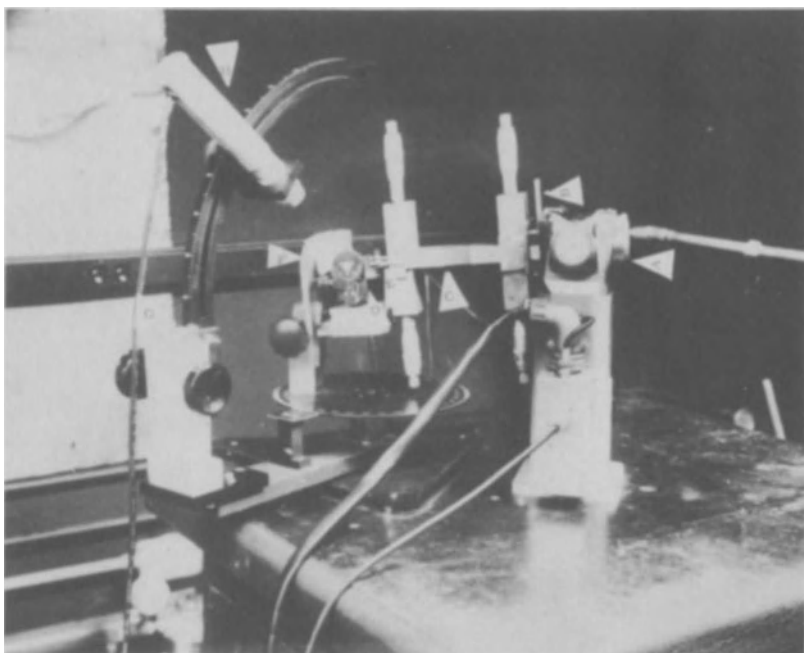


Fig. 11. Berg-Barrett x-ray topograph facility. *A*: X-ray source. *B*: Shutter. *C*: Collimator with adjustable front and back slits. *D*: Sample holder - two-circle goniometer. *E*: Plate holder. *F*: Lead shield. *G*: Fluorescent screen. *H*: Adjustable detector with graduated rotary stage for location of diffracted beam. *I*: Geiger counter tube.

layer reflection was used by several workers to study silicon defects. Figure 12, taken by Jungbluth¹⁹ of General Telephone and Electronics Laboratories, shows phosphorus-diffusion-introduced dislocations in (111) silicon, aligned in $\langle 110 \rangle$ arrays as a triangular crossed gridwork. In addition, there are also a number of spots which may be either impurity clusters or protrusions on the surface; the appearance of these spots is due to a shadow effect.

The geometry of Berg-Barrett reflections will be discussed briefly here. In the case of zero-layer reflections, where the specimen surface normal and the incident and reflected beam vectors are coplanar, the Bragg relationship, in a two-dimensional analysis, is satisfied only when $n\lambda = 2d \sin \theta$ for a given set of planes, where θ is the Bragg angle, d the interplanar spacing, λ the wavelength of the x-radiation, and n represents the order of reflection. Figure 13 shows the relationship of the surface and reflecting planes A and B to the incident and diffracted beam vectors for a zero-layer reflection, where a is the angle between the planes A and B , ϕ is the angle of tilt of the specimen into the beam, and e the angle between the diffracted beam vector and the normal to the specimen surface. Then

$$\phi = \theta - a$$

$$e = \theta + a - 90^\circ$$

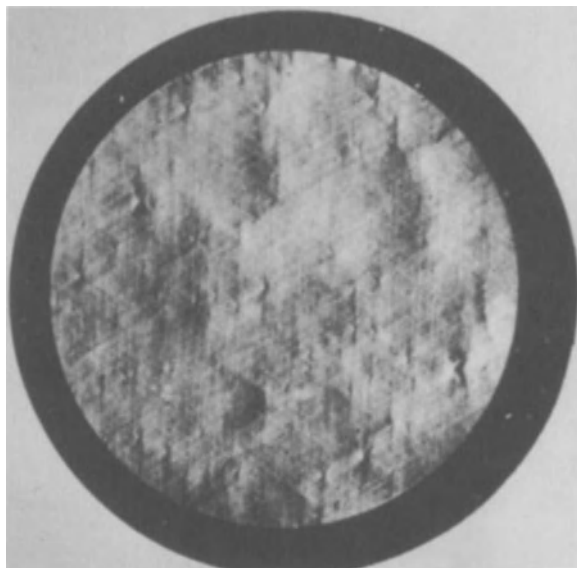


Fig. 12. Berg-Barrett zero-layer reflection scanning topograph of high-surface-concentration phosphorus-diffused junctions (diameter: 200 mils) (from Jungbluth¹⁹).

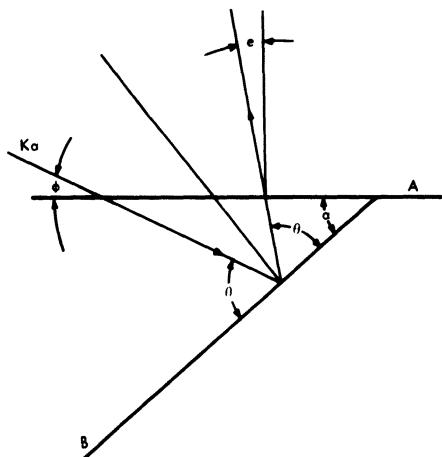


Fig. 13. Relationship of the surface and reflecting planes A and B to the diffracted beam vectors for a zero-layer reflection. θ is the Bragg angle, α is the angle between specimen surface and reflecting planes, ϕ is the tilt angle of the specimen into the beam, and e is the angle between the diffracted beam vector and the normal to the specimen surface.

TABLE III
Zero-Layer Reflection of (111) Silicon

Reflecting planes (hkl)	Bragg angle, θ	Angle between reflection of plane and (111) surface, α	Tilt angle $\theta - \alpha$	Radiation
111	5.13	0	5.1	Ag $K\alpha$
	6.50	0	6.5	Mo $K\alpha$
220	8.40	0	8.4	Ag $K\alpha$
	36.63	35.3	1.3	Cr $K\alpha$
311	33.13	29.5	3.6	Co $K\alpha$
	36.25	29.5	6.7	Fe $K\alpha$
400	57.58	54.7	2.9	Cr $K\alpha$
422	None	—	—	—
331	51.02	48.37	2.7	Fe $K\alpha$
(511) (333)	58.93	56.25	2.7	Co $K\alpha$

and e is positive when the reflected beam is inclined toward the target. Obtaining high-resolution Berg-Barrett reflection topographs requires small positive tilt angles of the order of 2 to 5° and small specimen-to-plate distances, approximately 5 mm. Table III gives useful reflections from (111)

silicon for common x-radiation.^{1,2} There are no zero-layer reflections permitting a small tilt angle from a low-index plane when a (111) silicon surface is analyzed with Cu $K\alpha$ radiation.

It is immediately obvious that we are quite restricted to a few tilt angles, and hence, to a limited number of penetration depth values. To use Cr $K\alpha$ radiation and the (220) reflection to examine (111) silicon, we are limited to very shallow penetration. As a matter of fact, other radiation will not produce useful (220) reflections either. Therefore the application of the zero-layer reflection topograph, although useful, is quite limited for (111) silicon.

Consequently, skew reflections in which the normal to the specimen surface and the incident and reflected beam vectors are not coplanar have been used to study defects in (111) silicon surface layers using a Cu $K\alpha$ radiation. The use of Berg-Barrett skew reflections permits a great degree of latitude in that one is permitted a choice of a number of planes from which to diffract using the same monochromatic radiation and a choice of tilt angles.

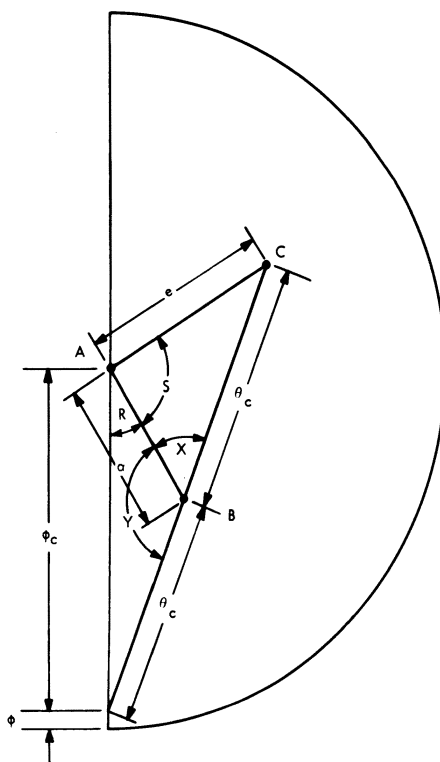


Fig. 14. Skew reflection interangular relationship for the general case where $\phi_c = 90^\circ - \phi$, $\theta_c = 90^\circ - \theta$; X is the interplanar angle between A and B , and $R + S$ is the angle between the incident and diffracted beams.

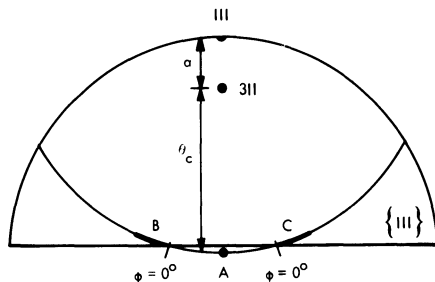


Fig. 15. Stereographic projection illustrating low, positive ϕ angle skew reflections of B and C for a (311) plane.

The analysis of Berg-Barrett reflections was carried out in spherical trigonometry by Juleff and co-workers.^{12,13} The relevant angles are defined for skew reflections in Fig. 14. The angular coordinates are as follows:

$$R = \cos^{-1} \left(\frac{\sin \theta - \sin \theta \cos a}{\cos \theta \sin a} \right)$$

$$e = \cos^{-1} (\sin \theta \cos a \sin \theta - \sin \phi)$$

$$S = \cos^{-1} \left(\frac{\sin \theta - \cos a \cos e}{\sin a \sin e} \right)$$

which, with the restriction

$$a + \phi > \theta$$

limits these equations to permissible skew reflections. The significance of this restriction is illustrated by the stereographic projection of Fig. 15, which represents the (311) reflection of Cu $K\alpha$ radiation from a (111) silicon surface. The zero-layer (311) reflection occurs at a negative tilt angle, and the incident x-ray beam is intercepted by the edge of the specimen before reaching the surface. In such a case, however, skew-reflection micrographs can be obtained over a range of positive tilt angles, as shown; values of ϕ of the order of $+3^\circ$ have been found to give the best images. At other tilt angles distortion may occur, and resolution may suffer and a practical limit must be set to the tilt angle for practical application. Juleff and La Pierre¹² calculated permissible skew reflections for a (111) silicon angle at a tilt angle of 2° . Recently Berkstresser and Pink²⁰ extended this calculation to include (100) and (110) silicon in addition to (111)-oriented silicon using Co, Fe, and Cr $K\alpha$ radiations for a tilt angle of 2° and Cu $K\alpha$ radiation at tilt angles of 1° , 2° , and 3° . It is interesting to note the appearance of a permitted (331) reflection at a 3.0° tilt angle which does not appear at small tilt angles. With variable tilt angle, variation in penetration depth can be obtained within a certain limit, allowing one to analyze the generation and propagation of defects in the depth of the surface layer.

Although for a given orientation there are a number of reflections one may choose by varying the angles and the radiation, a judicious choice of skew reflections to employ values of e as small as possible. Such reflections lessen the effect of distortion on the recording surface of the diffracting area. There is also a gain in resolution because of the shorter distance between the diffracting volume and the plate. The use of skew reflections permits the depth of penetration of the x-ray beam below the specimen surface to be varied by changing the tilt angle appropriately. Under favorable conditions a change in path length by a factor of five to ten is possible for some of the major reflections for (111) silicon wafers with tolerable loss of resolution in the image and/or a slight distortion of the image.

Considered next are a series of micrographs made in connection with an experiment on $n^+/n^-/p$ guard-ring diodes. These diodes were made by diffusing phosphorus into *p*-type silicon to form an n^- region, and then making a small-area, high-concentration shallow diffusion inside the n^- region to form a junction that would break down in avalanche mode at a relatively low voltage. Figure 16 is a Berg-Barrett skew-reflection topograph of an entire 1.1-in. wafer, assembled from sections each of which was taken in more or less exact diffraction position. At this magnification it is difficult to evaluate the quality of a wafer unless it is severely deformed. Figure 17 shows a wafer after the n^-

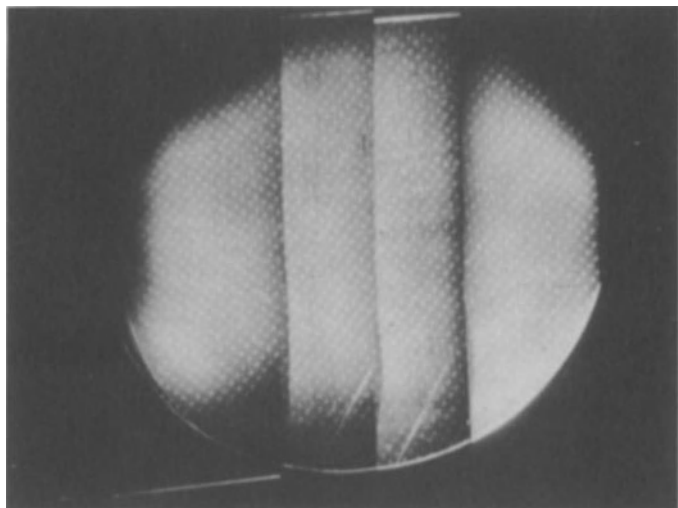


Fig. 16. Berg-Barrett (220) skew-reflection topograph of an *n/p* diffused silicon wafer of avalanche diodes with guard-ring structures. Made of four stationary section topographs. Device dimension, 6 X 10 mils.

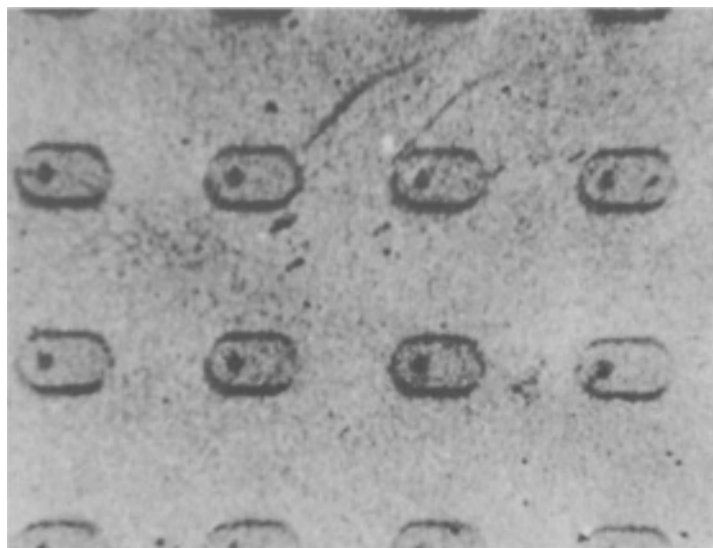


Fig. 17. (220) skew-reflection topograph of the wafer after the n^- guard-ring diffusion. 60 X.

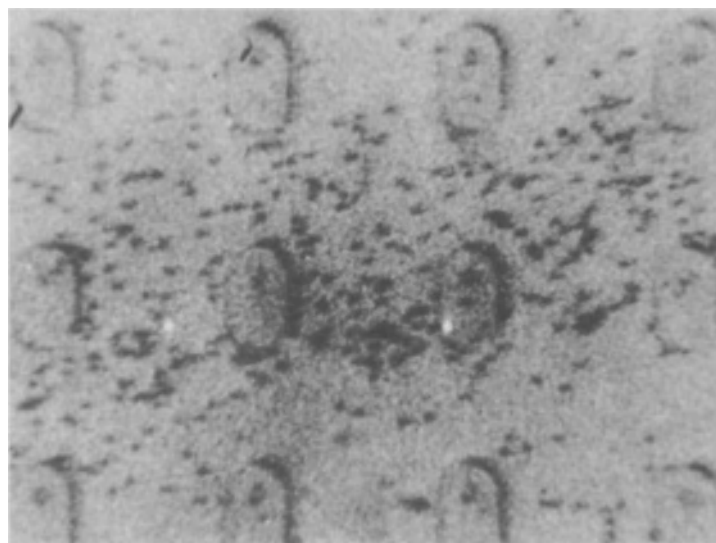


Fig. 18. (220) skew-reflection topograph of the wafer after the n^+ diode-junction diffusion.

diffusion and the oxide windows opened prior to the high concentration n^+ diffusion. There are some scratches and a few particulate images, due probably to dust particles on the surface. Figure 18 is a topograph of a similar wafer after a POCl_3 deposition and drive. There are numerous strained areas near the surface over the entire wafer, probably because of either (1) a high-P-content glassy source on the oxide surface due to the production by non-uniform deposition of strains in the oxide film which propagate to the silicon substrate, or (2) poor adhesion of the SiO_2 film at these areas. The strained areas disappeared when the phosphorus glass was etched off. However, the n^+ junctions in this wafer did not break down by avalanche, but by way of microplasmas, indicating the cause was a nonhomogeneous n^- region and the possible presence of diffusion pipes or similar defects.

Figure 19 is a Berg-Barrett (220) skew reflection topograph of a production silicon (111) integrated circuit wafer after epitaxial layer deposition and buried layer and isolation diffusion steps. The strong contrast may be due to the elastic strain along the edge of the silicon oxide windows. Slip dislocations are vividly revealed in the right side of this micrograph. These slip dislocations are in the (111) planes, probably within a depth of 1 μ from the surface.

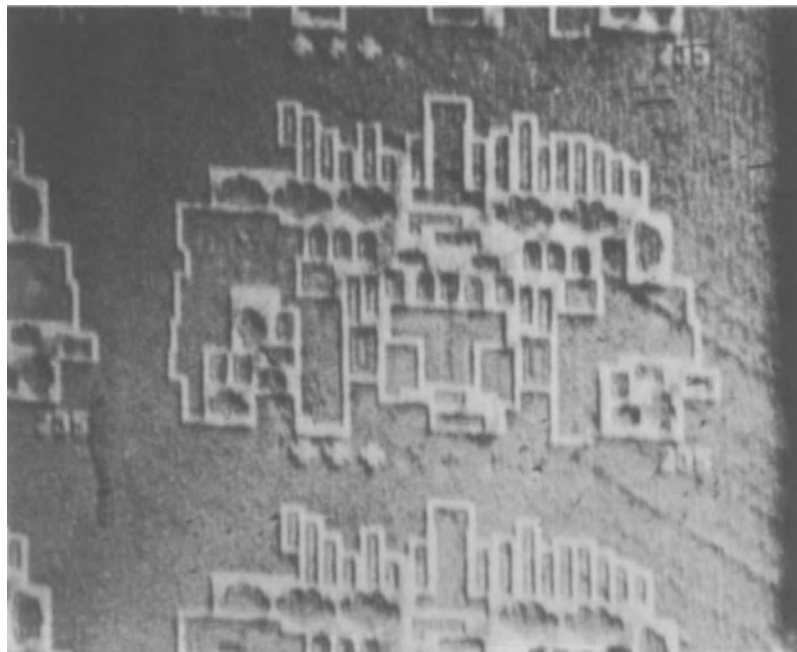


Fig. 19.(220) skew reflection of a silicon integrated circuit wafer, showing slip dislocations in the surface layer.

Effect of X-Ray Attenuation on Reflection Topography

The attenuation of a particular x-ray wavelength satisfying the Bragg law in a crystal is governed by two phenomena, primary extinction and absorption. In a perfect crystal the former effect predominates, and absorption plays a negligible part in attenuation. This was demonstrated by James¹⁴ in his calculations on the effects of absorption. For the study of elements or compounds with higher mass-absorption coefficients absorption would become the more significant factor. As the periodicity of the reflection lattice planes is perturbed by strains introduced by dislocations, precipitates, inclusions, etc., the attenuation by primary extinction will be destroyed, and diffraction will occur over a larger volume or deeper into the disturbed crystal. This is akin to rendering the crystal more mosaic-like.

The reduction by diffraction and absorption phenomena of the intensity of an x-ray beam as it passes through a perfect crystal of silicon can be determined by applying the James' formulation.¹⁴ Primary extinction is a function of the phase relationships between primary and secondary, or reflected, beams when the angle of incidence θ has a value lying within the range of total reflection. The intensity of the primary beam is reduced by a factor $e^{-2\delta}$ where 2δ is the extinction coefficient per plane. The extinction coefficient is given by

$$2\delta = \frac{1}{2} \pi N \lambda f (e^2 / mc^2) (d \csc \theta)$$

where N is the number of atoms per volume of unit cell, λ is the wavelength, f is the structure factor, d is the interplanar spacing, θ is the Bragg angle $e = 4.80 \times 10^{-10}$ esu, $m = 9.11 \times 10^{-28}$ g, and $c = 3.00 \times 10^{10}$ cm/sec. In performing the calculations we put $y = xd \csc \theta$, where y is the total path length, x is the number of planes transversed, and $d \csc \theta$ the path length per plane.

Absorption is caused by scattering and a "true absorption." The former effect is negligible except for very light elements; the latter effect predominates, and is caused by electronic transitions within the atoms of the absorbing material. If β is the amplitude absorption factor per plane, then the intensity is reduced by $e^{-2\beta}$ per plane, where $2\beta = (\mu_0/\rho)\rho d \csc \theta$. The quantity (μ_0/ρ) is the mass absorption coefficient, and is a function of the chemical composition of the absorbing material and the wavelength being absorbed; ρ is the density of the absorbing material. Again in the absorption calculations we set $y = xd \csc \theta$. The summation of these two effects, primary extinction and absorption, accounts for the total attenuation of the primary x-ray beam. At the other extreme, i.e., a highly imperfect crystal, the diffracting volume may be considered as a volume of randomly-distributed

crystallites. Cullity¹⁵ discusses this situation and treats the diffracting volume as a powder specimen. An expression is derived giving the intensity diffracted by a layer as a fraction of the total intensity which would be diffracted from a specimen of infinite thickness:

$$G_x = 1 - \exp\left\{-\mu x \left[\left(1/\sin \alpha\right) + \left(1/\sin \beta\right)\right]\right\}$$

where x is the depth of the diffracting layer, μ is the linear absorption coefficient, α is the angle between the incident beam and the specimen surface, and β is the angle between the diffracted beam and the specimen surface. This term is similar to the second term of the equation given by James¹⁴ for extinction contrast plus absorption. The depth of penetration in this case is far greater, at least for light elements and more energetic x-rays, than for primary extinction. If only these two effects are considered as affecting penetration (excluding anomalous transmission), then it can be seen that it is difficult to determine which effect is predominating at any given depth. Unless the crystal lattice becomes distorted, there is still a high degree of perfection, where primary extinction will predominate. Diffusions will change the lattice parameter appreciably, making the problem even more complex with respect to depths of penetration, since the lattice constant will depend upon the impurity concentration at any given point. It may be

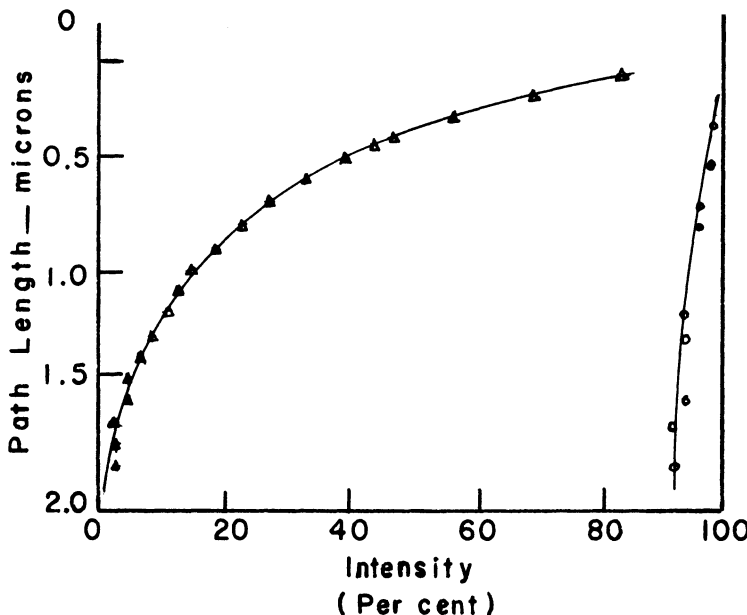


Fig. 20. Attenuation curves of chromium $K\alpha$ radiation by absorption (circles) and primary extinction (triangles on the (333) silicon plane.

TABLE IV
Attenuation of X-Rays by Primary Extinction in Silicon

Reflecting planes	<i>Ka</i> radiation source	Extinction, μ		
		50%	90%	95%
1. {111}	Mo <i>Ka</i>	0.78	> 2.00	> 2.00
	Cu <i>Ka</i>	0.39	1.20	1.60
	Co <i>Ka</i>	0.30	1.00	1.25
	Fe <i>Ka</i>	0.28	0.85	1.05
	Cr <i>Ka</i>	0.25	0.80	1.10
2. {220}	Mo	0.60	> 2.00	> 2.00
	Cu	0.28	1.00	1.20
	Co	0.25	0.75	0.95
	Fe	0.22	0.70	0.90
	Cr	0.20	0.60	0.80
3. {311}	Mo	0.90	> 2.00	> 2.00
	Cu	0.46	1.40	2.00
	Co	0.38	1.20	1.60
	Fe	0.35	1.10	1.40
	Cr	0.32	1.00	1.20
4. {400}	Mo	0.75	> 2.00	-
	Cu	0.35	1.20	1.40
	Co	0.30	0.95	1.20
	Fe	0.28	0.85	1.10
	Cr	0.23	0.80	1.00
5. {331}	Mo	1.10	> 2.00	> 2.00
	Cu	0.50	1.70	2.00
	Co	0.42	1.40	1.70
	Fe	0.41	1.20	1.80
6. {422}	Mo	0.86	> 2.00	> 2.00
	Cu	0.38	1.30	1.60
	Co	0.33	1.10	1.50
	Fe	0.31	0.95	1.40
7. {511}	Mo	1.20	> 2.00	> 2.00
	Cu	0.57	1.90	> 2.00
	Co	0.50	1.60	2.00
	Fe	0.46	1.50	1.80
8. {440}	Mo	0.94	> 2.00	> 2.00
	Cu	0.42	1.40	1.80
	Co	0.40	1.20	1.60

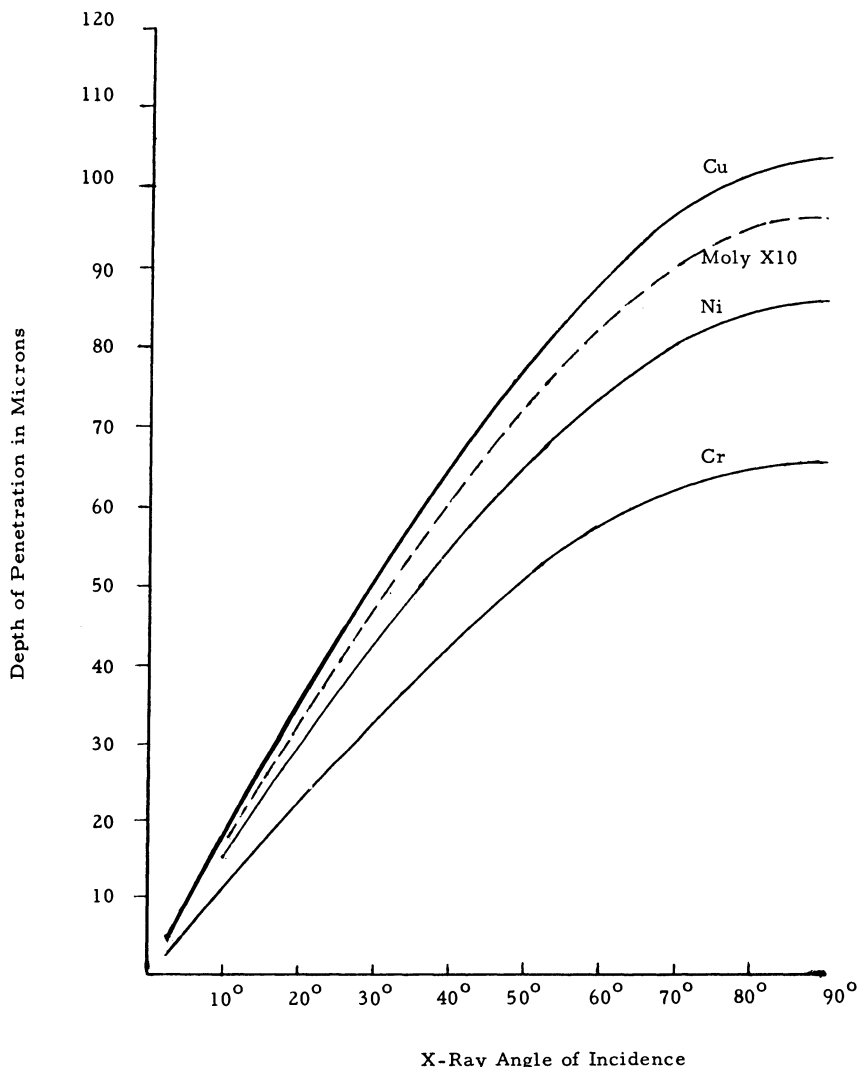


Fig. 21. Penetration depth of z-radiation in imperfect silicon crystal.

possible to calculate where the maximum diffraction volume due to extinction contrast and absorption occurs in perfect and in polycrystalline materials. However, the effects of strain due to work damage, inclusions, diffusion, dislocations, etc., or the effects of new phases produced by diffusion or impurity precipitation make it difficult, at best, to accurately determine

effective depths of diffraction if only one effect is present, and impossible if two or more effects of equal amplitude are present.

Based on these assumptions Berkstresser and Pink calculated x-ray attenuation by low-index planes of silicon with respect to molybdenum, copper, cobalt, iron, and chromium $K\alpha$ radiations. Calculations were performed on a computer, and data were plotted in print-out form. Figure 20 gives a typical plot of x-ray attenuation versus x-ray path length.

In Table IV we list the total path lengths for the attenuation of x-radiation due to primary extinction only (neglecting absorption) at 50, 90, and 95% intensity. This calculation of x-ray attenuation by absorption only assumes that the absorption coefficient is independent of the reflection, and neglects primary extinction effects. It is not a rigorous calculation; nevertheless, it is a useful first approximation. E. D. Jungbluth¹⁹ of our Bayside Laboratory has made this calculation for silicon, using Cu, Ni, Cr, and Mo $K\alpha$ radiations. Figure 21 is a plot of depth of penetration versus angle of incidence (for all reflection planes), again at a penetration depth which is responsible for 95% attenuation. It is seen that at high angle of incidence, penetration depth increases appreciably.

It is important to mention that in a skew reflection the diffracted beam is at an angle from the normal of the specimen surface. Therefore its path length through the emulsion of the photographic plate is correspondingly longer than a beam entering the emulsion along its normal. This reduces the resolution capability of this technique. One has to use thinner emulsion, e.g., 10μ thickness, to relieve this difficulty. With thinner emulsion, however, a decrease in image contrast may occur. The use of a narrower slit and long collimation tube, plus longer exposure, may improve the contrast, but speed of measurement is lost. In practice, many of these variables must be carefully considered and a compromise made of the experimental conditions.

Resolution and Other Limitations

There are a number of basic limitations common to all x-ray topography image-mapping techniques. The diffraction-contrast image is recorded on fine-grained photographic plates at a 1:l ratio; detailed study of the defect structure of the specimen must be made either on the plates under the microscope or on enlarged photographic prints. Lang gave the following maximum useful magnifications and resolution limit of x-ray topographs: for those taken with Mo $K\alpha$ radiation, 300X and 2μ ; and for those taken with Cr and Cu $K\alpha$ radiation, 600X and 1μ , respectively.

These are theoretical resolution limits under ideal conditions. For general applications effective magnification with Mo $K\alpha$ or Cu $K\alpha$ radiation is probably not greater than 200X, and practical resolution is no better than 5 μ . At high magnifications the grainy texture of the photographic plates also interferes with the clarity of the image contrast.

Another limitation is the lack of selectivity. Since x-ray topography is image-mapping of strain fields associated with defects, it does not differentiate among the types of defects. The only way to identify types of defects is to establish correlation by controlled experiments, supplemented by topographs

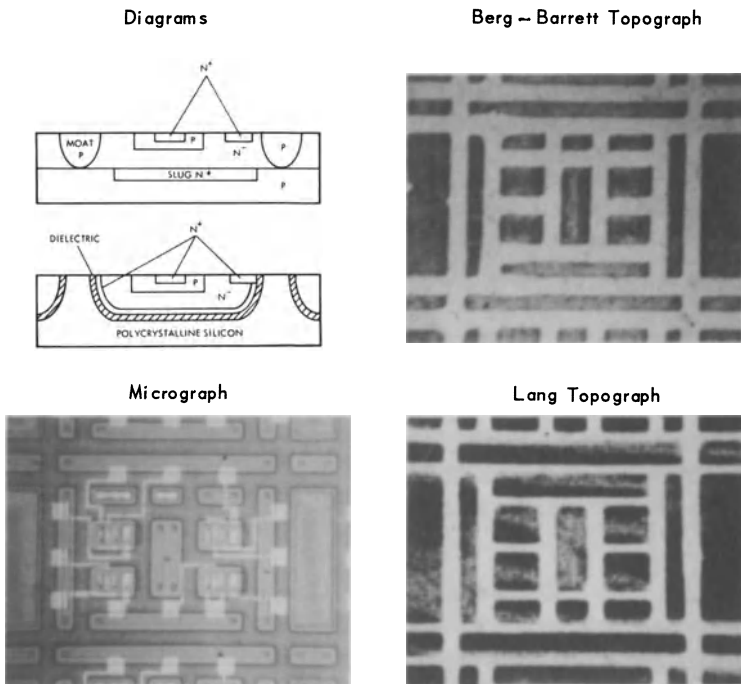


Fig.22. X-ray topographs of dielectrically-isolated silicon integrated-circuit wafer after aluminum metallization. (a) Schematic diagrams of pn junctions and dielectrically-isolated npn transistors. (b) Optical micrograph of dielectrically-isolated silicon-master-chip circuit. (c) Berg-Barrett skew-reflection topograph of such a circuit, showing imperfect photoetching of diffusion windows and line defects in surface layer. (d) Lang topograph of such a circuit. Strong background due to polycrystalline silicon refill interferes with defect detection.

TABLE V
Capability and Features of Berg-Barrett X-Ray Method

Feature	Limitation
Nondestructive	Exposure to x-rays of energy of 20 kV and above may introduce subtle changes, e.g., interface changes in a MOS structure which can be annealed out.
Noncontacting	The slice is placed onto a holder with wax; thorough cleaning is necessary if specimen is to be heat-treated.
Rapid process	Exposure time for Berg-Barrett topographs 2–10 min, plus sample orientation and film development.
Resolution (lateral)	Ultimate limit 1–2 μ ; practical limit $\sim 5 \mu$.
Selectivity	Configurations of dislocations may be determined using topographs from different reflecting planes; identity of other defects may be achieved by correlation experiments.
Area under examination	Nonscanning Berg-Barrett topographs, 1 cm \times 2.5 cm, topographs recorded at a 1:1 ratio and enlarged photographically or examined under microscope.
Capital investment	Camera can be assembled with parts under \$2000; x-ray generator and ratemeter extra.
Thickness of surface layer under examination	One tenth to several μ , but continuous variation not feasible.

taken on different reflections. Still x-ray topographs can only differentiate between types of defects when their population densities are relatively low. In a device of very complicated structure, such as a finished, high-component-density integrated circuit, the strain fields associated with dislocations introduced by the different diffusion cycles, precipitated metallic impurities, and impurity clustering and segregates may overlap. These usually cannot be resolved, and the overall observation must be used as guideline for accepting or rejecting the particular wafers for circuit-device fabrication.

We have recently taken x-ray diffraction topographs of dielectrically-isolated silicon integrated-circuit wafers (kindly furnished by W. Salmere of GT and E Laboratories). Figure 22 illustrates this particular application: (a) shows the difference between a *pn* junction isolated and a dielectrically-isolated transistor component, (b) is a micrograph of a master-chip circuit with aluminum contact metallization, (c) is a reflection topograph, and (d) a transmission topograph. The grainy structure in (d) is due to the polycrystalline silicon in the refill region. In (c) we can identify several diagonally-aligned lines, which are probably either surface scratches or slip lines. There are also a

number of KPR flaws, shown as poorly-defined dark regions. These flaws can be correlated with electrical measurements such as resistor values, etc. Similar applications are feasible with silicon/sapphire, silicon/spinel, Ge/GaAs, GaAs/sapphire, and other heteroepitaxial systems.

Table V summarizes the features and capabilities of the nonscanning Berg-Barrett method using our current facility. It is important to point out the possibility of "trade-off," by using, e.g., a longer distance between x-ray source and target for better image resolution at a sacrifice of longer exposure time. Recently Dionne¹⁶ reported an adaptation of a stationary-film technique developed by Carlson and Wegener¹⁷ to obtain large-area, high-resolution topographs with $K\beta$ radiation. Using Co $K\beta$ radiation Dionne examined stacking faults in silicon epitaxial films with instrument resolution in the range 0.1–2 μ over a 4 cm² area recorded. We cannot make any further comment on this point, since this is the only work concerning this modified process. Nevertheless, with improved instrumentation the capability of this technique can be expanded for useful application to the characterization of crystal surfaces.

SUMMARY

To summarize, we have described a few x-ray topography techniques useful in the study and characterization of surface layers. Techniques such as the composition topograph are useful for heteroepitaxial structures or similar layers of different chemical composition. Double-crystal topography and Berg-Barrett reflection techniques have more general applications. We also pointed out the advantages and limitations of the use of the Berg-Barrett technique in the detection and characterization of silicon surfaces for the fabrication of microelectronic devices and circuits. These nondestructive measurements are complementary to the electron-diffraction, electron-microscopy, scanning-electron-microscopy, infrared, and other techniques discussed in this volume.

ACKNOWLEDGMENT

The Berg-Barrett topography work was partly supported by WPAFB-MATE under contract AF33615-67-C-1508. We also are indebted to E. S. Meieran, J. K. Howard, R. D. Deslattes, and E. D. Jungbluth for permission to use figures taken from their work. V. Lyn, J. Sciola, and J. Mullins assisted in the x-ray reflection topographic work.

REFERENCES

1. A. R. Lang, *Brit. J. Appl. Phys.* **14**, 904 (1963).
2. I. A. Blech, E. S. Meiran, and H. Sello, *Appl. Phys. Letters* **7**, 176 (1965).
3. J. K. Howard and R. D. Dobrott, *Appl. Phys. Letters* **8**, 107 (1965); *J. Electro. chem. Soc.* **113**, 567 (1966).
4. J. K. Howard and R. H. Cox, The Crystalline Perfection of Melt-Grown GaAs Substrates and Ga(As,P) Epitaxial Deposits, *Advances in X-Ray Analysis*, G. R. Mallett, M. J. Fay, and W. M. Mueller, eds., Plenum Press, New York (1966) pp. 35-50.
5. E. S. Meieran, *J. Electrochem. Soc.* **114**, 292 (1967).
6. T. B. Light, M. Berkenblit, and A. Reisman, to appear in *J. Electrochem. Soc.*
7. R. D. Deslattes and B. Paretzkin, paper presented at the Symposium on Trace Characterization - Chemical and Physical, Oct. 1966.
8. J. B. Newkirk, *Trans. AIME* **215**, 483 (1959); *Phys. Rev.* **110**, 1465 (1958).
9. J. B. Newkirk, J. D. Young, and J. P. Spencer, *J. Appl. Phys.* **35**, 1362 (1964).
10. J. Tomiser and P. Skalicky, *Acta Physica Austriaca* **26**, 373 (1966).
11. F. C. Frank, B. R. Lawn, and A. R. Lang, *Proc. Roy. Soc. A* **301**, 239 (1967).
12. E. M. Juleff and A. G. LaPierre, *Intern. J. Electronics* **20**, 272 (1966).
13. E. M. Juleff, A. G. LaPierre, and R. G. Wolfson, The Analysis of Berg-Barrett Skew Reflections and Their Applications in the Observation of Process-Induced Imperfections in (111) Silicon Wafers, *Advances in X-Ray Analysis*, Vol. 10, J. B. Newkirk and G. R. Mallett, eds., Plenum Press, New York (1967) pp. 173-184.
14. R. W. James, *The Optical Principles of Diffraction by X-Rays*, Bell and Sons, London (1954), pp. 60-62.
15. B. D. Cullity, *Elements of X-Ray Diffraction*, Addison-Wesley Publishing Co., Reading, Mass. (1956), p. 267.
16. G. Dionne, *J. Appl. Phys.* **38**, 4095 (1967).
17. K. A. Carlson and R. Wegener, *J. Appl. Phys.* **32**, 125 (1961).
18. S. B. Austerman and J. B. Newkirk, *Proc. 15th Annual Conference on the Applications of X-Ray Analysis*, U.K. Bonse, M. Hart, and J. B. Newkirk, eds.,
19. E. D. Jungbluth, private communication.
20. R. Berkstresser and F. X. Pink, *Intern. J. Electronics* **23**, 443 (1968).
21. U. Bonse and E. Kappler, *Z. Naturforsch.* **13a**, 348 (1958).
22. M. Renninger, in: *Crystallography and Crystal Perfection*, G. N. Ramachandran, ed., Academic Press, New York (1963), p. 146.

ADDITIONAL SUGGESTED REFERENCES FOR
X-RAY DIFFRACTION TOPOGRAPHY

- J. Chikawa and J. B. Newkirk, "Effects of Trace Impurities on X-Ray Diffraction," in: *Trace Characterization, Chemical and Physical*, W. W. Meinke and B. F. Scribner, eds., National Bureau of Standards Monograph 100, Washington, D.C. (April 1967).
- W. W. Webb, "X-Ray Diffraction Topography" in: *Direct Observation of Imperfections in Crystals*, J. B. Newkirk and J. H. Wernick, eds., John Wiley (Interscience), New York (1962).
- U. K. Bonse, M. Hart, and J. B. Newkirk, "X-Ray Diffraction Topography," in: *Advances in X-Ray Analysis* Vol. 10, J. B. Newkirk and G. R. Mallett, eds. Plenum Press, New York (1967). An excellent general review.

- S. B. Austerman and J. B. Newkirk, "Experimental Procedures in X-Ray Diffraction Topography," *Ibid.* For experimental procedures.
- A. Authier, "Contrast of Dislocation Images in X-Ray Transmission Topography," *Ibid.* For diffraction theory.
- G. H. Schwuttke and J. K. Howard, X-Ray Stress Topography of Thin Films on Germanium and Silicon, AFCRL-67-0564 Scientific Report No. 2, 1967. SOT technique, but very readable.
- G. N. Ramachandran, *Crystallography and Crystal Perfection*, Academic Press, New York (1963) Excellent background reading.

IMPORTANT EARLY PAPERS ON X-RAY DIFFRACTION TOPOGRAPHY

X-Ray Transmission Topography (Scanning Transmission and SOT). Laue Geometry

- A. R. Lang, *J. Appl. Phys.* **29**, 597 (1958); **30**, 1748 (1959).
- G. H. Schwuttke, *J. Electrochem. Soc.* **109**, 27 (1962); *J. Appl. Phys.* **33**, 1538 (1962); **36**, 2712 (1965).

X-Ray Reflection Topography (Berg-Barrett Method). Bragg Geometry

- J. B. Newkirk, *Phys. Rev.* **110**, 1465 (1958); *Trans. AIME* **215**, 482 (1959).

Anomalous Transmission (Borrmann Method). Laue Geometry

- G. Borrmann, W. Hartwig, and H. Irmler, *Z. Naturforsch.* **13A**, 423 (1958).
- G. Borrmann, *Physik* **15**, 508 (1959).

Double-Crystal Topography. Bragg Geometry

- U. Bonse, in: *Direct Observation of Imperfection in Crystals*, J. B. Newkirk and J. H. Wernick, eds., John Wiley (Interscience) New York (1962).
- U. Bonse and E. Kappler, *Z. Naturforsch.* **13A**, 348, (1958).

High-Energy Electron-Diffraction and X-Ray Emission Analysis of Surfaces and Their Reaction Products

P.B. Sewell, D.F. Mitchell, and M. Cohen

*Division of Applied Chemistry
National Research Council
Ottawa, Canada*

A technique which can provide both structural and chemical information from surface films at the monolayer level has been developed. For structure studies the grazing incidence, high-energy electron-diffraction method has been applied in ultra-high vacuum. The portion of the specimen surface irradiated during electron-diffraction observations acts as a line source of x-rays located at the focus of a low-atomic-number x-ray spectrometer. The ultra-high-vacuum environment in the diffraction chamber is separated from that of the conventional vacuum spectrometer by an x-ray-transparent window. Characteristic $K\alpha$ radiation from monolayer quantities of both carbon and oxygen on a low-index surface of iron has been observed. Diffraction patterns and x-ray information may be obtained from such structures simultaneously. Attempts to calibrate the apparatus for carbon and oxygen layers on iron are discussed in some detail. The method appears well suited to the study of kinetic phenomena in surface films of mean thickness less than 100 Å.

INTRODUCTION

In recent years much attention has been given to the study of surface structure and ordered gas adsorption phenomena on single crystals in well-

controlled vacuum environments. Structural studies of this type have favoured the use of low-energy electron diffraction (LEED).¹ Increasing concern about the chemical composition of surface layers has resulted in the development of new techniques in Auger electron spectroscopy to permit elemental identification at the monolayer level.² Currently the combined techniques of LEED and Auger electron spectroscopy³ are being applied to surface studies using electron-beam energies generally below 1500 eV.

In contrast to experiments of this type, much information can be obtained about the surface of solids using electrons in the energy range of 20 to 100 keV. Since the early experiments of Thomson⁴ the method of grazing incidence, high-energy electron diffraction (HEED) has been used widely. In particular, it has found application in studies of thin-film growth associated with electrodeposition, gas/solid reactions, and condensation from the vapor phase. Investigations of this type have been reviewed by Pashley.⁵ They include extensive studies of surface morphology and the examination of films of mean thickness from about 1 to 1000 Å.

The HEED technique operates effectively at pressures of 10^{-4} to 10^{-5} torr and has been particularly successful in examining stable surface structures in conventional vacuum environments. This situation has been responsible, in part, for the delay in developing the technique in ultra-high vacuum. In addition, there has been much scepticism about the capability of the HEED method in monolayer studies.

High-energy electron-beam methods may be applied effectively to the study of "clean" surface phenomena⁶ A brief description of facilities for making such studies is given in the first part of this chapter, together with a discussion and demonstration of the sensitivity of the method. The second part is devoted to a description of a new approach to the examination of thin surface films by x-ray emission analysis. Preliminary results from a study combining reflection electron diffraction and x-ray emission analysis of monolayers will be described.

HIGH-ENERGY ELECTRON DIFFRACTION

Experimental

The same principles of vacuum practice used in the development of LEED facilities have been used to construct a demountable HEED apparatus. The main features of the instrument, constructed in stainless steel, are shown in Fig. 1. The design of the electron gun is taken from the work of Haine and Einstein⁷ and the gun is constructed so as to minimize outgassing during

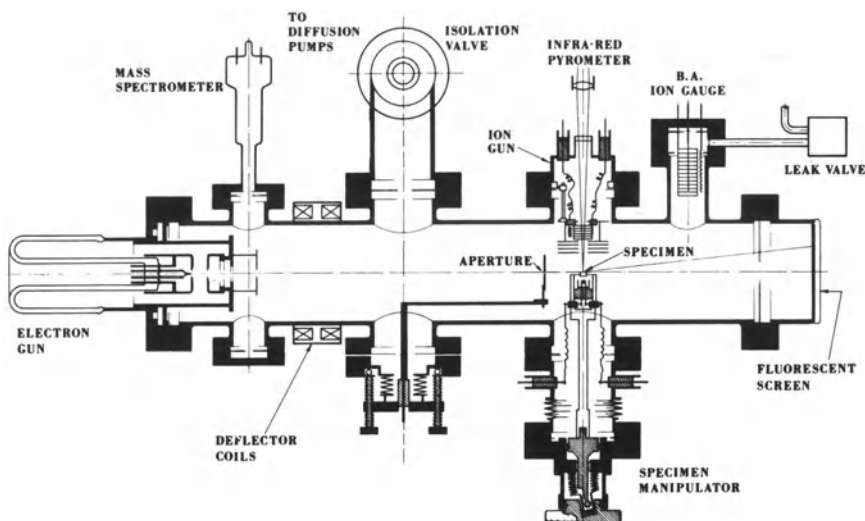


Fig. 1. Schematic diagram showing main features of ultra-high vacuum, high-energy electron-diffraction apparatus.

operation. The slightly divergent electron beam from the gun is limited in diameter at the specimen level by an aperture about 100μ in diameter placed 3 cm before the specimen. The beam is aligned with the aperture using magnetic deflection coils, and the aperture unit may be adjusted laterally to permit alignment with the x-ray spectrometer (see Figs. 4,5).

Electrons scattered from the specimen are observed on a 4 in. diameter, transmission-type fluorescent screen at one end of the apparatus. This has a willemite phosphor which is backed with an optically-opaque aluminum film about 5000 Å thick. Observation of diffraction patterns is not affected by light from sources within the apparatus. Diffraction patterns from specimens at temperatures up to 2000°K may be observed and recorded. The screen is photographed at unit magnification using an 88 mm, f/1.4 Oscillo Raptar lens.

Single-crystal specimens are generally of cylindrical form some 2–7 mm in diameter. They are supported by three small tungsten pins mounted radially on a molybdenum ring. This unit is located a few millimeters above a simple electron gun used to heat the specimen (Fig. 1). The entire specimen assembly is mounted on a manipulator which provides all the independent motions of the specimen required for grazing-incidence HEED studies. Mounted opposite the specimen is a simple ion gun, which can be used for ion bombardment at normal incidence using energies up to 500 eV. A window on the same flange (see Fig. 1) provides a view through the ion gun structure from which contin-

uous measurement of the specimen surface temperature can be made with an infrared pyrometer.

The system is pumped through a 2½ in. bakeable isolation valve by a trapped-oil diffusion pump using a low vapor pressure oil (Dow Corning 705). The pumping speed at the system is about 35 liters/sec for nitrogen. Additional pumping speed for active gas is obtained when required with a titanium getter attached to a 2½-in.-diameter port not shown in Fig. 1. Bake-out temperatures up to 300°C may be used, this limit being set by the presence of the x-ray spectrometer attached to the system at the specimen chamber level (see Fig. 5). With bake-out temperatures of 200–250°C the system may be cycled regularly to about 2×10^{-10} torr after a 16 hr bake. Residual gases are monitored with a small partial-pressure analyzer. At the base pressure the predominant gases are H₂, CO, CO₂, and H₂O.

Gases are introduced into the system *via* a bakeable leak valve. The high-voltage electron gun, the electron gun for specimen heating, and the ion gun all operate effectively up to a pressure of 10³ torr. Surface reactions over a wide range of temperatures may be followed continuously at pressures from 10⁻⁹ torr to 10³ torr. Modifications of the gas atmosphere by reactions with the hot filaments must always be considered.

Sensitivity

The ultimate sensitivity of the reflection high-energy electron-diffraction method has been the subject of investigation for many years. Early studies in this area were concerned with the adsorption of long-chain hydrocarbons on polished metal surfaces or cleaved mica substrates.⁸ Germer and Storks⁹ established that diffraction patterns could be obtained from a single monomolecular layer of stearic acid retracted onto polished chromium by the Blodgett–Langmuir method. From their experiments they made the accurate prophecy, “it seems to us that the study of adsorbed gas films by means of electron diffraction patterns observed photographically waits now only upon improvement in vacuum technique.” Other studies on the adsorption of single layers of xanthate and dithiophosphate molecules onto cleaved galena¹⁰ have demonstrated a two-dimensional ordering phenomena in such cases.

Of particular interest are the results of Newman and Pashley,¹¹ who measured by radioactive tracer methods the mean thickness of thin films of copper and silver bromide formed on atomically-flat (111) silver surfaces. These authors estimated that diffraction patterns could be obtained from a mean thickness of about 0.8 Å (7×10^{-8} g/cm²) of copper condensed from the vapor phase, and about 0.4 Å (2.6×10^{-8} g/cm²) of silver bromide formed by reaction of bromine with the silver surface.

In conventional HEED experiments we have examined a thin film of Fe_3O_4 grown as highly-oriented crystallites on a (100) iron surface.⁶ From measurement of electron micrographs of a replica of the film the mean size and distribution of the crystallites were determined. Intense diffraction maxima from about $5 \times 10^{-8} \text{ g/cm}^2$ of Fe_3O_4 were observed, suggesting that the limit of detection might be extended to $5 \times 10^{-9} \text{ g/cm}^2$ or less.

Diffraction maxima which may have been due to a single layer of gas adsorbed from the residual vacuum were reported by Haase.¹² These results were obtained during the growth of iron single-crystal films by condensation in vacuum onto cleaved NaCl. The results were not reproducible due to the high background gas pressure. Recently experiments on the controlled adsorption of oxygen onto the (110) nickel surface¹³ carried out in the apparatus described here, have shown that diffraction information may be obtained from ordered gas-adsorption structures with coverages as low as 10% of a monolayer.

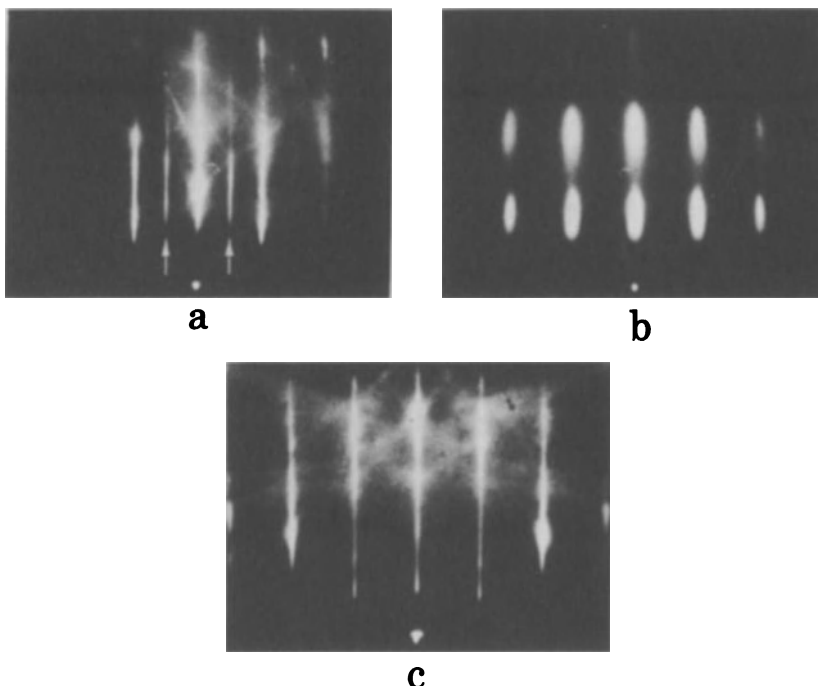


Fig. 2. Diffraction patterns recorded during the removal of an $\text{Fe}(100)\text{-c}(2\times 2)\text{-C}$ contamination structure (a) initial surface; (b) after 5 min at $10 \mu\text{A}/\text{cm}^2$, 500-eV argon ions; (c) after further argon-ion bombardment and 10 min anneal at 400°C

An example of diffraction effects from a two-dimensional ordered structure is given in Fig. 2a. This pattern was obtained from a (100) iron surface with the electron beam parallel to the [011] zone after hydrogen reduction of the surface oxide and further annealing to remove adsorbed hydrogen. The diffraction maxima indicated by the arrows do not belong to iron and can be attributed to a body-centered array of scattering centers having twice the period of the iron lattice (Fig. 3). This structure has been reported by Pignocco and Pellissier¹⁴ during LEED studies on the (100) iron surface and is designated as the Fe(100)-c(2X2)-? structure, since the atomic species associated with the structure is uncertain. If the structure is due to a uniform distribution of carbon on the surface, as shown in Fig. 3, about 6×10^{14} atoms/cm² are involved, or 6×10^9 g/cm² carbon.

Limitations

In the above discussion of sensitivity the diffraction patterns considered resulted from atoms having ordered arrays in either two- or three-dimensional networks. Such favorable circumstances do not always occur in practice. Gas can be adsorbed on surfaces in a random manner, and thin films frequently

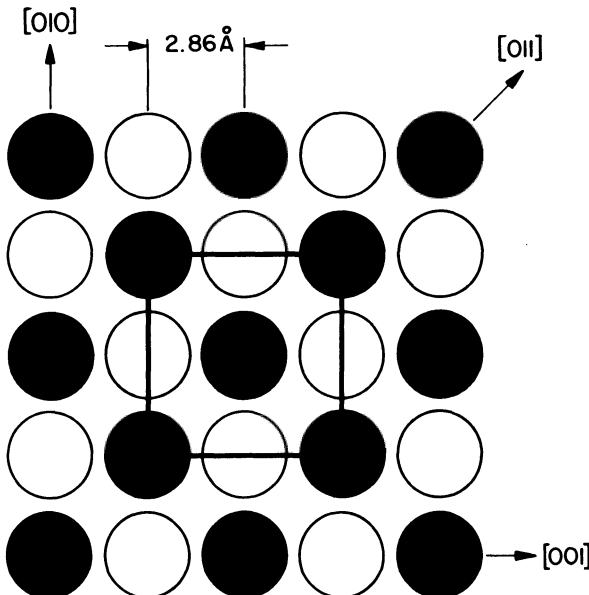


Fig. 3. Unit cell for Fe(100)-c(2X2)-C structure proposed by Pignocco and Pellissier.¹⁴

grow with amorphous structures. In the former case detection of the adsorbed gas layer by diffraction methods is difficult, particularly at low coverages. In the latter case the identification of unknown atomic species in the film from diffraction information is almost impossible.

A further limitation in the study of thin films by electron diffraction occurs when it is necessary to estimate the amount of material contributing to the diffraction pattern. This problem results, in part, from the many difficulties encountered in preparing thin films of known thickness, particularly in the 0–25 Å region. Greater uncertainty arises from a lack of knowledge of the ratio of coherent to incoherent electron scatter in the diffraction process. The intensity of diffraction maxima depends on many variables, such as the substrate morphology, the overgrowth morphology and epitaxy, and the extent of multiple-scattering phenomena.

Additional information regarding the nature of the surface layer would be most useful in surface studies by reflection electron diffraction, particularly if such information could be obtained during the course of diffraction observations. Elemental identification alone would assist greatly with the interpretation of diffraction patterns. Quantitative information obtained during the growth or removal of surface layers would be of great value in the study of thin-film kinetics. With these interests in mind we have developed a system which is capable of examining the characteristic x-ray emission originating from specimens during reflection electron diffraction studies. This experimental arrangement will now be described, together with some results from preliminary studies.

X-RAY EMISSION ANALYSIS OF SURFACES

Introduction

Since the development of the first practical electron-excited x-ray micro-analyzer by Castaing¹⁵ there has been extensive development of this method, particularly for application in metallurgy and mineralogy. One emphasis in instrumental development has been toward the production of efficient x-ray spectrometers capable of giving adequate intensity and resolution when examining the x-ray output from small sources. In a typical example an electron beam accelerated through 10–30 kV is focused to a spot some 2 μ in diameter and directed at normal incidence onto a metal surface. Electrons absorbed in the region below the surface excite characteristic x-ray emission from a volume of about 8 μ³, which for an assumed density of 5 g/cm³ would be 4×10^{-11} g of material. From a consideration of practical counting

statistics and the ratio of characteristic to continuous x-radiation Birks^{1,6} has estimated that under favorable conditions characteristic x-rays may be identified from as little as 10^{-14} g of material.

In a reflection electron diffraction experiment of the type described above the surface area irradiated at grazing incidence is determined by the width of the beam and the length of the specimen in the direction of the beam. For a 5-mm specimen and a 100- μ beam this area is $5 \times 10^{-3} \text{ cm}^2$. Hence for a single atomic layer in the surface about 10^{-10} g of material is irradiated. Since electron-beam currents used in both diffraction experiments and x-ray micro-analyzers are similar, usually in the range 10^{-8} – 10^{-6} A, the addition of an x-ray spectrometer from a commercial microprobe to an electron diffraction apparatus appeared to offer a practical solution to the development of a combined instrument. This approach has been made with the instrument to be described.

Experimental

A low-atomic-number curved-crystal spectrometer developed from the work of Henke^{1,7} by Ong^{1,8} for the Norelco AMR/3 microprobe has been

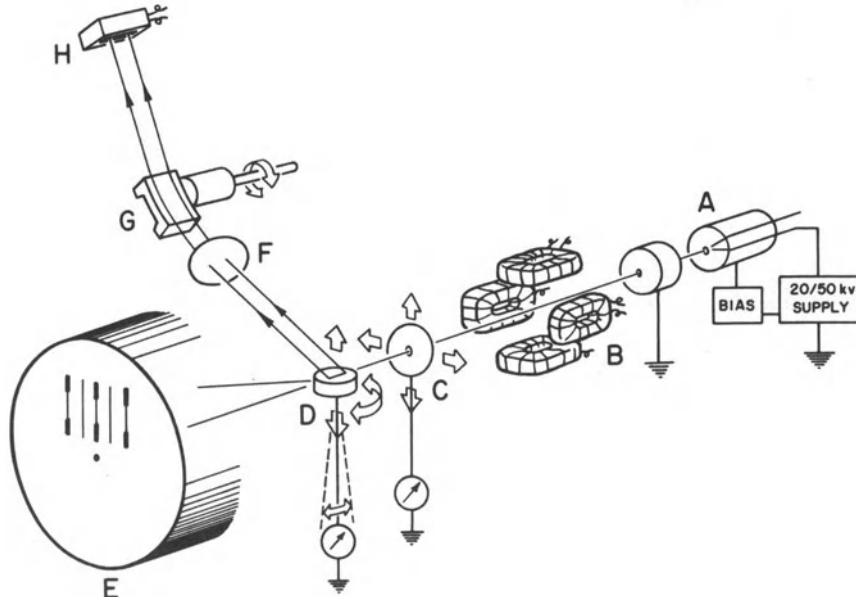


Fig. 4. Schematic diagram of combined electron diffraction and x-ray emission apparatus.

used for this study. The main features of the apparatus are shown in Fig. 4. Since the dispersing element G of the spectrometer is a continuously-bent mica crystal (with a lead stearate overlay), the line source of x-rays on the specimen surface D may be focused on the detector slit H for all wavelengths providing it is lying on the Rowland circle for the arrangement and is parallel to the axis of rotation of the spectrometer. In this instrument this source may be adjusted for optimum focus with the aid of the specimen manipulator controls and the adjustable aperture C . The total beam current to this aperture is monitored and is used with a feedback circuit to control the grid bias of the electron gun and hence the total electron emission. The current to the specimen can be monitored at the specimen level D or measured more accurately with a Faraday cage (not shown) placed between the specimen and the screen E with the specimen removed.

Some details of the spectrometer and the method of coupling to the specimen chamber of the diffraction tube are shown in Fig. 5. The main technological problem that arises with this instrument is the separation of the

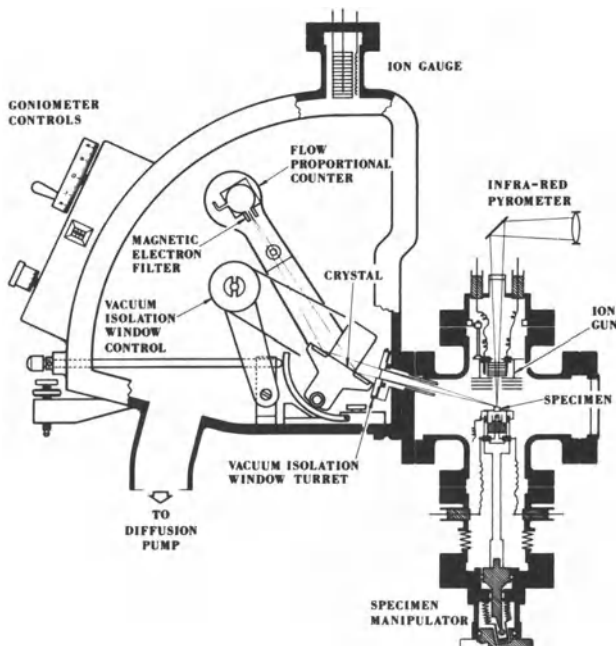


Fig. 5. Schematic diagram showing some details of the location of the x-ray spectrometer in relation to a specimen. This section is normal to the plane of the specimen shown in Fig. 1.

vacuum of the x-ray spectrometer from that of the controlled atmosphere of the diffraction tube. The arrangement described by Ong for the conventional Norelco micro-probe¹⁹ has proved satisfactory to date. The flow-proportional counter operates at 1 atm of *P*-10 gas (90% Ar-10% CH₄). For low-atomic-number studies the counter window consists of a thin multilayer film of formvar of total thickness about 6000 Å supported on a 100 mesh/in. nickel screen having a transparency of 76%.¹⁸ To handle gas diffusion through this window, and general outgassing from the spectrometer, a diffusion pump has been added to the base of the spectrometer. This provides about 35 liters/sec of pumping speed, and can hold the chamber pressure at about 5×10^{-4} torr. The pressure gradient between the two systems, from 5×10^{-4} torr in the spectrometer to as low as 10^{-10} torr in the diffraction tube, is maintained by a double layer of unsupported Formvar 1000 ± 500 Å thick mounted in the standard rotating turret of the Norelco spectrometer. A very small area of elastomer sealing is exposed to the "clean" vacuum system in this arrangement. Mass-spectrometric monitoring of the residual gases in the diffraction tube shows that no troublesome components, at the 10^{-10} torr level, can be attributed to the small exposed area of these seals, or to the thin window. When a 10-mil Mylar window is used between the systems the spectrometer can operate at 760 torr with the specimen region at the 10^{-6} – 10^{-7} torr level. With this arrangement preliminary optical and x-ray alignment can be performed using a thin willemite specimen on a polished metal substrate.

It can be seen from Fig. 5 that x-radiation from a specimen can be recorded during the heating or ion bombardment used to process the specimen surface. X-ray emission from a tungsten crystal up to 1500°K has been recorded without collapse of the thin Formvar membrane separating the systems.

The results reported in this chapter have been obtained using accelerating voltages between 40 and 50 kV and a beam current of $(3-8) \times 10^{-8}$ A at the specimen level. The cross-section of the electron beam at the specimen is determined by the shape of the aperture *C* of Fig. 4. To obtain adequate beam intensity without the complication of added electron optics, a beam of rectangular cross-section has been used. At the specimen level this beam is 300 μ wide in the plane of the specimen surface and 80 μ wide normal to the surface. Hence when the grazing angle of incidence between the beam and a flat surface is 1° a surface of 5 mm will completely intercept the beam. Most studies have been carried out with such geometry, the angle of incidence varying between 0.5° and 1.5°. The take-off angle for x-rays is 15°. The x-ray emission spectrum from a flat, electropolished surface of a high-purity iron specimen is shown in Fig. 6. Major lines are indicated, showing the order of reflection from both the mica (*M*) and lead stearate (*LSD*). The more

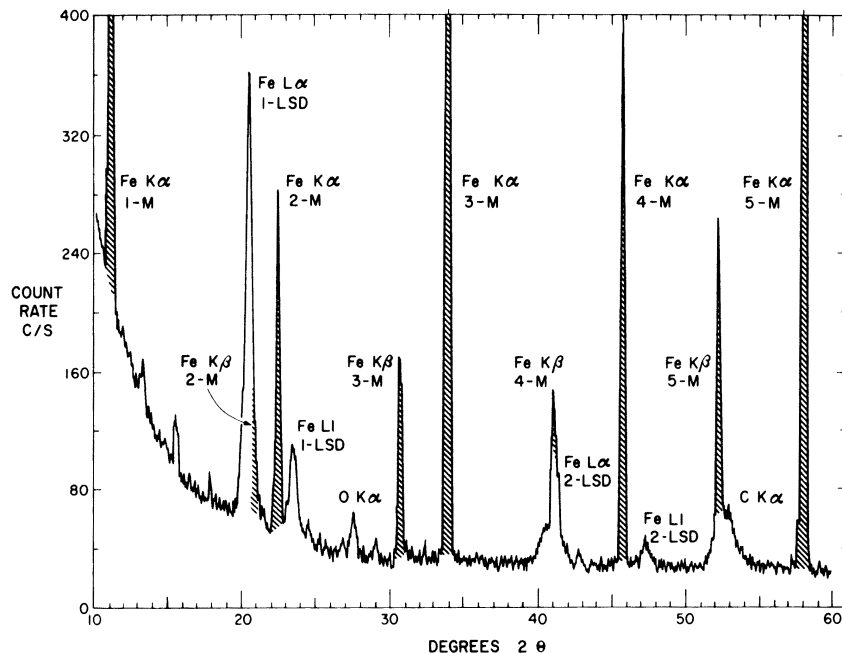


Fig. 6. X-ray emission spectrum from electropolished surface of high-purity iron. Electron beam at grazing angle of incidence, 40 kV, 3×10^{-8} Å. No electronic discrimination.

energetic $K\alpha$ and $K\beta$ lines, shown with cross-hatching, may be eliminated from the spectrum by the use of pulse-height analysis. This is particularly important when studying carbon in (or on) iron, since the strong $Fe\ K\beta$, fifth-order off mica falls close to the peak of the broad $C\ K\alpha$, first-order from lead stearate. The carbon peak in this example arises from a stage of specimen preparation when the surface was cut by spark erosion under oil. Carbon is retained in the surface of the specimen by this treatment, but can be removed by further electropolishing. The oxygen $K\alpha$ peak in the spectrum arises from the thin oxide film on the specimen surface. It can be studied without serious interference from iron radiation. The rise in the background at low 2θ values is similar to that reported by Ong for this spectrometer.¹⁹

Carbon

Interest in the study of carbon $K\alpha$ radiation emitted from the surface of solids arises particularly in connection with the preparation of "clean" surfaces. It is well known that trace hydrocarbons in vacuum systems may be

cracked by electrons and then polymerized on nearby surfaces. This phenomena has been studied in connection with the transmission electron-microscope²⁰ and more recently in electron-microprobe experiments.²¹ In more carefully controlled ultra-high vacuum studies carried out by low-energy electron diffraction, contamination structures due to carbon have been reported by several authors.^{14,22} The origin of this carbon is not always clear. In some cases it is produced from the gas phase, and in others by diffusion of carbon from the bulk of the specimen. Identification of such carbon structures has been attempted by chemical methods such as reaction with oxygen and/or hydrogen²² but in some cases this technique is not particularly successful.¹⁴ In the authors' experience, and from a survey of the literature, carbon contamination would appear to present one of the largest single problems relating to the chemistry of clean surfaces.

When the "clean" surface state is achieved, the mechanism of adsorption of carbon-containing gases such as CO, C₂H₄ is of interest in catalytic studies. The evaluation of the amount of carbon associated with such adsorption phenomena at the monolayer level would be of great interest.

In preliminary attempts to calibrate the apparatus for carbon *Ka* radiation stearic acid monolayers have been used. Two methods of producing monolayers on the surface of electropolished iron specimens have been tried. In the first instance the stearic acid layer has been produced by the method of Blodgett and Langmuir,²³ using a hydrophil balance to establish the presence of the compressed monolayer on a water surface. The specimen, resting on the base of the balance trough, is drawn up through the water surface in order to produce a single layer coverage. The second technique is that of retraction from a solution of stearic acid in nitrobenzene as described in detail by Timmons *et al.*²⁴ These authors have studied the adsorption of C¹⁴-labeled stearic acid on iron and have correlated the stearic acid coverage with the contact angle of methylene iodide on the surface. The contact angle of a sessile drop of methylene iodide has been used in the present study to check the coverage of stearic acid produced by both the above methods, and also as a check on the stability of the layer when subjected to the vacuum of the instrument. In addition, contact-angle measurements have been used as a sensitive test for the cleanliness of the electropolished iron surface.

Due to impurities in our nitrobenzene solution, the retraction method has not produced a complete monolayer. However, it has been found possible to withdraw specimens from the hydrophil balance trough through a stearic acid monolayer and obtain surface films with a contact angle of 71°± 2°, suggesting 100% coverage.²⁴ Such films appear stable for long periods in a vacuum of 10⁻⁷ torr, as no change in contact angle occurs during vacuum exposure.

Since it has been difficult to reproduce identical conditions of specimen irradiation during these preliminary studies, it is convenient to compare results in terms of the ratio $(N_T - N_B)/N_B$, where N_T is the total signal at the peak maxima and N_B is the background determined from measurements on either side of the peak, or, in specific cases, at the peak position.

Calibration was attempted on a 5-mm-diameter specimen of high-purity iron which had been mechanically polished to a $1\text{-}\mu$ finish and then electro-polished. When the electropolished specimen was rinsed in boiling distilled water for 2 min a reproducible carbon $K\alpha$ signal/background ratio of $0.3 \pm 10\%$ was obtained. After withdrawing the specimen through the stearic acid under conditions known to produce a contact angle of $71^\circ \pm 2^\circ$ the specimen was reloaded into the apparatus and evacuated to about 10^{-6} torr. At this pressure the vacuum environment is predominantly water vapor in the all-metal system.

Using a 40-kV beam, the electron-diffraction pattern from the stearic acid layer was observed and the C $K\alpha$ peak recorded while examining the surface from several directions. The background was recorded at 2θ values about $2\frac{1}{2}^\circ$ on either side of the C $K\alpha$ maximum. Prolonged observations showed that there was no significant loss or gain of carbon in the area irra-

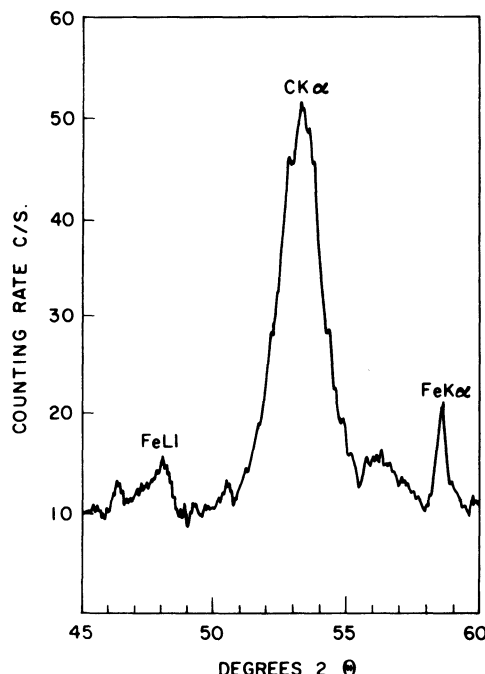


Fig. 7. Carbon $K\alpha$ signal from single layer of stearic acid on electropolished surface of iron. Electron beam at grazing angle of 1° , 40 kV, 6×10^{-8} A.

diated. The specimen was removed and the contact angle measured to check that the layer value was $71^\circ \pm 2^\circ$.

The ratio $(N_T - N_B)/N_B$ for a stearic acid monolayer was found to be 4.1 ± 0.3 . A record of the C $K\alpha$ peak obtained from a specimen giving this ratio is shown in Fig. 7.

If a figure of 18.9 \AA^2 is used for the area of a stearic acid molecule $\text{CH}_3(\text{CH}_2)_{16}\text{COOH}$,²⁴ a compact monolayer contains 95×10^{14} carbon atoms/cm². On the iron (100) surface a continuous surface array of carbon atoms with the c(2X2) structure described in Fig. 3 would contain 6.1×10^{14} carbon atoms/cm². Thus the ratio $(N_T - N_B)/N_B$ for such a layer is expected to be 0.26. A simple square array of carbon atoms on this surface would give a ratio of 0.52, which can be regarded as a tentative figure for monolayer coverage. In these experiments with stearic acid monolayers a typical background count at 2.5° on either side of the C $K\alpha$ position has been 10 counts/sec. For a reasonable counting time of 200 sec the total count is 2000, and the standard deviation $\sigma_B = \sqrt{2000} = 45$. The $3\sigma_B$ limit of detectability is $135/200$ counts/sec, or about 0.7 counts/sec. Hence at present the limit of detectability of carbon contamination on iron is about 10% monolayer, or $2.5 \times 10^{-9} \text{ g/cm}^2$.

Combined electron diffraction and x-ray emission observations on the Fe(100)-c(2X2)-C structure of Fig. 2 are of particular interest in the light of attempts to calibrate the system for carbon. A 2-mm-diameter surface parallel to the (100) plane of iron was prepared as described above. The specimen was annealed at 600°C in hydrogen to remove the surface oxide film. After this treatment the Fe(100)-c(2X2)-C diffraction pattern is produced. This has been observed in the LEED studies of Pignocco and Pellissier¹⁴ and in independent HEED studies by the present authors.⁶ Extra reflections associated with this structure when observed along the Fe[011] zone appear halfway between the normal iron reflection of Fig. 2a. When this surface is exposed overnight to the background gas in the instrument the carbon $K\alpha$ peak of Fig. 8a is recorded. This has an $(N_T - N_B)/N_B$ value of 1.7 ± 0.2 , corresponding to about three monolayers of carbon. When the specimen is heated to 600°C to remove adsorbed gas the ratio decreases to 0.8, as in Fig. 8b. The decrease of 0.9 corresponds to slightly more than one monolayer, and is associated with the desorption of CO from the surface. There is no significant change in the diffraction pattern. After ion bombardment with 500-eV argon ions for 5 min at $10 \mu\text{A}/\text{cm}^2$ the features from the c(2X2) structure disappear (Fig. 2b) and the C $K\alpha$ signal drops to a lower level with $(N_T - N_B)/N_B$ about 0.3, as in Fig. 8c. A small percentage of the Fe $K\beta$ line is passing through the pulse-height analyzer in this case. With an increasing period of ion bombardment the C $K\alpha$ peak disappears (Fig. 8d). Following

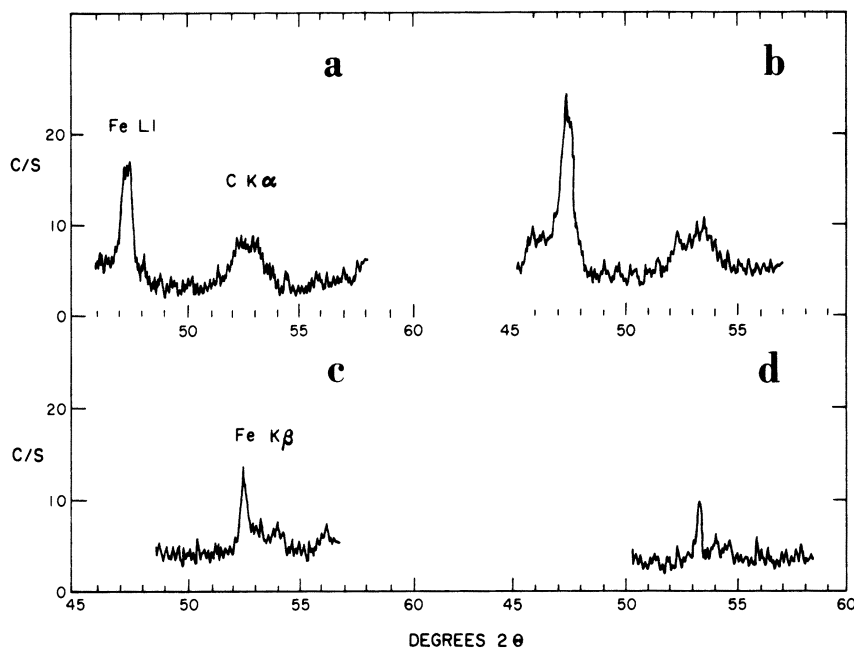


Fig. 8. Carbon $K\alpha$ peak from $\text{Fe}(100)-c(2\times 2)-\text{C}$ structure. Electron beam at grazing angle of 1° , 40 kV, 2×10^{-8} Å.

this stage a 10 min anneal at 400° causes the surface structure of the iron to recover (Fig. 2c), and there is no change in the carbon peak.

Thus it is established that the $c(2\times 2)$ structure in this case is associated with the presence of carbon on the surface of iron with a concentration of about one monolayer in the initial instance.

Oxygen

The study of thin oxide films is of particular interest to the authors due to their concern with corrosion phenomena. Preliminary experiments on the sensitivity of the apparatus for oxygen have been reported briefly in the literature.²⁵ A study was made on the $O K\alpha$ emission from the oxide film on the (100) iron surface. When prepared by electroplishing this is known to be covered by a film of cubic oxide ($\text{Fe}_3\text{O}_4-\gamma\text{Fe}_2\text{O}_3$) about 17 ± 2 Å mean thickness. Such an oxide may be considered as equivalent to about ten layers of oxygen in the close-packed plane of Fe_3O_4 . An oxide film of this type

gives rise to the O $K\alpha$ peak of Fig. 9a. This peak is about 15 counts/sec above a background of 10, or an $(N_T - N_B)/N_B$ value of 1.5.

During reduction of the oxide film in 10^{-4} torr hydrogen at 600°C the decrease in the O $K\alpha$ peak was monitored continuously until no trace could be detected (Fig. 9b). At this stage no diffraction pattern from the oxide film or oxygen-adsorption structure could be observed. On cooling, the specimen was exposed to the residual pressure of the apparatus, about 10^{-7} torr H_2O . A small O $K\alpha$ peak was detected after about 1 hr (Fig. 9c). No extra diffraction features could be observed, due possibly to the presence of a (1X1) structure. Using counting methods this peak was shown to have a $(N_T - N_B)/N_B$ value of 0.3.

The ability to observe oxidation and reduction reactions in terms of the O $K\alpha$ radiation shows promise as a most effective tool for thin-film kinetic studies. Such studies can be carried out in conjunction with electron-diffraction observations on the crystal morphology of the oxide and metal surface during the reaction.

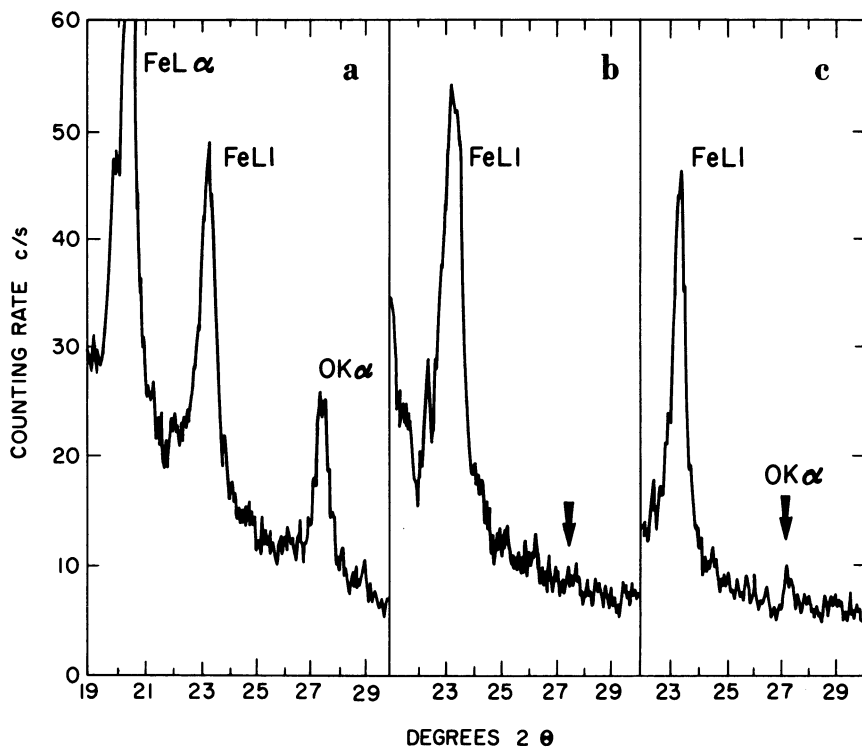


Fig. 9. The O $K\alpha$ peak from oxygen on iron. (a) air-formed film; (b) after H_2 reduction; (c) after exposure 10^{-7} torr H_2O for 1 hr.

Copper

To obtain an estimate of the sensitivity of the method for heavier elements, some observations on copper will be discussed briefly. The fifth-order Cu *Ka* peak off mica registers about 3000 counts/sec above a background of 3 counts/sec when a flat, specularly-reflecting surface on pure copper is examined at grazing incidence with 40-kV electrons and a current of 5×10^{-8} Å. This intensity is in good agreement with that expected from the Norelco AMR/3 spectrometer used in the conventional microprobe mode.

Detailed consideration of the depth from which the x-rays originate is beyond the scope of this chapter. However, if $\rho\bar{d}_n$ is defined as the distance normal to the surface above which 50% of the characteristic *Ka* radiation is produced, then $\rho\bar{d}_n = (\rho\bar{z}) \sin a$, where $\rho\bar{z}$ is the mean range for *Ka* production as defined by Green²⁶ and a is the grazing angle of incidence. For 40-kV electrons at normal incidence on copper Green²⁶ gives a value for $\rho\bar{z}$ of about 0.85 mg/cm² which gives $\bar{d}_n = 1 \mu$ for a density ρ of 8.5 g/cm³ for copper. If we consider the experimental case where $\sin a = 0.01$ ($a = 0^\circ 35'$), then \bar{d}_n is 100 Å. If the distance d_n is referred to a specimen which has its surface plane parallel to the close-packed (111) plane of copper ($d_{111} = 2.09$ Å) then the \bar{d}_n value of 100 Å corresponds to about 50 atomic layers below the surface.

If between 1 and 2% of the total Cu *Ka* signal comes from the first atomic layer, then a single close-packed layer of copper on a substrate of similar atomic number would be expected to give 15-30 counts/sec above a background of 3 counts/sec. Using the counting statistics suggested for the case of carbon this corresponds to a sensitivity of about 1-2% of a monolayer. This value is about five to ten times that reported for carbon and is in reasonable agreement with the increased sensitivity expected for characteristic x-radiation from heavier elements. Some preliminary experimental observations of a copper impurity on a tin surface support the above estimate of sensitivity.

SUMMARY

It has been shown that the techniques of high-energy electron diffraction and x-ray emission analysis may be applied effectively to the study of surface phenomena at the monolayer level. The grazing-incidence HEED technique alone can be applied to studies of ordering in surface layers in much the same way as the LEED method. Both methods give similar information about the two-dimensional structure of surfaces, and the sensitivity for the detection of surface structures is about the same.

The need for more detailed chemical analysis at the monolayer level has resulted in the recent activity in the field of Auger electron spectroscopy. This technique combined with LEED provides a powerful tool for surface analyses. In a similar fashion, the combination of the HEED method and x-ray emission spectroscopy offers a new approach to structural and chemical analysis of surfaces. The preliminary work in his field reported here has attempted to establish by calibration procedures approximate values for the sensitivity of x-ray emission analysis for the detection of carbon and oxygen at the monolayer level.

Although the x-ray emission method of surface analysis is experimentally more complicated than Auger electron analysis, it does offer some advantages. X-ray emission spectra of the elements are tabulated in detail. The background due to white radiation in x-ray spectra is fairly uniform, especially in the region used for the identification of light elements. The detection of heavy elements by x-ray emission presents no complications. In unpublished work from the authors' laboratory the emission of C $K\alpha$ radiation from surfaces bombarded at normal incidence with 500–1500-eV electrons has been studied. A marked increase in the signal/noise ratio is found which improves the detection limit for carbon to about 1% monolayer. This value compares favorably with the best reported sensitivities in Auger electron spectroscopy.

REFERENCES

1. H.E. Farnsworth, *Advan. Catalysis* 15, 31 (1964)
2. L.A. Harris, *J. Appl. Phys.* 39, 1419 (1968).
3. P.W. Palmberg and T.N. Rhodin, *J. Appl. Phys.* 39, 2425 (1968)
4. G.P. Tompson, *Proc. Roy. Soc. A* 128 649 (1930).
5. D.W. Pashley, *Advan. in Phys.* 5, 173 (1956).
6. P.B. Sewell M. Cohen, and D.F. Mitchell, "Surfaces and Interfaces," *Chemical and Physical Characteristics*, Vol. I, J.J. Burke, N.L. Reed, and V. Weiss, eds., Syracuse University Press, Syracuse, New York, (1967), p. 53.
7. M.E. Haine and P.A. Einstein, *Brit. J. Appl. Phys.* 3, 40 (1952).
8. G.I. Finch, *J. Chem. Soc.* 1137 (1938).
9. L.H. Germer and K.H. Storks, *J. Chem. Phys.* 6, 280 (1938).
10. H. Hagihara and H. Uchikoshi, *J. Phys. Soc. Japan* 17, Supp. B-II, 213 (1962).
11. R.C. Newman and D.W. Pashley, *Phil. Mag.* 46, 927 (1955).
12. O. Haase, *Z. Naturforsch.* 11a, 46 (1956).
13. P.B. Sewell and M. Cohen, *Appl. Phys. Letters* 7, 32 (1965).
14. A.J. Pignocco and G.E. Pelissier, *J. Electrochem. Soc.* 112, 218 (1964).
15. R. Castaing, Thesis University of Paris (1951); ONERA Publication No.55 (1951).
16. L.S. Birks, ASTM Special Technical Publication 349 (1964) p. 151.
17. B.L. Henke X-ray Fluorescence Analysis for Sodium, Fluorine, Oxygen, Nitroge Carbon, and Boron, *Advances in X-ray Analysis*, Vol. 7, W.M. Mueller, G.R. Malle and M.J. Fay, eds., Plenum Press, New York (1964), pp. 460-788.

18. P.S. Ong, Light Element Analysis with an Electron Microprobe, *Advances in X-ray Analysis*, Vol. 8, W.H. Mueller, P.R. Mallett, and M.J. Fay, eds., Plenum Press, New York (1965), pp. 341-351.
19. P.S. Ong, *The Electron Microprobe*, T.D. McKinley, K.F.J. Heinrich, and D.B. Wittry, eds., John Wiley and Sons, New York (1966), p. 43.
20. A.E. Ennos, *Brit. J. Appl. Phys.* **4**, 101 (1953).
21. P.J. Ong, *X-ray Optics and Microanalysis*, R. Castaing, P. Deschamps, and J. Philbert, eds., Hermann, Paris (1966), p. 181.
22. R.M. Stern, *Appl. Phys. Letters* **5**, 218 (1964).
23. K.B. Blodgett, *J. Am. Chem. Soc.* **57**, 1007 (1935).
24. C.O. Timmons, R.L. Patterson, and L.B. Lockhart Jr., *Colloid Interface Sci.* **26**, 120 (1968).
25. P.B. Sewell and M. Cohen, *Appl. Phys. Letters* **11**, 298 (1967).
26. M. Green, *Proc. Phys. Soc.* **83**, 435 (1965).

Surface Analysis with the Electron Probe

Gudrun A. Hutchins

*Sprague Electric Company,
North Adams, Massachusetts*

A number of analyses are described to illustrate the usefulness of electron probe microanalysis in the characterization of surfaces. The examples include segregation of impurities, effects of surface treatment, and studies of thin films.

INTRODUCTION

Analysis with the electron probe is particularly applicable to the characterization of surfaces because the thickness of the layer analyzed is ordinarily not much greater than 1 μ . This means that surface layers less than 100 Å thick are readily detectable. The electron beam diameter may be varied from less than 1 μ to more than 100 μ to give, respectively, a tiny spot analysis or an average over a larger area.

The basic components of an electron probe microanalyzer are shown in Fig.1. The specimen should be polished, or as smooth as possible, and is mounted on a micrometer stage. The light optics are concentric with the electron optics in most instruments. The position of the electron beam on the sample is observed and centered in the image field of the microscope with the aid of a specimen that luminesces under electron bombardment. The electron penetration into the sample, and therefore the thickness of the analyzed layer, is controlled by the electron accelerating voltage.

The x-ray spectrometer is typically of the focusing, curved-crystal type. For this reason the electron beam cannot be defocused to a diameter much greater than 100 μ without a decrease in the measured signal. X-ray intensity is recorded on a strip chart or displayed by a digital counter or oscilloscope.

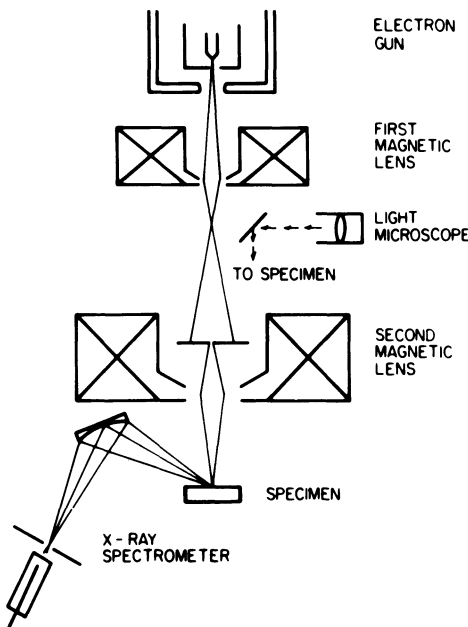


Fig. 1. Schematic diagram of electron probe microanalyzer.

There are two basic types of analysis. In the first a specific spot on the specimen is analyzed for all the elements present. This analysis may or may not be typical of the entire sample. In the second type of analysis the distribution of one particular element is studied. In this case the spectrometer is peaked for a characteristic line for that element, and the sample is moved relative to the beam.

For quantitative analysis a number of matrix corrections are required to convert measured intensity into weight per cent. These are discussed in considerable detail in the probe literature and will not be discussed here.

Typical limits of detectability are given in Table I. At first glance the values listed for the "bulk" analyses appear rather unimpressive. It should be emphasized, however, that the volume analyzed may be as small as $1 \mu^3$ and weigh 10^{-11} g. This would make the detectability limit 10^{-5} g in the best case. The difference between the two bulk cases is due to the high absorption of soft radiation and a high continuous background generally associated with a high-atomic-number matrix. Most actual cases lie somewhere between the values given in the first two lines of the table; a few ideal cases are better than the values in the first line. Surface layers of one monolayer or less can be detected without

TABLE I
Typical Detectability Limits

Type of analysis	Scan*	Manual†
"Bulk"		
Hard radiation low-Z matrix	0.1 wt. %	0.01 wt. %
"Bulk"		
Soft radiation high-Z matrix	1 wt. %	0.1 wt. %
Surface layer	3 $\mu\text{g}/\text{cm}^2$	$< 0.2 \mu\text{g}/\text{cm}^2$ \sim one monolayer $< 2 \times 10^{-15} \text{ g}/\mu^2$

*Spectrometer scan of unknown sample; signal recorded on strip chart.

†Quantitative determination of a particular element; peak and background signals counted for 100 sec or more.

difficulty. Thus the electron probe is very useful for detecting a contaminant present in relatively high concentration in a tiny volume or on the surface. It is not suitable for measuring a very low average concentration of an impurity.

SEGREGATION OF IMPURITIES

High-purity materials often contain a few spots in which the trace-element concentration is much greater than the average level. These few spots may be much more detrimental to the performance of the material than the overall impurity concentration.

Such a case is shown in Fig. 2. The sample is high-purity tantalum foil with an average iron content of 8 ppm as determined by emission spectroscopy. The sample has been anodically oxidized at 20 V, and most of the surface is covered by an oxide which gives the sample a deep purple interference color. The white rod-shaped areas are not covered by oxide and appear metallic. These bare spots were all found to contain more than 500 ppm iron; for this reason the oxide has not grown properly.

Figure 3 shows a vacuum-annealed piece of tantalum foil that has been lightly scratched with tweezers and anodically oxidized. Again the oxide is missing in the contaminated region. In this case the iron concentration is great enough to be detected by scanning, and Fig. 4 shows traverses across the scratch at three different positions. They were recorded with the beam focused, the spectrometer peaked for Fe $K\alpha$, and the sample motor-driven at 20 μ/min . The greatest peak shown corresponds to approximately 150 Å of iron.

For both of these samples the areas of interest were made visible by the oxidation, and the success of the experiment depended on this decoration technique. The first sample contained few iron-rich areas, and most of these would not have been detected by scanning. It is therefore very unlikely that any iron-rich spots would have been found by random searching.

Contaminated areas may often be recognized under a microscope without special treatment because they are discolored or less reflecting. Some oxides become semiconducting at impurity sites, and the color or intensity of the luminescence observed under electron bombardment may be different.

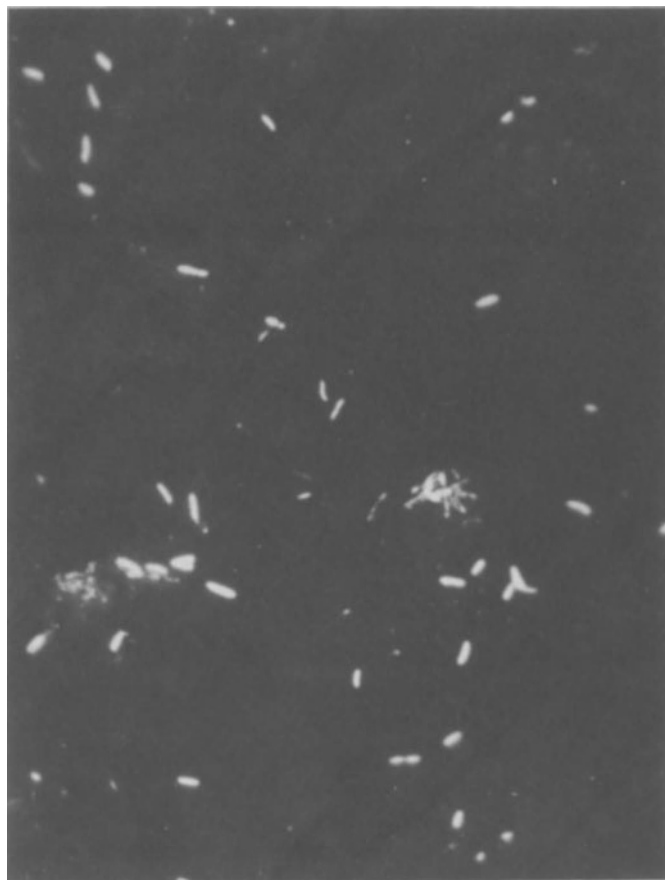


Fig. 2. Iron-rich areas on tantalum after anodic oxidation. 500 X.

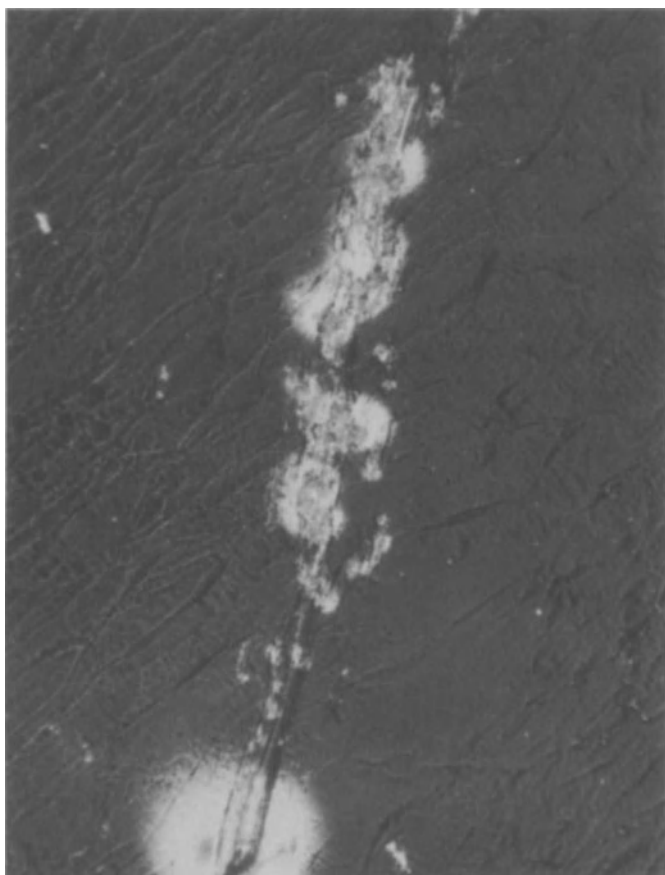


Fig. 3. Tweezer scratch on tantalum after anodic oxidation. 200 X.

A piece of high-purity aluminum foil is shown in Fig. 5 in the condition in which it was received from the supplier. The surface is dotted with a few large and many small specks of an impurity that are readily visible in polarized light with a metallographic microscope. However, these spots could not be recognized in the probe microscope with nonpolarized light, due to excessive light scatter from the rough rolling structure. It was found that these spots fluoresced under the beam; therefore the specimen was positioned with the probe microscope light turned off. The spots were found to be mixed chlorides of calcium and the fourth-period transition elements.

Since these contamination spots occurred only on the surface and were quite thin, they corresponded to a very small fraction of the sample volume. Thus they would have contributed very little to the average concentrations measured in a bulk analysis and could have been identified only with the electron probe.

A scan for aluminum in supposedly high-purity beryllium is shown in Fig. 6. This sample had been polished with diamond slurry to eliminate any possibility of contamination with polishing alumina. Although the average concentration of aluminum was only approximately 300 ppm, concentrations over 1 wt. % were measured in some areas. The erratic nature of the profile suggested that the aluminum may have been present in a second phase.

A photomicrograph of the specimen after it was etched with dilute sulfuric acid is shown in Fig. 7. The dark spots are areas that have been etched preferentially and correspond to the aluminum-rich spots in the scan. It can be seen that the etched spots are situated at the grain boundaries of the beryllium. Aluminum was not detectable in the middle of the grains. The aluminum was a bulk impurity and extended into the sample; therefore it would have been detected by any suitable bulk-analytical technique. The additional information

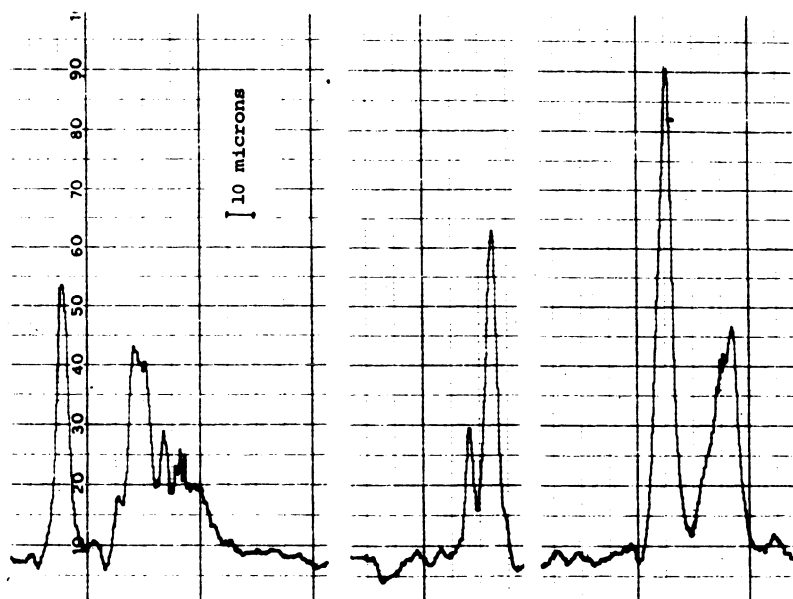


Fig. 4. Line scans for iron across the scratch shown in Fig. 3. The largest peak corresponds to 150 Å of iron.

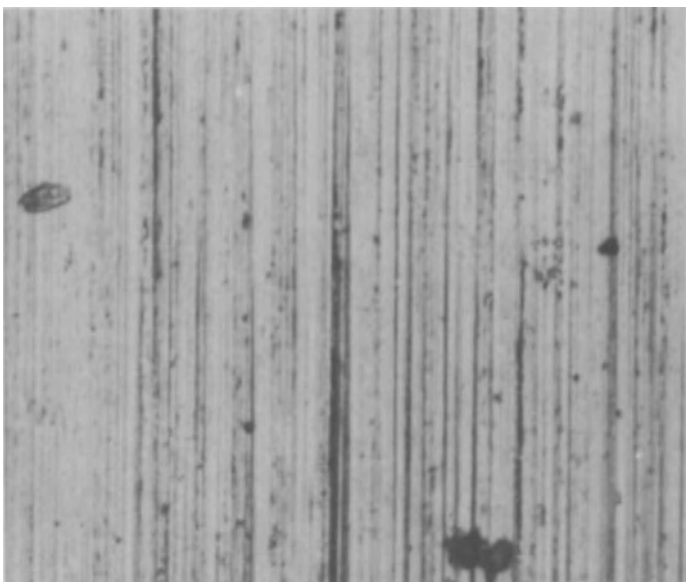
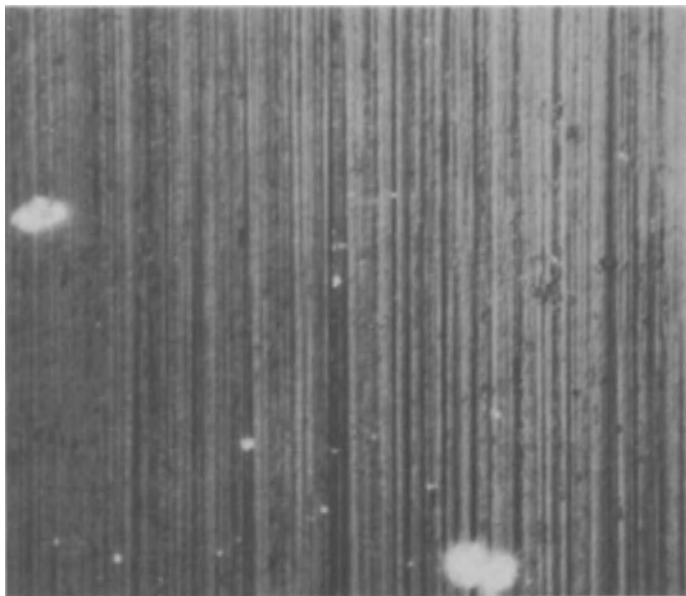


Fig. 5. Surface contamination on aluminum foil. Left: plane-polarized light. Right: crossed Nicols. Both photomicrographs show the same area, 200 \times .

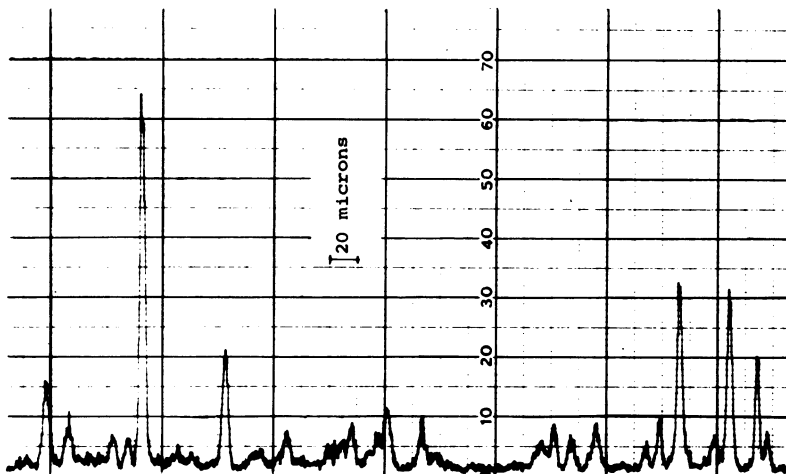


Fig. 6. Line scan for aluminum in beryllium sample. 50 on this scale corresponds to 1 wt. % aluminum.

obtained from electron probe analysis was that the aluminum was very segregated and apparently present in an intergranular second phase.

Unfortunately, this beryllium was chosen as a substrate for aluminum films. The very erratic measurements on these films led us to suspect that the substrate might contain aluminum. Ironically, several elements listed as possible impurities by the supplier were not detected, and the beryllium would have been an ideal substrate for any film except aluminum.

CHANGES IN COMPOSITION DURING SAMPLE PREPARATION

Any mechanical or chemical treatment of the specimen during sample preparation can change the surface composition. An example of the imbedding of polishing alumina in brass is shown in Fig. 8. The brass was relatively soft and porous and imbedding of the $0.1\text{-}\mu$ alumina could not be prevented. The scan is different from the scan on beryllium in Fig. 6; the peaks are not as distinct, and there are no aluminum-free areas.

The nickel was polished at the same time in the same mount. It was denser and harder and there was no indication of imbedded alumina.

For many soft samples contamination by the polishing abrasive cannot be avoided. In such cases the abrasive should be chosen so that it will not interfere

with the analysis. Polishing conditions can be optimized by measuring the amount of abrasive contamination with various polishing conditions.

Etching or other chemical treatments should be avoided if possible. They can leave residues or leach out some constituents preferentially. Most metallographic etches produce contrast between phases by preferential chemical attack, and are therefore unsuitable for electron probe analysis.

Occasionally it is necessary to lightly etch a specimen in order to identify the phase or area of interest. The possibility of compositional change should be

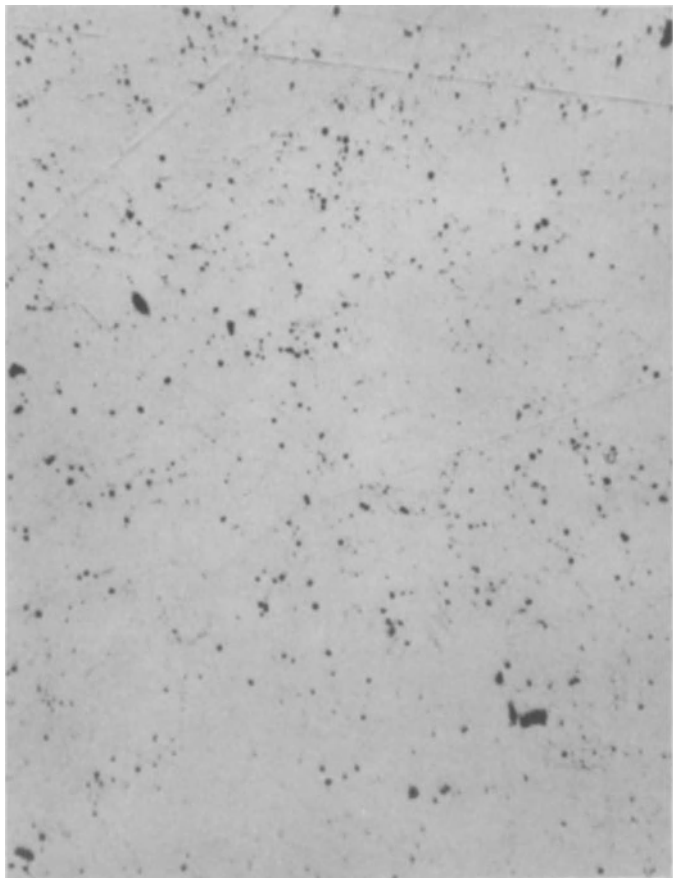


Fig. 7. Photomicrograph of beryllium sample after etching. Dark spots correspond to aluminum-rich areas in Fig. 6. 200 X.

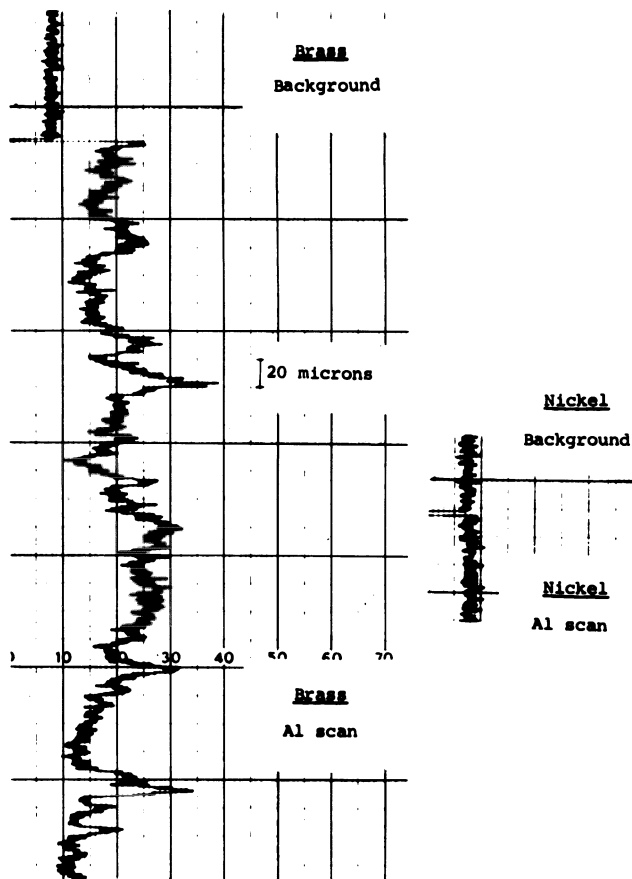


Fig. 8. Imbedded polishing alumina. Line scans for aluminum. 50 on this scale corresponds to 1 wt. % aluminum or nearly 2 wt. % alumina.

kept in mind in such a case. In case of doubt, the specimen should be prepared by two or more different methods and the results compared. Surface effects can often be differentiated from bulk concentration by analyzing the sample at two different beam voltages. Surface impurities will have a greater relative intensity at the lower voltage, since the surface layer will be a larger fraction of the analyzed volume. For example, the aluminum in brass was measured at 14 kV; if the same sample were measured at 20 kV, the aluminum signal relative to pure aluminum would be only half as great.

The effect of electropolishing on a tantalum-titanium alloy is shown in Table II. These measurements were made at 10 kV to limit the analyzed layer to approximately 1000 Å. The untreated alloy contained 20 wt. % titanium, or an

atomic ratio of 0.94 Ti to 1 Ta. During the electropolishing the titanium was removed preferentially, and the average surface concentration was reduced to 14.5 wt. % titanium, or an atomic ratio of 0.64 Ti to 1 Ta. This is a surprising

TABLE II
Compositional Change in Tantalum-Titanium Alloy
upon Electropolishing

Treatment	Wt. % Ti	Atomic ratio Ti: Ta
Untreated	20	0.94:1
Electropolished	14.5	0.64:1
Electropolished, anodically oxidized	11.0	0.62:1

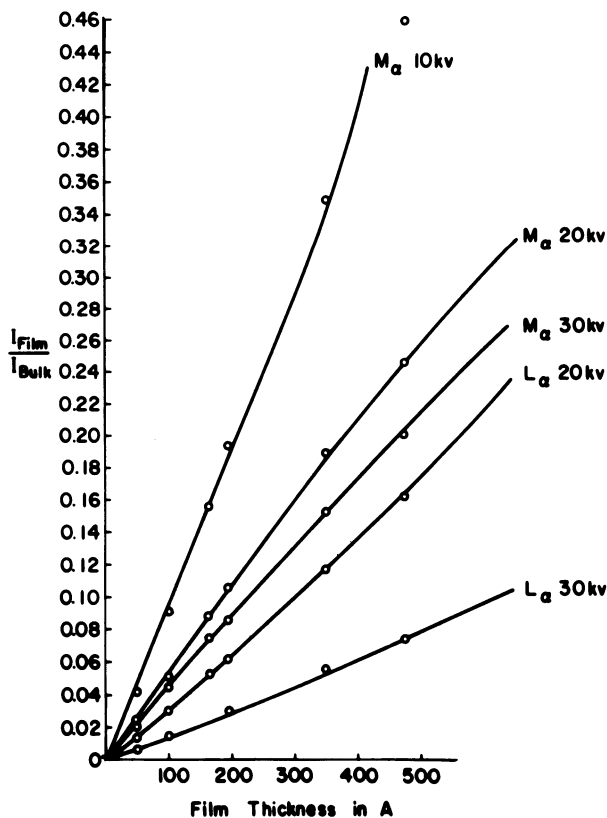


Fig. 9. Calibration curves for gold films on silicon.

result, because the alloy was a solid solution of the two metals and the electropolished surface appeared smooth and not etched. It is likely that the titanium concentration was much less than 14.5 wt. % in the upper layers and increased rapidly below the surface.

The electropolished surface was anodically oxidized to an oxide thickness of approximately 1600 Å. The titanium concentration dropped to 11 wt. % due to the presence of the oxygen. However, calculations based on stoichiometric oxides gave the same atomic ratio. Apparently the oxidation was not preferential.

This sample was prepared to evaluate the oxide of the 20 wt. % titanium alloy. Electron probe analysis showed that the oxide evaluated did not have the composition to be expected from the original material.

THIN FILM STUDIES

The electron probe is a useful tool for studying surface layers deposited intentionally. These would include thin films deposited by evaporation, sputtering, or chemical decomposition. Homogeneity on a micron or millimeter scale is easily checked, and a change in film thickness of a few Angstroms is readily detectable. For films of one element the mass thickness is nearly linear with measured x-ray intensity and can be calculated or read from a calibration curve.

Figure 9 shows some measurements of gold films on silicon that were used to test an equation for calculating film thickness from x-ray intensity.¹ The linear thickness of these films was measured by interferometry, and the solid lines are calculated curves. X-ray intensity relative to pure gold was measured for both soft *Ma* and hard *La* radiation at several values of the accelerating voltage.

Since the x-ray intensity measured with the electron probe is related to the mass thickness ρx , and interferometry measures the linear thickness x , density differences can be determined by comparing interferometry and probe measurements of the same films. It was found, e.g., that the chromium density of chromium films evaporated in a poor vacuum system at 3×10^{-5} mm Hg was only about 65% of the density measured for films sputtered in a system capable of 10^{-10} mm Hg.* Others have reported a similar dependence of density on pressure.^{2,3}

The compositional homogeneity of alloy or compound films can be checked easily. The quantitative composition of alloy or compound films can be determined readily if the films can be made thick enough so that the substrate

*The normalization factors for chromium listed in Table III given by Hutchins¹ should be increased by approximately 50% because of the density effect discussed here.

will not be measured. For elements having suitable soft x-ray lines the voltage may be lowered to 10 kV or less to limit penetration.

In some cases it is possible to determine both composition and mass thickness of very thin alloy films within a few per cent. However, if there is a large spread in the atomic numbers of the film elements, the conversion from x-ray intensity to weight per cent may be very inaccurate. Nonetheless, qualitative work is always possible, and quantitative comparisons between different films or between several areas on one film can be made.

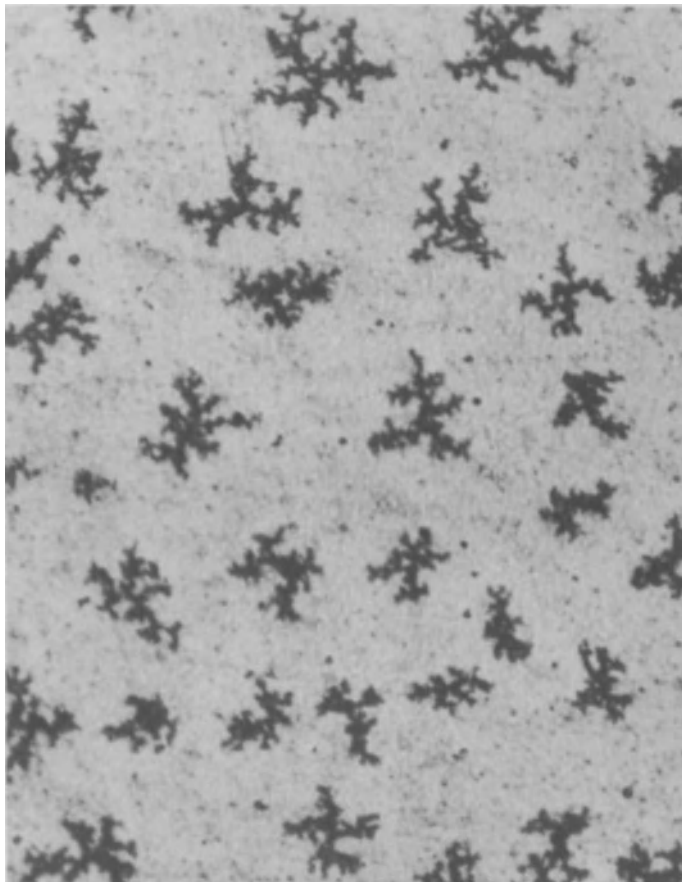


Fig. 10. Reaction of aluminum and silica films heated at 527°C for 2 hr. 200 X. Dendrites are low in Al and high in Si.

The final example involves the reaction of two thin films. It is an example of useful information obtained with the electron probe from very complex specimens. Other means of analysis would have yielded very little information in this particular study.

Amorphous silicon dioxide was electron beam evaporated onto a polished substrate of pyrolytic graphite. Aluminum was subsequently evaporated onto the SiO_2 without breaking vacuum. The film thicknesses were 2200 Å SiO_2 and 900 Å Al. The samples were heat-treated in a high-purity argon atmosphere in a furnace with temperature control better than $\pm 1^\circ\text{C}$. The purpose of the measurements was to study the aluminum penetration into the silica and the formation of complex phases.

The reaction at high temperatures was rather dramatic. Several phases were formed, and the films showed a pattern of interference colors. Figure 10 shows a sample heated for 2 hr at 527°C . This temperature is 50°C below the aluminum-silicon eutectic and 133°C below the melting point of aluminum.

The dendritic phase is bright blue in color and contains less aluminum and more silicon than the original film. This means that both Al and Si atoms have moved within the plane of the film to form a separate phase. The weight ratio is approximately 0.25 Al to 1 Si in the dendrite and 0.7 Al to 1 Si in the matrix.

Etching studies showed that part of the aluminum in the matrix was an unreacted surface layer which could be etched off without removing any silicon. The dendrites could be etched only with dilute hydrofluoric acid and were of the same composition down to the substrate.

Figure 11 shows a similar sample heated 24 hr at the same temperature of 527°C . The dendrites of Fig. 10 have become larger and correspond to the areas indicated A in Fig. 11b. This phase is now pale violet and some of the matrix is mixed with it. A new phase has formed and corresponds to the black bands labeled B. This phase is higher in aluminum and lower in silicon than the original film. Some of the matrix covered with partially-unreacted aluminum still remains, and is labeled M in Fig. 11b. Tiny micron-sized spots of the other two phases are mixed with it.

Figure 12 shows a spot-by-spot analysis of the sample shown in Fig. 11. The measurements were taken at $5\text{-}\mu$ intervals, and the silicon values were corrected for the high x-ray absorption in aluminum. The points have been joined for clarity; however, it is not expected that intermediate values would fall on the dashed line, since there is considerable segregation on the micron scale. The striking feature again is the tremendous amount of lateral movement of both Al and Si atoms that must have taken place to give this profile. This sample showed cracking and poor adhesion as other indications of the enormous changes occurring during heat treatment.

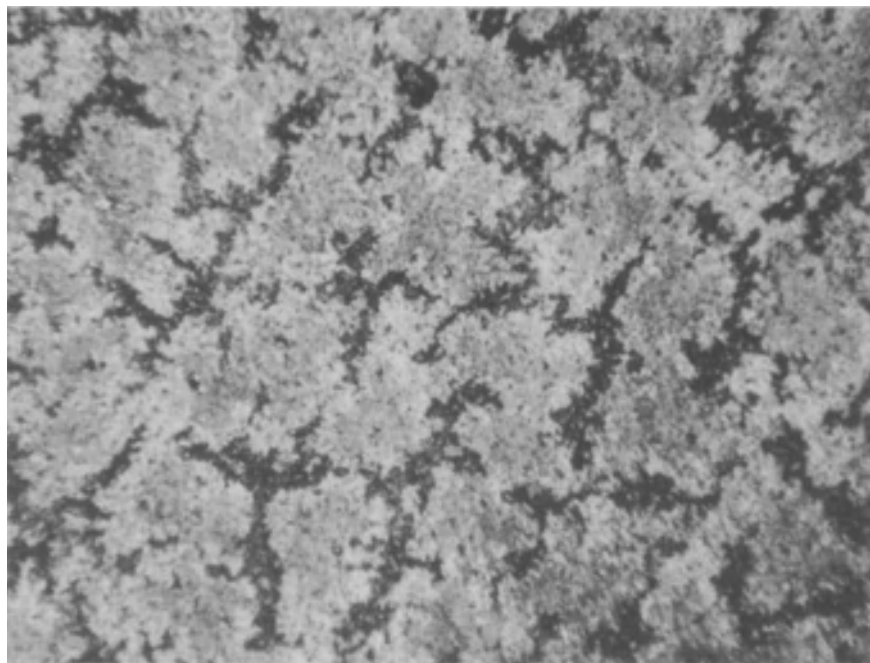
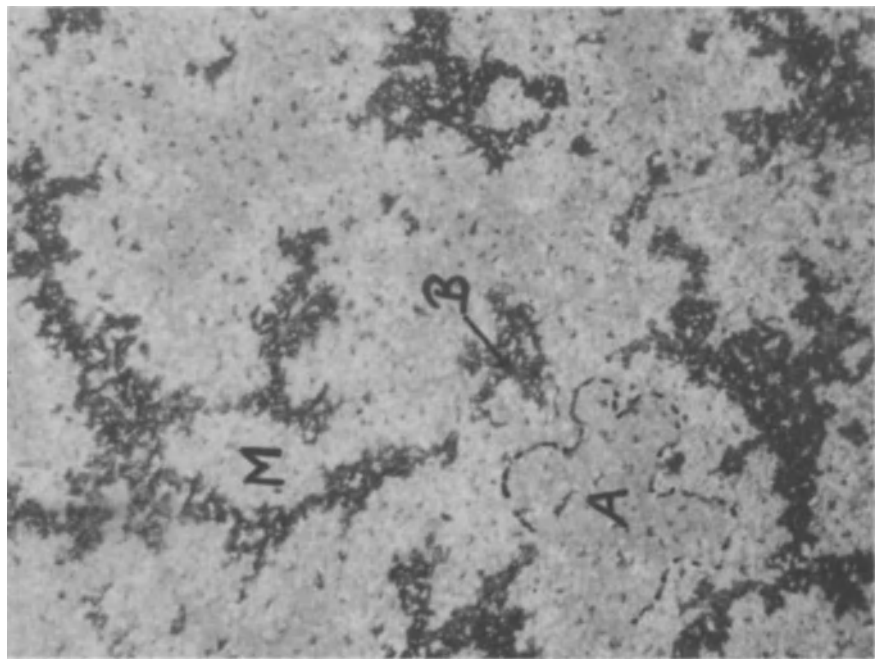


Fig. 11. (a) 200 X. (b) 500 X. Reaction of aluminium and silica films at 527°C for 24 hr. Phase A: Extension of dendrites, low Al and high Si. Phase B: New phase, high Al and low Si. Phase M: Matrix covered with partially unreacted Al.

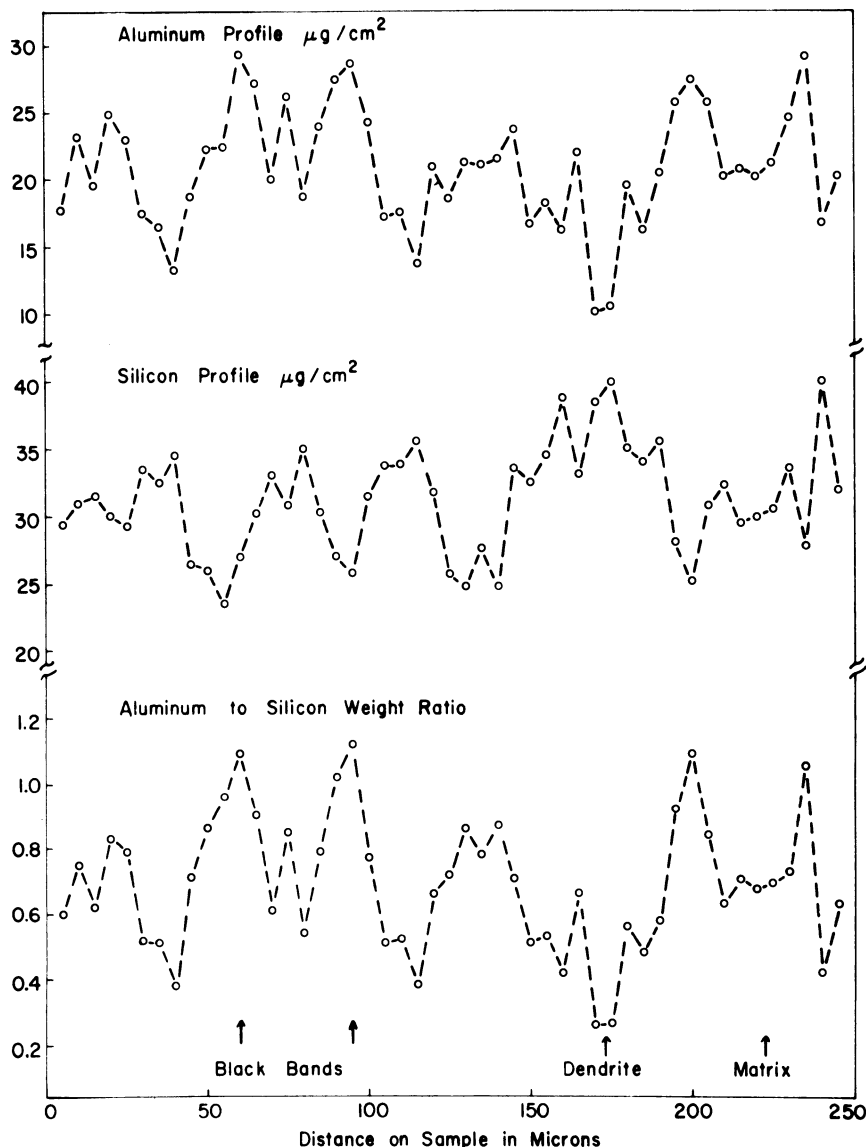


Fig. 12. Reaction of aluminum and silica films after 24 hr in argon at 527°C . Compositional profiles of sample shown in Fig. 11.

ACKNOWLEDGMENT

The author gratefully acknowledges the assistance of her colleague, Richard Wantman, who performed some of the analyses discussed.

REFERENCES

1. G. A. Hutchins, *The Electron Microprobe*, T. D. McKinley, K. F. J. Heinrich, D. B. Wittry, eds., John Wiley and Sons, New York (1966), p. 390.
2. A. R. Wolter, *J. Appl. Phys.* 36, 2377 (1965).
3. P. A. Gould, *Brit. J. Appl. Phys.* 6, 1481 (1965).

Experience with a Computer-Coupled X-Ray Spectrometer

F. Bernstein

*General Electric Company
Milwaukee, Wisconsin*

There are many ways of utilizing a small computer coupled to an x-ray spectrometer. A number of different applications are presented. These include storage of equations and constants for describing analytical systems where interelement effects are present. Two examples are discussed, one of which is analyzed by both theoretical and empirical approaches. In addition, use of mathematical functions to eliminate line interferences and the need for pulse-height selection is discussed.

INTRODUCTION

Over the past five years there have been a number of major changes in x-ray analytical instrumentation. The first change was the introduction of automated equipment, so that instrument functions could be placed under automatic control. The second and more significant change involved the coupling of small computers to the x-ray instrument. In addition to controlling instrument functions, these units are also capable of the following:

1. Automatic standardization of equipment.
2. Automatic calibration and calculation of linear regression equations from standards.
3. Automatic calibration of nonlinear relations using polynomial expressions.
4. Computation of per cent composition from stored linear regression equations.

5. For more complex analytical systems, storage of interelement equations and computation of elemental composition from x-ray intensity data.

It has been shown in a previous paper¹ that the automatic standardization feature which the General Electric XRD-410 incorporates provides excellent stability, so that instrument precision approaches the error due to counting statistics. With good sample preparation the only remaining problem is the description of the analytical system. For many systems satisfactory accuracy can be obtained with simple linear regression equations relating x-ray intensity to composition by a straight line which is best fitted to experimental data. In more complex systems where interactions occur between elements the straight line is inadequate to describe the analytical system. In this case two approaches are possible: (1) a fundamental parameter approach, and (2) multiple-regression techniques.

In the fundamental-parameter approach theoretical equations are set up to describe the intensity of an element. These equations involve description of the energy distribution in the primary exciting x-ray beam and terms for absorption and enhancement effects. This is a difficult approach which has been described in a paper by Criss and Birks², and is not within the scope of this paper. However, it should be mentioned that in analytical systems where only absorption effects are present the intensity relationships are more simply described by the following equation:

$$I_A a_A / W_A = I_B a_B / W_B \quad (1)$$

where I_A and I_B are the intensities of the element of interest from samples A and B respectively, W_A and W_B are the weight fractions of the element of interest in the mixtures of A and B , and a is defined as follows:

$$a = \mu_1 \csc \theta_1 + \mu_2 \csc \theta_2 \quad (2)$$

where μ_1 and μ_2 are mass-absorption coefficients for the incident radiation and the characteristic radiation, respectively, θ_1 is the angle which the exciting radiation makes with the sample surface, and θ_2 is the angle of take-off of the characteristic radiation from the sample surface.

Multiple-regression techniques are statistical tools which are used to study correlations between observed data and to form equations relating a dependent variable with several independent variables. These techniques are utilized in cases where interactions occur between elements in systems which cannot be adequately described by simple linear-regression techniques. Equations are

utilized for multiple-regression techniques in the following form:

$$\% A = K_0 + K_1 I_A + K_2 I_A I_B + K_3 I_A I_C \quad (3)$$

where I_A , I_B , and I_C are x-ray intensities of components A , B , and C , and the K_0 - K_3 are constants.

This form of the equation has been suggested by Lucas-Tooth and Pyne³ and by Mitchell and Hopper.⁴ The coefficients in the above equation are determined on a large computer by multiple-regression techniques using well-analyzed samples and x-ray intensity data to form the equations. In the empirical equation approach enhancement effects are assumed to be equivalent to negative absorption effects. In addition, the absorption of element A by element B is assumed to be linearly proportional to the concentration of B .

EXPERIMENTAL

Correction for Interelement Effects

An example of the application of the above techniques can be found in the analysis of a raw mix for the production of cement. A raw mix is essentially a mixture of calcium carbonate, silica, iron oxide, and alumina. In addition, it often contains up to several per cent potassium oxide. The ten samples utilized for this study are shown in Table I. Five of the samples show varying amounts of potassium up to several per cent, while the remaining five have approximately the same concentration. Consideration of the emission and excitation energies of calcium and potassium indicates that potassium should have severe absorption effects for calcium radiation. Thus for satisfactory analysis of calcium oxide it should be necessary to apply a correction factor for the amount of potassium present in the sample.

The effect of potassium on calcium can be seen from Fig. 1, which shows the plot of x-ray intensity versus CaO for the samples. The straight line shown in the figure was drawn through the five points which have approximately the same level of potassium, while the remaining five, which have higher amounts of potassium, deviate significantly from the line.

The following equation was utilized to correct for the interactions between calcium and potassium:

$$\% \text{CaO} = K_0 + K_1 I_{\text{Ca}} + K_2 I_{\text{Ca}} I_{\text{K}} \quad (4)$$

where K_0 , K_1 , and K_2 are constants and I_{Ca} and I_{K} are observed x-ray intensities for calcium and potassium, respectively.

One equation of the above form was generated for each sample using x-ray data and the chemical analyses of the samples. Utilizing multiple-regression techniques, the constants in the Eq. (4) were determined. When the measured x-ray intensities were substituted in Eq. (4) extremely good correlation was obtained between calculated and chemical values. The standard error of estimate for the ten samples was found to be 0.1%. The standard error of estimate is the root mean square of the deviations between calculated and chemical values for each sample. Study of the absorption coefficients of the various components for calcium radiation indicated that silicon could also affect calcium. This was confirmed by adding a silicon term to Eq. (4); the standard error of estimate was then found to be 0.06% calcium oxide.

Consideration of the sample analyses in Table I indicated that the only element capable of enhancing calcium is iron. Since iron is a relatively minor constituent and the total spread among the samples is small, it was felt that correction for matrix absorption using Eq. (1) should give satisfactory correlation with chemical analysis. This was done for the ten samples utilizing absorption coefficients as published by Theisen and Vollath⁵ in 1967. The results are shown in Fig. 2, which plots per cent calcium oxide versus x-ray intensity corrected for matrix absorption. It is evident that the correction procedure utilized has not adequately described the interaction which takes place in the samples. To further emphasize the fact that the scatter observed in Fig. 1 could be attributed to the potassium, a graph was made (Fig. 3) showing the deviations from the linear-regression curve plotted versus the potassium intensity in the samples. Since this relationship is reasonably linear, it can be concluded that the principal effect on calcium is due to potassium.

In view of the above it was decided to recalculate the absorption coefficient for potassium. This was done by assuming values for the overall

TABLE I
Analysis of Samples Used

	CaO	SiO ₂	Al ₂ O ₃	Fe ₂ O ₃	SO ₃	K ₂ O
1	42.05	12.19	3.57	1.97	1.79	1.33
2	40.79	13.27	3.86	2.04	1.77	1.86
3	43.13	11.14	3.19	1.86	1.54	1.44
4	44.33	9.54	3.01	1.62	1.41	1.67
5	39.71	13.99	3.95	2.13	1.54	2.26
6	42.38	12.26	3.60	1.95	1.83	0.85
7	41.39	13.40	3.94	2.09	1.80	0.91
8	43.64	11.23	3.25	1.88	1.58	0.74
9	44.93	9.62	3.03	1.67	1.40	0.71
10	40.58	14.25	4.05	2.18	1.93	0.94

mass-absorption coefficients of the samples such that their adjusted x-ray intensities fell on the line of Fig. 1. Absorption coefficients of all elements except potassium were considered to be known; the value for potassium was calculated for each of the five samples. Good agreement was obtained, but the potassium absorption coefficient was found to be approximately 50% higher than the published value. It does not seem reasonable that the coefficients are in error by such a substantial amount. One possible explanation may be that powder samples are not truly homogeneous, and thus heterogeneity effects within the sample may account for some or all of the deviations which were observed after application of theoretical corrections.

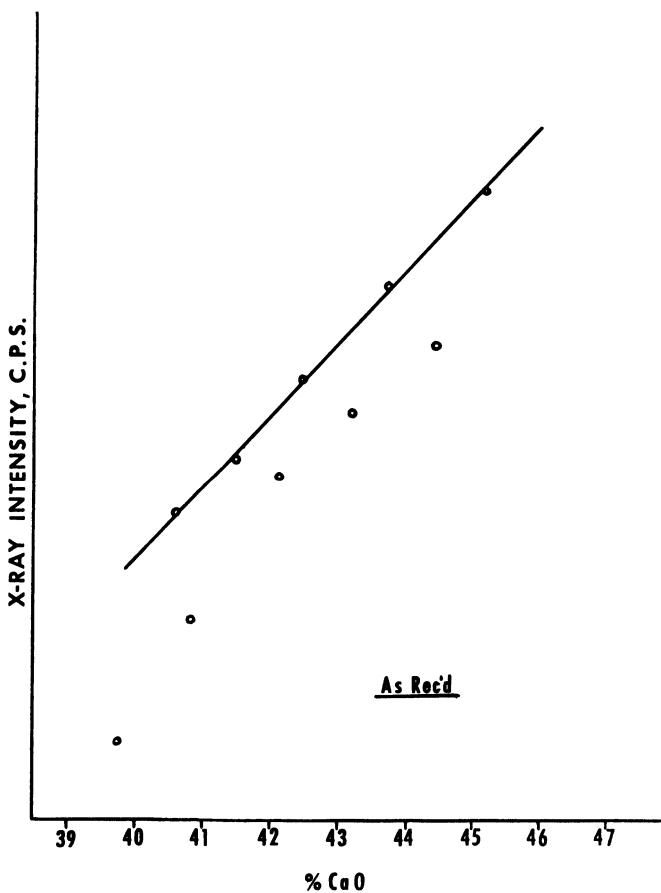


Fig. 1. Working curve for CaO in raw mix. Uncorrected data.

Multiple-regression techniques have also been applied to the analysis of stainless steels. Twenty-five samples of stainless steels containing nickel from 0.3 to 28% and chromium from 0.3 to 25% have been studied. Other elements present in the steel included molybdenum, tungsten, niobium, cobalt, and titanium, in addition to the usual residuals. Empirical equations for nickel and chromium similar in form to Eq. (4) were utilized, with correction terms for the elements specified above. Constants for the equations for nickel and chromium were determined on a time-sharing computer, and these constants were then stored in the memory of the XRD-410. Based upon these analytical equations it was found that nickel could be measured to 0.08% and chromium to 0.07% (standard error of estimate) when sufficient counts were accumulated to make counting statistics negligible.

Correction for Instrument Parameters

The remaining examples to be discussed relate to the ability of the instrument to store equations which can compensate for analytical problems other than interelement effects. The first example to be discussed is the analysis of manganese in steels containing varying amounts of chromium. With normal optics and a standard (200) lithium fluoride crystal it is impossible to resolve the manganese $K\alpha$ from the chromium $K\beta$ line. Several different approaches have been utilized to solve this analytical problem. One involves the use of a higher-resolution crystal, such as the lithium fluoride (220), and another the use of extremely fine collimation in the optics. Both of these will increase the separation of the lines and permit measurement of the manganese $K\alpha$ free from interference. Because of the ability of the XRD-410 to store equations and perform mathematical computations automatically, it was decided to compare results for the analysis of manganese using a mathematical correction for the interference with those obtained by using higher resolution. Standard (200) and high-resolution (220) lithium fluoride crystals were the analyzing crystals used for the x-ray measurements. Steels were selected which varied in composition of chromium from 0.2 to 20%, while manganese was in the range of 0.2 to 1.8%. U.S. National Bureau of Standards samples were used, primarily from the 1100 series. Measurements were made on the manganese and chromium $K\alpha$ lines using both crystals, and the manganese data were analyzed by linear regression methods. In addition, in both cases multiple-regression techniques were applied to equations which included a term for chromium correction as follows:

$$\% \text{ Mn} = K_0 + K_1 I_{\text{Mn}} + K_2 I_{\text{Cr}} \quad (5)$$

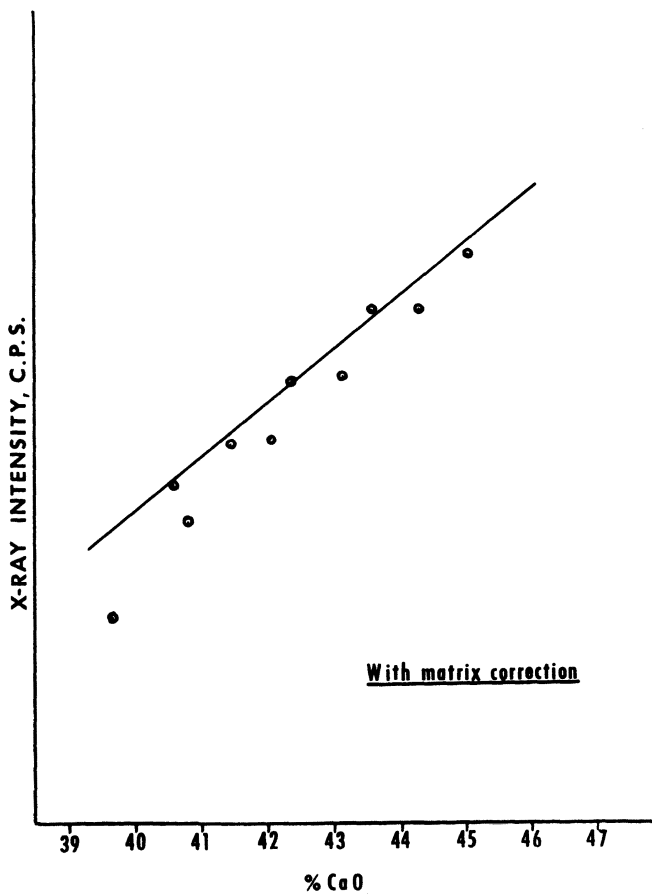


Fig. 2. Working curve for CaO in raw mix, with matrix absorption corrections.

The results are shown in Table II. Standard errors of estimate for each of the analytical approaches is shown. Obviously, the worst case is that of the standard (200) lithium fluoride crystal and uncorrected manganese intensity. It is quite interesting to note, however, that with multiple-regression techniques the values are identical for both the standard and high-resolution crystals. In addition, there is a slight but significant improvement when multiple-regression techniques are applied to the high-resolution crystal. This was surprising, since the peaks were apparently resolved when a recorder trace was examined.

It was shown in a previous paper¹ that analytical errors which arise due to crystal-tuning errors, 2θ errors, and changes in excitation could easily be

TABLE II
Manganese in Steels

Crystal	Method	Standard error of estimate
LiF (200)	Linear regression	0.15%
LiF (200)	Multiple regression	0.01%
LiF (220)	Linear regression	0.02%
LiF (220)	Multiple regression	0.01%

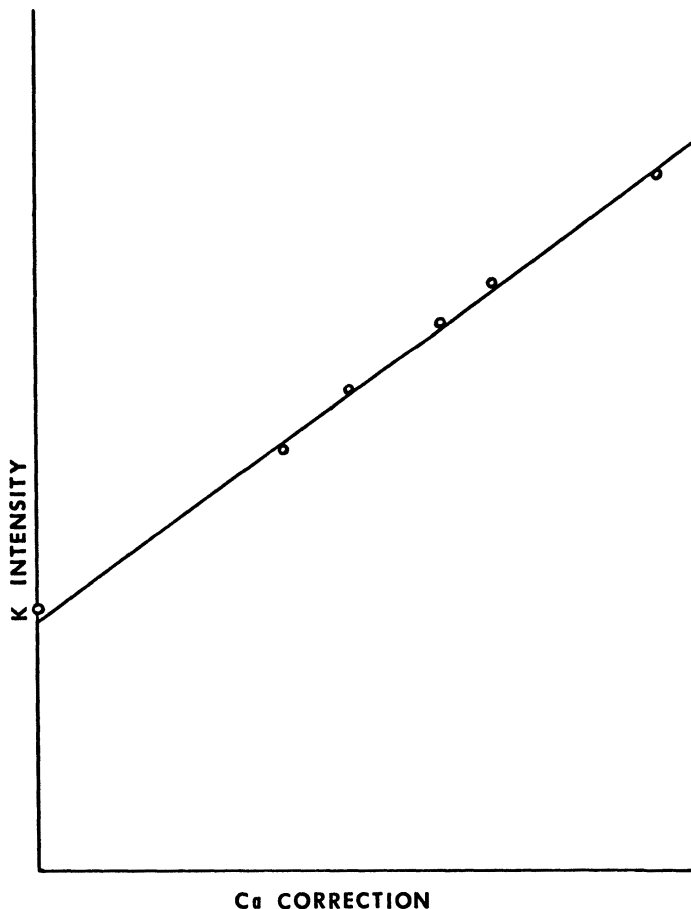


Fig. 3. Relationship between deviations from linear-regression curve and potassium intensity

eliminated using good standardization techniques. It was also shown that one of the most difficult errors to correct for is that of improper or incorrect setting of the pulse-height selector. For this reason it was decided to investigate the use of mathematical techniques in lieu of utilization of the pulse-height selector in a problem where this type of approach was difficult. An example of this is the analysis of magnesium in raw mix for cement.

Measurement of magnesium in raw mix is a difficult problem because of crystal fluorescence. Normally, ammonium dihydrogen phosphate is utilized as the analyzing crystal. This gives rise to phosphorus fluorescence from the crystal in addition to the magnesium pulses, and results in a pulse distribution similar to that shown in Fig. 4. It is evident that it is virtually impossible to set pulse-height selector settings such that all of the pulses of magnesium can be accepted and all of the phosphorus pulses rejected. In addition, changes in counter-tube temperature, pressure, or high voltage which result in a change in

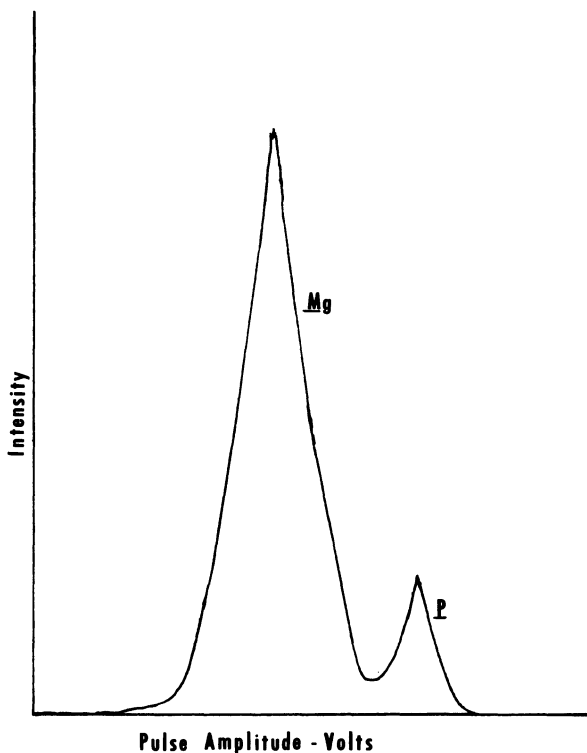


Fig. 4. Pulse-height scan showing relationship of magnesium and phosphorus pulses.

TABLE III
Magnesium in Raw Mix

Method	Pulse height selector	Standard error of estimate
Linear regression	No	0.34%
Linear regression	Yes	0.07%
Multiple regression	No	0.05%

the relationship of pulse-height selector windows and pulse families can result in serious analytical errors.

Ten samples of raw mix were utilized for this study, containing magnesium oxide from 0.7 to 4.2% and calcium oxide from 39 to 45%. Measurements were taken on magnesium *Ka* with and without pulse-height selector. In addition, measurements of calcium *Ka* intensity were taken on all the samples. Linear regressions were run using magnesium intensities with and without pulse-height selection. Multiple-regression techniques were applied using the following equation for the data taken without pulse-height selection:

$$\% \text{ Mg} = K_0 + K_1 I_{\text{Mg}} + K_2 I_{\text{Ca}} \quad (6)$$

The standard error of estimate is shown for each of the three methods in Table III. It is interesting to note that slightly better results were obtained with the calcium correction than with pulse-height selection alone, although both approaches show correlation which is quite acceptable. As might be expected, magnesium with no pulse-height selection is poor. In connection with crystal fluorescence, it should be noted that in addition to calcium there are two other possible sources in these samples. The first is iron and the second the chromium *K* radiation which is scattered by the samples. However, it did not appear necessary to include these in the equation in compensating for crystal fluorescence.

CONCLUSIONS

Computer-coupled instrumentation has been found to be extremely versatile. In addition to control of instrument operation, standardization, and calculation of per cent composition from simple linear-regression equations, the following functions have been developed:

1. For systems with interelement effects the computer is capable of storing and applying equations for calculation of per cent composition.

2. For analytical situations involving overlapping lines equations have been utilized to eliminate the interferences.
3. For analytical situations which normally require the use of pulse-height selection equations have been successfully applied in lieu of pulse-height selection.

In general, it is felt that the addition of a computer to an analytical instrument provides a challenge to the user to develop suitable mathematics for describing his problems. In the past the use of such functions would have been impractical with operator-controlled units, but the computer provides the capability of handling complex approaches with speed and dependability.

REFERENCES

1. F. Bernstein, in: *Developments in Applied Spectroscopy*, Vol. 6, Plenum Press, New York (1967).
2. J. W. Criss and L. S. Birks, *Anal. Chem.* **40**(7), 1081 (June 1968).
3. J. Lucas-Tooth and C. Pyne, The Accurate Determination of Major Constituents by X-Ray Fluorescent Analysis in the Presence of Large Interelement Effects, *Advances in X-Ray Analysis*, Vol. 7, W. M. Mueller, G. R. Mallett, and M. J. Fay, eds., Plenum Press, New York (1964) pp. 523-541.
4. B. J. Mitchell and F. N. Hopper, *Appl. Spectry.* **20**, 172 (1966).
5. R. Theisen and D. Vollath, *Tables of X-Ray and Mass Attenuation Coefficients*, Verlag Stahleisen, Dusseldorf (1967).

Use of Total Reflection at the Critical Angle for Dispersion of Ultrasoft X-Rays

Heribert K. Herglotz

*E. I. du Pont de Nemours & Co., Inc.
Engineering Physics Laboratory
Wilmington, Delaware*

X-ray analysis of elements below sodium in atomic number has not yet become popular in laboratories where routine analyses must be carried out by personnel of limited training. In search of simpler methods to overcome this barrier, the wavelength dependence for the critical angle of total reflection was investigated theoretically and scouted experimentally. Development of an x-ray spectrograph for the routine analysis of light elements is encouraged by these results.

This paper describes an incidental observation and the efforts undertaken many years later to test the observed effect for its usefulness in an analytical instrument.

Figure 1 shows a spectrogram obtained with a plane Siegbahn grating of 288 lines/mm. The radiation came from a graphite target excited by 9-kV electrons. Only the lower part of the film on which this spectrogram is recorded was directly exposed to the radiation reflected by the grating. The upper part of the film was covered by horizontal cellophane layers of 30, 60, and 90 μm thickness, respectively. The cellophane filter was inserted in the hope that it would help to identify higher orders of short-wavelength radiation that could have been reflected by the grating at the small angle of incidence of less than 1° . It is quite obvious that absorption by the cellophane wiped out all the x-radiation reflected and diffracted by the grating except the

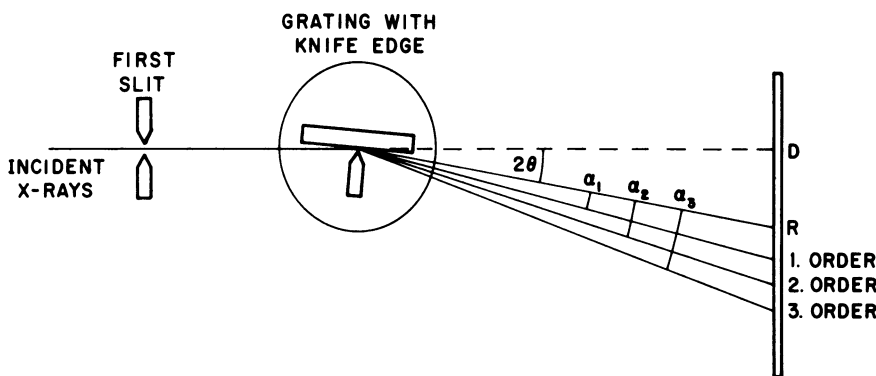


Fig. 2. Scheme of a ruled-grating x-ray spectrograph. *D*: Direct beam. *R*: Reflected beam. θ : Angle of incidence. $\alpha_1, \alpha_2, \alpha_3$: Diffraction angles of three orders of a wavelength.

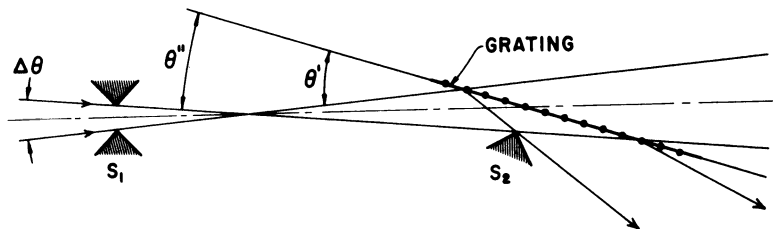


Fig. 3. Explanation of effect of Fig. 1. S_1 : First slit. S_2 : Knife edge (simulating second slit). θ' , θ'' : Angles of incidence. $\Delta\theta = \theta' - \theta''$, divergence.

$\theta_1 < \theta_c$ (Fig. 4.) with the critical angle θ_c a function of the wavelength:

$$\sin \theta_c \approx \theta_c \approx \sqrt{2\delta} \approx \lambda(\text{\AA}) \sqrt{2.7\rho} 10^{-3}$$

where $\delta = 1 - n$ and ρ is the density.

The observation described to this point was made 15 years ago, was described in a publication of broader scope,² and had no consequences; we were satisfied with our ability to explain the effect by well-established rules of x-ray physics. Many years later we remembered these results when analytical chemists desired extension of x-ray spectroscopy to the lowest atomic numbers of the periodic table. Oriented layers of long-chain molecules, first described as crystal surrogates by Siegbahn and Thoraeus,³ and the ruled gratings credited to Compton and Doan¹ have been developed to a high degree of performance and make analysis down to element number 4

directly reflected, or zero-order beam, which contains all reflected, undispersed wavelengths. Figure 2 recapitulates the basic concepts of ruled-grating x-ray spectroscopy¹ to simplify the interpretation of the experiment. The x-rays are collimated by a slit and the small gap between grating and opposing knife edge, substituting for a second slit. The direct beam from the source is absorbed by the grating in this arrangement. In our Fig. 1, the zero-order beam (R in Fig. 2) was intense enough to penetrate two cellophane steps, but not with uniform intensity. The section of the beam to the left was more penetrating than the part at the right. In other words: mere reflection of the x-rays on the glass had caused some wavelength-selection within the reflected beam. This effect had nothing to do with the dispersion by interference due to the periodic grooves of the grating. The explanation was found in the divergence of the incident beam, evident in Fig. 3, the concept of which is identical with that of Fig. 2. The plane of the grating is perpendicular to the page, so that only its trace appears, with the grooves indicated as dots. Because of the finite distance between slits 1 and 2, radiation impinges at a larger angle of incidence (θ') at one end of the grating than at the other (θ''). Consequently, the shorter, more penetrating wavelengths with a smaller critical angle of total reflection are eliminated where the incident angle is larger, in accord with the observation from Fig. 1. Recall that total reflection exists where the refractive index $n = (\cos \theta_1)/(\cos \theta_2) < 1$, and is observed when

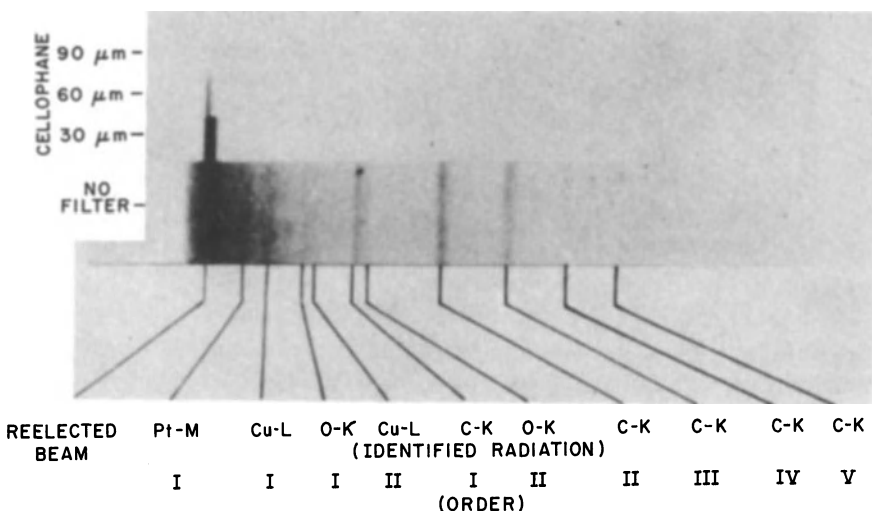


Fig. 1. Spectrogram of the radiation from a graphite target obtained with a Siegbahn grating of 288 lines/mm. Part of the spectrogram is covered with cellophane foils of 30, 60, and 90 μm thickness.

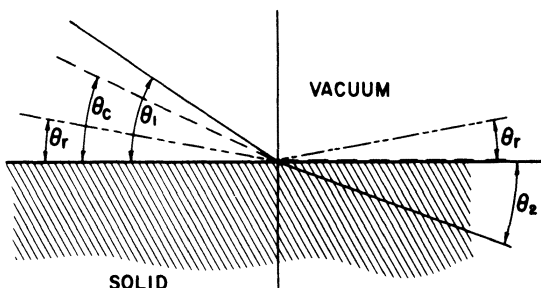


Fig. 4. Refraction and total reflection of x-rays. θ_1 : Angle of incidence. θ_2 : Angle of refraction. θ_c : Critical angle of total reflection. θ_r : Angle within the region of total reflection

(beryllium) possible. But analytical chemists still seek a simple method for routine analysis to be performed by semiskilled laboratory helpers. We wondered whether the wavelength dependence of the critical angle of total reflection, the cause of the effect seen in Fig. 1, could provide the simplicity needed in an analytical instrument. We do not yet have the final answer to this question, but I would like to report our efforts so far to obtain it.

To this end, we calculated reflection curves for the characteristic radiations of the light elements beryllium to fluorine on various reflecting materials by way of the Fresnel formulas.⁴ Figures 5 and 6 report some of these calculations for quartz, paraffin, and lithium fluoride as reflectors. The calculations for quartz served only to check our calculations by comparison with published,⁵ reliable data. Comparison of the reflection curves for carbon radiation on quartz and paraffin demonstrates the influence of the lower absorption of carbon radiation in paraffin and accounts for the well-defined critical angle on paraffin which is absent on quartz. By the same rule, the reflection curves of nitrogen radiation and carbon radiation on paraffin are strikingly different because nitrogen radiation, on the short-wavelength side of the absorption discontinuity, is heavily absorbed in the carbon of paraffin. A sharp critical angle exists only if absorption in the medium is low. Therefore we selected paraffin and lithium fluoride as reflectors. Paraffin is most suitable for carbon and boron radiation because these wavelengths are on the low-absorption side of the carbon of the reflector. Similarly, the absorption of N, O, and F radiation is low in lithium fluoride because of the favorable position of the absorption discontinuity of fluorine in conjunction with the low atomic number of the other constituent of the reflector, lithium.

These calculations suggested that a device composed of simple components could be useful for elemental analysis in this wavelength region. An indication of the signals to be expected and the resulting resolution can be

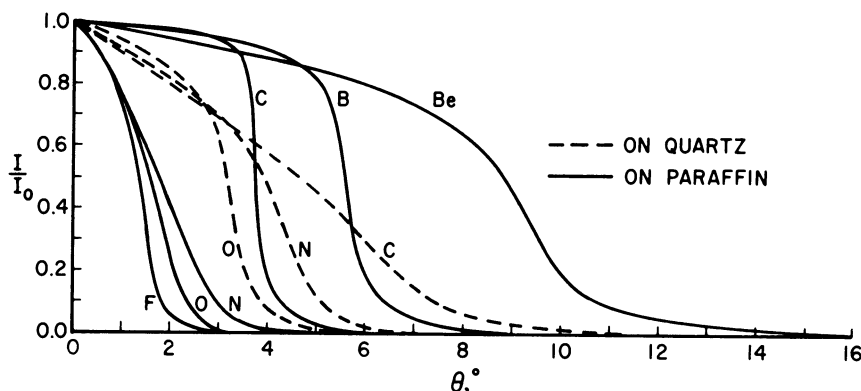


Fig. 5. Calculated reflection curves of characteristic radiations from oxygen, nitrogen, and carbon on quartz and from fluorine, oxygen, nitrogen, carbon, boron and beryllium on paraffin.

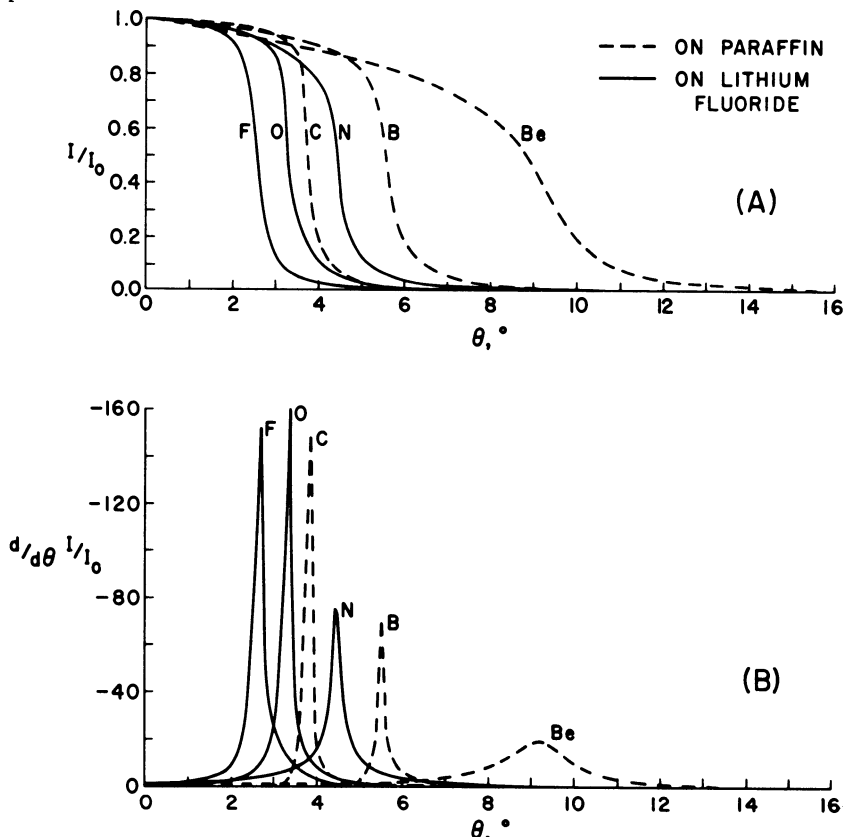


Fig. 6. Calculated reflection curves of characteristic radiations from elements fluorine, oxygen, and nitrogen on lithium fluoride and from carbon, boron, beryllium on paraffin; derivatives of reflection curves.

obtained from the derivative functions of the reflection curves shown in Fig. 6. Experimental verification of our calculation for a paraffin reflector and carbon radiation by photographic recording followed quickly,⁶ and is shown in Figs. 7 and 8. Paraffin should exhibit a sharp critical angle for carbon radiation because of its low absorption. It consists of hydrogen and carbon only and can be obtained free from the heavy-element contamination that would adversely affect absorption. Focusing-paraffin reflectors were prepared by high-vacuum evaporation of paraffin on concave glass lenses. The experimental arrangement of Fig. 7 with the concave reflector on a Rowland circle (in a high-vacuum vessel) produced the photographs of Fig. 8. The point

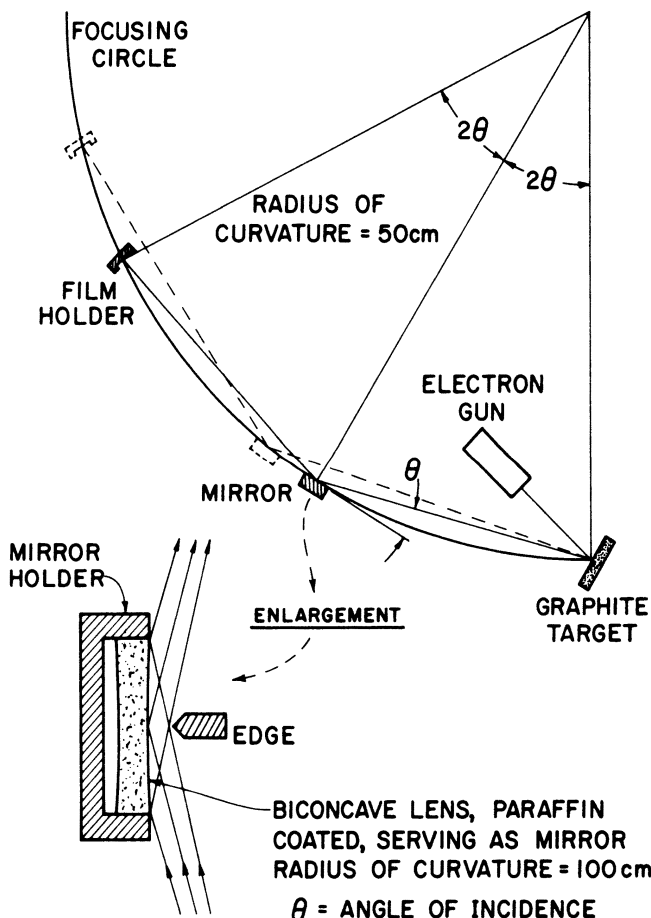


Fig. 7. Apparatus for paraffin mirror test (from Herglotz⁶).

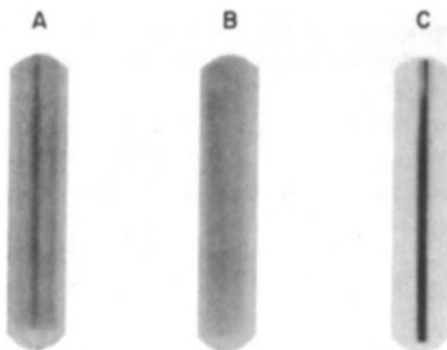


Fig. 8. Photographs from paraffin mirror test (from Herglotz⁶). (A) Line image of carbon-radiation point source obtained with spherical paraffin mirror. (B) Blank obtained with cathode heated, but no high voltage. (C) X-ray source replaced by visible-light source.

source on the graphite target, directly bombarded by electrons, produced a line image at 4θ , with θ the angle of incidence on the mirror. Moving the mirror along the Rowland circle varies the angle of incidence. If the mirror was set to an angle larger than 4° , the image disappeared, in accord with the calculation of Fig. 5.

Encouraged by the strength of the images in our photographic experiments of Fig. 8, we tried an extremely simple electronic readout system. I report this attempt even though it was unsuccessful, because it exemplifies the superior faculty of the eye-brain combination to record signals. It is unfortunate that this combination lacks digital readout. The disappearance at $\theta = 4^\circ$ of the strong line previously observed at $\theta = 3.5^\circ$ made us believe that very simple electronic means would be sufficient to replace the photographic film and led to the construction of a diode with electrometer readout (Fig. 9). X-rays entering through the open window release photoelectrons, which give rise to a current in the electrometer circuit. Detector and electrometer are kept at -500 V to prevent stray electrons from striking the photocathode. The reflection curve measured with this device is shown in Fig. 10. The logarithmic differential curve of Fig. 11 shows a peak near 4° , where Fig. 6 predicts it for carbon radiation. The logarithmic differentiation $(\Delta I/I)/\Delta\theta$ corrects the decrease of intensity impinging on the mirror due to increase of distance from the source. The data from a copper target exhibited in Figs. 10 and 11 were convincing evidence that the peak near 4° was attributable to C radiation. It is also quite apparent from these results that background radiation, mostly from fluorescent excitation of the mirror, exceeds the carbon signal by orders of magnitude. Therefore, this crude device was abandoned and replaced by that

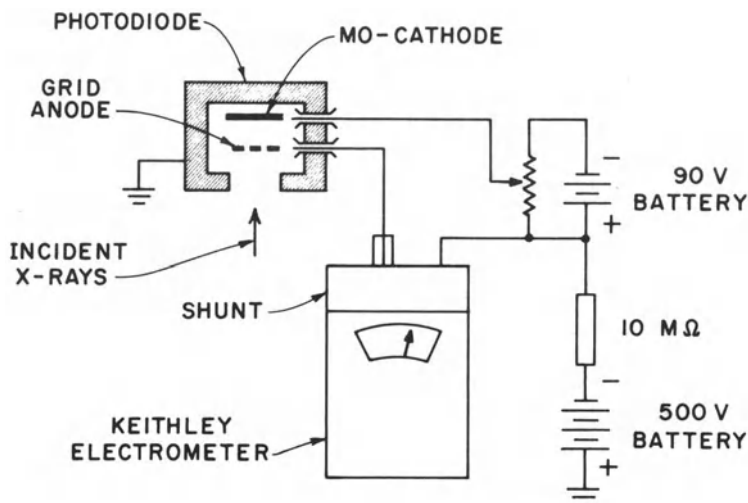


Fig. 9. Windowless photodiode and readout circuit for soft x-rays.

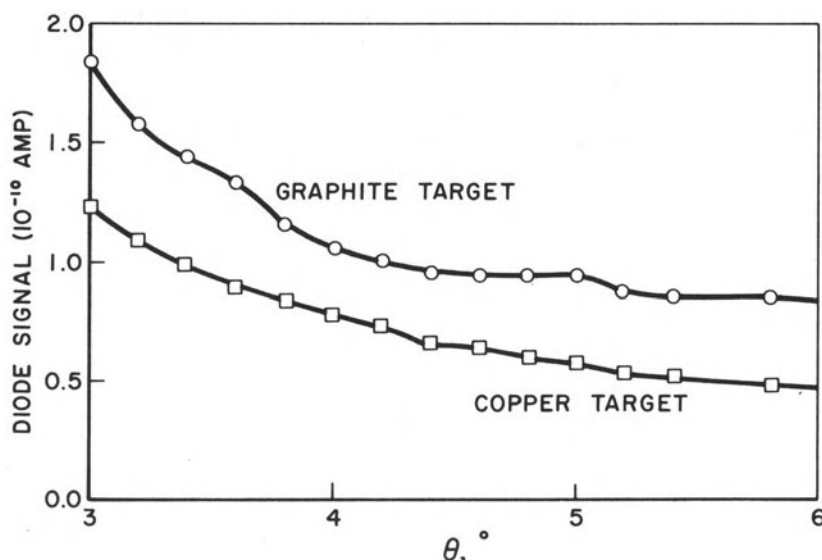


Fig. 10. Signal from open-window diode circuit versus incident angle θ , obtained with radiation from a carbon target and from a copper target.

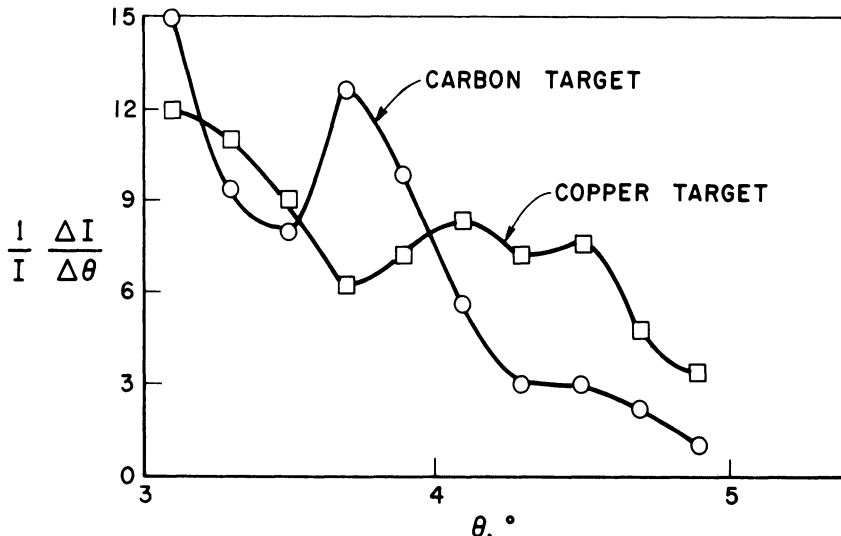


Fig. 11. Logarithmic derivative curves of diode signal versus incident angle.

of Fig. 12.⁷ The Rowland geometry was maintained, but the open-window photomultiplier now took the place of the simple photodiode. The background was reduced by traversing a slotted faceplate between mirror and photomultiplier. The multiplier signal was recorded by an electrometer recording system. Experiments for verification of a sharp critical angle were performed in the following way: the mirror was set for a definite incident angle of, e.g., 3.5° ; the vacuum vessel, housing the entire setup including x-ray source and windowless photoelectron multiplier, was then evacuated to $\sim 10^{-5}$ torr. With high voltage on x-ray source and multiplier the signal was monitored while the slit was traversing in front of the multiplier. The scan was then repeated in the reversed direction. Figures 13 and 14 represent some of the results with carbon and boron, which again confirm the reflection curves of Fig. 6. The precision of the Rowland circle and mirror mount was limited in this arrangement, which was built only to arrive at a decision on whether or not the critical angle concept should be pursued further. However, in spite of the crudeness of the arrangement a qualitative analytical task reported in the Figs. 15 and 16 was performed. The mirror was set for an angle of incidence $\theta \approx 4.5^\circ$, which is between the critical angles for the characteristic radiations of carbon and boron (Fig. 15). In this position boron radiation should be reflected, and carbon radiation should not. This prediction is verified in Fig. 16. The geometrical arrangement remained unchanged throughout the three steps of this experiment. The first scan was made with a

graphite target; for the second scan boron powder was rubbed into the target; and for the third scan the boron powder was wiped off. To eliminate possible influence from residual boron in the third scan, the target was painted with colloidal carbon ("Aquadac"). No reflection was observed with carbon as the target, but boron furnished a directed reflection. It is quite clear that the mirror had differentiated between the two radiations of 45 Å and 68 Å. The experimental arrangement for this differentiation would be inadequate for an analytical instrument, but it is not hard to imagine means for automatic recording of the derivative curves with signals proportional to the concentration of the emitting element. Admittedly, the differentiation displayed in

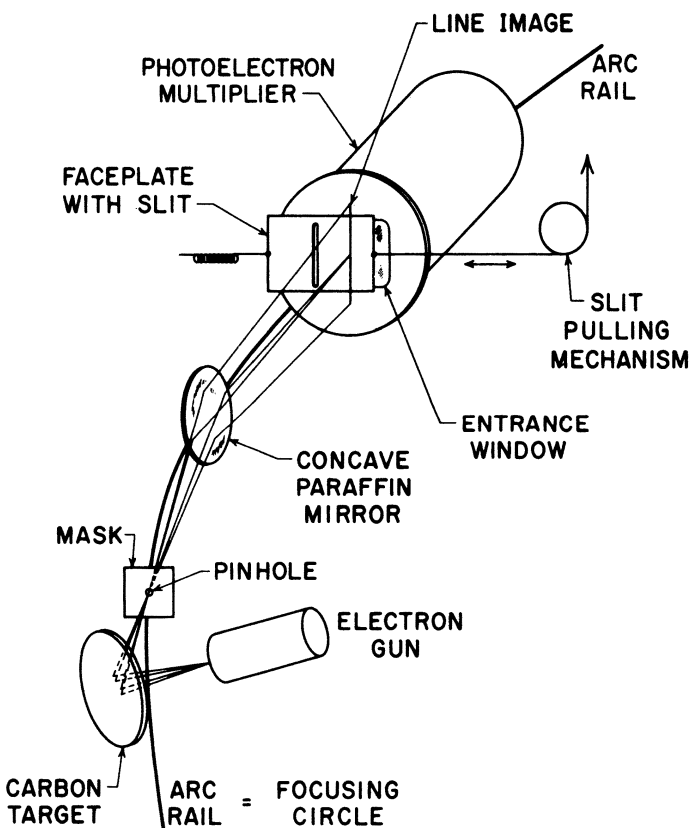


Fig. 12. Arrangement for experimental verification of critical angle by photoelectron multiplier readout (from Herglotz⁷).

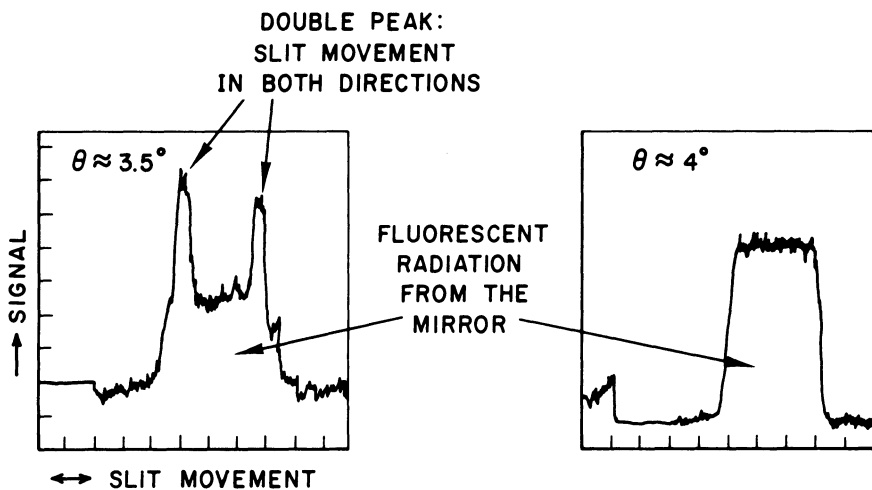


Fig. 13. Reflection of radiation from a carbon target by a concave paraffin mirror at two angles of incidence.

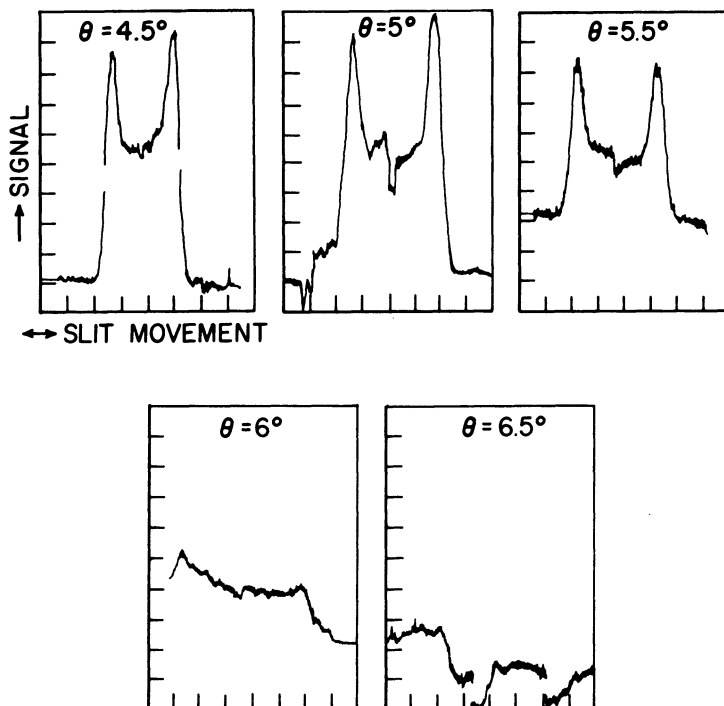


Fig. 14. Reflection of radiation from a boron nitride target.

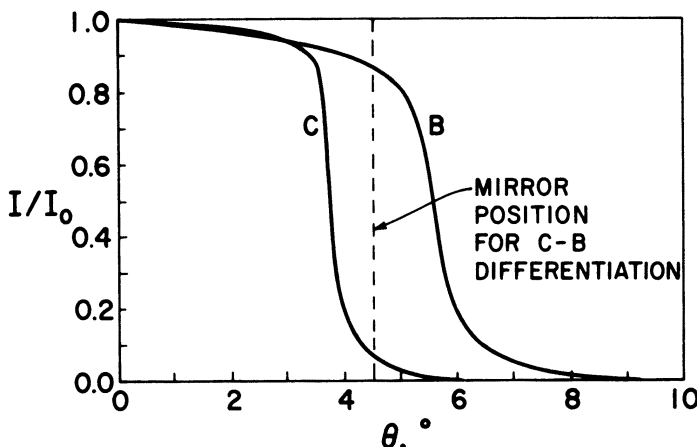


Fig. 15. Reflection curves for carbon and boron radiations.

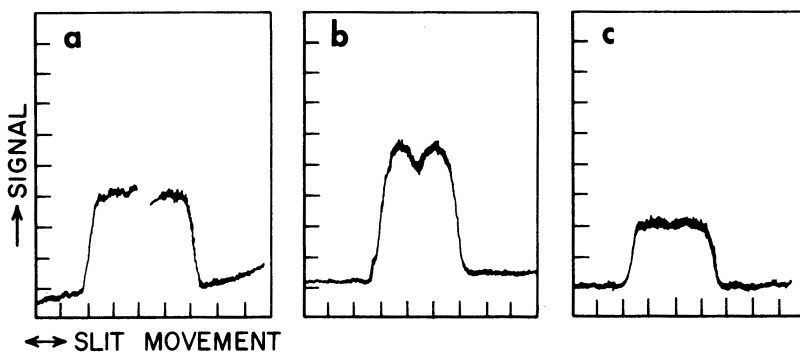


Fig. 16. Reflection with fixed mirror at intermediate position. (a) Pure graphite target. (b) The same target covered with boron powder. (c) Boron powder replaced by colloidal carbon.

Fig. 16 does not require high resolution, since the two wavelengths are separated by ~ 23 Å. Our calculation of resolutions $\lambda/\Delta\lambda$ in the wavelength region 18–67 Å for a spectrograph with paraffin and lithium fluoride mirrors yielded figures between 10 and 20.⁷ Specifically, for carbon radiation and a paraffin mirror the calculated resolution is 19. Therefore a paraffin mirror should be capable of separating wavelengths of 45 and 48 Å. By comparison, spectrographs based on the diffraction by oriented organic chain-molecules, such as lead stearate,⁸ are claimed to have a resolution up to 150⁸ and some of the recently suggested organic crystals such as octadecyl hydrogen maleate

exceed this figure. The higher resolution of diffraction instruments, however, might not be advantageous for a routine analytical instrument in this wavelength range, where the chemical and physical conditions under which the element emits greatly influence the shape of x-ray lines.^{8,9} This phenomenon is known to affect analytical results and can be remedied, or at least reduced, by decreased resolution of the instrument. Whether the limited resolving power of a spectrograph based on total reflection can be rated as another advantage in addition to its simple components and large signals will be determined only by further experiments with an arrangement more advanced than that reported here and better suited for analytical tasks.

REFERENCES

1. A. H. Compton and R. L. Doan, *Proc. Natl. Acad. Sci. US* **11**, 598 (1925).
2. H. Herglotz, Röntgenspektroskopie im ultraweichen Gebiet, Dokumentationszentrum für Technik und Wirtschaft, Vienna (1953).
3. M. Siegbahn and R. Thoraeus, *Ark. Mat. Astr. Fys.* **18**, No. 24 (1924).
4. A. H. Compton and S. K. Allison, *X-Rays in Theory and Experiment*, D. Van Nostrand Co., Princeton, N.J. (1960), p. 305.
5. E. Dershem and M. Schein, *Phys. Rev.* **35**, 292 (1930).
6. H. K. Herglotz, *Nature* **214**, 263 (1967).
7. H. K. Herglotz, *J. Appl. Phys.* **38**, 4565 (1967).
8. B. L. Henke, Application of Multilayer Analyzers to 15–150 Å Fluorescence Spectroscopy for Chemical and Valence Band Analysis, *Advances in X-Ray Analysis*, Vol. 9. G.R. Mallett, M. J. Fay, and W. M. Mueller, eds., Plenum Press, New York (1965), pp. 430–440.
9. H. K. Herglotz and E. Schiel, *Nature* **205**, 1093 (1965).

The Shift in Wavelength with Voltage of Certain X-Ray Lines

A. F. Burr and R. J. Liefeld

*New Mexico State University
Las Cruces, New Mexico*

The wavelength or energy of a characteristic x-ray line is generally considered to be independent of the energy of the particles (electrons, photons, protons, etc.) used to excite it. However, when a precise wavelength or a detailed line shape is needed, it is found that the exciting particle energy can be quite influential. Available data on some of these cases will be summarized and a few will be discussed in detail. The cases to be considered include threshold excitation of some first transition metal $K\alpha$ lines, wavelength shifts and shape changes due to self-absorption and satellites in the L spectra of these metals, gross structure introduced by self-absorption into the M spectra of the lanthanides, and wavelength shifts of M lines in lanthanum for near-threshold electron excitation. The significance of these changes for wavelength studies, elemental analysis, valance band studies, and chemical bonding will be discussed.

INTRODUCTION

The wavelengths or energies of characteristic x-ray lines are generally considered to be independent of the voltage producing them. However, when one considers the accuracy with which x-ray wavelengths can be measured — the Cu $K\alpha_1$ line, for instance, can be measured¹ with an accuracy of about 1 ppm on the x-ray wavelength scale, and isotope wavelength shifts of the order 0.1 ppm have been detected² — together with the many factors influencing line shapes, nobody should be surprised that some voltage dependence has been observed. In certain cases, however, the voltage dependence is quite gross and is easily observed. It is intended here to present certain examples of voltage-dependent lines, to describe them, and to give some indications of the causes of the changes observed.

SLIGHT SHIFT IN K WAVELENGTHS

The first example is taken from the work of Johannsson.³ He studied the Ka_1 line of chromium with a curved topaz crystal spectrometer for two different ranges of voltage across the x-ray tube. He produced the ordinary Ka_1 line by applying a voltage well in excess of the voltage necessary to excite the line. He then compared this line with a threshold line produced by the application of a voltage about 1 V in excess of that necessary to produce the line. Figure 1 summarizes his results. Note that he obtained a peak shift which averaged about 0.1 eV. Since the energy of the Cr Ka_1 line is about 5500 eV, the shift is very small. Indeed, it is not much greater than the uncertainty of the experiment itself. This shift can be explained in terms of bound-ejected-electron states, which are described in more detail below.

THE M SERIES OF LANTHANUM

The next example is much more dramatic and easily obtained. The spectrum shown in Fig. 2 is that of the Ma,β region of lanthanum.⁴ The spectrometer which was used to obtain it is a double-crystal vacuum spectro-

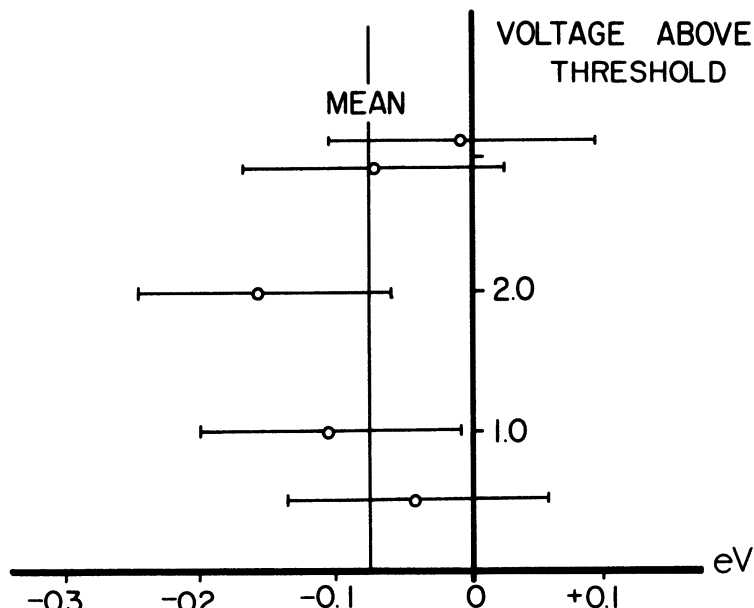


Fig. 1. The difference between the peak energy of the ordinary Cr Ka_1 line and the same line under threshold excitation conditions (from Johannsson³).

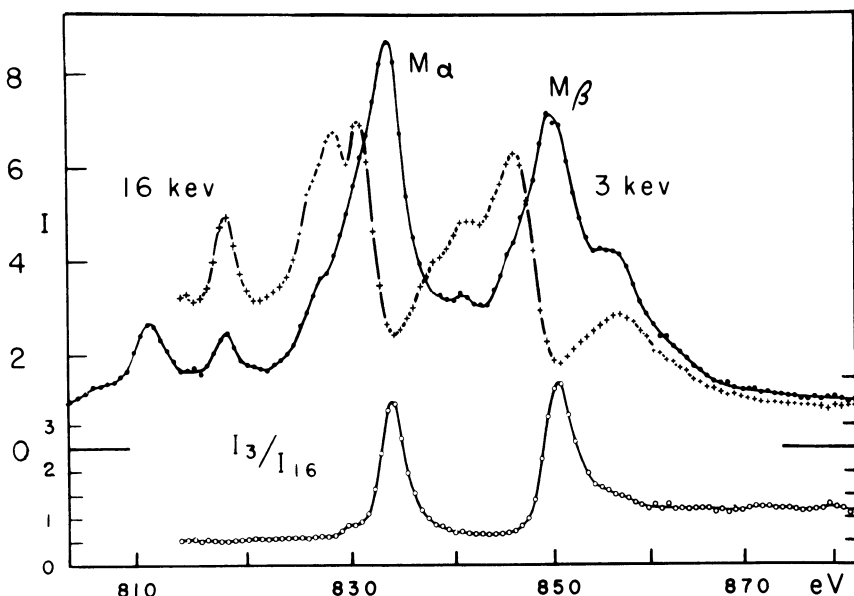


Fig. 2. Lanthanum M x-ray spectra under two different excitation conditions and their ratio.

meter using very large, high-quality KAP crystals. The target was a thick sheet of pure lanthanum mounted in an aluminum holder and polished to remove the oxide coating. It was placed in a special x-ray tube which was operated at a pressure of the order of 10^{-9} torr in order to reduce any chance of the target becoming contaminated. The spectrum was obtained by stepping the spectrometer across the region of interest at a rate which permitted the accumulation of a statistically significant number of counts at each point.

Figure 2 shows the results obtained with two different voltages across the tube, both well above the line excitation voltage. It is clear by looking at the two upper curves that merely increasing the voltage across the x-ray tube has greatly affected the spectrum obtained. The $M\alpha$ and $M\beta$ lines taken at 16 keV are broad and possess definite structure. The same lines taken at 3 keV are much narrower and well defined. They appear as conventional x-ray lines (with satellites). Note particularly that the peaks of the lines have shifted by about 3 V.

The bottom curve indicates the explanation of these drastic changes. This curve is a graph of the intensity ratio between the two top curves. It is a reasonable facsimile of the photon absorption curve of the lanthanum.* The

*The resemblance can be noted by comparing this curve with the absorption curve given by Fischer and Baun.⁵

16-keV electrons were able to penetrate much further into the target; hence the photons which they produced had a much greater probability of being absorbed on the way out. The 16-keV curve has much greater anode self-absorption than does the 3-keV curve. On the bottom curve the peak at 833 eV involves the absorption due to the M_V , level while the second peak at 851 eV represents the absorption due to the M_{IV} level.

It is clear that the major shape changes, peak shifts, and structure in the lines are all caused by self-absorption. A series of curves for all the lanthanides illustrating effects of self-absorption have been obtained by Fischer and Baun.⁵ Curves showing the effects of self-absorption in the lanthanides have also been obtained by means of fluorescent excitation.⁶

HIGH-ENERGY SATELLITES AS IN COPPER

The next example of voltage-dependent line-shape changes is taken from a series of curves⁷ run on a copper target using the same equipment previously described. The voltage across the x-ray tube ranged between limits set by the line threshold voltage on the lower end and the voltage at which self-absorption effects become significant at the upper end. Figure 3 shows seven of the curves taken at various voltages.

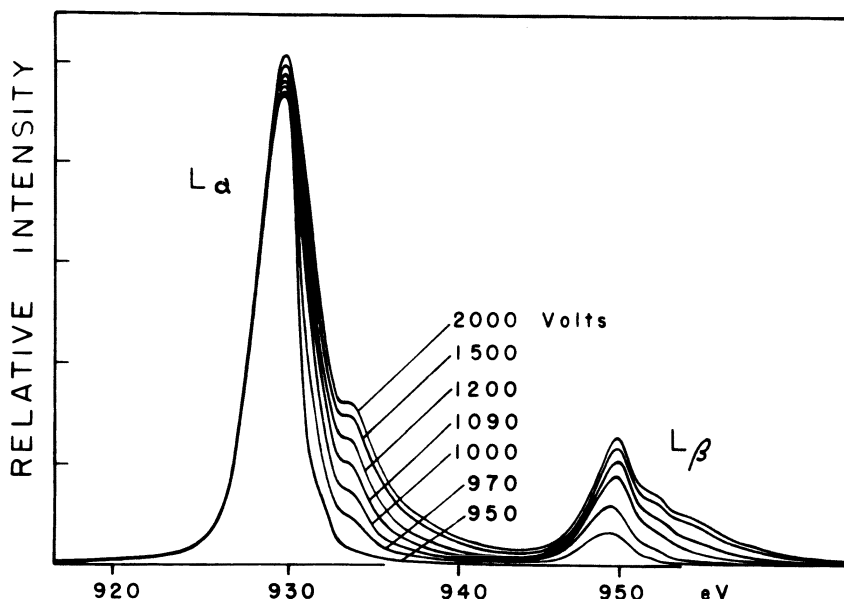


Fig. 3. Copper La, β x-ray spectra under several different excitation conditions.

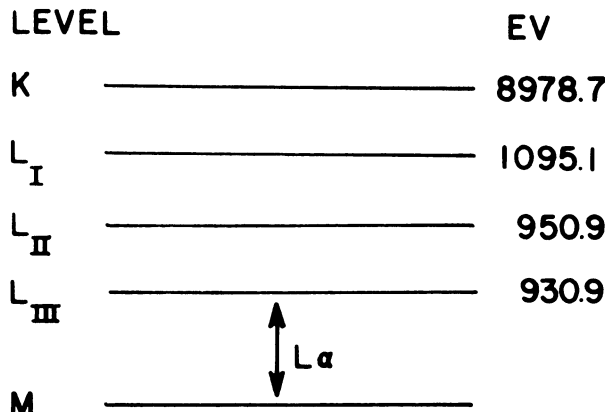


Fig. 4. Partial energy-level diagram of copper.

The La line provides a good example of the changes in line shape which take place under these conditions. Note that the shape changes considerably as the voltage across the tube is increased. The amount of asymmetry increases, its sign changes, the width increases, and the wavelength decreases – just how much depending critically on what criterion one uses to establish “the” wavelength of the line. The partial energy-level diagram of copper shown in Fig. 4 can be used to interpret these changes. As the voltage across the tube is increased enough energy is eventually given to the bombarding electrons to create holes in the L_{III} level. It is at this voltage that the La line is first excited. If the voltage is increased another 20 V, the electrons will have enough energy to create L_{II} holes as well. The creation of L_{II} vacancies increases the probability of an L_{III} vacancy because the L_{II} vacancy can become an L_{III} vacancy plus one or more M -shell vacancies by means of a radiationless Auger transition. The x-ray photon emitted when this latter L_{III} vacancy is filled radiatively will have a slightly higher energy than the photon from the regular L_{III} vacancy because that atom is also missing one or more M electrons. Similar “multiple-vacancy” satellite lines arise when the incident electron energy exceeds the L_I -shell excitation threshold, permitting additional transitions. Figure 3 shows these satellites appearing on the high-energy side of the regular line as the voltage is increased above 950 V.

THRESHOLD EXCITATION LINE SHAPES OF IRON

Eliminating the L_{II} vacancy does not completely eliminate voltage-dependent shape changes. A good example of these residual shape changes can

be found in the La line of iron⁷ as the voltage across the tube is raised from threshold to about 10 V above threshold. The same equipment as previously described was used. Since the intensity of the line with so little excess voltage is very small, the very high sensitivity of the spectrometer used was particularly useful.

The results are shown in Fig. 5. In this figure the arrows identify the voltage which was placed across the tube, and E_F stands for the Fermi energy. It can be seen from Fig. 5 that even at these voltages, well under the voltage necessary to create L_{II} vacancies, the line possesses high-frequency satellites. These satellites are unusual in that their positions as well as relative intensities vary with incident electron energy. They are probably caused by transitions involving a bound-ejected-electron state wherein the electron ejected from the core of the atom is not given enough energy to be knocked completely free of the atom but remains bound to the vacancy in the core. This same explanation can be used to explain Johansson's results³ in the first example.

VARIABLE-ENERGY LINES IN LANTHANUM

The final and most extreme example of voltage-dependent wavelength-shifts is taken from the M spectra of lanthanum.⁴ Figure 6 shows a number of

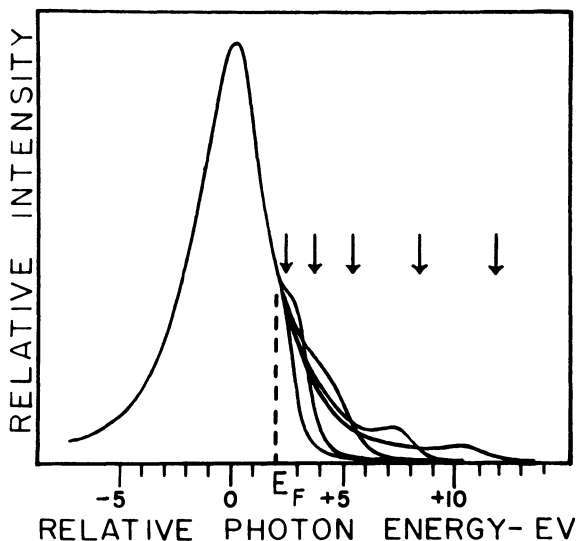


Fig. 5. Iron La x-ray spectra under several different excitation conditions.

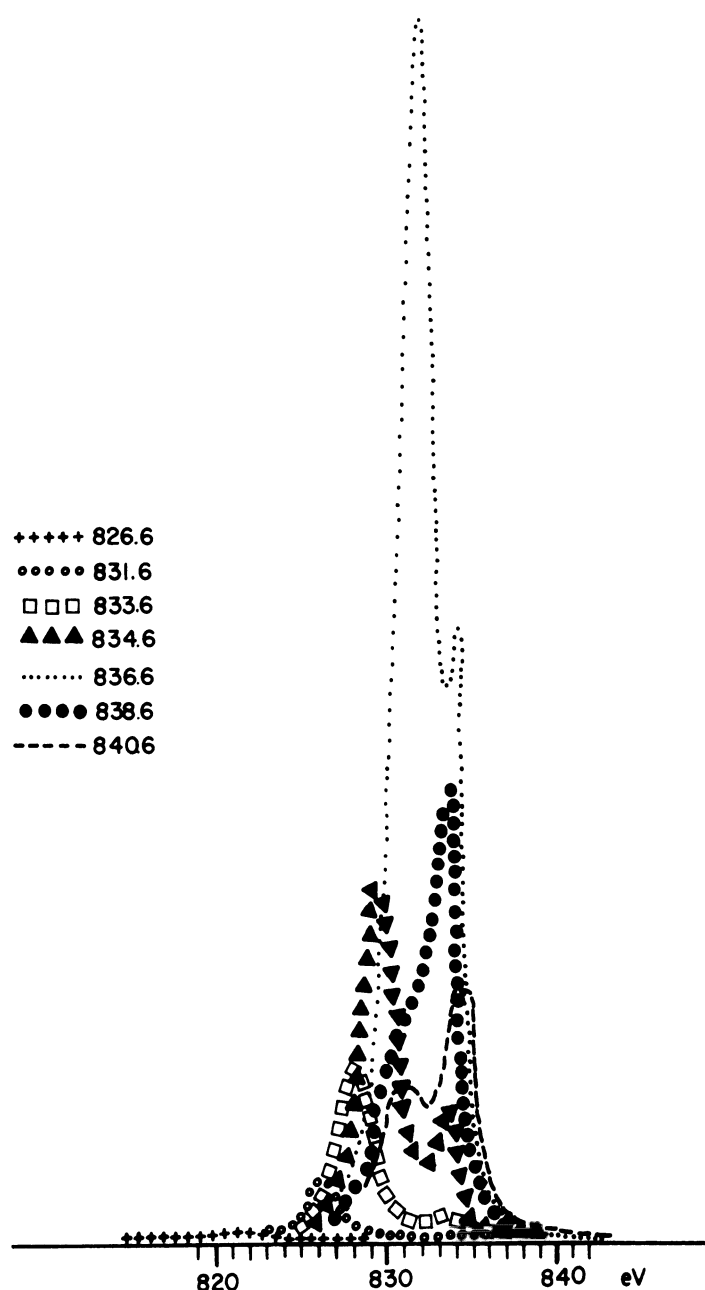


Fig. 6. Lanthanum *Ma* x-ray spectra under several different excitation conditions.

curves from the Ma region taken at various voltages just above the threshold voltage for creation of M_V vacancies. This series of curves was obtained with voltages well below the point where self-absorption distorts the spectra. Nevertheless, two distinct types of lines can be readily identified. One, which first appears with about 833.6 V across the tube, is a conventional line, in that its shape and position are independent of the exciting voltage.

The other line, which appears on the low-energy side of the conventional line, is most unusual. It first appears when the voltage across the x-ray tube reaches 826.6 V. The energy of the peak of this line is always 4.6 eV less than the energy of the bombarding electrons, and the peak shifts to the right in step with the exciting voltage. The intensity of this line also undergoes some dramatic changes. In the space of 10 V the intensity of this line goes from background to 100 times background, and then with a further increase of 5 V drops back toward background again. (The small residual line observed can be explained on the basis of some of the monochromatic incident electrons losing enough energy in the surface layers of the target to reduce their energy into the range which excites this unusual x-ray line).

The explanation of this line and its behavior is incomplete. However, a tentative explanation calls for bound two-electron excited states and depends heavily on the special character of the $4f$ levels involved.

SUMMARY

In summary, one can say that there are a number of physical processes which result in a voltage-dependent wavelength shift and shape change for characteristic x-ray lines. Examples of these changes due to self-absorption in lanthanum and high-energy satellites in copper have been shown. Also described were the effects of bound ejected electrons in K and L transitions and an example of a special movable x-ray line observable with monoenergetic incident electrons and caused by the special nature of transitions involving inner levels with high angular momentum.

SIGNIFICANCE

The significance of these findings depends strongly upon the particular application of x-ray spectroscopy in which one is interested. The most widely used application is to use x-rays to analyze samples for the elements contained in them. At the level of accuracy with which people are working today the findings presented here are of little concern. For example, the voltage

difference between the *L* lines of copper and nickel is about 80 V, while the maximum shift of any part of the copper line shown here is only about 5 V. There are two main methods of handling quantitative analytical data of this type theoretically.^{8,9} The empirical coefficient method should not be affected seriously by voltage shifts if the coefficients are obtained under excitation conditions roughly similar to that used for the sample. The variation near threshold shown here cannot be accounted for by the fundamental-parameter method. However, the wavelength region of disagreement is small, so that again the overall effect is negligible.

These findings have great significance for applications of x-ray analysis to valence-band studies. Most studies of this type have been badly affected by self-absorption. The variation of lines even at threshold places great, but perhaps not insolvable, difficulties in the way of interpreting the energy-level structure of valence bands.

Chemical binding and coordination studies are also greatly complicated, since it is difficult to tell unambiguously whether the changes observed, even if all the experiments are carried out at the same voltage, are due to chemical binding or are due to secondary effects through Auger transition rates or relative ease of finding bound excited states.

ACKNOWLEDGMENT

Much of the data presented here for which other references are not given were taken in the x-ray laboratory at New Mexico State University. More details on these and other measurements can be obtained from the references.

REFERENCES

1. J. A. Bearden, A. Henins, J. G. Marzolf, W. C. Sander, and J. S. Thomsen, *Phys. Rev.* **135**, A899 (1964).
2. R. B. Chester and F. Boehm, *Phys. Rev.* **166**, 1206 (1968).
3. P. Johansson, *Arkiv Fysik* **18**, 289 (1960).
4. A. F. Burr and R. J. Liefeld, *Bull. Am. Phys. Soc.* **13**, 576 (1968).
5. D. W. Fischer and W. L. Baun, *J. Appl. Phys.* **38**, 4830 (1967).
6. A. F. Burr, W. L. Baun, D. W. Fischer, C. Gilmore, and R. Labrie, *XIII Colloquium Spectroscopicum Internationale* (June 1967).
7. S. Hanzely and R. J. Liefeld, *Bull. Am. Phys. Soc.* **13**, 575 (1968).
8. L. S. Birks, *7th National Meeting Society for Applied Spectroscopy* (May 1968).
9. J. W. Criss and L. S. Birks, *Anal. Chem.* **40**, 1080 (1968).

Emission, Flame, and Atomic-Absorption Spectroscopy

Spectroscopic Study of Hot Gases

Firouz Shahrokhi

*UT Space Institute,
Tullahoma, Tennessee*

This is a study to predict total heat flux from a hot gas utilizing spectroscopic properties of the gas. A system such as the chemical rocket-engine plumes serves as a pertinent example. The thermodynamic equilibrium assumption has been questioned for such high-energy systems. A flame which is chemically reacting and is radiating a large percentage of its energy is shown not to be representative of an equilibrium system. In the reaction zone there is certainly not an equilibrium situation, and even in the outer cone the carbon particles and the CO₂ molecules do not appear to have time to equilibrate their energies. For these reasons an analysis of the radiation from a nonequilibrium flame is presented. The solution to the transport equation for an absorbing and emitting medium has been calculated based on a nonequilibrium gas. In this nonequilibrium state a measured spectroscopic intensity of volume emission of a given hot gas is presented and used, as well as the measured spectroscopic absorption coefficient. As in other branches of spectroscopy, the greatest emphasis has been placed on the measurement of spectral frequencies, because these frequencies are directly related to quantized energy levels of the flame molecules.

INTRODUCTION

Interest in the radiative properties of flames has stimulated research on the spectral analysis of flames to provide data for heat transfer calculations and for infrared analysis of flames and exhaust plumes. The method of analysis commonly found in the literature^{1,2} for the radiation emitted from a flame is to attempt to define a characteristic temperature and emittance of the

flame and then to consider the flame to be an emitting surface characterized by that emittance and temperature. The values for the emittance of the flame are obtained by measuring the absorptance of the flame and equating it to the emittance by invoking Kirchhoff's law. Due to the chemical reactions which occur in a flame, the assumption of thermodynamic equilibrium required to define the characteristic temperature of the flame and to justify invoking Kirchhoff's law is questionable. In addition, the optical thickness of a flame may be a very important factor in the energy emitted from the flame.

A flame can be characterized as a volume of hot gases which both emits and absorbs radiation. In the reaction zone there is certainly not an equilibrium situation, and even in the outer cone of hot gases the carbon particles and the CO₂ molecules do not appear to have time to equilibrate their energies³. Large flames may approach an equilibrium distribution of energy, especially the sooty flames of materials such as benzene. However, in general, the thermodynamic-equilibrium assumption must be questioned for flames.

For these reasons an analysis of the radiation from flames is proposed which does not require the assumption of equilibrium. The analysis is based on the differential equation describing the intensity of radiation emitted by an absorbing and emitting medium as a function of optical path length through the flame.

FUNDAMENTAL EQUATIONS

The transport equation for the intensity in an absorbing and emitting medium is

$$dI_\lambda/dx = -\beta_\lambda(x)I_\lambda + J_\lambda(x) \quad (1)$$

introducing an integrating factor

$$\frac{d}{dx} \left\{ I_\lambda \exp \left[\int \beta_\lambda(x) dx \right] \right\} = J_\lambda(x) \exp \left[\int \beta_\lambda(x) dx \right] \quad (2)$$

It is not possible, however, to experimentally determine the functional relationship between β and x . The value for β_λ determined by this experiment was the average of $\beta_\lambda(x)$ over the optical thickness of the flame. There is, of course, some question as to whether or not the same average value of β_λ will apply to the larger flames. Experimental evidence, which will be discussed below, indicates that such an assumption holds for practical purposes, and we have

$$I_\lambda \exp [\bar{\beta}_\lambda x] = \int J_\lambda(x) \exp (\bar{\beta}_\lambda x) dx + c \quad (3)$$

Again, the same argument of experimentally determining an average J_λ is used to obtain

$$I_\lambda \exp(\tilde{\beta}_\lambda x) = \frac{\bar{J}_\lambda \exp(\tilde{\beta}_\lambda x)}{\tilde{\beta}_\lambda} + c \quad (4)$$

or

$$I_\lambda = (\bar{J}_\lambda / \tilde{\beta}_\lambda) + c \exp(-\tilde{\beta}_\lambda x) \quad (5)$$

From the boundary condition $I_\lambda = 0$ at $x = 0$ a value for c may be obtained, and the equation becomes

$$I_\lambda = (\bar{J}_\lambda / \tilde{\beta}_\lambda)[1 - \exp(-\tilde{\beta}_\lambda x)] \quad (6)$$

For a flame having an optical thickness of L the intensity emitted is given by

$$I_{\lambda 2} = (\bar{J}_\lambda / \tilde{\beta}_\lambda)[1 - \exp(-\tilde{\beta}_\lambda L)] \quad (7)$$

When the flame is illuminated by an external source (such that I_λ at $x = 0$ is represented by $I_{\lambda 3}$) the evaluation of the constant in Eq. (6) gives

$$I_\lambda = (\bar{J}_\lambda / \tilde{\beta}_\lambda)[1 - \exp(-\tilde{\beta}_\lambda L)] + I_{\lambda 3} \exp(-\tilde{\beta}_\lambda L) \quad (8)$$

which for a flame of optical path length L becomes

$$I_{\lambda 1} = I_{\lambda 2} + I_{\lambda 3} \exp(-\tilde{\beta}_\lambda L) \quad (9)$$

$I_{\lambda 3}$ and $\tilde{\beta}_\lambda$ may be determined from Eq. (9) and J_λ may be computed from Eq. (7) using the experimentally determined values of $I_{\lambda 1}$ and $I_{\lambda 2}$. Utilizing these values in Eq. (6), the emitted intensity may be predicted from a flame of any optical thickness.

HEAT FLUX CALCULATIONS

The extrapolation program discussed in an earlier publication⁶ to determine the radiative heat flux to a target from a flame of arbitrary size is based on the following considerations: The flame is characterized by either a cylinder, a cone, or a sheet of flame for computational purposes. The diffusion flame produced from a cylindrical burner was considered to occupy a cylindrical volume having a mean diameter and a mean height. These mean values were determined by observing several pictures taken of the flame with a short exposure time. Although the flame tilted and changed shape somewhat, it was still found to occupy approximately the same volume. The diameter and height of cylinder superimposed on these several pictures were averaged to

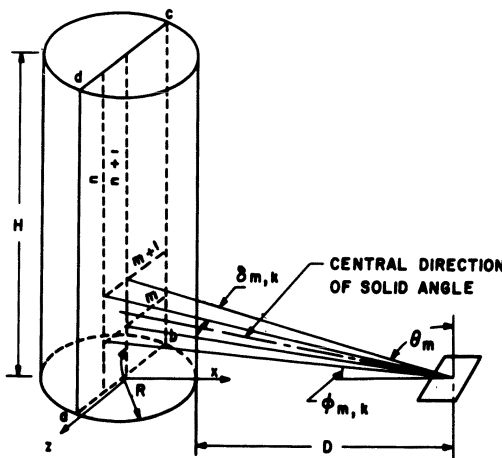


Fig. 1. Geometry for cylindrical flame.

determine the mean diameter and height used in computing the heat flux from the flame.

The monochromatic intensity being radiated by the flame is given by Eq. (6), where x is the optical path length through the portion of the flame being observed. The monochromatic flux to a target was computed by subdividing the flame into zones and multiplying the intensity emitted by that zone times the solid angle from the target subtended by the zone times the cosine of the angle between the normal to the target and the central direction of the solid angle.

For a cylindrical flame the flame was subdivided into N vertical strips and M horizontal strips on the plane through the centerline of the cylinder facing the target. Figure 1 shows the geometry used to compute the flux for the cylindrical flame. The total monochromatic flux at the target is given by

$$q_\lambda = \sum_{m=1}^M \sum_{k=1}^K \frac{2J_{\lambda mk}}{\beta_{\lambda mk}} [1 - \exp(-\beta_\lambda a_{mk})] \Omega_{mk} \cos \theta_{mk} \quad (10)$$

where β_λ is the monochromatic volume extinction coefficient, J_λ is the monochromatic volume emission, a_{mk} is the average optical thickness of the (m, k) zone, Ω_{mk} is the solid angle subtended by the (m, k) zone, and θ_{mk} is the angle between the normal to the surface and the central direction of the solid angle.

For a cylinder of height H and radius R divided into N vertical strips and M horizontal strips the following quantities were defined for a target at a distance D away from the edge of the flame:

$$k = N/2, \quad H_m = H/M, \quad R_n = R/n$$

$$\tan \delta_{mn} = \frac{R - (k - \frac{1}{2})R_k}{\{(D + R)^2 + [(m - \frac{1}{2})H_m]^2\}^{1/2}}$$

$$\tan \Phi_m = \frac{(m - \frac{1}{2})H_m}{D + R}$$

$$\tan \Phi_{mn} = \frac{(m - \frac{1}{2})H_m}{\{(R + D)^2 + [R - (k - \frac{1}{2})R_k]^2\}^{1/2}}$$

The projected area of the midsection of the optical depth perpendicular to the central direction of the solid angle is

$$A_{mk} = R_k H_m \cos \delta_{mk} \cos \Phi_{mk}$$

The solid angle Ω_{mk} and average optical depth A_{mk} are as follows:

$$\Omega_{mk} = \frac{A_{mk}}{r_{mk}^2} = \frac{R_k H_m \cos \delta_{mk} \cos \Phi_m}{(R + D)^2 + [R - (k - \frac{1}{2})R_k]^2 + [(m - \frac{1}{2})H_m]^2} \quad (11)$$

$$A_{mk} = \frac{2R}{\cos \Phi_{mk}} \{1 - \sin^2 r\}^{1/2}, \quad \sin \delta = \frac{(R + D) \sin \delta}{R} \quad (12)$$

$$\tan \delta = \frac{[R - (k - \frac{1}{2})R_k]}{D + R}$$

The total flux at the target was computed by numerically integrating the monochromatic flux using a 40-point Gaussian quadrature technique,

$$q = \int_a^b q(\lambda) d\lambda \text{ letting}$$

$$x = \frac{2\lambda - a - b}{b - a} \quad \text{and} \quad q = \frac{b - a}{2} \int_{-1}^1 q(x) dx$$

or by the quadrature formula

$$q = \frac{b - a}{2} \sum_{i=1}^n w_i q(x_i) \quad (13)$$

A computer program was developed to compute the geometric terms for

a given flame size and target position. The experimental data for J_λ and β_λ (see Figs. 2-6) from the spectrometer measurements (Figs. 7 and 8) were used in conjunction with the geometric factors to predict the flux. For the acetone and methanol flames the emission and absorption coefficients were found to be essentially independent of the position on the flame being observed by the spectrometer. Thus for the extrapolation on these flames J_λ and β_λ were considered to be constants. For sooty flames, such as cyclohexane and benzene, the values for J_λ and β_λ in the outer cone or sooty part of the flame were quite different from the values determined from the spectra taken near the base of the flame, where the radiation is coming principally from the reaction zone and inner cone of the flame.

Thus when the extrapolation is performed for large-diameter sooty flames the extrapolation grid must also contain the information of whether the grid points should be considered in the outer cone or the inner cone. This

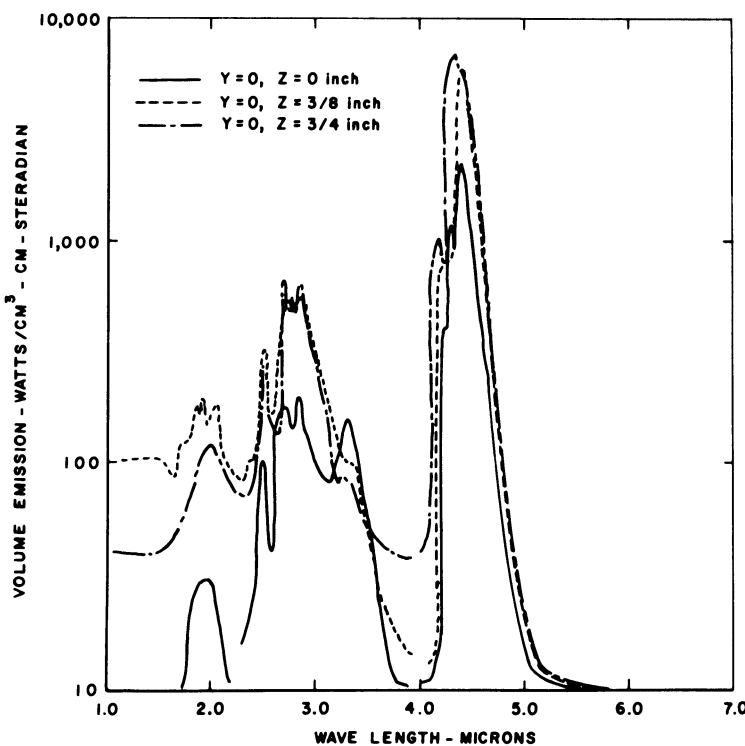


Fig. 2. Volume emission of acetone ($\gamma = 0$).

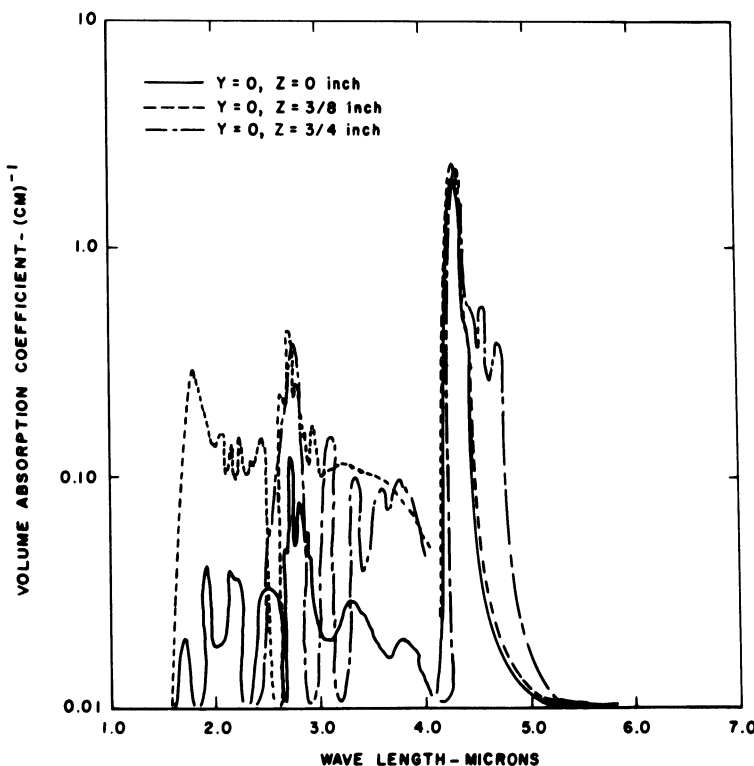


Fig. 3. Volume absorption coefficient for acetone ($\gamma = 0$).

is why the values for J_{λ} and β_{λ} have summing subscripts in Eq. (11).

For acetone and methanol flames the extrapolation program has been completed in a previous publication⁶ and the results compared to the flux measurements made with a HY-Cal Constantan foil-type Pyrheliometer. This pyrheliometer had a quartz window which did not transmit all of the radiation. In order to correct for this, a transmittance curve was measured for the window. A second integration was performed on the monochromatic flux multiplied by the transmittance of the window at that wavelength. This integral then determines the flux passing through the window incident on the pyrheliometer. This correction must be made for flames since the cutoff wavelength for quartz lies in the same spectral region as the CO_2 radiation. Figure 9 shows the total predicted flux from Eq. (13), the values measured with the pyrheliometer, and the total predicted transmitted flux, which is the predicted flux times the transmittance of the quartz window.

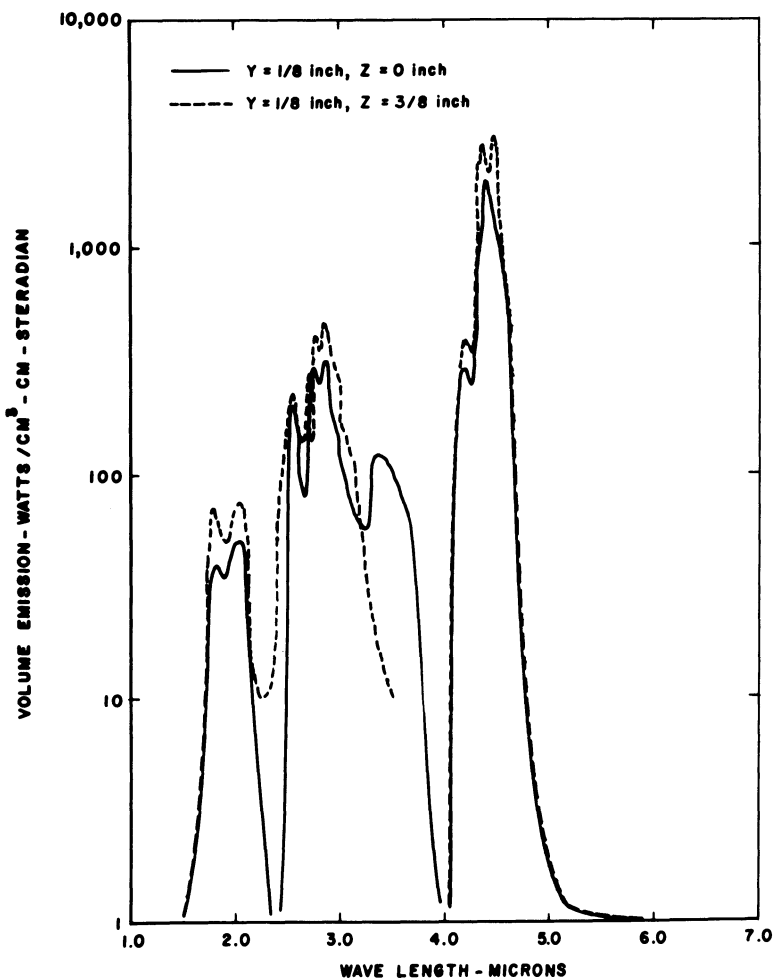


Fig. 4. Volume emission of methanol ($\gamma = 1/8$ in.).

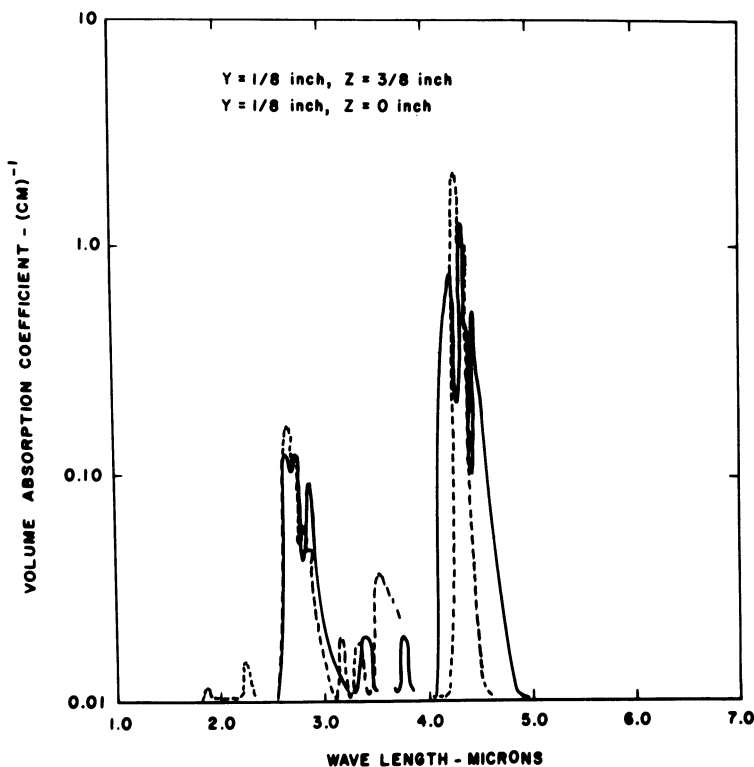


Fig. 5. Volume absorption coefficient of methanol ($\gamma = 1/8$ in.).

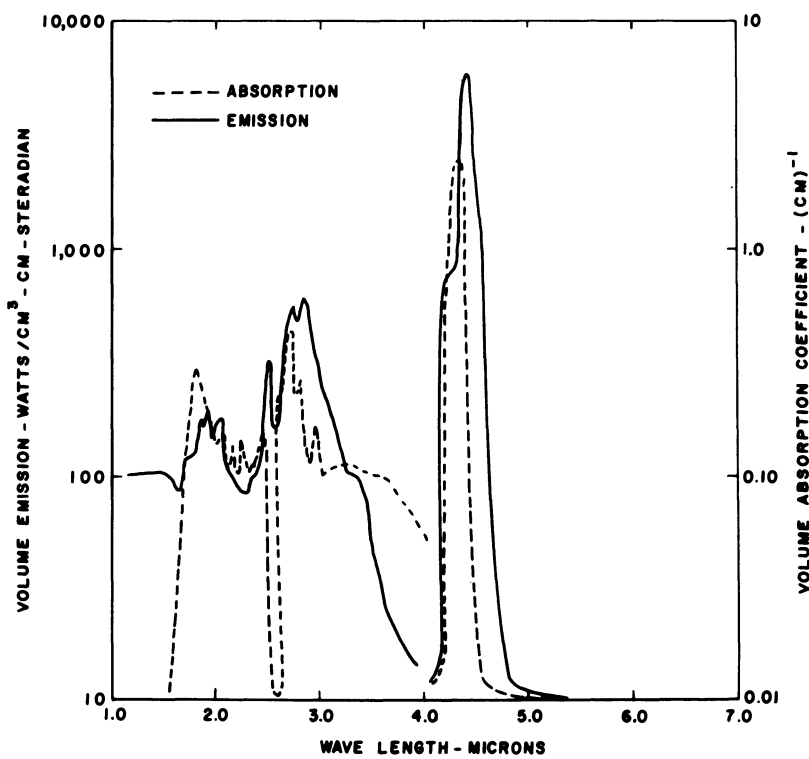


Fig. 6. Comparison of volume emission and volume absorption coefficient for acetone.

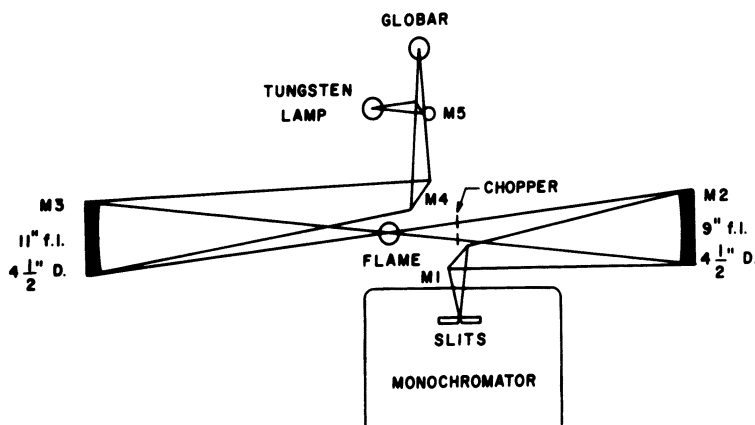


Fig. 7. Schematic of optics system.

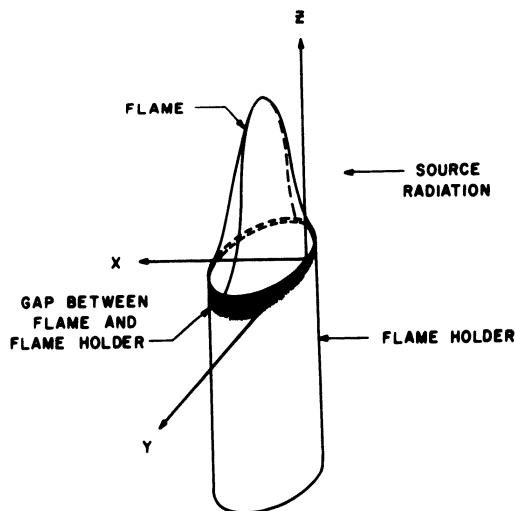


Fig. 8. Flame coordinate system.

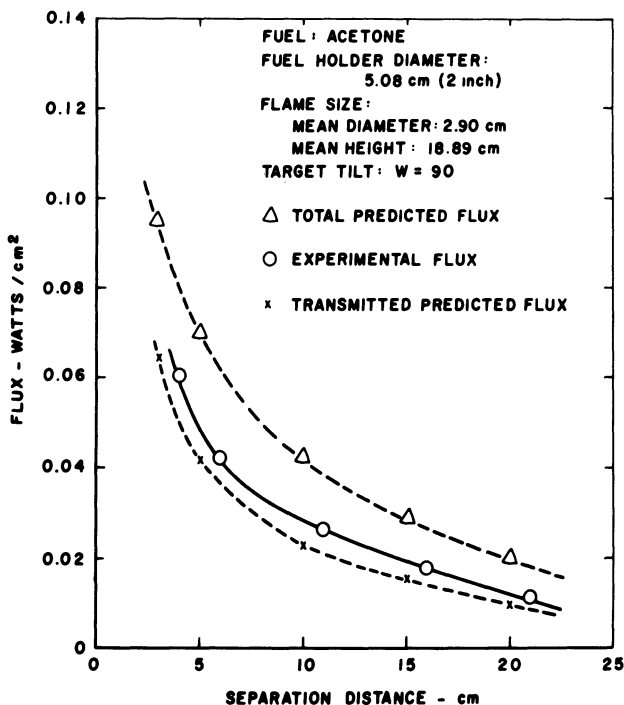


Fig. 9. Comparison of flux for an acetone flame (2-in.-diameter holder).

CONCLUSIONS

The comparison of the measured and the predicted transmitted flux are shown to be in good agreement by Figs. 10 and 11. From these results it was concluded that although the mixture of the gases in a flame was not homogeneous along an optical path, the average values determined by Figs. 12-17 for the volume absorption coefficient and the volume emission from the small laboratory-size flame extrapolates satisfactorily to predict the flux from a larger size flame. Thus once β_λ and J_λ have been determined by burning a fuel, the intensity emitted by a flame of the same fuel under the same burning conditions may be predicted from the transport equation.

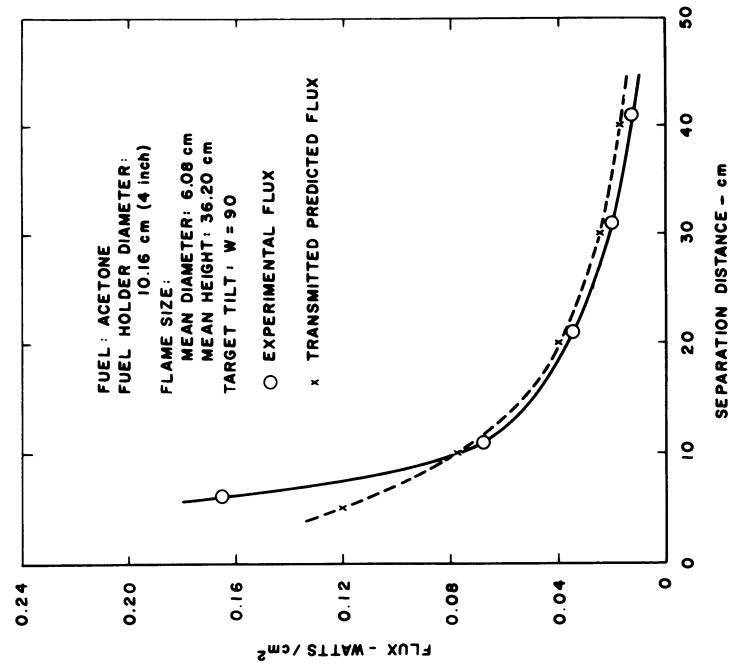


Fig. 10. Comparison of flux for an acetone flame (4-in.-diameter holder).

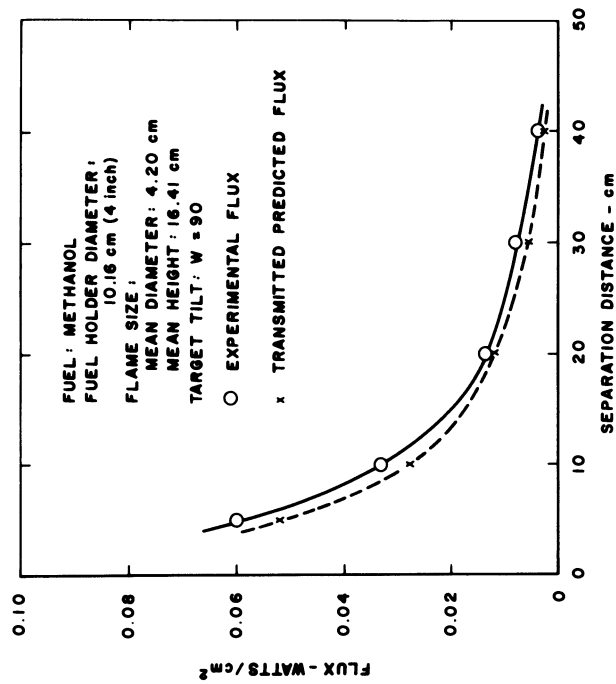


Fig. 11. Comparison of flux for methanol flame (4-in.-diameter holder).

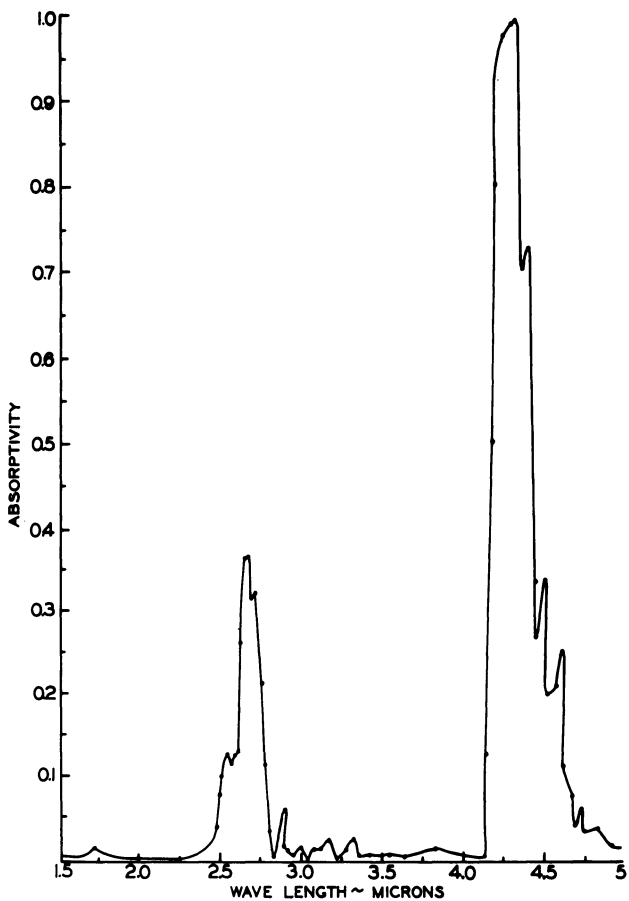


Fig. 12. Spectral absorptivity of acetone flame, optical path length, 0.8 cm.

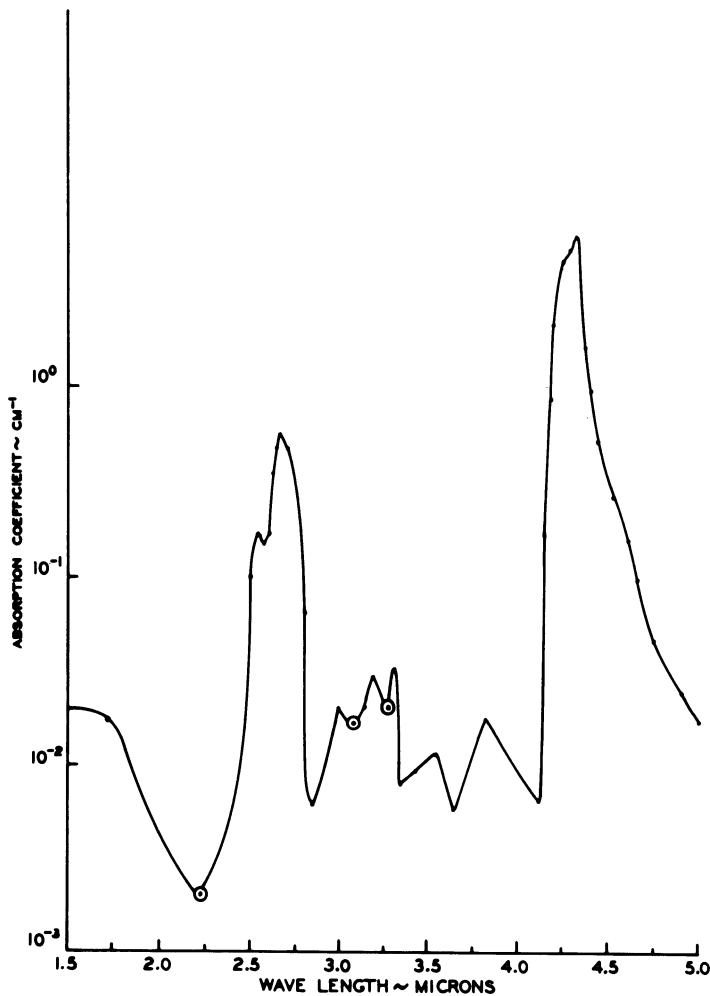


Fig. 13. Monochromatic absorption coefficient of acetone flame.

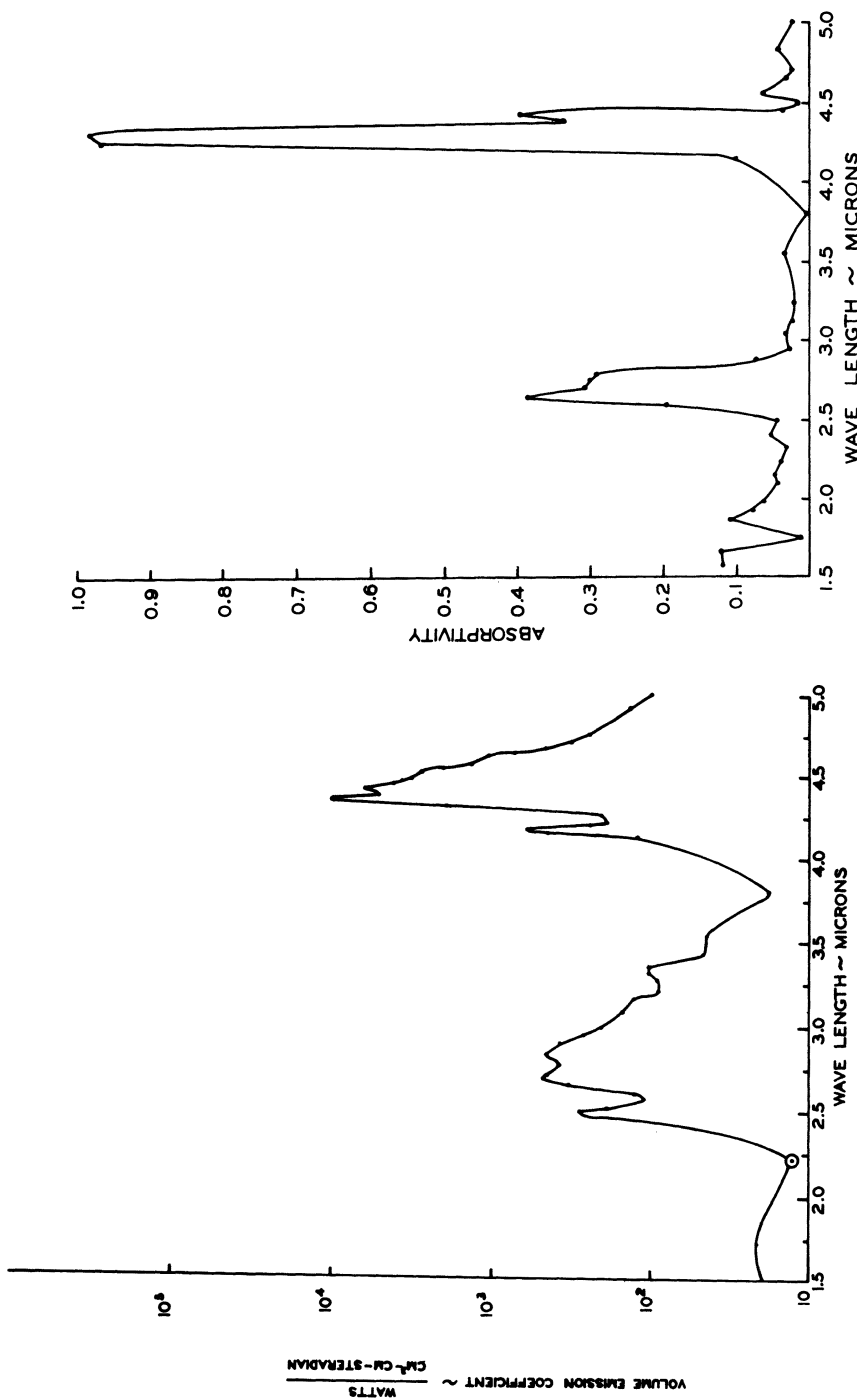


Fig. 14. Monochromatic volume emission coefficient of acetone flame.

Fig. 15. Spectral absorptivity of methanol flame.

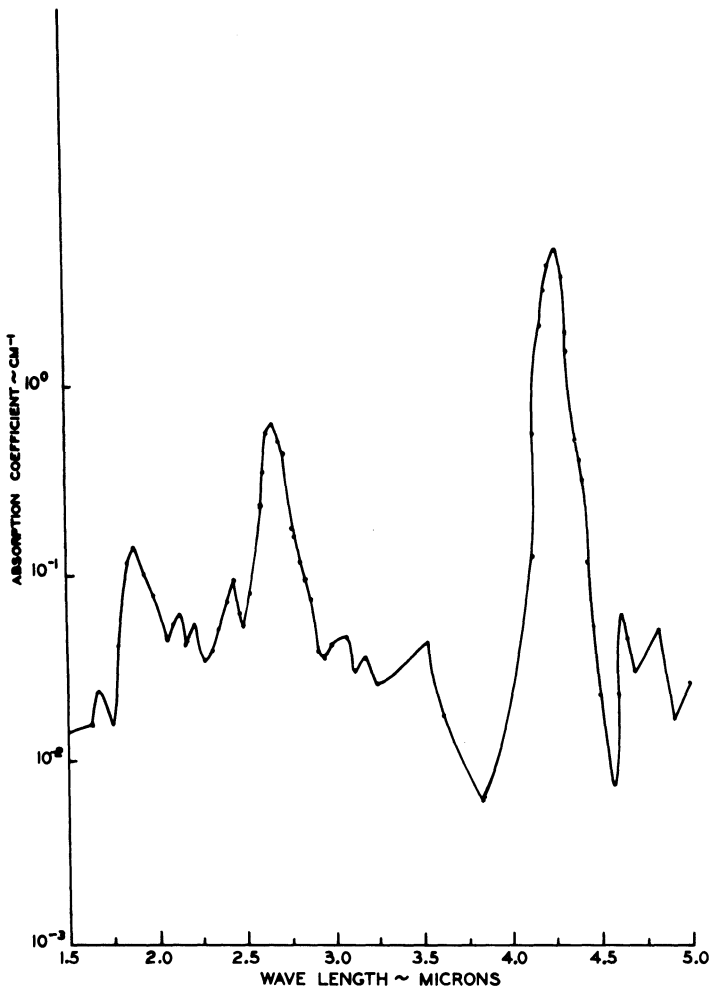


Fig. 16. Monochromatic absorption coefficient of methanol flame.

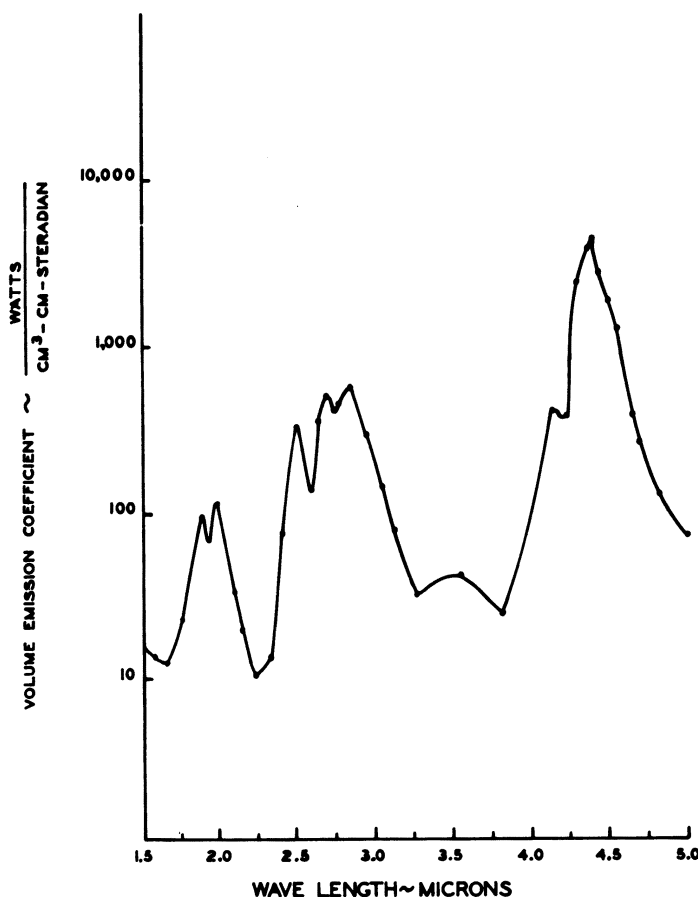


Fig. 17. Monochromatic volume emission coefficient of methanol flame.

REFERENCES

1. J. Kahrs, Field Calorimetry/Chemical Studies, Advanced Research Projects Agency, U.S. Army Chemical Research and Development Laboratories, Edgewood Arsenal, Maryland, 1965.
2. L. R. Ryan, G. J. Penzias, and R. H. Tourin, An Atlas of Infrared Spectra of Hydrocarbon Flames in the $1-5 \mu$ Region, AFCRL-848, Geophysics Research Directorate, Office of Aerospace Research (USAF), Hanscom Field, Bedford, Massachusetts, 1961.
3. A. Von Engel and J. R. Cogens, Flame Plasmas, in: *Advan. Electron. Electron. Phys.* 20, 112 (1964).

4. E. K. Plyler, L. R. Blaine, and M. Monk, Reference Wavelengths for Calibrating Prism Spectrometers, *J. Res. Natl. Bur. Std. (US)* **58**(4), 195–200 (April 1957).
5. J. C. Morris, Comments on the Measurements of Emittance of the Globar Radiation Source, *J. Opt. Soc. Am.* **51**, 798–799 (July 1961).
6. F. Shahrokhi, Numerical Technique for Calculation of Radiant Energy Flux Targets From Flames, Ph.D. Dissertation, The University of Oklahoma, 1965.

NOTATION

a, b	limits of wavelength integration (μ)
D	distance from edge of flame to target (cm)
H	mean height of flame (cm)
I_λ	monochromatic intensity ($\text{W cm}^{-2} \text{ cm}^{-1} \text{s}^{-1}$)
J_λ	monochromatic volume emission ($\text{W cm}^{-3} \text{ cm}^{-1} \text{s}^{-1}$)
L	optical thickness of flame
q_λ	monochromatic flux ($\text{W cm}^{-2} \text{ cm}^{-1}$)
R	mean radius of flame (cm)
T	temperature (Rankine degrees)
w_i	Gaussian quadrature integration weight factors
x	optical path length
β_λ	monochromatic volume absorption coefficient (cm^{-1})
θ	angle between normal to surface and central direction of the solid angle
Ω	solid angle (s)
$\sigma, \beta, \phi, \gamma$	angles defined in extrapolation program

Subscripts

λ	monochromatic quantities (wavelength)
1	quantities measured from flame with globar radiation incident
2	quantities measured from the flame
3	quantities measured from the globar
r	reference quantities
m, k	summing subscript

Analysis of Plant-Ash Solutions by Spark-Emission Spectroscopy

J. Benton Jones, Jr.,

University of Georgia.

Athens, Georgia

and Myron H. Warner

Ohio Agricultural and Development Center,

Wooster, Ohio

A method for analyzing plant tissue ash by direct-reading emission spectroscopy is described. The procedure developed gives highly reliable results for 16 elements. The method of converting instrument counts to concentration using a computer program is included.

INTRODUCTION

Direct-reading emission spectroscopy is being used at several laboratories^{1,2,5} to analyze plant tissue. This type of instrumentation makes possible rapid return of analytical results to farmers and growers submitting plant tissue for analysis and interpretation. The Ohio Plant Analysis Laboratory and its function is described elsewhere.⁴ This paper deals with the instrumentation and method employed to analyze plant tissue using a Jarrell-Ash 1.5-m direct-reading emission spectrograph (Atom Counter) with key-punch readout system.

The concentrations of most of the essential elements in plant ash are high. The major components are K, Ca, Mg, P, Si, and Na, while Fe, Mn, Al, Zn, Sr, Ba, Cu, B, Mo, and Co are in lesser concentrations. Typical ranges of plant tissue composition are given in Table V. Since most of the elements are in fairly high concentration, much of the effort described here was toward developing an analytical technique with a high degree of reliability.

EXPERIMENTAL

Apparatus and Operation

The apparatus and excitation conditions are given in Table I. The spectrograph is programmed for the determination of 16 elements. The spectral lines, exit slit widths, refractor plate, and photomultiplier tube characteristics are given in Table II. Lithium serves as the internal standard and mercury is used to maintain proper optical alignment between the entrance and exit slits. Background is read at 4046 Å and the instrument adjusts for background dynamically. The rotating-disc-solution technique is employed. The buffer solution containing the plant ash is transferred semiquantitatively to a porcelain boat. Care is taken to maintain a constant depth of solution.³ The boat is placed on the platform in the arc stand and raised into position. The rotating disc is partially submerged in the buffer solution. The high voltage supplied to the lithium photomultiplier tube is adjusted to give an exposure of approximately 30 sec duration. Analysis time per sample on the spectrograph is approximately 2 min.

Table I
Apparatus and Spectrometer Operating
Conditions

Power source	Jarrell-Ash compact Atom Counter Varisource #43-050
Output	25,000 v; capacitance, 0.005 mf; inductance, 155 ϕ resistance, residual; current, 4 A; four breaks per half cycle.
Spectrometer	Jarrell-Ash 1.5-m compact Atom Counter, Model 66-000; 30,000 lines/in. grating; 5.4 Å/mm dispersion; wavelength coverage 2000–8000 Å
Entrance slit	25 μ
Electrodes	Sample: High-purity graphite disc 0.492 in. in diameter and 0.200 in. thick (National Carbon Co. #AGKSP L-4075) Counter: High-purity graphite rod 0.180 in. in diameter (National Carbon Co. #AGKSP L-3951)
Speed of disc rotation	12 rpm
Sample holder	Porcelain boat, Coors #2, D-39
Analytical gap	3 mm
Time of excitation	Preburn 20 sec, exposure approximately 30 sec (controlled by internal standard)

TABLE II
Optical and Photomultiplier Characteristics

Element	Spectral line (Å)*	Refractor plate	Exit slit (μ)	Photomultiplier tube	Grade†
K	4044.0	Glass	75	RCA 931A	C
P	2553.3X2	Corex	75	Japan R106	B
Ca	3158.8	Quartz	75	RCA 1P28	B
Mg	2795.5	Quartz	75	RCA 1P28	B
Na	5889.9	Glass	75	RCA 931A	D
Si	2881.6X2	Corex	75	RCA 1P28	B
Mn	2593.7	Quartz	75	RCA 1P28	B
Fe	2599.4N2	Corex	75	RCA 1P28	B
B	2496.8X2	Corex	10	Japan R106	B
Cu	3274.0	Quartz	75	RCA 1P28	C
Zn	2138.6	Quartz	75	Japan R106	B
Al	3944.0	Glass	75	RCA 931A	C
Sr	4607.3	Glass	75	RCA 931A	B
Mo	2816.2X2	Corex	75	RCA 1P28	B
Co	3453.5	Quartz	75	RCA 1P28	B
Ba	2335.2	Quartz	75	Japan R106	D
Hg	4358.0	Glass	25	RCA 931A	E
Li	2741.3X2	Corex	75	RCA 1P28	E
Background	4046	None	75	RCA 931A	C

*X2 means read in the second order.

† Designated by Jarrell-Ash.

Four digit counts for each photomultiplier are recorded by means of both an IBM typewriter and key punch. One punch card contains the identification plus the four digit readouts for all 16 elements. It serves as input for an IBM 1620 computer program that converts spectrograph counts to per cent concentration for the elements K, P, Ca, Mg, Na, and Si and parts per million for the elements Mn, Fe, B, Cu, Zn, Al, Sr, Mo, Co, and Ba. Concentration is based on the original green dry weight.

Preparation of Chemical Standards and Buffer Solution

Five chemical standards were prepared from reagent-grade stock solutions. The concentration and composition of the stock solution are given in Table III. The chemical standards were prepared covering the range and

TABLE III
Composition of Stock Solution and Prepared Chemical Standards

Element	Reagent	Concentration of element in stock solution (g/liter)	Amount of stock solution (cc) to prepare 20 cc of a chemical standard*				
			#1	#2	#3	#4	#5
K	KCl	50.0	0.40	0.80	3.20	6.40	8.00
P	H ₃ PO ₄	10.0	0.20	0.40	1.60	3.20	4.00
Ca	CaCO ₃ †	40.0	6.00	4.00	1.00	0.40	0.20
Mg	MgCO ₃ †	25.0	3.20	1.60	0.64	0.32	0.16
Na	NaCl	0.4	0.14	0.28	0.70	2.80	4.20
Mn	Mn†	1.0	2.40	1.60	0.40	0.16	0.08
Fe	Fe†	1.0	0.08	0.24	1.60	4.00	6.00
B	H ₃ BO ₃	0.1	0.12	0.24	0.80	2.40	4.00
Cu	Cu†	0.1	0.16	0.40	0.80	2.40	4.00
Zn	Zn†	0.1	0.20	0.80	1.60	3.20	4.80
Al	AlCl ₃ ·6H ₂ O	0.4	0.10	0.60	4.00	10.00	15.00
Sr	SrCO ₃ †	0.1	20.00	8.00	2.40	0.80	0.40
Ba	BaCl ₂ ·2H ₂ O	0.1	8.00	4.00	1.20	0.40	0.20
Mo	(NH ₄) ₂ MoO ₄	0.01	0.20	0.80	2.00	3.00	6.00

*Stock solutions are pipetted into platinum crucibles, taken to dryness, and the residue taken up in 20 ml of buffer solution.

†Dissolved in concentrated HNO₃.

element composition ratio expected in plant tissue (see Table IV). These standards are different than those frequently prepared for spectrographic analyses when a single stock solution is diluted and all elements vary in concentration together.

Aliquots of various stock solutions were pipetted into 100-ml platinum crucibles. Two methods of drying, one by heat, the other freeze-drying, were employed. Freeze-drying produced a more desirable residue, which went quickly into solution. However, no significant differences in standard performance could be detected between those prepared by heat or freeze-drying. Chemical standards were stored in polyethylene dropper bottles. Fresh standards were made every three weeks.

Sample Preparation

Fresh plant material is dried at 80°C and ground in a standard Wiley mill to pass a 20-mesh stainless-steel screen. One gram ± 0.005 g of the

ground, green dried plant material is weighed into a 20-ml capacity high-form-fused silica crucible. The sample crucibles are placed in a cool muffle furnace, brought up to 500°C in about 40 min, and muffled a total of 4 hr. The length of ashing is not critical. Samples are usually completely ashed after the first hour at 500°C.

After muffling, the ashed samples are cooled and 5 ml of an acid buffer solution is slowly pipetted into the crucible. The ash solution is stirred and allowed to stand 45 min. Prior to transfer to the boat the solution is again thoroughly stirred. The presence of suspended carbon particles in the solution (and occasionally silica) does not affect the emission or analytical results.

Buffer Solution and Internal Standard

Hydrochloric acid has been the most frequently used acid in buffer mixtures.^{1,2,5} Commonly used internal standards are Co and Ni. The nature of the buffer has varied depending on whether K and occasionally Na are to be determined elements. Since K, Na, and Co are elements determined in this

TABLE IV
Composition of the Chemical Standards Based
on Green Dry Weight of Plant Tissue

Element	Chemical standard number				
	#1	#2	#3	#4	#5
per cent					
K	0.50	1.00	4.00	8.00	10.00
P	0.05	0.10	0.40	0.80	1.00
Ca	6.00	4.00	1.00	0.40	0.20
Mg	2.00	1.00	0.40	0.20	0.10
Na	0.02	0.04	0.10	0.40	0.60
parts per million					
Mn	600	400	100	40	20
Fe	20	60	400	1000	1500
B	3	6	20	60	100
Cu	4	10	20	60	100
Zn	5	20	40	80	120
Al	10	60	400	1000	1500
Sr	500	200	60	20	10
Ba	200	100	30	10	5
Mo	0.5	2.0	5.0	7.5	15.0

program, other elements had to be selected to serve as a buffer and internal standard. After some study Li was selected to serve as both the buffer and internal standard. Lithium is not present to any great extent in most plant tissues.

Although HCl is widely used in buffer solutions, it is very corrosive. HNO₃ has not been generally used in buffer solutions; however, it is consumed in the arc and very little corrosive action is obtained.

A study was undertaken to determine the effect of HCl and HNO₃ on analytical results. Buffer solutions of equal acidity were prepared with Li serving as the internal standard as well as the buffer. Ten chemical and 8 plant-tissue standards were prepared and taken up in one of the two buffer solutions. Each standard was analyzed in triplicate and calibration curves were determined and compared between the two buffer solutions. There was no consistent significant difference between the two sets of standards prepared with HNO₃ or HCl as to variance, slope, or position of the analytical curves. HNO₃ was then chosen as the acid. The buffer is made as follows: 50 g of lithium carbonate (Li₂CO₃) are dissolved in 200 ml of concentrated HNO₃. After the reaction is complete the solution is diluted to 1 liter with distilled water. The solution is sufficiently acidic to dissolve plant ash.

SPECTROGRAPH CALIBRATION

The spectrograph is calibrated daily by obtaining counts from five chemical and eight plant-tissue standards of known concentration. The relationship of concentration (*Y*) to emission counts (*X*) is known to be of the form $Y = AX^B$. Therefore to transform counts into concentration by the above formula, it becomes necessary to estimate *A* and *B*. Since $\log Y = a + b \log X$ is a linear form of the required equation, counts and concentrations are transformed to $\log X$ and $\log Y$, and *a* and *b* are estimated by the well-known least-squares technique.

Within a wide range of count values the values of *a* and *b* may be different (i.e., a nonlinear relationship may exist). This nonlinear function is not readily estimable from counts as variable as those from the emission spectrograph. So for any element where the relation of counts to concentration is not linear the range is separated into two parts, each of which is presumed to be estimated by a linear function. Upper and lower limits of concentration for each element are determined by experience. If two functions are necessary, limits must be specified for both. In this case the upper limit of one function should be larger than the lower limit of the second function. This technique allows for both functions to have common points used in their estimation.

Thirteen values of known concentration, with the corresponding emission counts, are entered for each element. The pairs of values within the limits are used for the least-squares estimation of a and b for one or two functions, as required. If the coefficient of determination is less than 0.99, the individual points are searched for outliers. An outlier is defined as any point lying more than 1.96 times the standard error of the estimate away from the computed line. If one or more outliers exist, they are reset to the computed point \pm one standard error of estimate. The reset points replace the outliers and a new least-squares estimate is computed.

If two equations are called for, the upper limit of one and the lower limit of two is the point of intersection of the two lines. Limits which were originally defined in terms of concentration are determined in terms of counts.

After the a and b coefficients are determined values of sample counts lying within the limits are entered as X and the corresponding Y is determined. The determined Y represents the concentration of the sample.

ANALYTICAL RESULTS

With dynamic background correction counts versus concentrations plot as straight lines on log log graph paper within the concentration ranges shown in Table IV, except for Mo, for which two linear functions adequately describe the relationship. Without dynamic background correction calibration curves for P, Fe, Cu, Al, Na, and Ba become curvilinear particularly in the lower concentration range. Linearity of the calibration relationship makes possible the computer evaluation of the required parameters without intervention of human judgment.

A series of 13 standards (five chemical and eight plant tissue) were analyzed on 12 different days, and the means, standard deviations from the mean, and coefficients of variability (CV) were determined. The results are given in Table V. The highest CV's were obtained with elements Co and Na, for the concentration of both elements is near the limits of detectability. The CV's for all the other elements indicate that the analytical and calibration procedures are adequate, considering the material being analyzed. The vast majority of the CV's were ten or less for all elements except Co and Na. In an earlier study an estimate of the source of variability between that associated with sample preparation and instrumentation was made. In general, a large proportion of the variability was found to be associated with sample preparation. Therefore, duplicate burns of the same ash solution did not increase precision, as did analyses of different aliquots of the same plant material. When a high degree of precision is required, duplicated ashed samples should be analyzed.

TABLE V
Extremes in Concentration and Coefficients of Variability
for three standards Analyzed on 12 Different Days

Element	Concentration and standard deviation		Coefficient of variability	
	Lowest concentration	Highest concentration	Lowest	Highest
per cent				
K	0.52 ± 0.03	10.06 ± 0.11	1.1	8.1
P	0.06 ± 0.01	1.01 ± 0.06	3.3	11.9
Ca	0.11 ± 0.01	5.55 ± 0.37	4.2	10.2
Mg	0.04 ± 0.01	1.56 ± 0.31	5.3	25.1
Na	0.01 ± 0.008	0.51 ± 0.12	10.8	70.2
ppm				
Mn	16 ± 2	583 ± 51	5.6	18.4
Fe	15 ± 1	1851 ± 65	3.4	15.9
B	4 ± 1	167 ± 11	5.0	32.0
Cu	6 ± 2	128 ± 20	8.9	23.6
Zn	6 ± 0.8	229 ± 40	6.9	16.0
Al	51 ± 5	6857 ± 569	8.2	22.5
Sr	15 ± 3	433 ± 28	5.2	19.7
Mo	0.6 ± 0.2	15.8 ± 2.4	8.0	30.5
Co	1.4 ± 0.3	15.1 ± 3.2	17.5	46.3
Ba	4 ± 0.6	173 ± 22	5.4	14.6

SUMMARY

The instrumentation and methods employed to analyze plant ash described in this paper have given highly satisfactory results. The analytical techniques are well adapted to routine procedures and provide a rapid method of analyzing plant ash for 16 elements.

REFERENCES

- Dale Baker, G. W. Gorsline, C. B. Smith, W. I. Thomas, W. E. Grube, and J. L. Ragland, *Agron. J.* **56**, 133–136 (1964).

2. P. N. Carpenter, Maine Agr. Exp. Sta., Misc. Publication 666 (1960).
3. R. P. Eardley and H. S. Clarke, *Appl. Spectry.* 19 69-72 (1965).
4. J. B. Jones, Jr., Ohio Report 52, 24-26 (1967).
5. A. L. Kenworthy, Proc. 36th Annual Meeting, Council of Fertilizer Applications, Stillwater, Oklahoma, Aug 29, 1960, National Plant Food Institute, pp. 39-50.

Routine Industrial Analysis of Stainless Steels

Robert L. Chapple* and Charles A. Spellman†

*Joslyn Stainless Steels
Fort Wayne, Indiana*

Techniques and equipment for ensuring that given stainless steel melts are being prepared to specification are discussed. The development of working curves and correction factors to aid in routine analysis is described.

INTRODUCTION

In a production, quality-control laboratory there is very limited time for research of even the applied variety. When a new analysis is required, of course, procedures and techniques are developed. This work is interspersed with the routine analyses and many times is accomplished on weekends. Consequently, unlike most research, *all* results do not have value. Only those that "work" are considered valuable, and we define "work" as "that procedure which gives the right answer, *fast*."

The equipment referred to in this paper and the accompanying figures is defined as follows:

1. *X-ray*. Norelco Universal Vacuum Fluorescent Spectrograph equipped with fine and coarse collimators and quick change x-ray tubes (both W-target and Cr-target tubes are employed). Flow-proportional and scintillation counters are used as detectors. The source is 60 kV, 50 mA, with MA stabilization.

*Chief Metallurgist.

†Chief Chemist.

2. *D.R.* Baird 3-m Air Direct-Reading Emission Spectrograph. Grating with 30,000 lines/in. Source is high-voltage rf spark and high-voltage ac arc.

3. *Atomic absorption.* Perkin-Elmer model 303 Atomic Absorption Unit equipped with nitrous oxide and Boling three-slot burners. Modified with dual aspirators.

4. *Lo carbon Analyzer.* Leco Model 589-600 Chromatographic (used for carbon analysis from ppm up to 0.2%).

5. *Hi carbon analyzer.* Leco Model 589-900 Chromatographic (used for carbon analysis from 0.2 up to 3.5%).

6. *Sulfur analyzers.* Leco Automatic Titration Units.

In the routine, day-to-day analysis of stainless steels there are basically two sets of chemical variants that are of interest, namely, those the customer wants to know, and those the producer wants to know. All stainless steels are melted and ordered to some set of specifications. The chemical analysis called out in these specifications is commonly referred to as the "ladle analysis". Each producer normally certifies that the material he ships meets the specification to which it was ordered. To do this, he lists the actual "ladle analysis" or chemical composition of that particular heat, or batch, of steel.

Normally, the ladle analysis of stainless steels consists of carbon, manganese, phosphorous, sulfur, silicon, chromium, nickel, molybdenum, copper, and cobalt. In addition, any element which is intentionally added to impart specific properties to the steel is analyzed and reported.

The second set of chemical variants is of interest only to the producer. This set is commonly known as the "residual analysis" of the heat. The elements included in this group are usually of very low concentration in the steel. They are usually not intentionally added but rather come from the material used to make the steel. They rarely affect the end use of the material or its useful properties. They may seriously affect the production of the basic material, however, and hence their interest to the producer. Included in these residual elements are columbium, tantalum, titanium, selenium, aluminum, tungsten, vanadium, lead, tin, zinc, boron, hydrogen, oxygen, and nitrogen.

Figure 1 shows the instrumentation used at Joslyn to analyze for these various elements.

SAMPLING AND SAMPLE PREPARATION

The primary function of the chemistry laboratory is to assist the Melt Shop and ensure that all steel is melted to specification. In light of this, we will concern ourselves here primarily with the techniques and equipment used in this function. Some of the secondary functions will also be mentioned briefly.

	C	Mn	P	S	Si	Cr	Ni	Mo	Cu	Co	Cb	Ta	Tl	Se	Al	W	V	Pb	Sn	Zn	B	N ₂	H ₂	O ₂	Zr	Te	Ag	As	Sb	Cd
Baird D.R.	X	X		X	X	X	X	X	X	X	X	X	X	X	X	X	X	X	X	X	X	X	X	X	X	X	X	X	X	
X-Ray		X							X	X	X	X	X	X	X															
Leco C		X																												
Leco S			X																											
Leco Gas																										X	X	X		
Wet		X	X			X	X	X	X	X	X	X	X	X	X	X	X	X	X	X	X	X	X	X						
A.A.		X			X			X	X	X	X	X	X	X	X	X	X	X	X	X	X	X	X	X	X	X	X	X	X	X

Fig. 1. Instrumentation used at Joslyn Stainless Steels for the determination of various elements

During the making of a heat samples are continually taken and sent to the laboratory for analysis. We have found that samples cast in a ceramic sleeve 2½ in. high with an I.D. of 1½ in. and O.D. of 2½ in. work very satisfactorily for our analyses. These samples are cast on a copper chill plate to somewhat control the repeatability of grain size and orientation.

Sample preparation consists of cutting the cast sample in half transversely with an abrasive cutoff. The cut surface is then faced on an abrasive belt of 80 grit. This is sufficient for the D.R. If x-ray analysis is required, we have found that a further polishing on 120 grit paper disks is necessary for good repeatability. On either machine a single face on the surface to be analyzed is essential.

PRELIMINARY ANALYSIS

About midway through the making of a heat a sample is taken which we call a preliminary sample, and usually refer to as "prelim" or "P-1." From the results of the analyses of this sample the final additions are made to the heat to bring it into specification. While this sample is being analyzed many reactions are taking place in the furnace as well as many mechanical actions in the steel-making process. It is therefore essential that the analysis of this sample be both rapid and reliable. We average about 13–14 min for complete analysis of Mn, P, Si, Cr, Ni, Mo, Cu, Co, and Pb, including sample preparation.

First let us consider the x-ray portion of the analysis. For the prelim analysis, working curves are used which were originally made from routine samples analyzed several times by conventional wet analyses. In every case the wet analyses were "backed-up" by analyses of NBS standards. More recently

so-called "synthetic standards" have been made for use in producing working curves. These samples are made in a small 5-lb induction furnace, so that the analysis closely approximates that of routine samples, but with one element varied as desired. With these controlled samples it was found that in some cases the element of interest displayed a linear function from 0% to the highest percentage of interest when plotted against the time required to accumulate a fixed number of counts.

Other elements were found to be enhanced or absorbed by interfering elements within the sample matrix and thus required corrections.

In the analysis of the prelim sample from a stainless steel heat it was determined that apparently Cr was the only element which was sufficiently influenced to require correction.

In all cases the normal analysis of a stainless steel grade was used as the base point. Using 18 Cr and 8 Ni as the base for the nickel correction, it was found that for each 1% Ni over the 8% base an addition of 0.06% was required to the apparent Cr answer.

Molybdenum was found to have an even greater absorption effect on Cr. Since most stainless grades contain 0.20-0.50% Mo, this range was used as the base and thus requires no correction. For any concentration of Mo over 0.50%, however, the correction factor was found to be 1/3 of the amount of Mo present. This factor is an additive factor to the apparent Cr. For example, in a sample containing 0.62% Mo an addition of 0.04% would be required to the apparent Cr.

Several other elements were found to interfere with the determination of chromium, tungsten being a notable example. No corrections were found to be necessary, however, either due to their relatively insignificant effect, or to their presence in stainless steel in such minute quantities. At present, therefore, only the nickel and molybdenum corrections are being used, and the procedure works quite well on the common grades of stainless steel.

With these working curves and correction factors at hand we can proceed to the actual analysis. The indication of quantity of an element present may be taken from the read-out panel in two forms: (1) as the number of total counts in a fixed time, or (2) as the total time to accumulate a fixed number of counts. We have used both, but prefer the fixed-count technique because it "works," in the sense of our previous definition.

The reference sample (which can be almost any concentration, but speeds up the analysis if it contains a larger percentage of the element sought) is analyzed first and the total time required to accumulate the fixed number of counts is recorded. The unknown sample is then presented for analysis and again the time required to accumulate the same number of counts is recorded. The time required for the unknown is then ratioed to that of the reference.

This ratio is then used to enter the working curve to determine the actual percentage of the element present. Any correction factors are then applied to gain the final result.

Figure 2 shows some of the total-count values used in the analysis for some representative elements.

This ratio technique partially obviates drift and small variables in equipment which could affect absolute values. Another interesting and very useful aspect of this technique is the fact that the reference sample need not be a point on the working curve. Thus a so-called "universal reference" can be made which contains useful amounts of all the elements which are of routine interest. This reduces to a single sample the reference samples needed for routine analysis.

One other technique that has been found useful in reducing the human error inherent in rapid routine analysis is that known as the "half-count technique." In this technique each sample is run a second time using one-half the fixed number of counts. The ration of unknown time to reference time, of course, is not altered when the fixed count is halved in both instances, and thus a check is obtained on all readings.

The prelim analysis on the Baird Direct Reader is somewhat more complicated due to the increased severity of interelement effects associated with emission spectrographic analysis. At the stage in the steel-making process where this sample is taken there is a considerable variation in composition from heat to heat. Therefore it is almost impossible to predict, even roughly, the composition of the sample. For this reason even working curves for various grades are not satisfactory.

The technique employed for prelim analysis is best described as one of successive approximation. Working curves have been prepared for each element of interest without respect to grade. It has been found necessary, however, to

FIXED COUNTS FOR VARIOUS ELEMENTS	
<u>Element</u>	<u>Total Counts</u>
Cr	1,024,000
Ni	1,024,000
Mo	1,024,000
Cb	512,000
Se	512,000
Cu	256,000
Mn	128,000
V	102,400

Fig. 2. Total count values.

have separate curves for the straight chrome grades and the chrome-nickel grades.

A reference sample of known composition is then selected from the same grade as the unknown. This reference is then sparked and the read-out clocks set to conform to the working curves. Duplicate runs are made to ensure accuracy. The unknown sample is then sparked twice and the clock readings averaged. These values are then used to enter the working curves. If the resulting analysis does not fall within predetermined ranges of the composition of the reference sample, a new reference sample is selected whose composition more closely approximates that of the unknown. The entire procedure is then repeated until a reference sample is found that is close enough to the composition of the unknown to obviate most of the inter-element effects.

Some empirical correction factors (or, as we like to call, them "finagle factors," and this probably more accurately describes them) have been developed. These, however, are not infallible, and are only used with the utmost prudence.

LADLE ANALYSIS

While the heat is being teemed into the ingot molds one final sample is taken. From this sample the final or ladle analysis is derived. Some of the problems noted earlier are considerably diminished in running the ladle analysis. This is primarily due to the fact that the composition of the sample is known within very narrow limits. Thus working curves for the x-ray were prepared using samples of each given grade of stainless.

By choosing a reference sample from the same grade as the unknown, thus having the composition very similar in both, the need for correction factors is eliminated.

Similarly, on the D.R. the correct reference sample is readily available without resorting to the successive-approximation method.

OTHER RESPONSIBILITIES

In addition to the primary responsibility of support to the Melt Department, already mentioned, many other areas are encountered daily. These include product or check analyses; lost identity samples; analyses of customer service samples, scrap, and raw materials; checking parts from the maintenance department, etc. Basically, the procedures are the same: working curves are prepared in the area of interest, and the mechanics of operating the various instruments are similar. Often, however, long and tedious hours are spent

developing working curves and the necessary correction factors when the compositions vary from standard 10Cr-8Ni or 18Cr-8Ni-3Mo grades of stainless to something like 10Cr-42Ni-2Cu-2Mo composite samples. The rule soon develops, "Never throw away a working curve, it may be needed again."

Most alloy or ore samples are run on the x-ray using a powder sample produced in a Spex Shatterbox. Reference samples in powder analysis come from two sources: (1) actual powdered ore samples which have been analyzed by conventional wet methods and (2) synthetic samples produced by mixing pure powdered samples of compounds of the elements of interest.

The extreme variation in the physical nature of samples is probably one of the most vexing problems. Many fixtures and "gadgets" have been created to cope with this continuing problem. As an example, sample cups have been made for the x-ray with varying exposure hole sizes down to $\frac{1}{2}$ in. Experience has proven that the repeatability of answers with exposure hole size less than $\frac{1}{2}$ in. is not acceptable.

An almost infinite variety of fixtures have been devised for holding samples to present to the D.R.

TABLE 1

Element*	Detection limit
Ag	0.001
As	0.05
Al†	0.002
Cd	0.00025
Co	0.002
Cu	0.0001
Fe in Ti	0.001
Mn	0.001
Ni	0.001
Pb	0.0002
Se	0.025
Sb	0.001
Sn	0.005
Te	0.0025
Ta	0.002
V†	0.001
Zn	0.0005

*Element in iron-base matrix
unless otherwise specified.

†In either iron or titanium.

ATOMIC ABSORPTION ANALYSIS

Atomic absorption analysis, a fairly recent acquisition, has proved invaluable in trace analysis work. Although almost too slow for routine quality-control work, this technique has been used with considerable benefit in determining the low end of working curves for the D.R.

Procedures have been developed for determining the elements to the detection limits given in Table 1.

Most of these detection limits are reached by chemical extraction of the element of interest prior to the atomic absorption analysis.

The procedures used are those published in Perkin-Elmer Newsletters, or minor variations thereof. The detection limits were lowered on some elements by using two atomizers as suggested by Piper.¹

One other advantage of atomic absorption is the possibility of working with minute samples when these are all that is available. For example, a fairly thorough job can be done on a sample as small as 0.1 g. Only the major analysis can be obtained by this method, of course, since the dilution involved will make trace-element concentration too low to be detected.

REFERENCE

1. K.G. Piper, *Atomic Absorption Newsletter* 6(3), 73-74 (1967).

Some Difficult Working Areas in Atomic-Absorption Flame Photometry

Juan Ramírez-Muñoz

*Beckman Instruments, Inc.,
Fullerton, California*

Some specific problems encountered in quantitative determinations by atomic-absorption flame photometry are reviewed. These result from instrument limitations, analytical behavior of analytes, and chemical composition of original and/or prepared samples. Different methods are discussed which may be used to overcome these difficulties by choosing better working conditions, different types of flames, and proper sample preparation. Chemical interference is discussed in detail and illustrated with experimental results obtained in the study of several frequent interference systems. Attention is given to calibration procedures and data processing and representation.

INTRODUCTION

Atomic-absorption flame photometry has been considered for several years, and still is considered at present, as a simple instrumental method for quantitative analysis. The availability of many types of instrumentation and the outstanding capability of using prepared samples in the form of homogeneous solutions have simplified the task of analysts wishing to perform their determination by means of this relatively new method. Great sensitivity for many elements, good selectivity, and acceptable accuracy and precision have completed the list of necessary analytical characteristics for a flame-photometric method.

The extremely good sensitivity achieved for some elements and the practical absence of spectral interference attracted the attention of flame

photometrists toward the newly-introduced atomic-absorption procedures, and in a matter of a few years the number of contributions has grown in this field at a rate which compares favorably with other analytical methods. At certain stages the analysts have found or have been told that some determinations could not be made. New developments have then gradually opened new application fields, and new analytes have been added to the list of capabilities of atomic-absorption flame photometry.

At present some limitations still exist. Several of these are reviewed in this chapter. Three main types of limitations affect quantitative determinations: (1) instrument limitations, (2) limitations due to the analytical behavior of analytes, and (3) limitations due to the chemical composition of original and/or prepared samples. Some examples will illustrate the cases discussed below.

EXPERIMENTAL

Data in the author's laboratory were obtained with a Beckman Model 979 Atomic-Absorption Spectrophotometer equipped with potentiometer recorder. Some tests were done with the use of the following accessories: (1) Transmittance/absorbance display, (2) linear concentration display, (3) automatic sample sequencer, (4) printer and control unit, and (5) scale expander. Two types of burners were used: (1) Turbulent Flow Burner (air-hydrogen flame), and (2) Laminar Flow Burner (mainly air-acetylene flame and nitrous oxide-acetylene flame). The instrument was optimized for each analyte (lamp current, gas pressures, slit width, and burner elevation). Solutions used were aqueous, except when specified.

Calculations have been performed by computer techniques as described elsewhere.¹ Some graphical representations have been studied first at the scope connected to the computer, and then reproduced by an automatic plotter from computer data.

RESULTS AND DISCUSSION

At times it is difficult to determine if limitations are due to instrument characteristics alone, to the analyte studied, or to both. Instrument and analyte limitations have been grouped together and are discussed in the same section. Those limitations which have their origin in the chemical composition of samples, such as those which result from concomitant components, are discussed separately.

Instrument and Analyte Limitations

Short-Wavelength Region. Atomic-absorption analytical lines of some elements appear in the short-wavelength region close to the short-wavelength end of the available working range. This end is established by the occurrence of several factors: (1) Limited transparency of optical parts, (2) limited sensitivity of photodetectors, (3) absorption by the air, and (4) absorption by the flame.

Figure 1 shows the transmission curve of the air-acetylene flame. Different gas mixtures behave slightly different at this extreme end.²

Lamps for some of these elements are relatively weak, in particular, those for arsenic and selenium. This obliges the operator to work with large slit widths and high gain; high gain will produce high noise observable at 0% absorption level and at the top of the absorption signal.

The determination of arsenic and selenium has been carefully studied and fully reported.³ The lack of available energy (weak lamps, and absorption by the air, optics, and flames) has been compensated in part by working at 10-mV span at the recorder, instead of 100 mV, and using noise suppression. The use of 10-mV span allows the utilization of narrower slits.

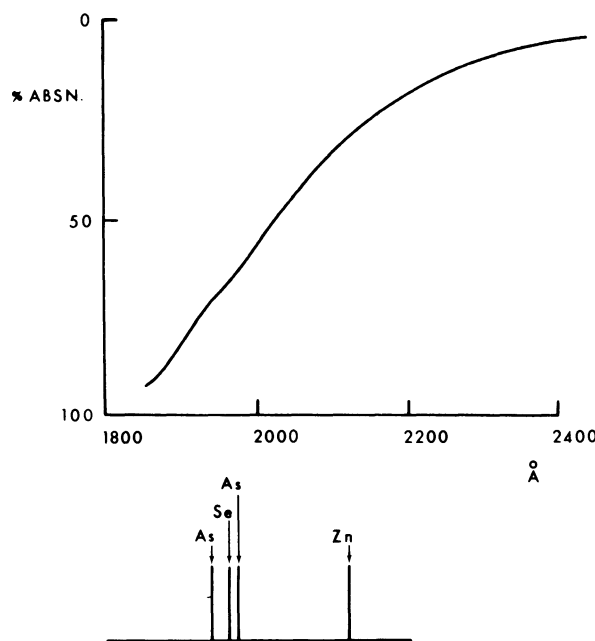


Fig. 1. Absorption produced by the air-acetylene flame at short wavelengths.

TABLE I
**Arsenic and Selenium (Laminar Flow Burner, Air-Acetylene Flame,
Single Pass, Hot Operation)**

Experimental conditions				
Element	Wavelength Å	Recorder span, mV	Photomultiplier	Percentual concentration limit (PCL), ^a ppm
As	1937	100	1P28 A	0.93
As	1937	100	R-106	0.82
As	1937	10	R-106	0.59
Se	1961	100	1P28 A	0.25
Se	1961	10	1P28 A	0.18

^a ppm of analyte to obtain a signal of 1% absorption.

Better sensitivity has been achieved when using air-hydrogen flame and some improvement of sensitivity was also achieved by using more sensitive photo-detectors at this region. An R-106 photomultiplier was tested for these purposes (see Table I).

The nature of the solution fed into the burner can also influence the results. For instance, for arsenic most tests were done with arsenic chloride solutions. Arsenic in the form of arsenite has been proven to produce higher-sensitivity results.

Need of High-Temperature Flames. Low-temperature flames do not provide enough heat to reduce certain analytes to the atomic state. For this reason some elements were not included in the early lists of elements determinable by atomic absorption and effort was devoted to the study of high-temperature flames which would provide greater heat.

A variety of flames have been studied.² High-temperature flames lead to a shift of the equilibrium established between oxides and free atoms, and/or between saltlike compounds and free atoms, thus helping liberation of atoms, which are the entities that participate in the real absorption process. An insufficient number of free atoms leads to low sensitivity or to lack of absorption. One of the most typical examples has been the case of molybdenum. This analyte does not show practical absorption with air-hydrogen flames (turbulent flow burner), but does show sensitivity in air-acetylene flames (laminar flow burner), and still better sensitivity in nitrous oxide-acetylene flames (see Table II). Refractory compounds of molybdenum need high temperature and high reducing conditions to liberate a sufficient amount of free molybdenum atoms, which act as active absorbing entities.

A first step was, of course, the use of fuel-rich flames. Air-hydrogen and air-acetylene fuel-rich flames have been used. A double effect was

TABLE II
Molybdenum (Laminar Flow Burner, Single Pass, Hot Operation)

Wavelength, Å	Flame	Type of flame ^a	Percentual concentration limit (PCL) ppm
3133	air-acetylene	lean-rich	0.80
3133	air-acetylene	rich	0.29
3133	N ₂ O-acetylene	rich	0.084

^a According to fuel gas richness.

TABLE III
Fuel-Rich Air-Hydrogen Flame (Turbulent Flow Burner)

Element	Experimental conditions			Percentual concentration limit (PCL), ppm	
	Wavelength, Å	Number of burners	Number of passes	Lean flame	Rich flame
Ag	3281	1	3	0.087	0.030
Ca	4227	3	3	0.032	0.018
Cr	3579	1	1	10.	0.85
Mn	2795	3	3	0.034	0.022
Sr	4607	3	3	0.034	0.014

achieved: higher temperature and higher reducing properties. Higher reduction was a benefit in the oxide-type compound decomposition. Molybdenum shows better sensitivity in a fuel-rich air-acetylene flame, as do certain other elements such as chromium, iron, nickel, and cobalt. Fuel-rich air-hydrogen flames have been studied in the determination of several elements.⁴ Several examples are given in Table III.

Very hot and reducing flames and 90% ethyl alcohol solutions have been used for aluminum (oxygen-acetylene flame, fuel-rich, turbulent flow burner). Sensitivity achieved was, however, lower than that obtained with nitrous oxide-acetylene flame.

The definite jump toward high sensitivity for many elements has resulted from the adoption of the nitrous oxide-acetylene flame in laminar flow burners. Premix gas flames of this type have helped to include beryllium, boron, aluminum, silicon, germanium, rare earths, and many other elements in the list of atomic-absorption analytes (see Table IV).

For other elements the air-acetylene flame (premix gas flame, laminar flow burner) is still the best choice for higher sensitivity. At the temperature of the air-acetylene flame a considerable amount of atoms become free and absorb at the absorbing cell. At higher temperatures some elements undergo excitation, which in turn decreases the number of available free atoms. A typical example is calcium (see Fig. 2).

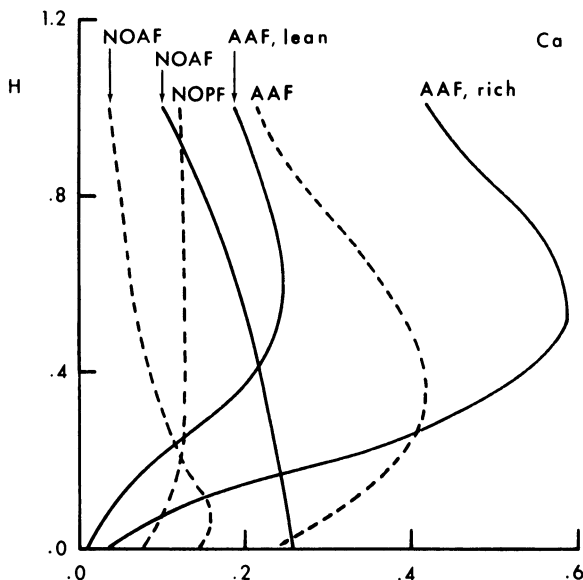


Fig. 2. Flame profiles of calcium, laminar flow burner. Solid line, hot operation (1 ppm); dashed line, cold operation (10 ppm).

Short-Lived Elements. "Short lived" refers to the lifetime of free atoms liberated at the flame. Two experimental procedures can be used to illustrate atom distribution: flame patterns, and flame profiles. Flame profiles have the advantage of being easier to prepare and can be combined with the variable concentration to present three-dimensional diagrams as three-dimensional flame profiles. Flame profiles are a graphical representation of the dynamic distribution of active free atoms over the burner. The maximum concentration of active atoms at a given height over the burner head corresponds to the maximum of the curve or surface.

The distribution of the free-atom population can be modified by many factors such as flame temperature, chemical composition of the aspirated solution, fuel-richness and gas streaming velocity with a given gas mixture, and burner geometry.

Flame profiles obtained with a burner system under a given set of experimental conditions can differ from those obtained with other burners or conditions. For this reason flame photometrists should check their particular system for the optimum burner elevation in order to bring the richer zone of the flame up to the most appropriate position with respect to the optical beam. Burner elevation should be rechecked any time that sample composition or working conditions change. Long and short-lived analytes are illustrated in

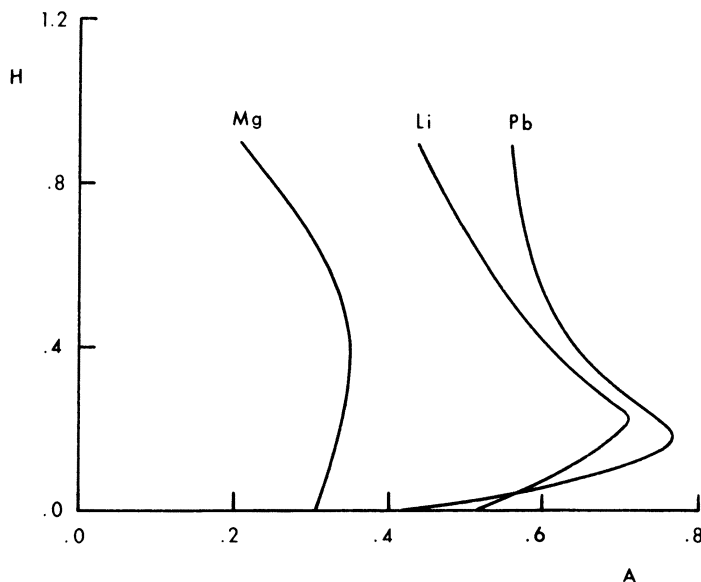


Fig. 3. Flame profiles for different elements of different free-atom life (laminar flow burner, air-acetylene flame).

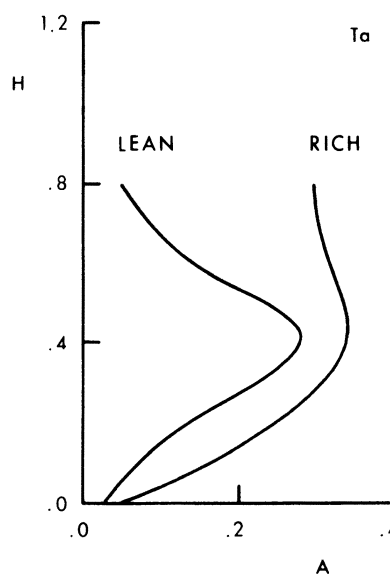


Fig. 4. Change of flame profile of tantalum (1000 ppm) with working conditions (laminar flow burner, lean and fuel-rich nitrous oxide-acetylene flame).

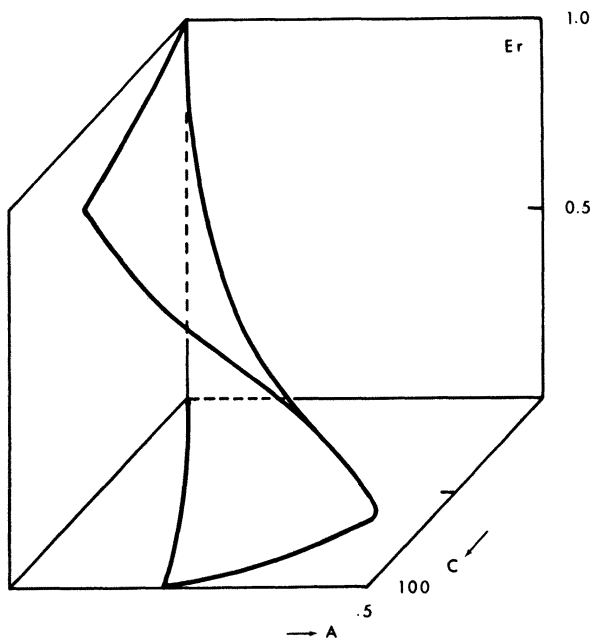


Fig. 5a. Three-dimensional flame profile of erbium (laminar flow burner, nitrous oxide-acetylene flame).

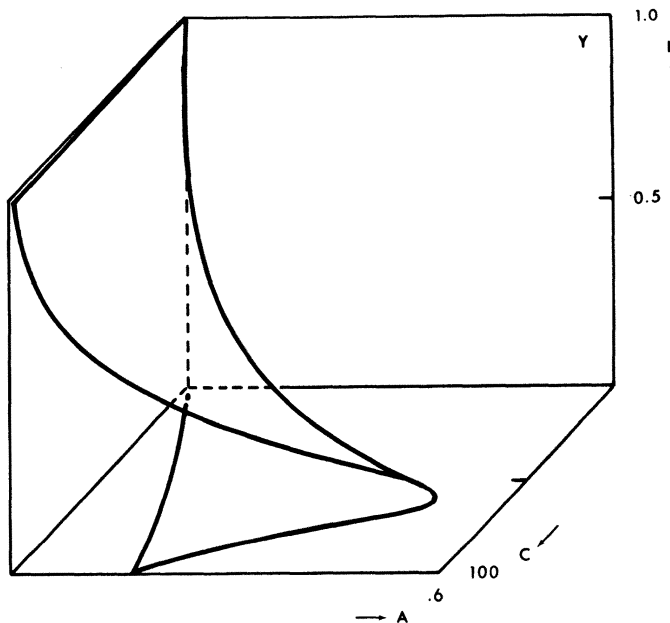


Fig. 5b. Three-dimensional flame profile of yttrium (laminar flow burner, nitrous oxide-acetylene flame).

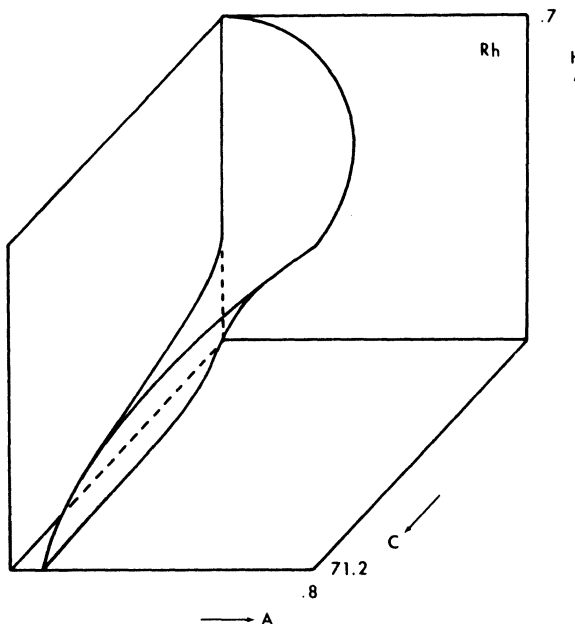


Fig. 6. Three-dimensional flame profile of rhodium (laminar flow burner, air-acetylene flame).

Fig. 3. In Figs. 2 and 4 the effect of shape change of flame profiles with working conditions is clearly shown. In Fig. 5 some three-dimensional flame profiles are represented.

Burner elevation is a highly critical variable for some analytes due to the sharp maximum observed, because of their short life as free atoms (Fig. 5) or because of their abnormal distribution at the very top region of the flame, such as is the case for rhodium (Fig. 6). In the latter case a compromise should be established, as at higher zones of the flame over the burner more sensitivity is obtained, but the noise (due to flame flickering) can also increase. In this case sensitivity may be sacrificed to obtain less-noisy readings.

In any of these cases multiple pass of the beam through the flame does not help too much if the factor of sensitivity increase is lower or much lower than the number of passes. Values for different elements are shown in Table V. Some more comments on triple pass are included below.

Low-Feeding-Rate Samples. Here sample composition, if it modifies viscosity, is a predominant characteristic which makes the instrument appear as the partial cause of sensitivity limitation. This is a suction capillary problem caused by the high viscosity of samples. In some cases this phenomenon appears as a consequence of the effects of one of the concomitants added during sample preparation or as a consequence of preexisting components in the sample; these effects have been found in the analysis of aqueous samples

containing 30–40% acetic acid,⁵ and in other cases because of the original matrix, as in oil analysis. Forced feeding can be a solution in this situation. This has been done by motor-driven syringe feeding in the analysis of oils.⁶

A reduction of feeding rate (in ml/min) results immediately in a drop of sensitivity as less of the analyte reaches the flame per unit of time.

In nonsevere reductions of feeding rates, as in the case of acetic-acid-containing solutions mentioned above, just the use of a series of compensated standards with equal amount of acid is the most appropriate way of solving the problem. This does not enhance sensitivity, but results are accurate. Forced feeding is an actual way of restoring, at least partially, the loss of sensitivity caused by high viscosity.

An increase of support-gas flow or pressure is perhaps not to be recommended. The plateau of the feeding rate curve (feeding rate versus flow or pressure of the support gas) actually indicates the limiting setting for maximum aspiration. In fact, when working with solutions of different

TABLE IV
Elements Determinable with High-Temperature Flames
(Nitrous Oxide—Acetylene Flame) Using the Beckman Model 979
Atomic Absorption Spectrophotometer

		ELEMENTS DETERMINABLE BY ATOMIC ABSORPTION SPECTROPHOTOMETRY															
		ELEMENTS FOR WHICH THE NITROUS OXIDE-ACETYLENE FLAME (NOAF) IS RECOMMENDED															
		ELEMENTS WHICH MAY, UNDER SOME SPECIAL CIRCUMSTANCES, BE DETERMINED WITH NOAF															
H																He	
Li	Be																
Na	Mg															P	S
K	Ca	Sc	Ti	V	Cr	Mn	Fe	Co	Ni	Cu	Zn	Ga	B	C	N	O	F
Rb	Sr	Y	Zr	Nb	Mo	Tc	Ru	Rh	Pd	Ag	Cd	In	Al	Si	As	Se	Cl
Cs	Ba	La	Hf	Ta	W	Re	Os	Ir	Pt	Au	Hg	Tl	Sn	Sb	Te	I	Kr
Fr	Ra																Xe
			Ce	Pr	Nd		Pm	Sm	Eu	Gd	Tb	Dy	Ho	Er	Tm	Yb	Lu
			Th	Pa	U		Np	Pu	Am	Cm	Bk	Cf	Es	Fm	Md	No	Lw

*See Mo in Table I also.

**Ca, Sr, Ba: NOAF recommended when high chemical interference is expected. Sn: Use of a hot flame such as NOAF necessary for some tin lines such as 2355 Å.

TABLE V
**Triple Pass (Laminar Flow Burner, Air-Acetylene Flame,
 Hot Operation)**

Element	Wavelength Å	Percentual concentration limit (PCL), ppm		
		Single pass (a)	Triple pass (b)	Factor (a/b)
Au	2428	0.085	0.032	2.7
Ca	4227	0.013	0.0060	2.2
Cr	3799	0.018	0.015	1.2
Cu	3248	0.013	0.0060	2.2
Fe	2483	0.015	0.0083	1.8
Ga	2944	0.49	0.23	2.1
In	3040	0.22	0.13	1.7
Mg	2852	0.0012	0.00058	2.1
Mn	2795	0.0051	0.0033	1.5
Ni	2320	0.016	0.0085	1.9
Pd	2476	0.066	0.027	2.4
Pt	2659	0.67	0.26	2.6
Rh	3435	0.066	0.028	2.4
Te	2143	0.097	0.079	1.2
Tl	3776	0.32	0.12	2.7
Zn	2139	0.0025	0.0012	2.1

viscosity, the curve may change both in height of the plateau and situation with respect to the horizontal scale.

High-Acid Samples. Effects of high-acid solutions are not confined only to corrosion problems. An excess of acid produces two main changes: variation of viscosity and sometimes variation of free-atom distribution in the flame. Both changes can result in variations of sensitivity. Variation of viscosity has already been mentioned for aqueous samples containing 30–40% of acetic acid.

The effects of hydrochloric acid at moderate concentrations (0.5*N*) have been studied in detail.⁷ Even at this relatively low concentration, in this type of analytical system it is typical to see a signal reduction and free-atom redistribution (see Fig. 7). Signal reduction and free-atom redistribution are consequences of a shift of the dynamic equilibrium established between bound atoms and free atoms.

Low-Sensitivity Elements. This problem has been the concern of atomic-absorption flame photometrists for several years, and even yet contributions are published and communicated for new means to increase the sensitivity of determinations of some analytes.

Increase of sensitivity has been achieved in several ways: (1) by elongating the absorption cell (long horizontal tubes or multiple passes

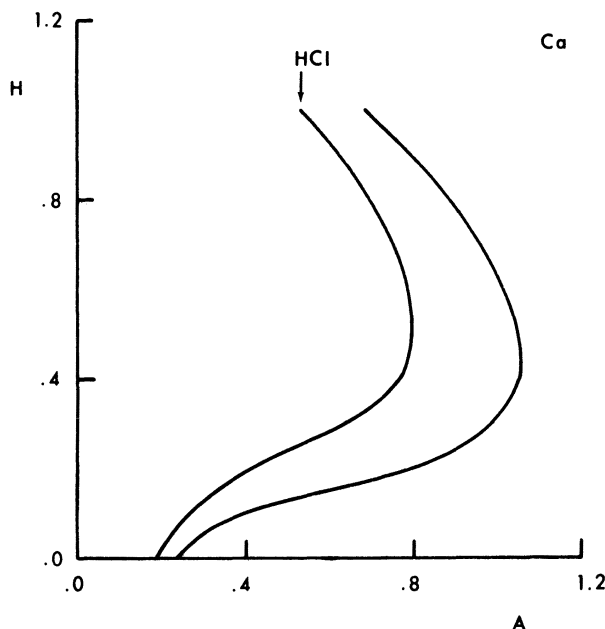


Fig. 7. Change of flame profile of calcium (presence of 0.5*N* HCl). The flame profiles were obtained with fuel-rich air-acetylene flame with laminar flow burner.

through the flame), (2) by the use of heated spray chambers, and (3) by the addition of organic solvents.

An indirect method which actually results in an apparent increase of sensitivity is preliminary concentration; e.g. by simple organic solvent extraction or by chelating organic solvent extraction. Actually, the preliminary concentration modifies (increases) the relative concentration of the analyte in the final sample and thus the signal obtained appears larger. The absolute analyte contents (in mass units) is theoretically unchanged by preliminary concentration.

Long horizontal tubes (long tube adapters) can be used with low absorption flames and long-lived elements. Multiple pass of the optical beam through the flame requires the same characteristics. Flames with high absorption at the analytical wavelength need an excessive compensation during zeroing operations. In turn, short-lived free atoms do not benefit in this way, as some of the beam passes through portions of the flame which are very poor in free atoms. In addition, multiple pass with flames which are highly emitting at the analytical wavelength can result in a noticeable increase of noise, even in ac system instruments.

The use of heated spray chambers had helped improve sensitivity for many elements. Burners equipped with such spray chambers bring to the

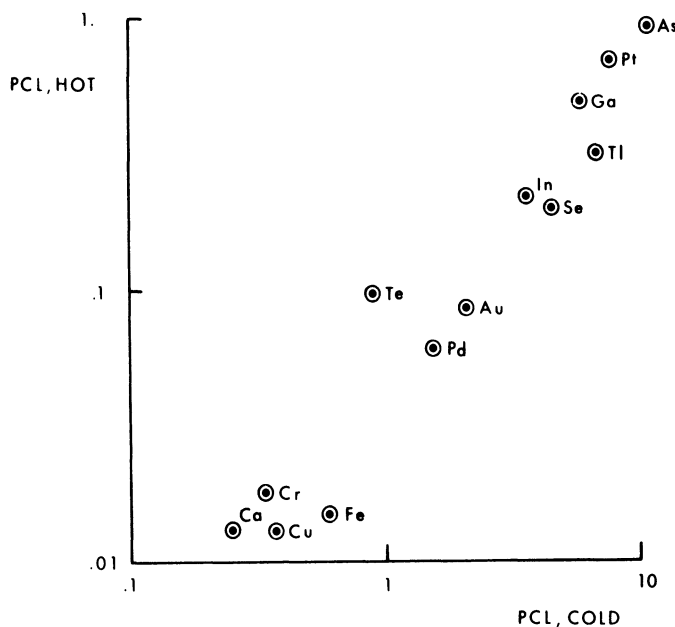


Fig. 8. Situation of different elements according to percentual sensitivity achieved in hot and cold operation (laminar flow burner, air-acetylene flame).

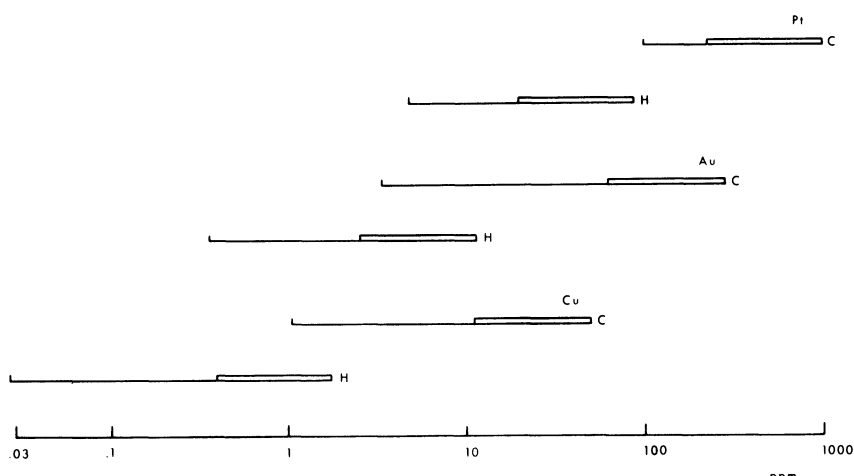


Fig. 9. Extension of the dynamic concentration range of several elements by working with a laminar flow burner in hot and cold operation. Solid zones correspond to concentrations extending from 30 times up to 135 times the percentual concentration limit (PCL). The tail of the range ends at 7 times the fluctuational concentration limit (FCL).

flame a concentrated aerosol in which most of the solvent has previously been eliminated. The efficiency is found higher if compared with that of burners using cold spray chambers.

The ratio of sensitivities obtained in hot and cold operation with the same burner differs from element to element. This particular behavior can easily be explained as a result of the differences between the evaporation and vaporization rates in the same flame of two completely different types of aerosol. Figure 8 illustrates in a double-sensitivity scale the response of some elements. The capability of hot and cold operation in a single burner offers the possibility of extending the dynamic concentration range by a considerable factor (see Fig. 9).

The use of organic solvents, which has been so much recommended in emission-flame photometry, has also had an impact in atomic absorption. In some cases this has just been a way to reach higher temperature. This was the case of tests done at the author's laboratory some time ago with turbulent flow burners for the determination of aluminum with oxygen-acetylene flame and 90% ethyl alcohol solutions. In other cases the organic solvent phase coming from extraction processes is fed into the burner directly. In this way some elements show a certain increase of sensitivity. It has been observed that in hot operation the temperature of the heated spray chamber can be critical. Figure 10 represents cases in which these phenomena can be observed for single and mixed organic solvents.

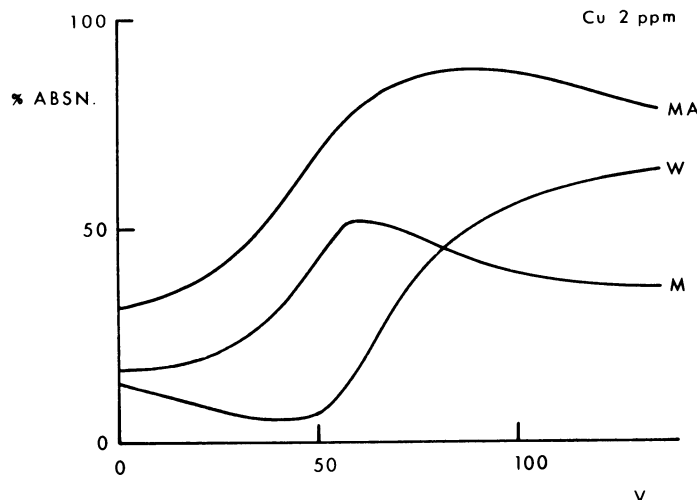


Fig. 10. Signal size changes of lead in different solutions (W, water; M, Methyl isobutyl ketone; and MA, methyl isobutyl ketone plus 25% ethyl alcohol). In abscissae, voltage settings of a VARIAC® used to change the temperature of the spray chamber during the hot operation in a laminar flow burner.

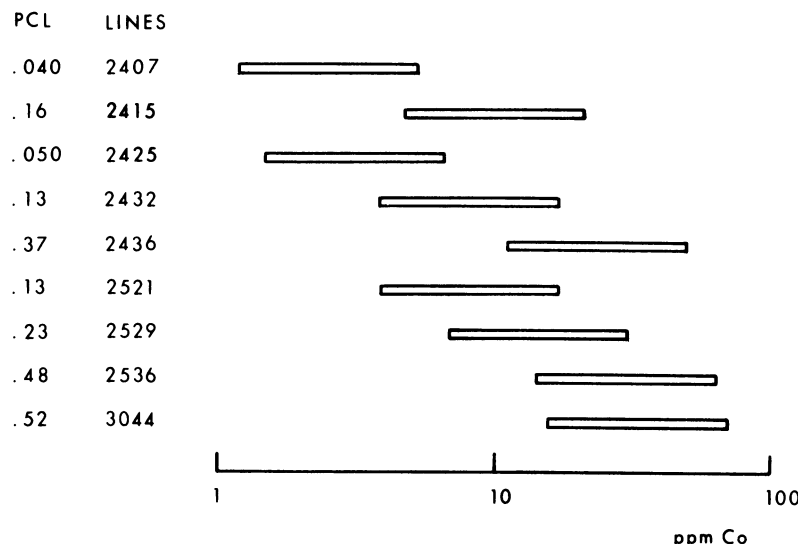


Fig. 11. Coverage of the concentration range by different cobalt lines. Zones extend from $30 \times$ PCL up to $135 \times$ PCL (see caption of Fig. 9), in laminar flow burner, air-acetylene flame.

High-Sensitivity Elements. High-sensitivity elements can be handled by simple dilution down to the appropriate concentration level. In fact, undiluted solutions of high-sensitivity elements produce absorptions which are too high, higher than 75–80%, signals which are situated far away from the recommended interval for normal reading.² It can happen that high dilutions are not desirable, e.g., if it is desired to determine several analytes in a single solution without the trouble of multiple dilutions. In these circumstances lines of lower sensitivity can be used. Figure 11 shows the concentration range covered by several analytical lines.

Critical Flame Conditions. Flame conditions given by pressure or flow settings of combustion gases are in general important factors in atomic-absorption determinations. They determine signal size, and, as a consequence, sensitivity. But flame conditions are extremely critical for some analytes. Slight changes of fuel pressure, e.g., drastically change the recorded signals (see Fig. 12). Optimum settings should be carefully checked each time the instrument is reset for a new session.

Limitations Depending on Sample Composition

Limitations in the applicability of atomic-absorption determinations due to the presence of disturbing concomitant components have been and are the

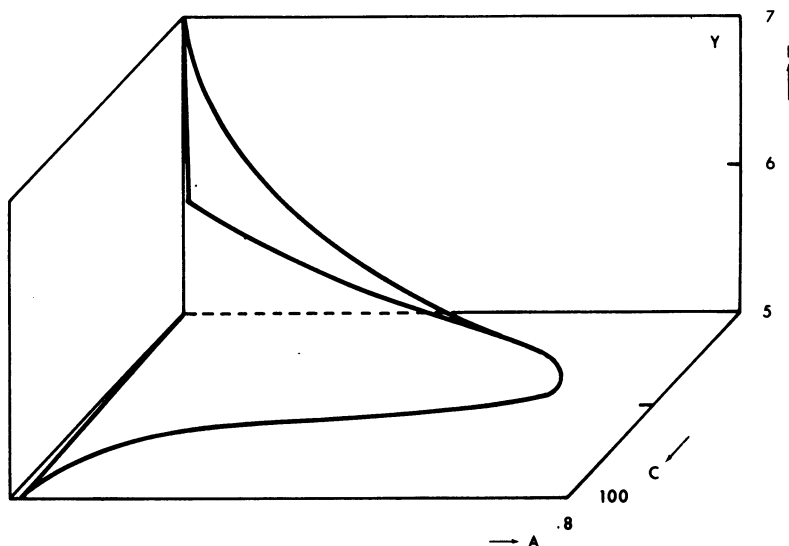


Fig. 12. Three-dimensional fuel-pressure profile of yttrium (laminar flow burner, nitrous oxide-acetylene flame).

subject of many contributions in the atomic-absorption field. Authors have presented the problem from the three main points of view: (1) effects found on the analyte by the presence of such components when experimental numerical data are collected, (2) attempts to interpret the mechanism involved in such processes, and (3) procedures proposed to overcome the disturbing effects by proper choice of instruments or by chemical means.

Instrument proposals have mainly been confined to the use of hotter flames, which can decompose temperature-resistant compounds, as mentioned in preceding paragraphs.

A variety of chemical methods have been proposed. All of them involve some specific preparation of samples and/or standard. Essentially, they can be grouped into two main categories: procedures with separation and procedures without separation of the constituents.

Procedures Involving Separation of Constituents. These procedures are used when other simpler procedures fail. Separation is always time consuming, expensive, and subject to losses and contaminations. Separation can be considered in two ways: (1) separation of one or several macrocomponents from the analyte or analytes, and (2) separation of the analyte or analytes from other components. Specific (single separations) and selective (group separations) have been utilized. In the author's laboratory determinations of lead and iron in biological materials, and gold in minerals were carried out after separation of analytes.

Organic solvent extraction is preferred whenever it is possible. In order to know up to which degree the separations are analytically valid, it is recommended that a series of recovery tests be done. If recovery is noticeably lower than 100%, standards should be extracted using the same conditions as the samples.

Procedures Involving No Separations. These procedures tend to involve modification of the chemical composition of samples and/or standards. A new chemical system is presented to the flame. This system acts with different behavior than the original chemical system. Disturbances can be compensated, diminished, or practically avoided. Results, then, will be more reliable and representative of actual analyte concentrations. These procedures are simple, as they only involve additions to the samples, to the standards, or both, during the preparation steps. Modified solutions are then measured in the instrument in the usual way. Buffering techniques (massive additions) can be considered in this category.

The simplest procedure consists of *compensating the standards* with similar concentrations of the interfering components (moderate additions). The use of compensated standards is a way of modifying the calibration curve to obtain a practically perfect match of samples and standards. Some examples are cited below.

1. *Acid Solutions.* Systems containing HCl and systems containing acid have been studied by the compensation of standards.⁷ In this way standards show the same signal-reduction effects as samples and these can be compared with the series of synthetically-prepared standards.

2. *Alcoholic Solutions.* Solutions containing ethyl alcohol have been measured by comparison with standards containing the same concentration of alcohol.⁸ In this case both samples and standards present similar viscosity properties and the feeding rate is kept similar.

3. *High-Iron Systems.* Several analytes have been determined by compensating the standards with iron in the form of iron chloride.⁹ Iron and chloride ions modify the atom-liberation equilibrium in the same extent in samples and standards. Even in those cases in which there is no modification of sensitivity it is convenient to compensate the standards to match standards and samples in chemical composition.

4. *High-Sodium Systems.* These systems have been carefully studied,¹⁰ and it has been found that a series of analytes can easily be determined by the compensation of standards with NaCl. As in the preceding case, the compensation of standards corrects the shift of atom-liberation equilibria due to the presence of high concentrations of sodium and chloride ions.

With this type of procedure a decrease in signal should be expected when the concentration of the interfering component reaches some given value. It is of

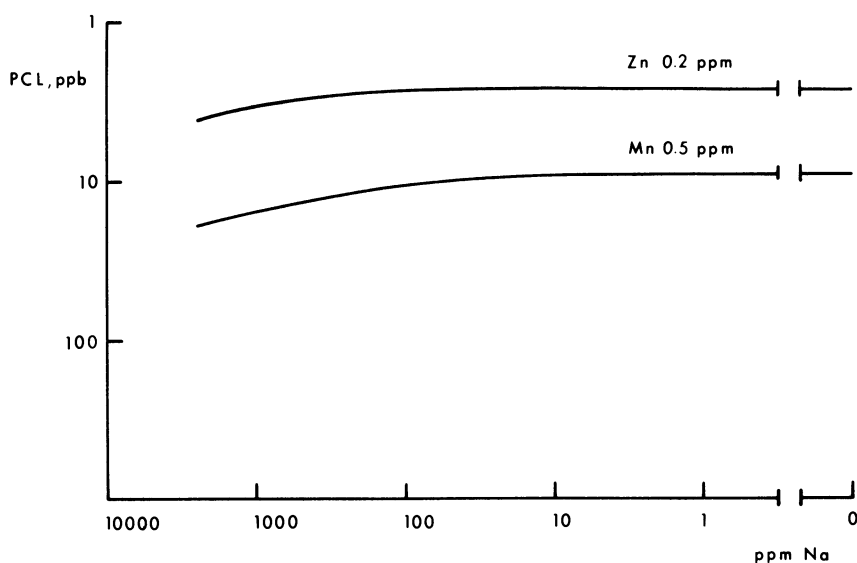


Fig. 13. Interference diagrams for zinc and manganese, in laminar flow burner, air-acetylene flame, in the presence of sodium (as NaCl).

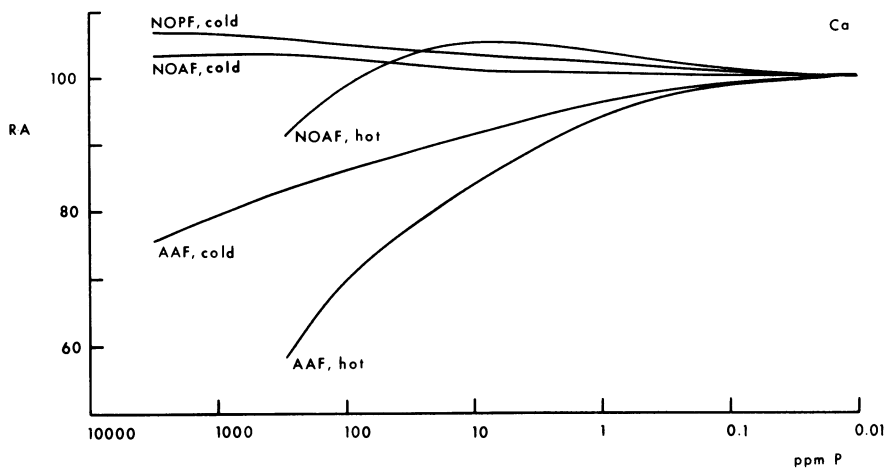


Fig. 14. Interference diagrams for calcium, in laminar flow burner, in different flames, in the presence of phosphorus (as phosphate).

much interest to study in advance the analytical response of each analyte in these conditions at increasing concentrations of the interfering component. This study leads to the preparation of interference diagrams where the *limiting interference ratio* [(concentration of the interfering component)/(concentration of the analyte)] can be established at which the sensitivity begins to decrease as a consequence of interference effects (see Fig. 13).

Another simple procedure consists in the application of the *addition method*. This truly is a method of the compensation of standards, as known concentrations of the analyte are exposed to the same type of chemical system in which the analyte is included. Advantages and limitations of the addition method have been discussed elsewhere.¹¹ Similar policy is followed in the *dilution method*.² The dilution method is a modification of the conventional addition method.

Finally, the use of *releasers* and *protectors* constitutes a third way of overcoming interference effects. Differences between releasing and protecting action are well known.² Releasers or protectors are added to both samples and standards.

In the author's laboratory special attention has been devoted to the determination of calcium in severely-interfered systems.¹² The use of lanthanum as releasing agent presents advantages over the strontium as releaser and EDTA as protector. The use of lanthanum in combination with the utilization of high-temperature flames has allowed good sensitivity to be obtained at low calcium concentration. Preliminary studies of these systems have given the opportunity of preparing complete sets of interference diagrams. Some examples are presented in Fig. 14.

CONCLUSIONS

In spite of the fact that at present it is impossible to consider atomic-absorption flame photometry as a problem-free instrumental method, the use of appropriate equipment and parameters, of sufficiently hot flames, and of carefully chosen procedures of sample preparation and instrument calibration allows rapid and reliable determination of a great number of analytes in a variety of original samples with enough sensitivity, accuracy, and precision. There are some elements which still present low sensitivity in simple analytical systems and there are still some complicated analytical systems which require preliminary separation and/or concentration of the analytes. However, the most severe interference problems, which so often are encountered in practical applications, seem to be soluble with a minimum of sample preparation work. As in other instrument methods, a great deal of time is still required for sample

feeding and data processing in routine applications in determinations of one or several analytes in a great number of samples. This time can be cut down by means of the new sample-feeding devices and by computer data reduction. Thus rapidity in achieving final results is still a standing characteristic in atomic-absorption applications.

ACKNOWLEDGMENT

The author is very grateful to Dr. W. F. Ulrich for reading the original manuscript and for providing suggestions, and to Mr. M. E. Roth for his help in some parts of the experimental work.

REFERENCES

1. J. Ramírez-Muñoz, J. L. Malakoff, and C. P. Aime, *Anal. Chim. Acta* **36**, 328 (1966).
2. J. Ramírez-Muñoz, *Atomic-Absorption Spectroscopy*, Elsevier Publishing Company, Amsterdam (1968).
3. J. Ramírez-Muñoz, *Rev. Soc. Quim. Mex.* **12**, 26A (1968).
4. J. Ramírez-Muñoz, R. O. Brace, R. W. Claus, and N. Shifrin, *Flame Notes (Beckman)* **2**, 30 (1967).
5. J. Ramírez-Muñoz, *Rev. Univ. Ind. Santander* **9**, 57 (1967).
6. R. J. Manning, *Flame Notes (Beckman)* **2**, 75 (1967).
7. J. Ramírez-Muñoz, M. E. Roth, and M. Östring, *Flame Notes (Beckman)* **1**, 93 (1966).
8. J. Ramírez-Muñoz and M. E. Roth, *Flame Notes (Beckman)* **2**, 81 (1967).
9. J. Ramírez-Muñoz and M. E. Roth, *Flame Notes (Beckman)* **3**, 2 (1968); **3**, 17 (1968); **4**, 1 (1969).
10. J. Ramírez-Muñoz, *XIII Colloquium Spectroscopicum Internationale Ottawa*, Adam Hilger Ltd., London (1968), p. 288.
11. J. Ramírez-Muñoz, *Inform. Quim. Anal.* **19**, 154, 183 (1965).
12. W. F. Ulrich and J. Ramírez-Muñoz, paper presented to the 1968 ASTM Meeting, June 23–27, 1968, San Francisco, Calif.

A New Look at Calcium Flame Interferences

R. E. Popham[†] and W. G. Schrenk

*Department of Chemistry
Agricultural Experiment Station
Kansas State University, Manhattan, Kansas*

A detailed study of the effects of PO_4^{3-} , SO_4^{2-} , AlCl_3 , and $\text{Al}(\text{NO}_3)_3$ on the flame-spectroscopic behavior of Ca led to some clarification concerning the origin and nature of these common interferences. By utilizing atomic absorption and emission as well as molecular and ion-emission measurements, the relative concentrations of the following Ca species in the flame could be studied: Ca^* , Ca° , Ca^{+*} , and $\text{CaOH}-\text{CaO}^*$. Data indicated that the depressive effects of the interfering substances were similar on each Ca species studied. Thus the mechanism by which these interferences originate cannot be due to shifts in the equilibria of the reactions of CaCl_2 in the flame. Results also showed that the Al interference was not due to a gas phase reaction between CaO and Al_2O_3 to form CaAl_2O_4 or some similar Ca aluminate. The AlCl_3 interference on Ca was eliminated in the nitrous oxide flame, but that due to $\text{Al}(\text{NO}_3)_3$ was not. Therefore in the nitrous oxide flame it was possible to determine effects of Ca and Al excitation as well as the effects of Al on Ca excitation. The association of Ca ions with PO_4^{3-} and SO_4^{2-} in solutions to form probably CaSO_4 and $\text{Ca}_3(\text{PO}_4)_2$ would be consistent with our results. The effects of Al salts would appear to be due to the occlusion of CaCl_2 in matrices of AlCl_3 and $\text{Al}(\text{NO}_3)_3$.

*Contribution No. 644, Department of Chemistry, Kansas State University.

[†]Work performed in partial fulfillment of the requirements for the Ph.D. degree in chemistry. Present address, Department of Chemistry, Southeast Missouri State College, Cape Girardeau, Mo.

INTRODUCTION

Despite a volume of papers concerning a multitude of interferences in both flame-emission and absorption spectroscopy, much about their actual causes remains unknown. The effects of PO_4^{-3} , SO_4^{-2} , and Al on the alkaline earth metals, Ca in particular, have been studied extensively. Three mechanisms by which those substances may interfere with Ca are suggested in the literature. Data supporting the mechanisms, however, are often lacking or inconclusive.

One proposed mechanism involves formation of compounds between the interfering substances and Ca. The newly formed compounds would be less volatile and more difficult to dissociate than the original Ca analyte at temperatures of commonly used flames. Compounds previously suggested include $\text{Ca}_2\text{P}_2\text{O}_7$, $\text{Ca}_3(\text{PO}_4)_2$, Ca_3P_2 , CaSO_4 , $\text{Ca}_x\text{P}_y\text{O}_z$, $\text{Ca}_x\text{S}_y\text{O}_z$, CaAl_2O_4 , $\text{Ca}_3\text{Al}_2\text{O}_6$, and $(\text{CaO})_x(\text{Al}_2\text{O}_3)_y$.¹⁻⁹

A second proposed mechanism involves a matrix effect in which the original analyte, CaCl_2 , is occluded or trapped in a matrix of the interfering substance upon evaporation of the solvent from the droplets entering the flame. In this case CaCl_2 might be enclosed in a solid matrix of AlCl_3 , $\text{Al}(\text{NO}_3)_3$, Al_2O_3 , Al_xO_y , or some $\text{P}_x\text{--O}_y$, or $\text{S}_x\text{--O}_y$ matrix.^{10,11} Therefore the flame must have sufficient energy to break up the matrix and dissociate the CaCl_2 for one to observe Ca in the system.

The third proposed mechanism involves an effect on the equilibria of the various reactions of CaCl_2 occurring in the flame. In this case the interfering substance is thought to promote reactions of CaCl_2 that remove ground-state atoms from the flame.^{12,13}

A related problem is to ascertain the origin of the interferences. The interferences might originate in three places: in solution before aspiration into the flame, in the first stages of atomization during the conversion of $\text{CaCl}_2(l)$ to $\text{CaCl}_2(g)$, or in a gas-phase reaction between the products that result from atomization of interfering substances with Ca in the flame.

INSTRUMENTATION

A Jarrell-Ash model 82-360 Ebert-mounted 0.5m grating monochromator with Jarrell-Ash electronics, including a 90-cps mechanical chopper, ac amplifier, Sargent recorder (Model S-72150), and a 1P28 photomultiplier detector were used. Converting the instrument from an atomic-absorption unit to a flame-emission photometer involved removing the spectral source and repositioning the mechanical chopper in front of the entrance slit to the monochromator.

The sampling system was a Jarrell-Ash Tri-Flame premix laminar flow burner, No. 82-368. Fuel and oxidant flow rates were controlled by Jarrell-Ash regulators and monitored with R. G. I. flow meters, type number F-1300. The spectral source was a Westinghouse Ba, Ca, and Sr multielement lamp, Model WL 23034.

Stock solutions of Ca were made by dissolving analytical reagent grade CaCO_3 in a minimum amount of HCl unless otherwise stated. Solutions of PO_4^{3-} , SO_4^{2-} , and Al were made from reagent grade $(\text{NH}_4)_3\text{PO}_4$, $(\text{NH}_4)_2\text{SO}_4$, anhydrous AlCl_3 , and $\text{Al}(\text{NO}_3)_3 \cdot 9\text{H}_2\text{O}$.

RESULTS AND DISCUSSION

Several salts of Ca were prepared to determine the effect of the anion on the efficiency of production of Ca° in the flame. Reagent grade CaCO_3 was dissolved in minimum HCl, HI, HBr, H_2SO_4 , $\text{HC}_2\text{H}_3\text{O}_2$, HNO_3 , H_3PO_4 , or HClO_4 to obtain solutions containing 1000 ppm Ca. The solutions were diluted to a concentration of 20 ppm Ca and studied by both atomic emission and absorption under identical conditions at 4227 Å in premixed air-acetylene and nitrous oxide-acetylene flames. The results of the atomic-absorption measurements at four experimental conditions are shown in Table I. The efficiency of the production of ground state Ca atoms depended on the salts aspirated into the flame and on experimental conditions. The magnitude of the absorption depressions substantially decreased when measurements were made higher in the flame and increased at the base of the flame when the flame was converted from fuel-lean to fuel-rich. These two trends would be expected if the absorption depression depended on the vaporization and dissociation of a compound in the flame.

Since no significant absorption depression occurred in the nitrous oxide-acetylene flame for any of the salts studied, physical differences in the solutions, such as viscosity or aspiration rate, cannot explain the results obtained in the air-acetylene flame. The solutions were also studied by atomic emission at 4227 Å and by molecular emission of CaO at 5540 Å under the same conditions used for the atomic-absorption measurements. The magnitude and behavior of these interferences were nearly identical with those obtained by atomic absorption.

Pungor and Konkoly-Thege^{1,3} have suggested that anion interferences with Ca are due to the kinetically-controlled conversion of the Ca analyte to CaO in the flame. If that were so, salts most severely depressing Ca° in the air-acetylene flame should produce the most intense CaO emission. However, that condition was not observed.

TABLE I
**Absorption of 20 ppm Ca Aspirated as Several Different
 Salts into the Flame**

Salt	Depression of absorption (%)		
	C ₂ H ₂ / air, fuel-lean*	C ₂ H ₂ / air, fuel-rich†	C ₂ H ₂ / N ₂ O, fuel-lean‡
<i>Measurements made immediately above burner head in flame</i>			
CaCl ₂	—	1.2	—
Ca(ClO ₄) ₂	—	—	—
CaBr ₂	1.0	—	1.3
CaI ₂	9.2	20.7	1.8
Ca(C ₂ H ₃ O ₂) ₂	11.3	26.5	0.9
Ca(NO ₃) ₂	17.7	36.4	—
Ca ₃ (PO ₄) ₂	28.7	43.7	0.9
CaSO ₄	29.4	45.6	—
<i>Measurements made 1.5 cm above burner head in flame</i>			
CaCl ₂	7.3	4.0	—
Ca(ClO ₄) ₂	4.8	2.8	—
CaBr ₂	4.8	—	—
CaI ₂	—	2.9	—
Ca(C ₂ H ₃ O ₂) ₂	8.0	4.4	—
Ca(NO ₃) ₂	1.6	2.2	—
Ca ₃ (PO ₄) ₂	11.2	9.3	—
CaSO ₄	16.1	10.2	—

*C₂H₂ flow at 1.90 liters/min; air flow at 7.70 liters/min

†C₂H₂ flow at 2.35 liters/min; air flow at 7.70 liters/min

‡C₂H₂ flow at 4.60 liters/min; N₂O flow at 7.10 liters/min

The observed signal depressions must therefore be due to the chemical properties of the Ca salts. An attempt to relate the magnitude of the signal depression to the crystalline melting points or free energies of formation of the salts did not yield consistent relationships.

Utilizing atomic absorption, atomic emission, ion emission, and molecular emission, it was possible to study the relative concentrations of those Ca species in the flame shown in Fig. 1. Such a study should confirm if the interferences with Ca were due to a shift in any equilibrium reaction in the flame. If the effect of Al on Ca were due to the formation of CaAl₂O₄, or some similar Ca aluminate, by the gas-phase reaction of CaO with Al₂O₃ in the flame, as suggested by Rubeska and Moldan⁹ and Halls and Townshend⁷ comparing the effect of Al on CaO with the effect of Al on the other Ca species should confirm it.

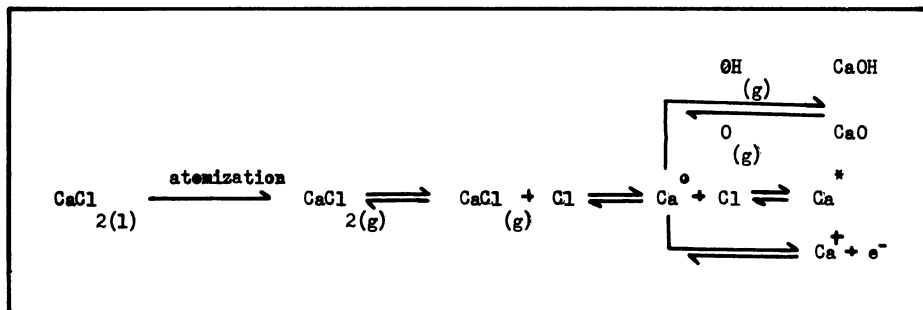


Fig. 1. Flame dissociation of CaCl_2 . Ca^+ : singly-ionized atom, 3968 Å. Ca° : ground-state Ca atom, 4227 Å. Ca^* : excited-state Ca atom, 4227 Å. CaCl : excited Ca molecule, 6216 Å. CaO/CaOH : excited Ca molecule, 5540 Å.

Figures 2, 3, and 4 illustrate the effects of increasing amounts of PO_4^{3-} , SO_4^{2-} , and Al, respectively, on each Ca species studied under identical conditions in a premixed air-acetylene flame. Results indicate that all Ca species were affected equally by the interfering substances. This suggests that the equilibrium reactions of Ca in the flame were not significantly shifted in a direction to cause the removal of ground-state Ca atoms. Since the CaO band emission was not depressed more than that of other Ca species, it is doubtful that the mechanism of the Al interference involved the gas-phase reaction of CaO with Al_2O_3 in the flame.

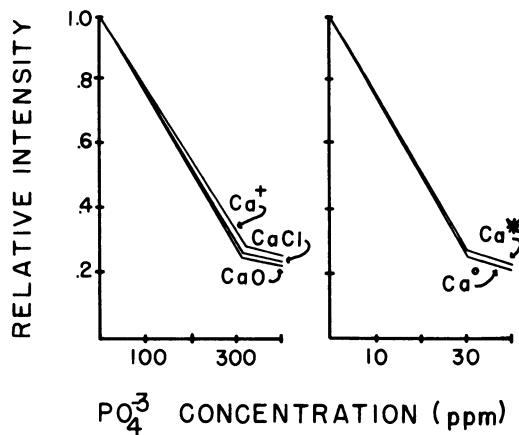


Fig. 2. Effect of increasing PO_4^{3-} concentration on relative signal intensities of various Ca species in an air-acetylene flame.

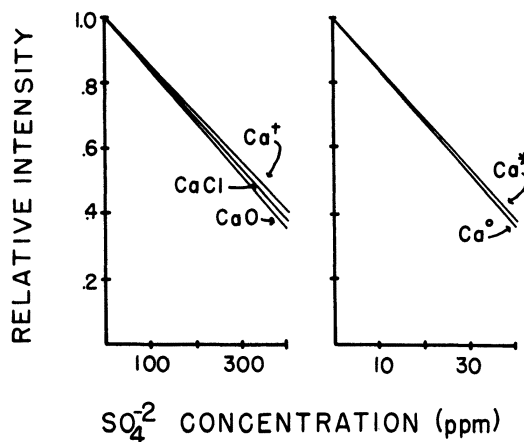


Fig. 3. Effect of increasing SO_4^{2-} concentration on relative signal intensities of various Ca species in an air-acetylene flame.

Since the Ca species were affected equally by the interfering substances, it would appear that the origin of the interferences must lie somewhere between the conversion of $\text{CaCl}_2(l)$ to $\text{CaCl}_2(g)$ in the flame, or they must originate by some interaction of ions in solution before aspiration into the flame. Elimination of Al and PO_4^{3-} interferences on Ca in the dual-atomizer experi-

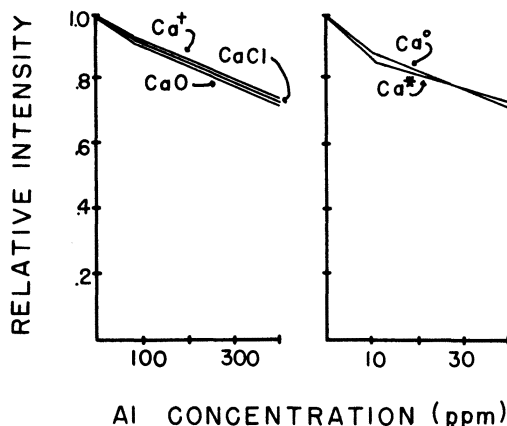


Fig. 4. Effect of increasing Al (AlCl_3) concentration on relative signal intensities of various Ca species in an air-acetylene flame.

ments^{10,14} in which separate atomizers were used to aspirate CaCl_2 solutions and solutions of Al or PO_4^{3-} into the same flame suggest that intimate contact of CaCl_2 with the interfering substances in the droplets aspirated into the flame was a necessary criterion for interference to occur.

Figure 5 shows effects of increasing amounts of Al [as AlCl_3 and $\text{Al}(\text{NO}_3)_3$,] NO_3^{-1} , and Cl^{-1} (as NH_4NO_3 and NH_4Cl , respectively) on the absorption of 20 ppm Ca in a premixed air-acetylene flame under different

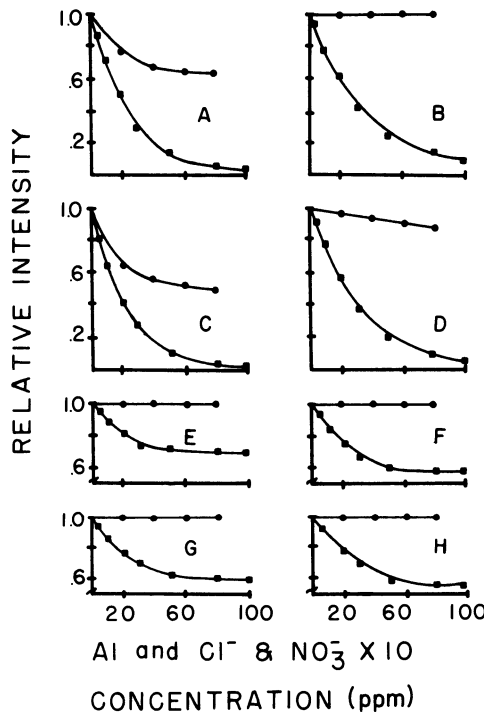


Fig. 5. Effect of increasing concentrations of Al [as AlCl_3 and $\text{Al}(\text{NO}_3)_3$], Cl^{-1} , and NO_3^{-1} on the absorption of Ca. (A), (B), (C), and (D) show the effect of Al added as $\text{Al}(\text{NO}_3)_3$ and the effect of NO_3^{-1} added as NH_4NO_3 on the absorption of 20 ppm Ca. (E), (F), (G), and (H) show the effect of Al added as AlCl_3 and the effect of Cl^{-1} added as NH_4Cl on the absorption of 20 ppm Ca. (A) and (E) Results in fuel-lean flame immediately above the burner head. (B) and (G) Results in fuel-lean flame at 1.5 cm above the burner head. (C) and (F) Results in fuel-rich flame immediately above the burner head. (D) and (H) Results in fuel-rich flame at 1.5 cm above the burner head. ● Results for solutions containing Cl^{-1} or NO_3^{-1} ■ Results for solutions containing Al as AlCl_3 or $\text{Al}(\text{NO}_3)_3$.

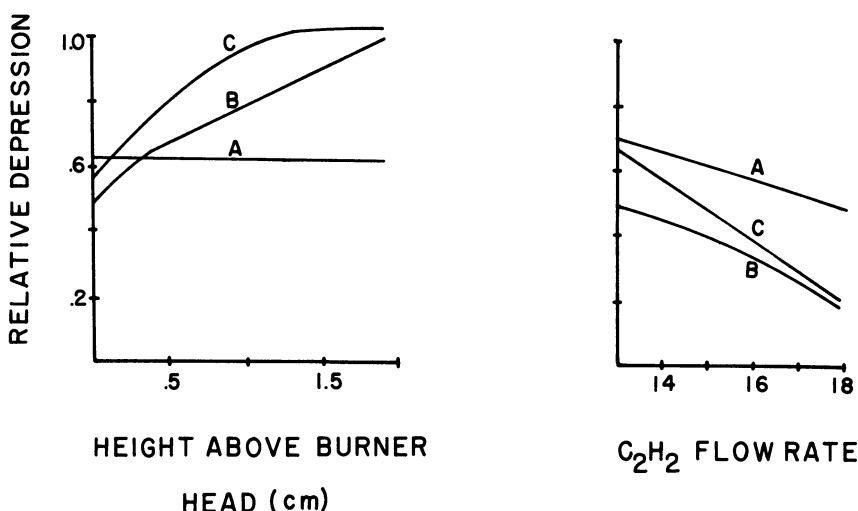


Fig. 6. Effects of varying fuel flow rate and the burner height on absorption of Ca atoms, 4227 Å, in the presence of Al, SO_4^{-2} , and PO_4^{-3} . (A) Results for solution of Ca plus Al. (B) Results for solution of Ca plus PO_4^{-3} . (C) Results for solution of Ca plus SO_4^{-2} . Note that units of fuel flow rate are arbitrary, and correspond to direct flow meter readings.

experimental conditions. Although NO_3^{-1} ions interfered with Ca immediately above the burner head in both fuel-rich and fuel-lean flames, NO_3^{-1} did not contribute significantly to the observed $\text{Al}(\text{NO}_3)_3$ over that of AlCl_3 . At 1.5 cm above the burner head in the flame the NO_3^{-1} interference was almost eliminated, while that of $\text{Al}(\text{NO}_3)_3$ remained the same as observed immediately above the burner head. Adding Cl^{-1} ion had no effect on Ca under any condition studied.

In contrast to the anion interferences — NO_3^{-1} , PO_4^{-3} , and SO_4^{-2} — effects of both Al salts (see Fig. 5) on Ca were relatively independent of flame conditions and position of measurement in the flame. The effects of the position at which measurements were made in the flame and the effects of fuel-flow-rate changes on the magnitude of these interferences are illustrated in Fig. 6.

Figure 7 shows the effect of $\text{Al}(\text{NO}_3)_3$ on the emission signal produced by Ca in the nitrous oxide flame. Interference effects of AlCl_3 and NO_3^{-1} observed in the cooler air-acetylene flame were eliminated. Depressive effects of $\text{Al}(\text{NO}_3)_3$ were substantially reduced and almost eliminated in a fuel-rich flame at 1.5 cm above the burner head. In contrast to results obtained in the

air-acetylene flame, experimental conditions, fuel-to-oxidant ratio, and positions of measurement in the flame affected the magnitude of the interference caused by $\text{Al}(\text{NO}_3)_3$.

The occurrence of significant interference of $\text{Al}(\text{NO}_3)_3$ on Ca in the nitrous oxide flame suggested the possibility of observing the emission of both Ca and Al in the presence of the other. In cooler flames emission of Al was not detectable, but in the nitrous oxide flame Al could be determined by measuring the emission of the 3944 Å resonance line. Since relatively high concentrations of Al were necessary to produce useful Al emission intensities, the concentration of Ca was increased five times over concentrations used in the previous studies. The higher Ca concentration prevented the use of the Ca resonance line, 4227 Å, due to self-absorption. Therefore Ca was measured using the CaO band head emission at 5540 Å.

Figure 8 (A) illustrates the relative emission intensity of 100 ppm Al when 50–500 ppm Ca was added, (B) illustrates the relative emission intensity of 100 ppm Ca when 50–500 ppm Al as $\text{Al}(\text{NO}_3)_3$ was added, (C) illustrates the relative depression of Ca emission intensities when 100 ppm Al was added to different concentrations of Ca, and (D) illustrates the relative depression of Al emission intensities when 100 ppm Ca was added to different concentrations

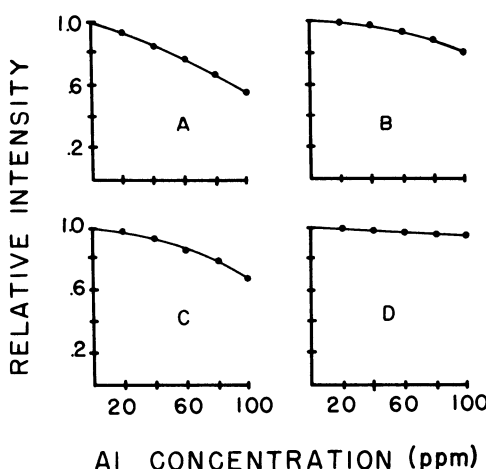


Fig. 7. Effects of $\text{Al}(\text{NO}_3)_3$ on the emission of 20 ppm Ca in a nitrous oxide-acetylene flame. (A) Results in fuel-lean flame immediately above burner head. (B) Results in fuel-lean flame at 1.5 cm above burner head. (C) Results in fuel-rich flame immediately above burner head. (D) Results in fuel-rich flame at 1.5 cm above burner head.

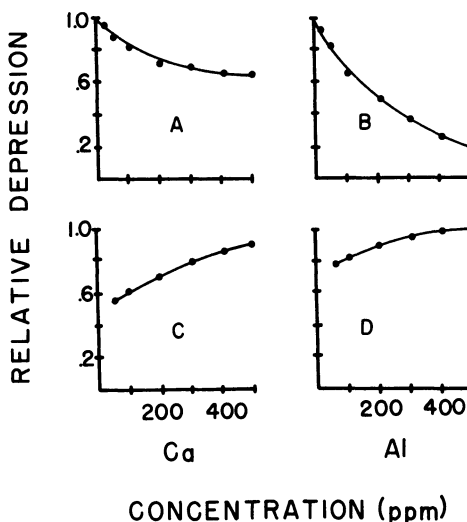


Fig. 8. Mutual interference effects of the Ca and $\text{Al}(\text{NO}_3)_3$ system in the nitrous oxide-acetylene flame. (A) Relative emission intensity of 100 ppm Al in the presence of 50-500 ppm Ca. (B) Relative emission intensity of 100 ppm Ca in the presence of 50-500 ppm Al. (C) Relative depression of emission intensity of 50-500 ppm Ca in presence of 100 ppm Al. (D) Relative depression of emission intensity of 50-500 ppm Al in the presence of 100 ppm Ca.

of Al. The results indicate that the Ca and Al system produced a mutual interference effect, the magnitude of which was more severe on Ca than on Al. The distinct differences in Figs. 8 (A) and (B) do not lend themselves to the compound-formation theory as a basis of Al interference on Ca. If compound formation were occurring, a fixed ratio of Ca Al atoms should be removed from the flame, and the shapes of the two curves should be somewhat similar. On adding Ca to 100 ppm Al, a plateau on the curve was reached at 200 ppm Ca. Adding more Ca had no effect on the Al emission. However, no such plateau was observed when Al was added to 100 ppm Ca.

It has been suggested^{7,9} that the reason for the greater interference of $\text{Al}(\text{NO}_3)_3$ than AlCl_3 on Ca is due to $\text{Al}(\text{NO}_3)_3$ forming Al_2O_3 or Al_xO_y in the flame more readily than does AlCl_3 . If that were so, detecting Al as AlCl_3 by atomic emission should be more sensitive than detecting Al as $\text{Al}(\text{NO}_3)_3$. However, under identical conditions 100 ppm Al in the form of both salts produced approximately the same emission intensities.

CONCLUSIONS

Results of these studies indicated that the interferences of AlCl_3 , $\text{Al}(\text{NO}_3)_3$, PO_4^{3-} , and SO_4^{2-} could not be attributed to effects on the equilibria of the flame reactions of CaCl_2 . Since the interfering substances affected equally all Ca species studied in the flame, origin of the interferences seems to have occurred in solution or during the first stages of atomization. The gas-phase reaction of CaO with Al_2O_3 to form CaAl_2O_4 cannot, on the basis of our data, explain the Al interference on Ca. The NO_3^{-1} and Cl^{-1} ions did not contribute to effects of AlCl_3 and $\text{Al}(\text{NO}_3)_3$ on Ca. It is difficult to conceive of compound formation or ion association of CaCl_2 with AlCl_3 or $\text{Al}(\text{NO}_3)_3$ in the solution. Therefore the origin of the Al interference appears to be somewhere in the first stages of atomization, the conversion of $\text{CaCl}_2(l)$ to $\text{CaCl}_2(g)$ in the flame. Data were consistent if one considers the effects of Al on Ca to be due to a matrix effect whereby CaCl_2 is occluded in a solid matrix of AlCl_3 or $\text{Al}(\text{NO}_3)_3$ on evaporation of the solvent from the droplets in the flame.

Formation of a compound by association of Ca ions with PO_4^{3-} and SO_4^{2-} in the solutions seems to explain the anion interferences logically. That the magnitude of the interferences depends strongly on such experimental conditions as position of measurement in the flame and fuel-to-oxidant ratio supports the compound-formation mechanism. Upon adding H_3PO_4 and H_2SO_4 to CaCO_3 , solutions of $\text{Ca}_3(\text{PO}_4)_2$ and CaSO_4 were probably being aspirated into the flame. The magnitude and behavior of the Ca emission and absorption of these solutions were identical to the results obtained when equivalent amounts of PO_4^{3-} and SO_4^{2-} [as ammonium salts] were added to solutions of CaCl_2 .

REFERENCES

1. C. A. Baker and F. W. J. Garton, Atomic Energy Research Establishment (Great Britain) Rept. AERE-R-3490(1961).
2. J. H. Gibson, W. E. L. Grossman, and W. D. Cooke, *Anal. Chem.* **35**, 266 (1963).
3. L. Leyton, *Analyst* **79**, 497 (1954).
4. B. V. L'vov, *Spectrochim. Acta* **17**, 761 (1961).
5. A. Strasheim and J. P. Nell, *J. S. African Chem. Inst.* **7**, 78 (1954).
6. J. Yofe and J. R. Finkelstein, *Anal. Chim. Acta* **19**, 166 (1958).
7. P. J. Halls and A. Townsend, *Anal. Chim. Acta* **36**, 278 (1966).
8. M. Margoshes and B. L. Valee, *Anal. Chem.* **28**, 180 (19556).
9. I. Rubeska and B. Moldan, *Anal. Chim. Acta* **37**, 421 (1967).
10. C. Th. J. Alkemade, *Anal. Chem.* **38**, 1252 (1966).
11. C. Th. J. Alkemade and M. H. Voorhuis, *Z. Anal. Chem.* **163**, 91 (1958).

12. D. J. David, *Analyst* **84**, 536 (1959).
13. E. Pungor and I. Konkoly-Thege, *Mikrochim. Acta*, **1959**, 712.
14. W. Schunkneckt and H. Schinkel, *Z. Anal. Chem.* **162**, 266 (1958).

Some Experimental Considerations in Atomic Absorption

F. I. Grunder and E. A. Boettner

*Department of Industrial Health
The University of Michigan
Ann Arbor, Michigan*

A study of the various parameters that must be optimized for the best atomic-absorption analysis has been made. Two of the instrument variables we have investigated are the burner and hollow-cathode lamp. A comparison of the total consumption and laminar flow burners for Fe, Mg, and Pb is given, evaluating sensitivity, analytical precision, and possible interferences. A study of hollow-cathode lamps is also presented in which single and multielement types are operated both with ac current and with dc current in conjunction with a chopper. The effects of various lamps and their manner of operation on sensitivity and precision are given for the analysis of aqueous solutions for Fe, Mg, Pb, and Ca. For Fe, e.g., a change from 0.065 to 0.305 absorbance units was obtained for a 10 ppm aqueous standard, depending on the choice of lamp and whether it was used with ac or dc. Advantages and disadvantages of the various possibilities are discussed.

INTRODUCTION

Atomic absorption has become a commonplace analytical technique for the determination of metals in a wide variety of samples.^{1,2} Our interest in atomic absorption as an analytical tool covers a range of applications, from water solutions^{3,4} to biological specimens and air pollutants. This interest includes a number of elements, and the instrument variables and the possibil-

*This investigation was supported in part by USPHS Research Grant No. 00494 from The National Center for Urban and Industrial Health.

ity of chemical interferences must be thoroughly examined for these elements. A few elements (Fe, Mg, Pb, and Ca) which we have studied in detail are discussed below. In all cases aqueous standards were used, as our immediate interest was in the instrument variables rather than in the chemical interferences which have been studied in some detail previously.⁵⁻⁷

An investigation of some instrument factors involved included a study of several types of burners presently available and an evaluation of various hollow-cathode lamps and the methods used to operate them. In all cases the information obtained is presented from the point of view of its effect on precision and sensitivity. A discussion of the use of the analytical curve for an evaluation of the analytical precision and sensitivity of burners and lamps is also included.

PROCEDURE

The Jarrell-Ash triflame burner was available for comparison of the total consumption and laminar flow burners. This burner was used as a single-flame total-consumption burner and as a 10-cm slot laminar flow burner. When used as a total consumption burner with the Jarrell-Ash model 32-360 instrument the multipass optics and an air-hydrogen flame were used. When used as a laminar flow burner a single optical pass was made through an air-acetylene flame. A premix burner of the Perkin-Elmer type was also available and was used with their model 290 atomic-absorption spectrophotometer.

For purposes of comparing lamps several hollow-cathode lamps for each element were used, representing various types and ages. For iron, e.g., four different lamps were available: a newly-purchased single-element lamp, an older single-element lamp, and two recent multielement lamps. Similarly, lamps were obtained for lead, calcium, and magnesium. All the lamps were manufactured by Westinghouse and distributed by the Jarrell-Ash Company for use with their instruments. An adaptor was constructed so the Westinghouse lamps could also be used with the Perkin-Elmer instrument. In this manner the different burners could be compared independent of lamp differences. The Jarrell-Ash instrument is equipped with a hollow-cathode power supply which can be used either as a dc or as a pulsed source. If the power supply is used as a dc source, the light beam is chopped by means of a mechanical chopper; if it is used as a pulsed source, the beam is modulated electrically.

Aqueous standards were prepared for each element studied, and analytical curves were prepared using the various instrument options that were available. Where precision data were necessary the standards were analyzed over a period

of several days to obtain sufficient data to be statistically significant. The concentration that was necessary to produce 1% absorption was found for the elements studied and for several other elements. Some of the more significant results have been selected for consideration and discussion.

RESULTS

Burners

A comparison of the available types of burners was made, and the first point considered was the effect the burner might have on the calibration curve. Fig. 1 shows the calibration curves obtained for magnesium using the high-efficiency total consumption (HETCO) and the laminar flow burners. One

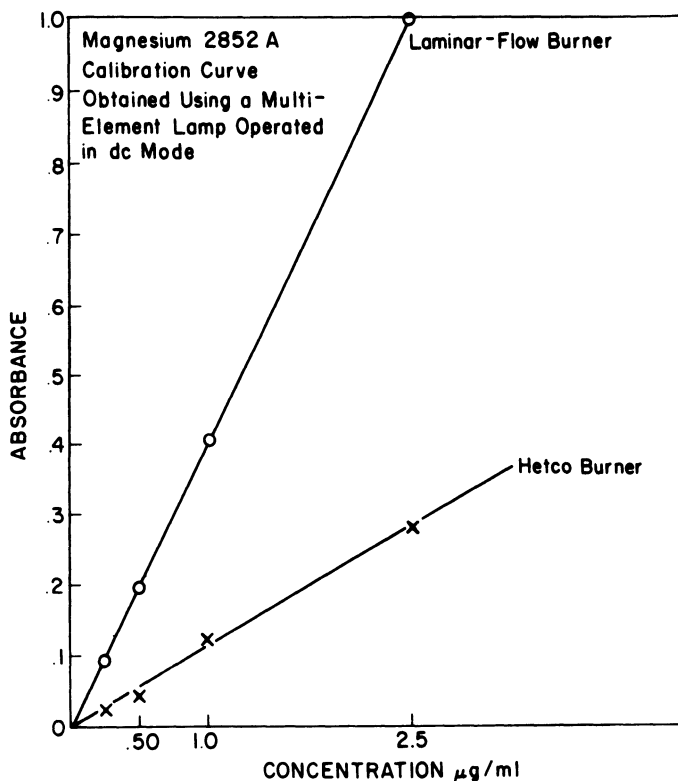


Fig. 1. Calibration curves for magnesium using laminar flow and HETCO burners.

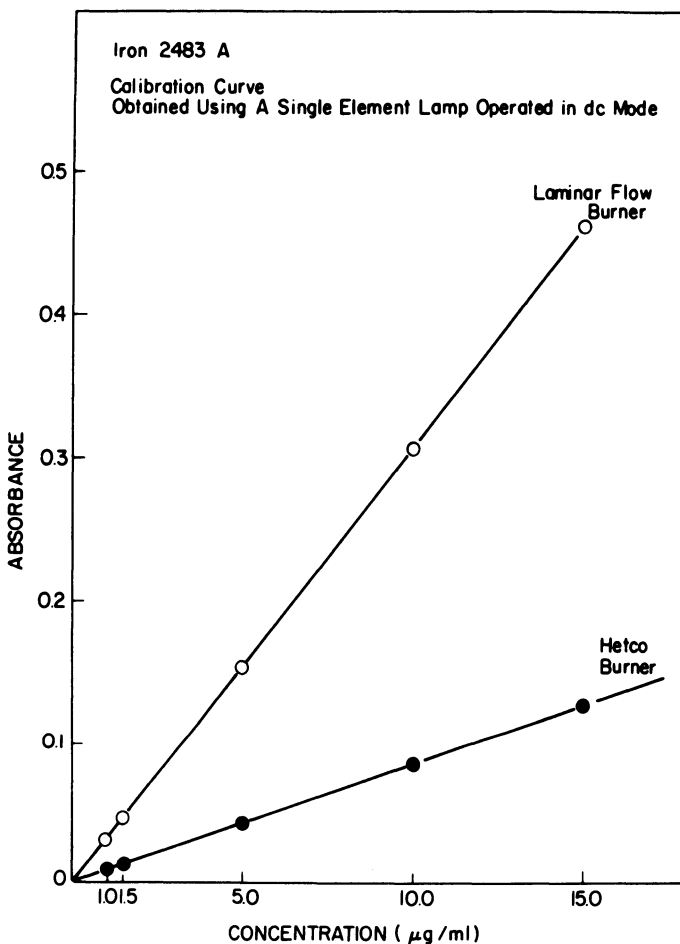


Fig. 2. Calibration curves for iron using laminar flow and HETCO burners.

multielement lamp was used and it was operated in the dc mode at the optimum current to fix the other variables. Prior to obtaining these curves a study of the effect of flame composition and burner height and angle was made in order to select the conditions which gave maximum absorption for each burner. It is apparent that the curve obtained using the laminar flow burner has a greater slope than that of the HETCO burner. Since sensitivity is determined by the slope of the calibration curve⁸ the laminar flow burner must be considered to be more sensitive than the HETCO burner. One might also expect an increase in precision, as will be shown below, since more

absorption per unit can be obtained at lower concentrations. At the 0.25 $\mu\text{g/ml}$ standard, e.g., 0.06 more absorbance units are obtained for the laminar flow burner. These slope differences were obtained for the other elements studied, as, e.g., in Fig. 2 for the case of iron. Here a single-element lamp was used in the pulsed mode of operation to obtain the analytical curves. There could be three possible explanations for this change in slope. One could be the difference in fuels, since the HETCO burner used an air-hydrogen flame, whereas the laminar flow burner used an air-acetylene flame. In an attempt to avoid this problem, the HETCO burner was operated with acetylene as the fuel; however, it was found that the flame was too unstable and noisy to operate in this manner. No conclusion could be reached concerning any effects due to fuel differences. A second explanation could be associated with the different optical arrangements. The HETCO burner was used with multipass optics, which passes the light from the hollow-cathode lamp through the flame five times. The laminar flow burner used a periscope arrangement for deflecting the light to the slit after only one pass. No attempt was made to evaluate the effect of the two optical systems, since these are the systems that normally would be obtained from the manufacturer for use with the two respective types of burner. The other possible explanation, which has been discussed in the literature,^{1,7,9} has to do with the drop size. For the total consumption burner all of the solution that is aspirated reaches the flame, and consequently, there is a certain maximum drop size beyond which the atomic vapor cannot be released. For the laminar flow burner a glass diverter and spoiler are used to break up the droplets into a fine mist. Any drops that do not break up are drained off, allowing only this fine mist to reach the flame for combustion. This process allows a higher percentage of the solution to be converted to a finer drop size, which the flame can more efficiently convert to an atomic state. One or all of these explanations may be credited with the differences in slope obtained using the two burners. In any case, the laminar flow burner provided the greater sensitivity for the elements studied.

Referring back to magnesium in Fig. 3, the precision was plotted versus concentration for both the total-consumption and laminar flow burners. The same lamp, method of operation, and current were used to obtain both curves. In this instance the laminar flow burner shows better analytical precision at the lower concentration, but the precision for the total-consumption burner becomes as good at 1.0 $\mu\text{g/ml}$, where a precision of 1% standard deviation is obtained. These curves were computed on the basis of data obtained over several days from aqueous standards. By using per cent standard deviation (defined as 100 times the standard deviation divided by the mean) as a measure of precision one can observe how concentration affects analytical quality. The curves were not extended to the 2.5 $\mu\text{g/ml}$ concentra-

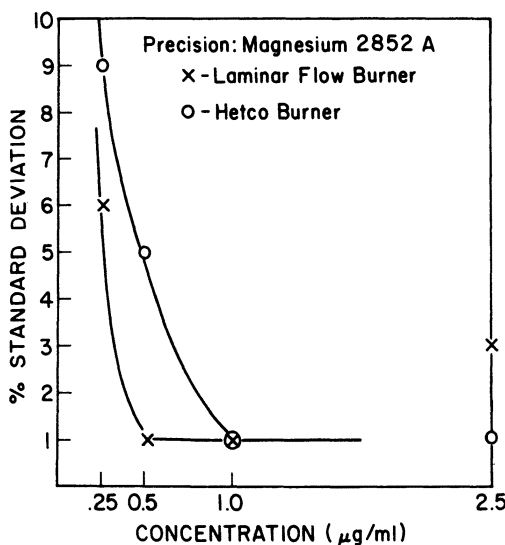


Fig. 3. Per cent standard deviation as a function of concentration for magnesium using the laminar flow and HETCO burners.

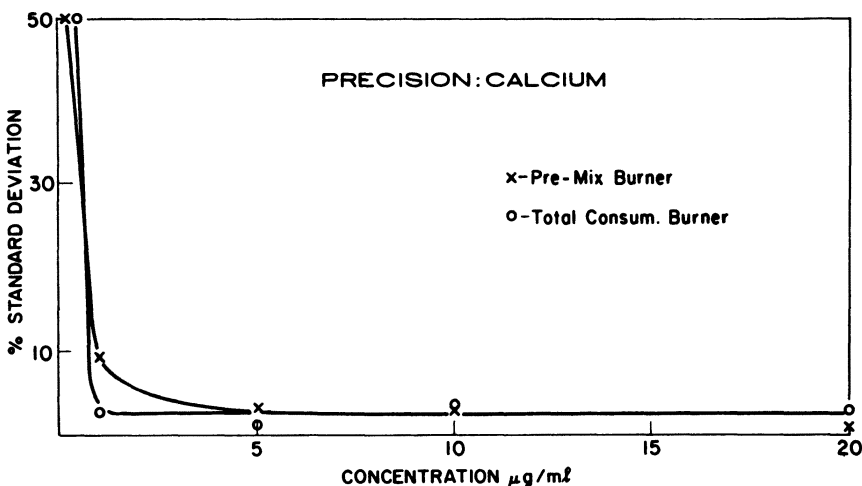


Fig. 4. Per cent standard deviation as a function of concentration for calcium using the premix and total-consumption burners.

tion because almost complete absorption was obtained and any precision data were not considered reliable. This same effect has been observed in previous work with the premix and total consumption burners.¹⁰ Figure 4 shows a comparison of the analytical precision for calcium using the Perkin-Elmer premix burner and the total-consumption burner. Again at low concentrations better precision is observed for the premix burner, but about equal or slightly better precision is observed for the HETCO burner at higher concentrations. This was found to be the case for most of the elements considered. Thus the selection of the burner type for best precision depends primarily on the concentration range of interest. Table I shows a comparison of the limits of detection (in ppm) for the HETCO burner, the laminar flow burner of Jarrell-Ash, and the Perkin-Elmer premix burner that was used with their model 290. The values agree closely with those published by Mavrodineanu.¹¹ They are generally of the same order of magnitude for the two types of burner except for Pb, Hg, and Ag, where the HETCO burner excels. Therefore even with the better sensitivity obtained with the premix burner the limits of detection for the two types of burner were found to be of the same order of magnitude. One would then conclude that differences between the two types of burner are small when considering all three factors, sensitivity, precision, and limit of detection.

Hollow-Cathode Devices

The next factors considered were the hollow-cathode lamp and the method of operation. The effect of the various hollow-cathode devices on the analytical curves for four elements of interest was examined. Figure 5 shows

TABLE I
Comparison of the Limits of Detection for the Total-Consumption,
Laminar Flow, and Premix Burners (in ppm)

Element	HETCO	Laminar flow	Perkin-Elmer Premix
Na	0.03	0.03	
Ca	0.10	0.20	0.20
Mg	0.01	0.01	0.05
Fe	0.10	0.20	0.50
Pb (2833 Å)	0.50	1.50	1.50
Cu	0.03	0.250	
Hg	0.50	25.0	
Cd	0.05	0.06	
Zn	0.01	0.03	
Ag	0.07	0.20	

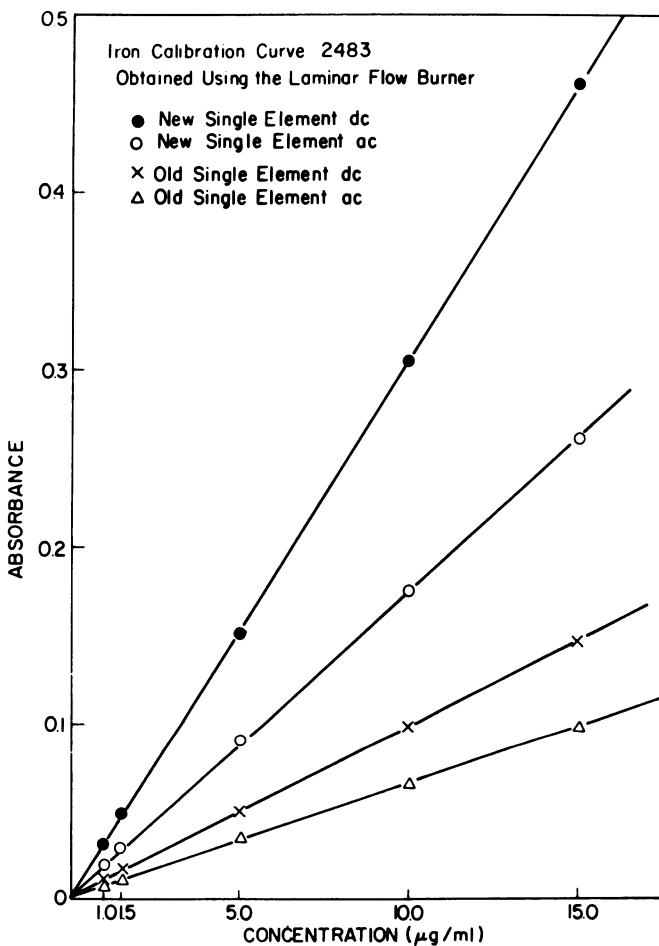


Fig. 5. Analytical curves for iron using two different lamps and two modes of operation.

four analytical curves for iron, and illustrates two points. First, the new single-element lamp shows better sensitivity than the old lamp whether used in the dc mode or the pulsed mode. By plotting current versus absorption for each lamp in each mode the current for maximum absorption was determined and used to construct these curves. Looking at the 10 $\mu\text{g}/\text{ml}$ standard, one can go from 0.065 to 0.310 absorbance units (almost a factor of five), depending on the choice of lamp and how it is operated. Some decrease in slope with age is expected because of factors that affect lamp life. These factors include gas clean up (loss of fill gas due to absorption by sputtered cathode material)

and out gassing problems that may be experienced by the manufacturer. Second, when using the optimum current the slope of the curve is greater for the dc than for the pulsed mode for both lamps, giving rise to better sensitivity. These lamps were of the same type, the only differences being age and type of fill gas. The older lamp was filled with argon and the new one with neon. Therefore for each individual lamp careful choice of mode of operation is necessary to succeed in obtaining the highest sensitivity. This was found to be true for all cases studied. Figure 6 gives the analytical curves for

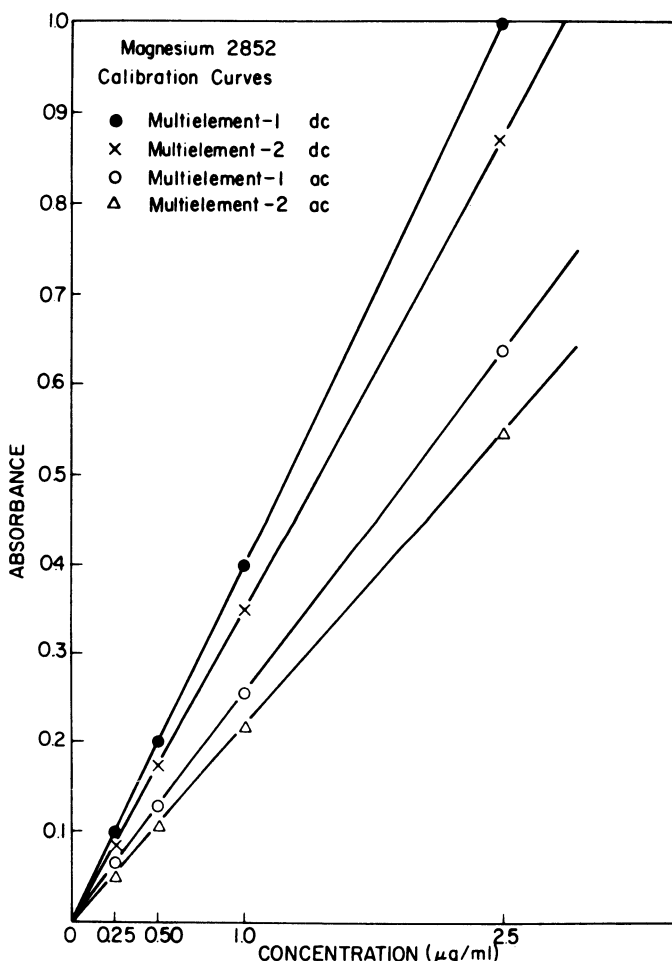


Fig. 6. Analytical curves for magnesium using two multielement lamps and two modes of operation.

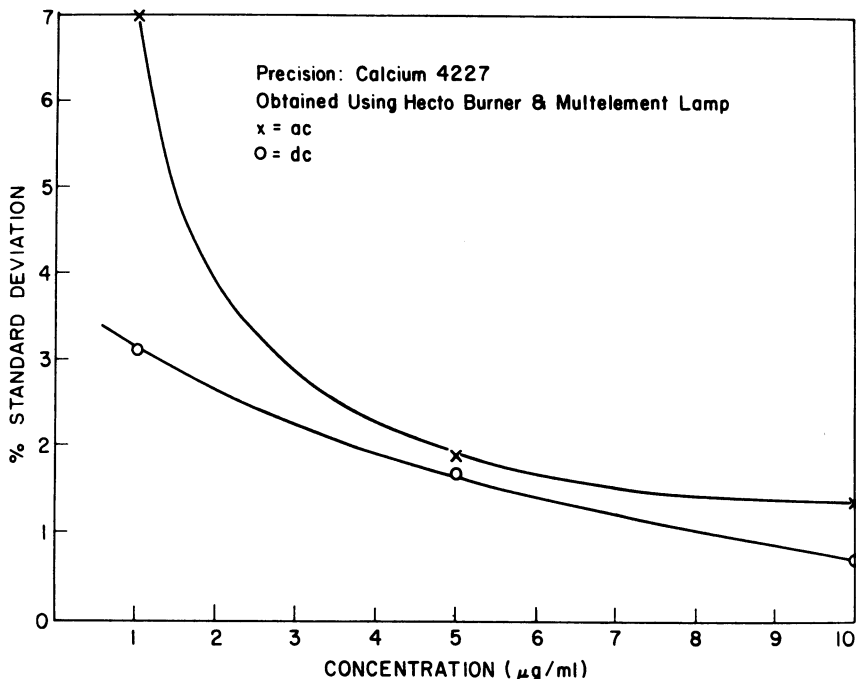


Fig. 7. Analytical precision for calcium using the two modes of operation.

magnesium obtained from two multielement lamps, and shows that differences can occur for what should be equivalent lamps. Since both multielement lamps were purchased about the same time, they should have been similar in performance. Therefore it is conceivable that one could obtain a new lamp and not do as well with respect to sensitivity and precision as reported in the literature because of the differences between lamps.² As mentioned earlier, these differences could be attributed to some of the problems encountered by the manufacturer.

Precision as well as sensitivity may also be affected by lamp choice and the method of operation. Figure 7 shows precision, expressed as per cent standard deviation, plotted versus concentration for calcium using the HETCO burner. At a concentration of 10.0 $\mu\text{g}/\text{ml}$ a precision of 0.7% standard deviation is obtained for the dc mode. In all cases examined the analytical precision is better where the lamp is operated in the dc mode. Figure 8 illustrates the differences in precision obtained with different lamps for the case of lead. The new single-element lamp has better analytical precision, but since the old lamp has been in use for several years, some difference would be

expected because of aging and use. The analytical curves for lead are also shown in Fig. 8 to illustrate how differences in slope indicate some of the differences in analytical precision. Calcium and lead have been used to illustrate the variation in precision that can occur due to operational differences and aging. The possibility of inherent differences between supposedly identical lamps also exists, as was illustrated for magnesium in Fig. 6. One of the multi-element lamps used for magnesium gave a 2% standard deviation at 0.25 $\mu\text{g}/\text{ml}$, as opposed to a 4% standard deviation for the other lamp. Both lamps were used in the dc mode.

One has no control over the variability between lamps before a purchase, but once the lamp has been purchased one must then decide on

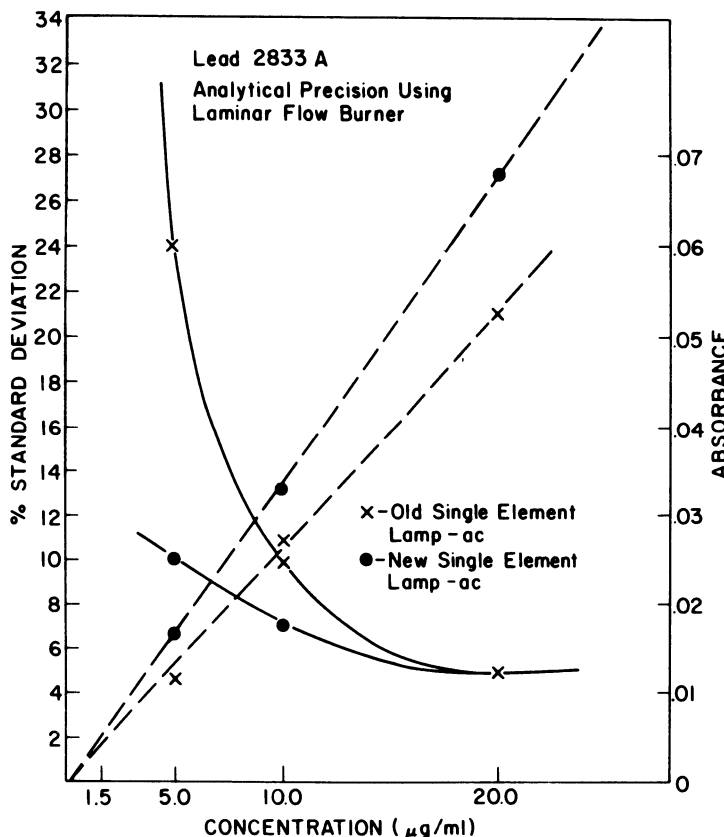


Fig. 8. Analytical precision and the corresponding calibration curves for lead using two lamps.

how to operate it, selecting both mode and current. For the cases studied the dc mode gave better sensitivity and precision; however, for some of the elements at lower wavelengths, such as As or Te, the opposite may be true. For elements like As, one may actually gain sensitivity due to the increased signal over the noise. One must also establish some criteria for determining when the lamp no longer meets the particular standards of sensitivity and precision for an analysis. Thus one must decide which particular lamp best meets one's needs, how to operate it, and when to turn it in for a new model.

Relationship between Sensitivity and Analytical Precision

It was mentioned earlier that an increase in precision was expected due to the higher absorption readings that could be obtained, depending on the choice of burner and lamp usage. This increase can be explained in terms of the system noise and its relationship to concentration. System noise can be broken down into two parts: (1) the noise level due to the hollow-cathode lamp and the detection and amplification system, which remains relatively constant for a given analytical system, and (2) the noise level due to the flame system, which can increase with concentration, depending on how efficient the burner is in breaking down the material. At concentrations for which only a small amount of absorption is obtained the system noise makes a sizable contribution. If, e.g., one obtained 2.0% absorption for an aqueous standard but had a 1.0% noise level, the signal-to-noise ratio would be small and the 1.0% noise would be a significant portion of the total signal. At higher concentrations this effect becomes less pronounced, since the ratio of signal to noise is quite large. Experimentally, it has been found that beyond a certain optimum concentration the analytical precision becomes essentially constant because both the amount of absorption and the standard deviation increase in the same proportion. Any increase in standard deviation at these higher concentrations is almost entirely due to the flame system. Thus if one can obtain more absorption for the lower concentrations by using a different burner or lamp, one would expect a corresponding increase in precision. This suggests that the slope of the analytical curve together with the signal-to-noise ratio can be used to monitor an analysis, showing not only when the burner is not functioning properly, but also when the hollow-cathode lamp has deteriorated to a point where it is no longer useful. For lead, e.g., in Fig. 8 the slope of the upper analytical curve is 1.27 times greater than that of the lower curve. The old lamp can no longer be used at all in the dc mode and cannot be used effectively at the lower concentrations in the pulsed mode. Perhaps a slope can be established below which the lamp will be completely

useless. This has also been observed for iron, with an older lamp producing analytical curves having lesser slopes than curves produced with a newer lamp. It is therefore possible to estimate the analytical precision, expressed as per cent standard deviation, using the slope of the analytical curve and the signal-to-noise ratio.

CONCLUSIONS

This study was conducted for the purpose of evaluating some of the various components available for atomic absorption and their use for analysis in a situation where the type of samples and the elements of interest may vary considerably. The conclusions reached are as follows:

1. The selection of a burner depends on the sample type and the concentration range of interest for each element, with each type of burner having its advantages and disadvantages. For the elements studied here the laminar flow burner is more sensitive and shows better precision at low concentrations. The total-consumption burner produces better limits of detection and is as good or better with regard to precision at higher concentrations. The one difference not noted previously was in audible noise, where the total-consumption burner excels by far, being capable of drowning out any conversation in the vicinity of the instrument. However, noise has little to do as far as any gain or loss in sensitivity and precision is concerned for a particular analysis.
2. Lamp selection and operation appears to be quite important from an analytical point of view. Consideration should be given to whether a single-element or multielement lamp is desirable and to the type of fill gas to use. After purchase of the hollow-cathode device consideration must be given to the mode of operation. For the cases studied above the dc mode of operation appears to be superior both from the sensitivity and precision point of view, although each element should be studied individually before any analysis. Differences are noted between similar lamps, but the analyst can do little about this when faced with making a lamp purchase.
3. The analytical curve appears to be the single most important piece of information available to the analyst. The curve and its associated slope, together with the signal-to-noise ratio, can give information on how well the burner and hollow-cathode lamp are functioning.

REFERENCES

1. James W. Robinson, *Atomic Absorption Spectroscopy*, Marcel Dekker, New York (1966).
2. J. E. Allen, *Analyst* **86**, 530 (1961).
3. M. J. Fishman and S. C. Downs, U. S. Geol. Survey Water Supply Papers 1540C (1966).
4. F. I. Grunder and E. A. Boettner, *Am. Ind. Hyg. Assoc. J.* **28**, 391 (1967).
5. Keiichiro Fuwa, Pablo Pulido, Robert McKay, and Bert L. Vallee, *Anal. Chem.* **36**, 2407 (1964).
6. P. B. Adams and W. O. Passmore, *Anal. Chem.* **38**, 630 (1966).
7. Herbert L. Kahn, Principles and Practice of Atomic Absorption, in: *Trace Inorganics in Water*, Robert F. Gould, ed. (Advances in Chemistry Series No. 73, 1968), Chap. 11, pp. 183-229.
8. H. Kaiser, *Trace Characterization - Chemical and Physical*, W. Wayne Meinke and Bourdon F. Scribner, eds., National Bureau of Standards Monograph 100, Washington, D.C. (1967), p. 153.
9. Richard N. Kniseley, Arthur P. D'Silva, and Velmer A. Fassel, *Anal. Chem.* **35**, 910 (1963).
10. E. A. Boettner and F. I. Grunder, Water Analysis by Atomic Absorption and Flame Emission Spectroscopy, in: *Trace Inorganics in Water*, Robert F. Gould, ed. (Advances in Chemistry Series No. 73, 1968), Chap. 13, pp. 236-246.
11. R. Mavrodineanu, *Encyclopedia of Industrial Chemical Analysis*, F. D. Snell and C. L. Hilton, eds. John Wiley (Interscience) New York (1966), Vol. 1, pp. 171, 172.

An Experimental Device for Atomic-Absorption Spectroscopy

J. D. Johnson, G. K. Yamasaki, and J. C. Burger

*Westinghouse Electric Corp.
Elmira, New York*

Devices combining the functions of light source and resonance detection have been designed and constructed in an attempt to further simplify existing atomic-absorption systems. Absorption data for copper and nickel are presented. From our brief evaluation it is concluded that this combined hollow-cathode emission-resonance detector device can perform as the heart of a simple analytical system for atomic-absorption analysis.

INTRODUCTION

As early as 1904 quite extensive work on the phenomena of atomic absorption and atomic fluorescence was reported by Wood.¹⁻⁴ These same techniques formed the basis for analytical systems designed by Sullivan and Walsh⁵, who employed hollow-cathode lamps as resonance line selectors for the determination of calcium, magnesium, sodium, potassium, and lead.

The basic components necessary for a resonance-detection system are shown in Fig. 1, in which the hollow cathodes of the source and resonance

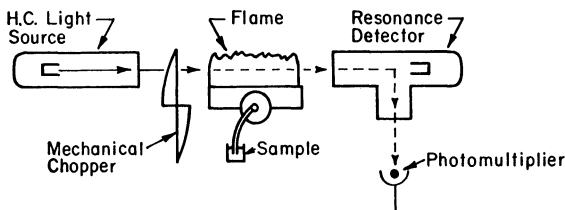


Fig. 1. Conventional resonance-detector system.

detector must be constructed so as to contain the element being determined. Spectral lines emitted by the hollow-cathode source are passed through an aspirator-burner system where the material to be analyzed is thermally decomposed to its atomic state. This results in the absorption and attenuation of the atomic resonance lines present in the beam of light, the degree of which is related to the concentration of the sample in the aspirated solution. The beam of light is now optically focused so as to fall upon a cloud of atomic vapor in the resonance lamp or device to produce atomic fluorescence. This fluorescent radiation is finally monitored at right angles to the incident beam through a side window by means of a light-sensing device such as a photomultiplier.

The light beam from the hollow-cathode source may be chopped or the source electrically pulsed so as to permit separation of the absorption signal from dc background noise by means of ac amplification.

EXPERIMENTAL

Apparatus

An examination of the resonance-detection process led to the idea of incorporating the light source and the resonance detector into one dual-function device. This would eliminate the necessity of two separate devices and could simplify power-supply requirements. Various dual-function devices were constructed and tested in the experimental setup which is schematically shown in Fig. 2. A small-bore total-consumption burner was used in all the experiments, although a slot-type burner might have been more advantageous. A concave front-surface mirror was used to reflect the light beam from the device back into a resonance-detection area, providing the added feature of double-passing the flame. The various light-source-resonance-detector configurations tested were modifications of the standard Westinghouse shielded designs, and they were operated quite satisfactorily from a regular hollow-cathode power supply.

As we were attempting only to prove the basic concepts, no attempt was made to optimize the equipment used to conduct the experiments reported here. For this reason no single component is necessarily ideal, and they are listed in Table I for purposes of identification only.

Results

The first device was constructed for the determination of copper and zinc. An interference filter peaked at 3252 Å with a ± 40 Å half-intensity bandwidth

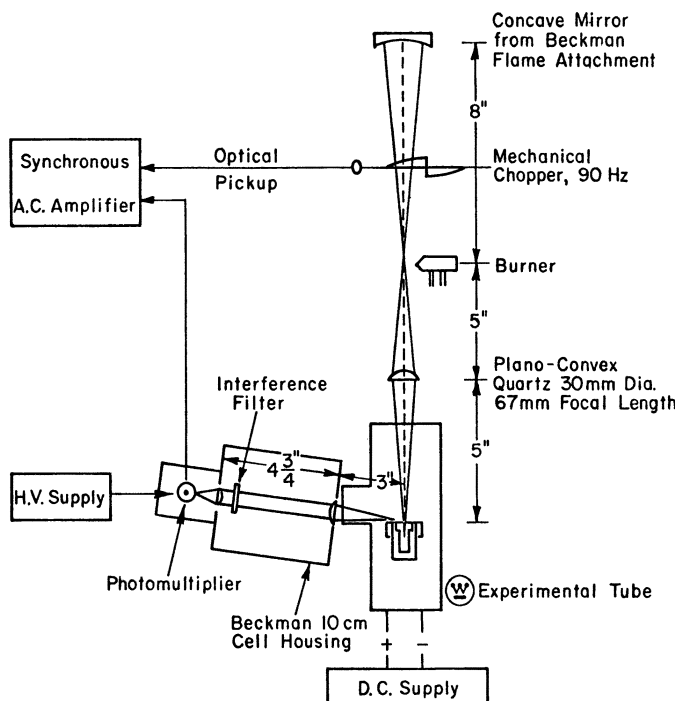


Fig. 2. Schematic diagram for experimental system.

TABLE 1
Apparatus for Combined Emission-Resonance
Detection System

Concave mirror, first surface, 4 in focal length, Beckman 9200
Mechanical chopper, 90 Hz, JACO 82-375A
Total-consumption burner, small bore, Beckman 4050
Plano-convex quartz lens, 30 mm diameter, 67 mm focal length, JACO
Cell housing, 10 cm, Beckman 4400
Interference filter, OCLI 11-5251-25
Photomultiplier, Hamamatsu R136
DC supply, Harrison Laboratories # HVR 6521A
HV supply, Keithley # 240
AC amplifier, Brower Laboratories # 130
Recorder, Sargent, M.R.

was used to isolate the copper 3247 and copper 3274 Å region. A spectral scan of the region passed by this filter was made by placing a Schoeffel-Littrow monochromator between the filter and the photomultiplier. This scan is shown in Fig. 3. Note the presence of lines other than the copper resonance lines. The monochromator was used to show the various lines passed by the filter and was not used during the collection of any of the absorption data presented.

By adjusting the focus of the returning light beam in front of the cathode and by selecting the region of resonance response with the lenses in the Beckman cell to house the contribution of all lines passed by the filter measurable signals of 25–500 mV at the recorder were obtained. For efficient signal measurement it is important to select the region of highest resonance response so the signal-to-noise ratio will be high. Noise in this case will be mostly that contributed by general background radiation and radiation from other, unwanted lines passing through the system.

With the system shown in Fig. 2 a full-scale signal of 250 mV presented with a 10X scale expansion has been held constant for a period of 48 min to within $\pm 0.6\%$ relative. Warm-up time of the device to achieve this stability is approximately 10 min. Figure 4 presents the data for the response and sensitivity for copper. Sensitivity for 1% absorption was measured at 0.48 and

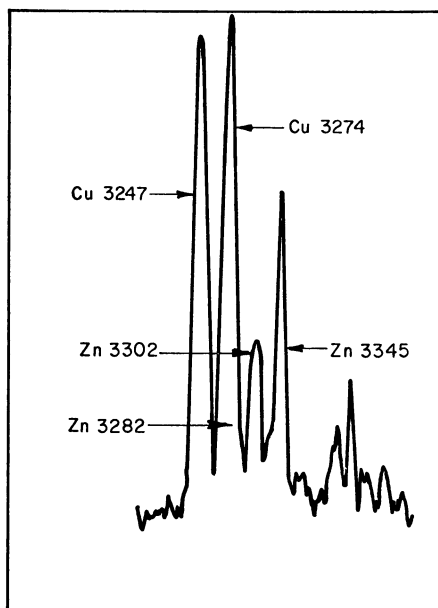


Fig. 3. Spectral scan of region near copper 3247 and 3274 Å lines

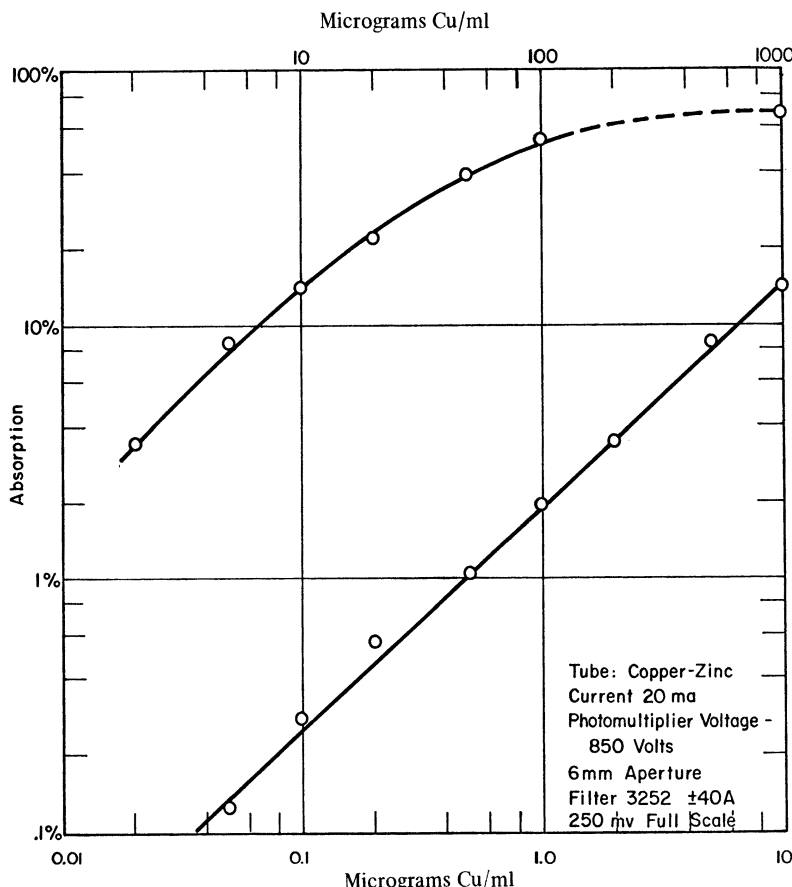


Fig. 4. Copper absorption curve using the experimental system described.

0.46 μg of copper per milliliter on two separate days. With a 10X scale expansion 0.05 μg of copper per milliliter was detectable above the blank. Since we are observing two resonant lines of copper of unequal strength and since some zinc and neon lines are also a part of the detected signal, it is logical that the slope be less than the theoretical 45° and that the absorption for 1000 μg of copper per milliliter be near a maximum of 70% absorption.

To test this system with a transition element having more complex resonance spectra, we chose nickel with a neon gas fill. A Corning ultraviolet glass filter #7-54 with a half-intensity band range of approximately 3200–4400 Å was used in front of the photomultiplier. Thus the U_1 and U_2 lines of nickel at 3414.8 and 3493.0 Å were included, as well as many other lines of nickel and neon.

The data of Fig. 5 for nickel indicate a sensitivity at 1% absorption of 6.0 μg of nickel per milliliter, with a reasonable linearity for more than two orders of magnitude, with again less than the theoretical slope. These sensitivities, particularly that of copper, are within one order of magnitude of those reported in the literature for commercial atomic-absorption instruments. No attempt has been made as yet to lower these limits of detection with other burners, gas mixtures, or organic solvents. We have only sought to demonstrate the feasibility of this system.

These initial experiments, even without optimization, have shown analytical sensitivities approaching those of a conventional atomic-absorption unit. In addition the basic simplicity of this dual-purpose component should permit its use in a variety of applications.

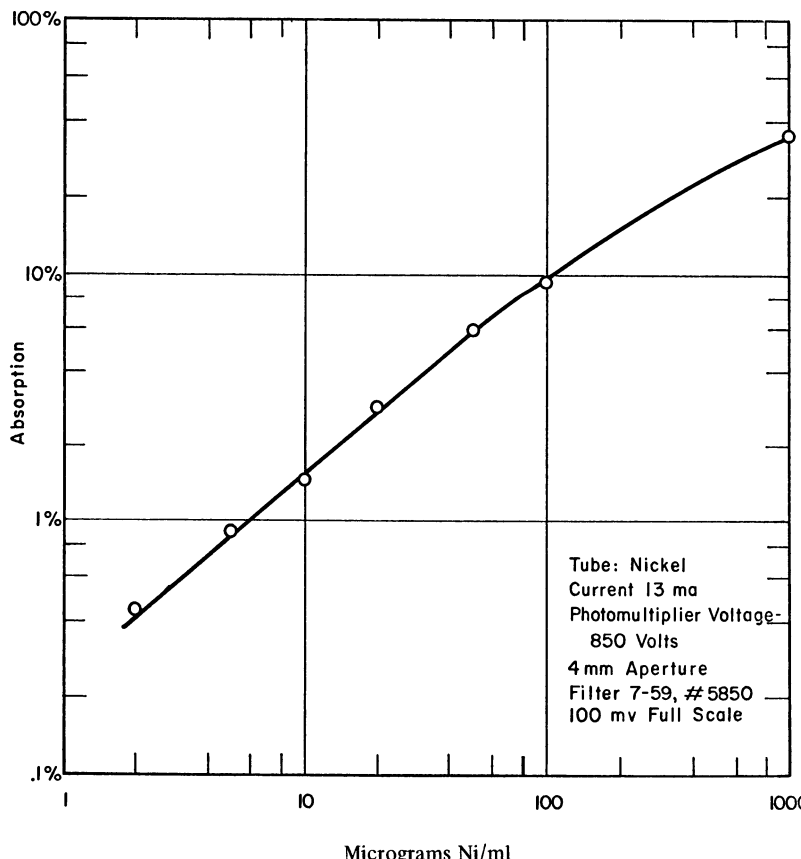


Fig. 5. Nickel absorption curve using the experimental system described.

Additional resonance windows with multielement cathodes would permit a simultaneous multielement analysis, providing the spectral regions for the resonance line or lines of each element can be adequately separated. Several resonance-detection systems such as demonstrated here may also be arranged radially in a horizontal plane around a single sample burner.

A versatile adaption to some existing instruments would substitute a Cassegrain collimator for the quartz field lens in our system. This would produce a fairly stigmatic and parallel beam to pass the sample area and be reflected by a plane mirror instead of a concave one. If this plane mirror is then mounted on the chopper, the system operates not only as we have described, but the beam passing through the chopper is also available for other measurement, such as monochromator detection, separate resonance detection, or total integration for control of the system.

For a sequential rather than simultaneous multielement determination with these combination devices the output from a single resonance window may be switched to two or more sets of filters and photomultipliers. Some experiments have been conducted with a device containing calcium, magnesium, aluminum, and lithium in this manner.

In conclusion, experiments performed using this new device have shown that a simple analytical system can be constructed. Although preliminary data have been presented, additional investigations are needed to fully develop the analytical capabilities and the areas of application for this dual-purpose device.

REFERENCES

1. R. W. Wood, *Proc. Am. Acad.* **XI**, 396 (1904).
2. R. W. Wood, *Phil. Mag.* **10**, 513 (1905).
3. R. W. Wood, *Phil. Mag.* **23**, 689 (1912).
4. R. W. Wood, *Physical Optics*, 3rd ed., Macmillan, New York (1934).
5. J. V. Sullivan and A. Walsh, *Spectrochim. Acta*, **22**, 1843 (1968).

Indirect Atomic-Absorption Spectrometric Methods of Analysis

David F. Boltz

*Department of Chemistry
Wayne State University
Detroit, Michigan*

The direct determination of certain metals is impractical because of oxide formation in the use of flame atomizers, and the direct determination of nonmetals is often not feasible because either a suitable source of incident radiant energy is unavailable or the absorption lines are in the vacuum-ultraviolet region. Indirect methods are being developed to circumvent some of these difficulties. The general technique involves the formation of a complex consisting of the desired constituent and a metal which can be determined directly by atomic-absorption spectrometry. It is important that the ratio of desired constituent to metal be stoichiometric and it is advantageous if this complex is extractable from aqueous solution with an immiscible organic solvent. Specific indirect methods for germanium, phosphorus, silicon, nitrate, thiocyanate, etc., will be discussed.

One of the most significant developments in analytical chemistry within the last decade has been the genesis of atomic-absorption spectrometry as a rapid, sensitive, and extensively applicable method of determining trace quantities of elements. However, numerous claims have been made relative to the superiority of atomic-absorption spectrometry over spectrophotometry, flame-emission spectrometry, and other methods with respect to specificity, sensitivity, freedom from interference, and applicability to analytical problems, claims which are often misleading. It is realized by those working in the field of atomic-absorption spectrometry that the sensitivity of atomic-absorption spectrometric methods is highly dependent on many instrument factors, such as

type of hollow-cathode tube, current, type and position of burner, fuel-support gas, and sensitivity of detector and associated readout system. The composition of the sample solution is also an important consideration. Slavin¹ has shown that the effect of diverse ions is often dependent on the type of burner employed. He used schlieren patterns to show that the exclusion of oxygen from the flame was important in determining elements tending to form refractory oxides. However, there remains several elements which can not be determined very satisfactorily because of (1) oxide formation in the flame, or (2) occurrence of resonance lines in the vacuum- or far-ultraviolet region, or (3) unsuitable means of atomizing the desired constituent.

In the course of a systematic spectrophotometric study of methods for the determination of nonmetals it has often been necessary to resort to indirect methodology in order to develop satisfactory methods. Presently we are extending this same indirect methodology to atomic-absorption spectrometry. Several indirect methods applicable to the determination of nonmetals and organic substances by atomic absorption spectrometry have been reported by Christian and Feldman.² It is the objective of this chapter to review indirect atomic-absorption methods which have been developed for the determination of metals and nonmetals and to indicate some of the potentialities of indirect methods. With the availability of atomic-absorption spectrometric apparatus in numerous laboratories it is advantageous to be able to determine as many constituents as possible utilizing this equipment, even though alternate methods may be preferable.

There are two general methods in indirect atomic-absorption spectrometry. Method 1 involves the determination of the effect of a desired constituent on the formation of an absorptive chemical system. Thus a specific constituent may cause a diminution of absorbance for a particular absorptive system, or it may cause an enhancement of absorbance. For example, small amounts of sulfate, orthophosphate, and ribonuclease have been observed to decrease the absorbance due to calcium by amounts in proportion to their concentration.² Glucose decreases the interference of sulfate on the absorbance due to calcium, and this effect is proportional to glucose concentration within limited concentration ranges. Bond and O'Donnell³ also utilized this general method in determining fluoride.

The diminution of the absorbance of the magnesium resonance line at 2852 Å was measured using an air-coal-gas flame. Sulfate, phosphate, and aluminum ions caused serious interference. Alternate methods were also developed based on the enhancement of the absorbance for either the zirconium line at 3601 Å or the titanium line at 3643 Å when a nitrous oxide-acetylene flame was used. The procedure utilizing the zirconium line is less sensitive but is not subject to the sulfate interference.

Method 2 involves the formation of a stoichiometric compound containing the desired constituent and the determination of either (1) the amount of an equivalent constituent in this compound or (2) the amount of excess reagent by atomic absorption spectrometry.

PRECIPITATION METHODS

The formation of a highly insoluble precipitate is one approach in developing an indirect method for a metal or an anion. Chloride has been determined indirectly by precipitation of silver chloride, dissolution of the precipitate in ammonia solution, and the atomic absorption spectrometric determination of the equivalent silver.⁴ Cyanide can be determined by precipitation of silver cyanide and determination of the excess silver by atomic-absorption spectrometry.⁵ The sulfur content of biological samples was determined by conversion to sulfate, precipitation of barium sulfate, and determination of the barium.⁶ Sulfur dioxide has been determined by conversion to sulfate, precipitation of lead sulfate in an ethanolic solution, removal of precipitate by centrifugation, and determination of excess lead in the supernate by the atomic-absorption method⁷. Ammonium ion precipitates with molybdophosphoric acid to give an insoluble precipitate, $(\text{NH}_4)_3\text{PMo}_{12}\text{O}_4\cdot$. This precipitate dissolves in basic solution and the molybdenum equivalent to the ammonium can be determined by measurement of the absorbance of the molybdenum line at 313.3 $\text{m}\mu$.⁵

EXTRACTION METHODS

The conversion of the desired constituent to a compound or complex extractable with an immiscible solvent is another useful technique. Phosphate was determined indirectly by extracting molybdophosphoric acid with 2-octanol, aspirating the extract directly into an air-acetylene flame, and measuring the absorbance of the molybdenum line.⁸ Another indirect procedure uses *n*-butyl acetate as extractant and a nitrous oxide-acetylene flame.⁹ Phosphate and silicate have been determined successively by formation of molybdophosphoric and molybdsilicic acids, isolation at each heteropoly acid by sequential extraction, and then measurement of the molybdenum associated with each nonmetal.^{10,11} Germanium has been determined by a similar procedure based on the formation and extraction of 12-molybdochermanic acid.¹² Vanadate under controlled conditions forms a mixed heteropoly complex with molybdophosphoric acid in which the P:V:Mo ratio is 1:1:11. The

extraction of molybdovanadophosphoric acid with a 4:1 diethyl ether:1-pentanol mixture, followed by transfer of the molybdate to a basic aqueous phase prior to atomic-absorption measurement of the molybdenum is the basis of an indirect method for vanadium.¹³ Niobium has also been determined indirectly by the formation and extraction of a mixed heteropoly complex, molybdoniobophosphoric acid. In this method the excess molybdophosphoric acid is removed by extracting with isobutyl acetate prior to the extraction of molybdoniobophosphoric acid with butanol. The molybdoniobophosphoric acid has a P:Nb:Mo ratio of 1:1:11. Kirkbright *et al.*¹⁴ determined 5-50 µg of niobium by this indirect method.

Thiocyanate forms a dithiocyanatodipyridine copper(II) complex, Cu(Py)₂(SCN)₂, which is extractable with chloroform. The copper equivalent to the thiocyanate is determined using the 324.7 mµ line. The optimum concentration range is 0.1–15 ppm of thiocyanate.¹⁵ It has been reported that nitrate can be determined indirectly by extracting the complex Cu(2,9-dimethyl-1,10-phenanthroline)₂NO₃ in methyl isobutyl ketone and measuring the copper.¹⁶ Perchlorate forms a similar complex with neocuproine and copper(I), which is extractable with ethyl acetate. This indirect atomic-absorption spectrometric method is applicable to the determination of 12.5–125 µg of perchlorate.¹⁷

There are undoubtedly many additional indirect methods which can be devised. The amplification aspect of heteropoly chemistry offers many unique potential applications. Table I summarizes representative methods bases on molybdoheteropoly compounds. The formation and extraction of ion associates involving charged metal chelate is another attractive approach worthy of further study. The utilization of stoichiometric atomic-absorption spectro-

TABLE I
Indirect AAS Methods Based on the Formation
of Molybdo-Heteropoly Compounds

Desired constituent	Compound	Element determined	Equivalent ratio	Ref.
P (PO ₄ ⁻³)	H ₃ PMo ₁₂ O ₄₀	Mo	1P:12Mo	(⁸⁻¹¹)
Si (SiO ₃ ⁻²)	H ₄ SiMo ₁₂ O ₄₀	Mo	1Si:12Mo	(^{10,11})
Ge (GeO ₃ ⁻²)	H ₄ GeMo ₁₂ O ₄₀	Mo	1Ge:12Mo	(¹²)
As (AsO ₄ ⁻³)	H ₃ AsMo ₁₂ O ₄₀	Mo	1As:12Mo	(⁵)
V (VO ₃ ⁻)	H ₃ PMo ₁₁ VO ₃₉	Mo	1V:11Mo	(¹³)
Nb (NbO F ₅ ⁻²)	H ₃ PMo ₁₁ NbO ₃₉	Mo	1Nb:11Mo	(¹⁴)

metry has not been investigated very thoroughly. Although a direct, specific, and sensitive analytical method is always preferred, the substitution of a well-delineated indirect method is acceptable.

REFERENCES

1. W. Slavin, *Atomic Absorption Newsletter* **6**, 9 (1967).
2. G. D. Christian and F. J. Feldman, *Anal. Chim. Acta* **40**, 173 (1968).
3. A. M. Bond and T. A. O'Donnell, *Anal. Chem.* **40**, 560 (1968).
4. U. Westerlund-Helmerson, *Atomic Absorption Newsletter* **5**, 97 (1966).
5. R. Danchik and D. F. Boltz, *Analytical Letters* **1**, 901 (1968).
6. D. A. Roe, P. S. Miller and L. Lutwak, *Anal. Biochem.* **15**, 313 (1966).
7. S. Rose and D. F. Boltz, *Anal. Chim. Acta* **44**, 239 (1969).
8. W. S. Zaugg and R. J. Knox, *Anal. Chem.* **38**, 1759 (1966).
9. T. Kumamaru, Y. Otani, and Y. Yamamoto, *Bull. Chem. Soc. Japan* **40**, 429 (1967).
10. G. F. Kirkbright, A. M. Smith, and T. S. West, *Analyst* **92**, 411 (1967).
11. T. R. Hurford and D. F. Boltz, *Anal. Chem.* **40** (1968).
12. R. J. Jakubiec and D. F. Boltz, *Anal. Chem.* **41**, 78 (1969).
13. R. J. Jakubiec and D. F. Boltz, *Analytical Letters* **1**, 347 (1968).
14. G. F. Kirkbright, A. M. Smith, and T. S. West, *Analyst* **93**, 292 (1968).
15. R. Danchik and D. F. Boltz, *Anal. Chem.* **40**, 2215 (1968).
16. T. Kumamaru, Y. Otani, and Y. Yamamoto, *Bull. Chem. Soc. Japan* **40**, 429 (1967).
17. W. J. Collinson and D. F. Boltz, *Anal. Chem.* **40**, 1896 (1968).

Atomic-Absorption Spectrophotometry in Mineral and Trace-Element Studies in Man

**Dace Osis, Kathryn Royston, Joseph Samachson,
and Herta Spencer**

*Metabolic Research Section
Veterans Administration Hospital
Hines, Illinois*

Analyses of calcium, magnesium, and zinc in the diet and in urine and stool have been performed with the atomic-absorption spectrophotometer. Complete metabolic balance studies of calcium, magnesium, and zinc were performed under constant metabolic conditions in man during different intake levels of these elements. These studies have led to a better understanding of the interrelationship of minerals and trace elements in man.

INTRODUCTION

The availability of the atomic-absorption spectrophotometer greatly facilitates studies of the metabolism of minerals and trace elements in man. Analyses of calcium, magnesium, and of zinc can now be performed accurately and rapidly, and a large number of these analyses can be performed in a short period of time. These analyses permitted the determination of metabolic balances of calcium, magnesium, and zinc under controlled dietary conditions in adult man.

EXPERIMENTAL

All studies were performed on the Metabolic Research Ward. The patients received a constant, analyzed low-calcium diet which contained an average of

*Supported by research grant AM-5572 from the U.S. Public Health Service.

220 mg calcium and 750 mg phosphorus. Complete 24-hr urine collections were obtained daily and all stool specimens were collected throughout the studies, which lasted for a minimum of 24–30 days in each study phase. These collections were obtained in specially acid-washed plastic containers. Aliquots of the total volume of urine, of the six-day pool of homogenized stool, and of the food were used for the analyses. The fluid intake was kept constant. The food intake of two days was used for analysis in each six-day period. The classical strict metabolic control was used.¹

All analyses of calcium, magnesium, and zinc were performed with the Perkin-Elmer atomic-absorption spectrophotometer, Model 303, using a digital concentration readout (DCR) #1. For analysis of calcium and magnesium the single-element lamps were used, while for the analysis of zinc the Zn–Ca combination lamp was used. The settings used for the three elements are shown in Table I.

Calcium Analyses in Biological Samples

In performing calcium analyses, prior to the reading of the samples the instrument was zeroed in to read 100 on the DCR using redistilled H₂O and 5% LaCl₃ in the same dilution as the samples to be read. Calcium standards prepared with redistilled H₂O and 5% LaCl₃ were used in concentrations ranging from 0.1 mg% to 0.8 mg%. Analyses of biological samples for calcium using the atomic-absorption spectrophotometer have been previously reported.^{2,3}

Calcium analyses of urine were performed by using an appropriate amount of urine which was diluted to 10 ml with redistilled H₂O and 5% lanthanum chloride. The amount of urine used depended on the calcium concentration of the urine. For the calcium analyses of stool and food 50 gm of the homogenized samples were used, 1 ml of 50% NaOH was added, and the samples were dried in an oven at about 95°C overnight and were then

TABLE I
Settings for Calcium, Magnesium, and Zinc
on the Atomic-Absorption Spectrophotometer

	Calcium	Magnesium	Zinc
Wavelength	212	285	214
Range	Visible	UV	UV
Slit	4 (1 mm, 13 Å)	5 (3 mm, 20 Å)	5 (1 mm, 7 Å)
Source-hollow cathode	10 mA	6 mA	15 mA
Fuel-acetylene	7–8	5–6	5–6
Air	5–6	5–6	5–6

ashed in a muffle furnace at 550°C. The ashed samples were brought into solution using 3*N* HCl, were diluted with redistilled water to a volume of 100 ml, and were then filtered. The final volume of the ashed samples of stool or food used for calcium analysis depended on the calcium concentration of the sample. Individual foods like beef, bread, and others were prepared in the same manner as the food aliquots using 20-g samples. Further steps in the analyses of stool, food, and of individual food items were the same as those used for the analyses of urine samples.

Magnesium Analyses in Biological Samples

The use of the atomic-absorption spectrophotometer for the analyses of biological samples for magnesium has been reported.²⁻⁸ Prior to the readings of the samples the instrument was zeroed in to read 100 on the DCR with redistilled H₂O for magnesium analyses of urines, stools, and foods and with 0.25% SrCl₂ for magnesium analyses of blood and saliva. Standards in the range of 0.1 to 0.8 ppm magnesium were used for standardization of the instrument. The diluents of the standards were redistilled H₂O for the standards of urine, stools, and foods and 0.25% SrCl₂ for the standards of blood and saliva.

Magnesium analyses of urine were performed by direct dilution of 0.5 ml of urine to a 50 ml volume using redistilled H₂O. Magnesium in stool and food was determined on aliquots of the same ashed samples which were used for the analysis of calcium. These samples were diluted with redistilled H₂O to obtain a final concentration of magnesium which ranged from 0.1 to 0.8 ppm. Serum magnesium was determined on 100 µl of serum which was diluted with 0.25% SrCl₂ to a 5 ml volume.

Zinc Analyses of Biological Samples

Analyses of stable zinc in biological samples using the atomic-absorption spectrophotometer have been reported.⁹⁻¹¹ For the analysis of urine for zinc the instrument was zeroed in to read 100 on the DCR using redistilled H₂O. Standards ranging from 0.1 to 0.6 ppm of zinc diluted with redistilled H₂O were used for standardization of the instrument. For stool and food analyses the instrument was zeroed in to read 100 on the DCR using redistilled H₂O and H₂SO₄ in the same strength as would be present in the ashed sample. Standards for stool and food ranged from 0.1 to 0.8 ppm of zinc for standardization of instruments again using redistilled H₂O and H₂SO₄ in the same concentrations as the zero blank.

Zinc analyses of urine were performed on undiluted samples of urine. Zinc analyses of stool and food were performed by using wet ashed samples. For analyses of stool or food 10-g samples were ashed in a 100-ml Kjeldahl flask using concentrated H_2SO_4 and 30% H_2O_2 . The clear, ashed sample was then diluted with redistilled water to give a final reading range on the atomic-absorption spectrophotometer from 0.1 to 0.8 ppm of zinc. This necessitated a dilution of about 250 times for stool samples and a five to ten times dilution for food samples, depending on the zinc content of stool and food, respectively. With every series of stool and food analysis a blank using redistilled H_2O , concentrated H_2SO_4 and 30% H_2O_2 , was processed in the same manner. This blank was made up in the same dilution as the sample to be read. The reading of the blank was subtracted from the concentration reading of the sample.

In addition, recovery studies were performed with almost every series of analysis of urine, stool, food, or blood for calcium, magnesium, and zinc. Recovery of these elements in urine was performed by adding a known amount of the element to be analyzed to the diluted urine sample. Prior to the reading of the sample for urine the recovery for all elements ranged from 95–100%. For stool and food recoveries a known amount of the element was added to the sample prior to the ashing. Recovery for calcium in stool and food ranged from 96–102%, for magnesium from 95–100%, and for zinc from 97–100%. Recoveries of magnesium added to serum ranged from 93–101% and for zinc from 92–99%. All analyses for calcium, magnesium, and zinc were performed in duplicate.

RESULTS AND DISCUSSION

The analyzed values for dietary calcium ranged from 200 to 225 mg/day, for magnesium from 230 to 265 mg/day, and for zinc from 10 to 13 mg/day.

Calcium balance studies were performed during both low-and high-calcium intake. In order to keep the nitrogen and phosphorus intake constant during the high-calcium study, calcium was added in the form of calcium gluconate tablets to the constant low-calcium diet. Table II shows the calcium balances of ten patients performed during low- and high-calcium intake. The duration of the studies was an average of 24 days for each study phase. The low-calcium intake was 213 mg/day. On this intake the urinary calcium excretion was 99 mg/day, the stool calcium 234 mg/day, and the calcium balance was slightly negative, -121 mg/day. The slight negativity of the calcium balance is normal on this calcium intake.¹² In the high-calcium study, the calcium intake was raised to 1718 mg/day by adding calcium gluconate tablets to the constant low-calcium diet. These study conditions assured the constancy of the nitrogen and

TABLE II
Calcium Balances during Low-
and High-Calcium Intake

Patients	Calcium (mg/day)			
	Intake	Urine	Stool	Balance
10	213	99	234	-121
10	1718*	115	1459	+144

*High calcium intake due to addition of calcium gluconate tablets.

TABLE III
Magnesium Balances
during Different Intakes of Calcium and Phosphorus*

Patients	Intake (mg/day)		Magnesium (mg/day)			
	Calcium	Phosphorus	Intake	Urine	Stool	Balance
15	211	835	260	97	119	+44
12	1270	1345	262	104	118	+40

*Values are averages for 15 patients in the low-calcium study and for 12 patients in the high-calcium study.

phosphorus intake in the low- and high-calcium studies. During high-calcium intake the urinary calcium excretion rose only slightly, to 115 mg/day, while the stool calcium increased markedly, to 1459 mg/day, and the calcium balance was now positive, +144 mg/day. The effect of added calcium on the calcium balance is of great importance in patients with certain pathophysiologic states such as osteoporosis.¹²

Magnesium balance studies were performed during both low-and high-calcium intake. Table III shows the data obtained in studies performed on 15 patients during the intake of low-calcium, low-phosphorus diet and on 12 patients during an intake of higher levels of calcium and phosphorus. The magnesium intake was kept constant in the low- and high-calcium studies. Despite the difference in the intake levels of both calcium and phosphorus, the urinary and fecal excretions of magnesium and the magnesium balances were practically identical in the two studies.

The effect of changing the magnesium intake on the magnesium balance was also investigated. Table IV shows the data obtained. On an intake of 266 mg magnesium per day the urinary magnesium excretion was 86 mg/day, the fecal magnesium excretion was about twice this value, 162 mg/day, and the magnesium balance was slightly positive, +18 mg/day. When the magnesium intake was decreased by about 50 mg, i.e., from 266 mg/day to 212 mg/day, the urinary magnesium excretion remained in the same range as on the higher intake, while the magnesium excretion in stool also decreased by about 50 mg to 117 mg/day and the magnesium balance was less positive, +5 mg per day.

Magnesium balances in man have been recently reported.^{6,8} However, further studies on magnesium balances in man performed under constant dietary conditions are necessary in order to determine the effect of different intake levels of calcium and phosphorus on magnesium metabolism.

Extensive studies of zinc metabolism have been performed in the past few years as a result of the availability of the atomic-absorption spectrophotometer.¹¹ In the present study, balances of stable zinc were performed under constant, controlled dietary conditions. Table V shows the

TABLE IV
Effect of Lowering Magnesium Intake*

Study	Magnesium (mg/day)			
	Intake	Urine	Stool	Balance
1	266	86	162	+18
2	212	90	117	+ 5

*Studies 1 and 2 were performed in the same patient. Values are averages for 2½ days in each study phase.

TABLE V
Zinc Balances in Man*

Days	Zinc (mg/day)			
	Intake	Urine	Stool	Balance
6	13.1	0.49	12.3	+0.31
6	12.1	0.46	11.2	+0.44
6	12.5	0.42	11.8	+0.28
6	11.7	0.47	10.6	+0.63

*Values are averages for each six-day metabolic period.

TABLE VI
Zinc Balances during Low and Medium Calcium Intake*

Patient	Calcium intake (mg/day)	Zinc (mg/day)			Balance
		Intake	Urine	Stool	
4	200	12.3	0.57	11.0	+0.73
5	1300	12.3	0.53	11.6	+0.17

*Values in the low-calcium study are averages for four patients; values in the high-calcium study are averages for five patients. Average duration of each study was 24 days.

TABLE VII
**Reproducibility of Calcium, Magnesium,
and Zinc Analyses**

Element	Days	Urine	Stool	Food
Calcium	6	46	265	197
	6	53	231	214
	6	46	239	198
	6	48	222	221
Magnesium	6	92	147	233
	6	81	126	243
	6	76	137	241
	6	84	134	237
Zinc	6	0.60	6.6*	11.7
	6	0.52	6.9*	11.3
	6	0.53	8.7*	13.0
	6	0.49	7.7*	11.5

*Values are low due to low protein intake, which had a low zinc content.

results of a study performed on low-calcium intake for 24 days. Each value represents the average for six days. The zinc intake fluctuated slightly in the four six-day periods and ranged from 13.1 to 11.7 mg/day. The urinary zinc excretion was similar in the four six-day periods and averaged 0.45 mg/day. The fecal zinc excretions appear to vary with the zinc intake and ranged from 12.3 mg/day to 10.6 mg/day, and the zinc balances were slightly positive, ranging from +0.28 mg to +0.63 mg/day and averaged +0.42 mg/day. These data demonstrate the similarity of the zinc balances in successive six-day periods and the reproducibility of the data in the same subject.

Subsequently, the effect of different intake levels of calcium on zinc metabolism was investigated. Table VI shows data on zinc balances during the intake of low and intermediate levels of calcium. The duration of the studies averaged 24 days for each of the two study phases. The studies were performed during a low calcium intake of 200 mg/day on four patients and during an intermediate calcium intake of 1300 mg/day on five patients. The zinc intake of 12.3 mg/day was kept constant during both intake levels of calcium. The urinary and fecal zinc excretions were similar during low- and intermediate-calcium intake, and the zinc balances were slightly positive, +0.73 mg and +0.17 mg, respectively, on the two intake levels of calcium used.

The reproducibility of the analyses of calcium, magnesium, and zinc is shown by data in Table VII. The urinary and stool excretions represent analyses of four consecutive six-day periods in the same patient. The analyses of food are also those of four consecutive periods.

The coefficient of variation in the analyses of calcium, magnesium, and zinc of urine, stool, and food was determined (Table VIII). The coefficient of variation for calcium in these samples was small and ranged from 1.3% to 3.6%, and for magnesium it ranged from 4.2% to 6.3%. Similarly, the coefficient of variation for zinc analyses of urine, stool, and food was small and was greatest for urine, most probably due to the fact that the urinary zinc excretions were very low.

SUMMARY

The metabolism of minerals and trace elements in man was studied with the aid of the atomic-absorption spectrophotometer. These analyses greatly

TABLE VIII
Error in Analysis of Calcium, Magnesium, and Zinc
in Urine, Stool, and Food

Sample	Calcium			Magnesium			Zinc		
	Average values	S.D.*	C.V.(%)†	Average values	S.D.*	C.V.(%)†	Average values	S.D.*	C.V.(%)†
Urine	106‡	3.46	3.26	125‡	5.19	4.15	0.69‡	0.087	12.6
Stool	728‡	9.43	1.30	129‡	8.06	6.25	12.8 ‡	0.648	5.06
Food	201	7.30	3.63	249	11.83	4.75	12.5	0.565	4.53

* S.D. = Standard deviation.

† C.V.(%) = Coefficient of variation.

‡ Excretions. A minimum of 20 samples was used for excretions and food.

facilitated the determination of metabolic balances of calcium, magnesium, and zinc under constant metabolic conditions in man during various study conditions.

REFERENCES

1. W. Bauer and J.C. Aub, *J. Am. Dietet. Assoc.* **3**, 106 (1927).
2. J. B. Willis, *Spectrochim. Acta* **16**, 259 (1960).
3. J. B. Willis, *Anal. Chem.* **33**, 556 (1961).
4. J. B. Dawson and F. W. Heaton, *Biochem. J.* **80**, 99 (1961).
5. W. K. Stewart, F. Hutchinson and L. W. Fleming, *J. Lab. Clin. Med.* **61**, 858 (1963).
6. A. M. Briscoe and C. Ragan, *Am. J. Clin. Nutr.* **19**, 296 (1966).
7. H. Spencer and J. Samachson, Secretion of Alkaline Earth Metals in Saliva, in: *Secretory Mechanisms of Salivary Glands*, L. H. Schneyer and C. A. Schneyer, eds., Academic Press, New York (1967), p. 101.
8. H. Spencer, D. Osis, I. Lewin, and J. Samachson, *Intern. Assoc. Dent. Res. Program and Abstracts*, p. 115(a) (1967).
9. H. E. Parker, Perkin-Elmer Newsletter, No. 13 (1963).
10. J. B. Willis, *Anal. Chem.* **34**, 614 (1962).
11. A. S. Prasad, ed., *Zinc Metabolism*, Charles C. Thomas, Springfield, Ill. (1966).
12. H. Spencer, J. Menczel, I. Lewin, and J. Samachson, *Am. J. Med.* **37**, 223 (1964).

Mass Spectrometry

Investigation of Solids by Means of an Ion-Bombardment Mass Spectrometer

H. W. Werner

*Philips Research Laboratories
N. V. Philips' Gloeilampenfabrieken
Eindhoven, Netherlands*

An ion-bombardment mass spectrometer has been applied to the investigation of thin layers and bulk materials. The specimen is mounted in the ion source of the mass spectrometer and bombarded continuously with argon ions of 11 keV energy. Only those particles leaving the surface directly as ions are extracted from the ion source, and are separated according to their m/e ratio. The influence of oxidation on the ion yield has been studied. A method has been derived for indicating metal oxides present in concentrations decreasing as a function of depth. With this method the diffusion profile of indium diffused into a germanium matrix was found to be in good agreement with the theoretical diffusion profile, thus proving the proportionality between ion current and concentration, both as a function of concentration and depth. The coefficient of diffusion of indium in germanium determined from our measurements is in good agreement with the values found by others using methods different from ours.

INTRODUCTION

Widely used methods for the analysis of solids are emission spectroscopy, x-ray fluorescence analysis, neutron-activation analysis, and spark-source mass spectrometry.

The increasing interest in the properties of surfaces had led to the development of another mass-spectrometric method: the ion-bombardment mass spectrometry.

Besides its usefulness for the analysis of surfaces, this method may also be used to study bulk composition and catalytic processes.¹⁻⁶

In the ion-bombardment mass spectrometer the ions of the sample are generated by continuously bombarding the surface of the sample with a beam of primary ions. The properties of the primary-ion beam, such as current density, energy, beam cross section, are well defined and constant. They can, moreover, be easily varied. Impurity concentrations can be determined by this method as a function of depth. Averaging across the concentrations obtained for different-depths in the bulk gives the average concentration in the consumed bulk volume.

Scanning across the surface with an ion beam^{2,3} or using a secondary ion image^{2,4} provides information about the composition along the surface.

Our experience with this method will be discussed below, especially with regard to the indication of oxides and the determination of diffusion profiles in solid germanium single crystals.

DESCRIPTION OF THE APPARATUS

The sample under investigations is placed (Fig. 1) in the ion source of a single-focusing sector-type mass spectrometer.⁷ The primary ion beam i_p is extracted from a modified Penning source and consists of argon ions of 11 keV energy; it impinges on the surface at an angle of 20°. Those particles of the sample which leave the surface directly as positive or negative ions will be separated according to their mass-to-charge ratio. An electron beam for the ionization of particles sputtered as neutrals is also incorporated in our mass spectrometer, but has not been used in this investigation. Currents of the positive ions between 10^{-9} A and 10^{-15} A are detected with a dc amplifier and, currents between 10^{-15} A and 10^{-20} A with an ion-to-electron converter.⁸ For the negative ions only the dc amplifier can be used.

During bombardment of the sample a mass spectrum is obtained by variation of the magnetic field. Mass indication is achieved by measuring the magnetic field with a Hall probe assembly. The digitized signal of the Hall probe is recorded simultaneously with the mass spectrum on an 18-channel UV recorder.

The primary-ion source consists of a modified Penning ion source, a unipotential lens, and two pairs of electrostatic deflection plates. With the aid of this ion optics system and some diaphragms a fraction of the ion current extracted from the Penning ion source may be selected to hit the target.

One mercury diffusion pump is used between the Penning ion source and the mass spectrometer, and another one at the mass-spectrometer ion

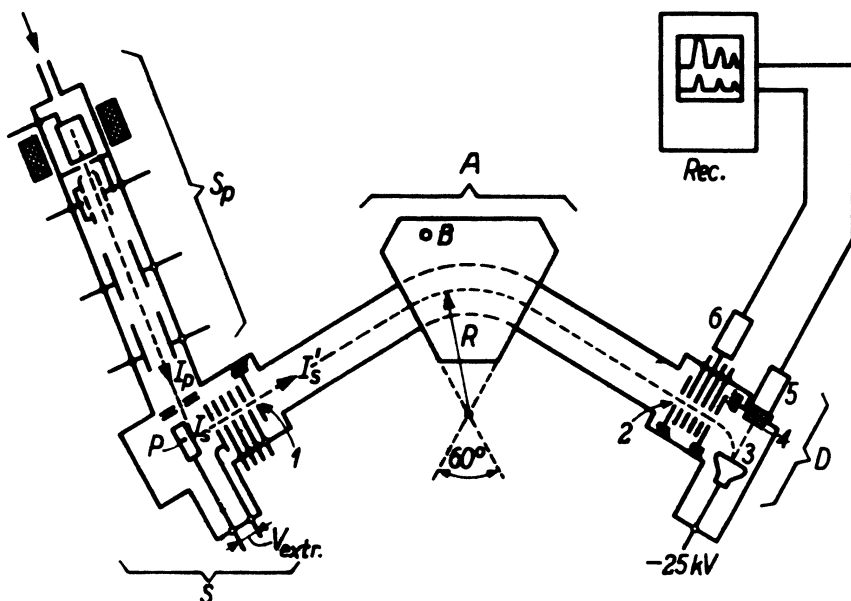


Fig. 1. Schematic representation of the ion-bombardment mass spectrometer.

source. A typical value of the total background pressure after bake out is 2×10^{-7} torr, the Penning ion source not yet in operation. The background gas then consists mainly of H₂, CH₄, H₂O, CO, and CO₂.

To operate the Penning ion source, one has to maintain an argon pressure in the Penning ion source of 10^{-3} torr, which increases the argon partial pressure in the mass-spectrometer ion source to 10^{-5} torr. The pressure of the residual gases mentioned before rises to 3×10^{-7} torr, as an additional component, oxygen, is now found at a pressure of 6×10^{-10} torr.

During bombardment two processes take place at the surface of the sample: (1) molecules from the residual gas atmosphere hit the sample and remain on it according to their sticking probability, and (2) these particles are desorbed due to the bombarding primary ions.

For carrying out an analysis of the sample this rate of desorption must be larger than the rate of adsorption.

An estimate shows that for a primary-ion current density j_p between 6 and $13 \mu\text{A}/\text{cm}^2$ – values used in most of our measurements – and an energy of the argon ions of 11 keV this requirement is met at the above-mentioned residual gas pressure of 3×10^{-7} torr.

THE SECONDARY IONS

The Mass Spectrum of the Secondary Ions

As an example we discuss the spectra from an aluminium target after different times of bombardment. The spectrum of the positive ions (Fig. 2) consists, among other things of Ar^+ , the target ions Al^+ , and Al^{2+} , and the cluster ions Al_2^+ , and $(\text{AlMg})^+$. We also find oxides (AlO^+), and in most cases Na^+ and K^+ .

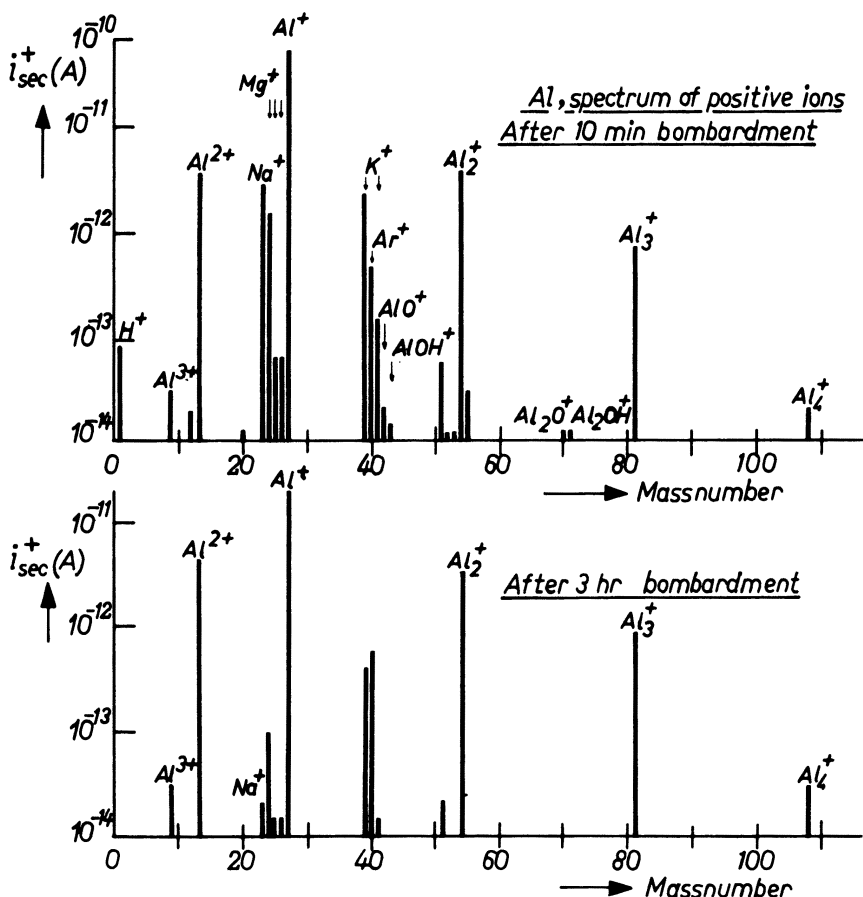


Fig. 2 Spectrum of positive ions from an aluminium sample after 10 min and after 3 hr of bombardment.

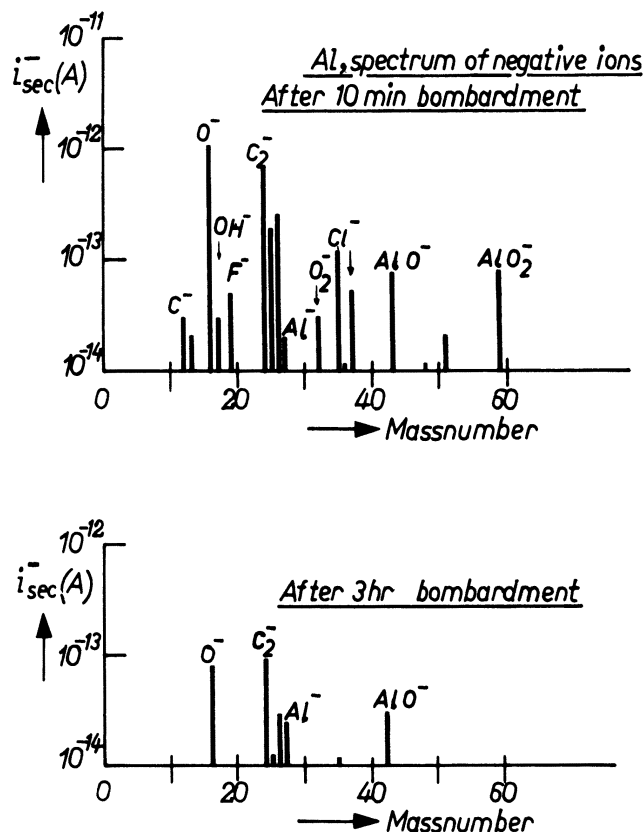


Fig. 3. Spectrum of negative ions from an aluminium sample after 10 min and after 3 hr of bombardment.

The spectrum of the negative ions (Fig. 3) consists of the target ion Al^- and of O^- , Cl^- , OH^- , F^- , and C^- . After three hours of ion bombardment some of the peaks originally present in the spectrum of both the positive and the negative ions have disappeared. These peaks were due to elements which had been present in a "surface zone" extending not too far into the bulk.

The Origin of the Secondary Ions

The mechanism leading to the emission of positive ions from the sample under ion bombardment is not yet fully understood.⁹⁻¹³ However, a

TABLE I

**Properties of the Secondary Ions from an
Ion-Bombardment Ion Source**

Ion yield (positive and negative ions)	
	Information on surface and bulk composition (semiquantitative analysis)
Energy spread of the secondary ions	
	Information on the origin of the ions [bulk material, surface layers (cf. time dependence), molecules from the gas phase]
Secondary ion current as a function of time	
	Information on: Chemical state (oxidation), use of positive and negative ions Surface layers (cf. energy spread) Diffusion profiles

simplified picture of this mechanism may be given as follows:¹⁴ the primary ions penetrate the target to a given average depth. By collisions they transfer their energy to the target atoms. A fraction of these collisions results in target atoms having a momentum pointing toward the surface. These particles in turn may transfer sufficient energy to other target atoms, which may be put into an ionized state and, if sufficiently close to the surface, be emitted from the target. Due to neutralization processes^{12,15,16} only a fraction of these ions originally produced inside the target are able to leave the target still in an ionized state.

**PROPERTIES OF THE SECONDARY IONS FROM
AN ION-BOMBARDMENT ION SOURCE
WHICH MAY BE USED FOR ANALYTICAL PURPOSES**

The properties of interest are summarized in Table 1.

Yield of Positive Ions

An element of mass M gives the ion current $i_{M,\text{coll}}$ at the ion collector. This ion current $i_{M,\text{coll}}$ is defined as the sum of the currents of all the isotopes of the element M under consideration,

$$i_{M,\text{coll}}^+ = i_p (c_M/10^6) S_M^+ \eta^+ = i_{\text{sec}} \eta^+ \quad (1)$$

where i_p is the primary-ion current at the target, c_M is the concentration of the element M (in ppm at.), S_M^+ is the absolute yield of secondary, positive ions of element M , η^+ is the fraction of the secondary ion current i_{sec} arriving at the collector (η^+ may depend on mass M and on the conditions of extraction — e.g., geometry, extracting voltage V), and i_{sec} is the current of the secondary ions emitted from the target. Previous studies have shown that the matrix may have slight influence on S_M^+ ^{7,18} and that S_M^+ is independent of the concentration^{7,17,18} in the particular concentration range considered. The influence of the degree of oxidation on S_M^+ will be discussed later.

For practical reasons, however, we deal with the relative ion yield of element M with respect to iron, which is defined as

$$S_{\text{rel}}^+ = \frac{S_M^+}{S_{\text{Fe}}^+} = - \frac{i_{M,\text{coll}}^+}{i_{\text{Fe},\text{coll}}^+} \frac{i_p \eta_{\text{Fe}}^+}{i_p \eta_M^+} \frac{c_{\text{Fe}} 10^6}{c_M 10^6} \quad (2)$$

Assuming that i_p and the conditions of extraction are kept constant, and taking $\eta_{\text{Fe}}^+ = \eta_M^+$ and $c_M = c_{\text{Fe}}$, S_{rel}^+ becomes

$$S_{\text{rel}}^+ = i_{M,\text{coll}}^+ / i_{\text{Fe},\text{coll}}^+ \quad (3)$$

Values of S_{rel}^+ are given in Table II.

Limit of Detection

In order to estimate the limit of detection, we assume optimum conditions for the mass spectrometer. By optimum conditions we mean that there is no line coincidence between the isotope of the element used for calculation and any other mass line, and that there is no tail of any intense mass line extending onto the position of the isotope under consideration. As the second requirement cannot be met in all cases with the limited resolution of a single-focusing instrument, the use of a mass spectrometer with higher resolution is advisable for analytical purposes.

The minimum detectable concentration $c_{\min,M}$ (in ppm at.) of an element with mass M is (see Appendix A):

$$c_{\min, M} = \frac{10^6 i_{\min, i} (100/a_i)}{i_r, \text{coll} (100/a_r) S_{\text{rel}}^+} \quad (4)$$

where $i_{\min, i}$ is the minimum detectable ion current of the isotope i belonging to the element M , a_i is the abundance (%) of isotope i , i_r, coll is the ion current of the iron isotope r (reference) measured at the collector, and a_r is the abundance (%) of isotope r .

The minimum detectable ion current when using an ion-to-electron converter⁸ is limited for practical reasons (maximum time allowed per mass peak) to about 10^{-19} A . It is independent of i_p .

The total iron current at the collector, $i_{\text{Fe}, \text{coll}} = i_r, \text{coll} 100/a_r$, using the extraction conditions of our mass spectrometer amounts to $1.4 \times 10^{-12} \text{ A}$ for $i_p = 1 \mu\text{A}$. Estimates according to Eq. (4) for the minimum detectable concentrations of some elements in an iron matrix, using the above values, are given in Table III.

Increasing the primary ion current i_p will improve the minimum detectable concentration, but the amount of material consumed will also increase.

TABLE II
Relative Yield S_{rel}^+ of Some Elements for the
Formation of Positive Ions

Element	Al	Cr	Ti	Mo	W	Re	Fe	Si	Ta	Au
S_{rel}	15.4	9	8	3.2	0.5	2.5	1	3.6	0.2	0.02

TABLE III
Calculated Minimum Detectable Concentrations $c_{\min, M}$
of Some Elements in an Iron Matrix

Element (isotope)	S_{rel}^+	Matrix (isotope used)	i_p (μA)	A (cm^2)	$c_{\min, M}$ (ppm at.)
Al (27)	15.4	Fe (56)	1	0.15	0.005
Ti (48)	8	Fe (56)	1	0.15	0.01
Si (28)	3.6	Fe (56)	1	0.15	0.02
Cu (63)	0.35	Fe (56)	1	0.15	0.3
Ta (181)	0.2	Fe (56)	1	0.15	0.4
Pb (208)	0.04	Fe (56)	1	0.15	3
Au (197)	0.02	Fe (56)	1	0.15	4

Material Consumption

The minimum detectable concentration $c_{\min, M}$ and the volume $\dot{z}A$ consumed per unit of time are related by: (see Appendix B)

$$c_{\min, M} = \frac{10^6 i_p^+ (100/a_i)}{\dot{z} A \kappa S_{\text{rel}}^+} \quad (5)$$

where \dot{z} is the layer thickness (cm) sputtered away per second, A is the area of the target (cm^2) hit by the primary-ion beam, and κ is a constant for a given element (see Appendix B).

The values for $c_{\min, M}$ and the (matrix) layer thickness sputtered away during an analysis (≈ 1 hr) for primary-ion currents of 1, 10, and 100 μA are given in Table IV. For the determination of diffusion profiles 10 μA for i_p and the corresponding $c_{\min, M}$ are the limit, whereas for bulk analysis one would even like to have values for i_p between 100 μA and 1000 μA in order to average over a larger depth during the analysis.

Negative Ions

The absolute yield of the negative ions S_M^- , their relative yield S_{rel}^- , and the minimum detectable concentration when using the current of the negative

TABLE IV
Calculated Minimum Detectable Concentrations $c_{\min, M}$ of Some Elements
in an Iron Matrix and Consumed (Matrix) Material

Element (isotope used)	S_{rel}^+	Matrix					
		Matrix (isotope used)	A (cm^2)	i_p (μA)	$c_{\min, M}$ (ppm at.)	Layer Thickness removed in 1 hr, \dot{z} ($\text{\AA}/\text{hr}$)	Volume consumed in 1 hr, \dot{V} (mm^3/hr)
Ti (48)	8	Fe (56)	0.15	1	0.01		
Ta (181)	0.2	Fe (56)	0.15	1	0.4	860	0.0013
Au (197)	0.02	Fe (56)	0.15	1	4		10
Ti (48)	8	Fe (56)	0.15	10	0.001		
Ta (181)	0.2	Fe (56)	0.15	10	0.04	8600	0.013
Au (197)	0.02	Fe (56)	0.15	10	0.4		100
Ti (48)	8	Fe (56)	0.15	100	0.0001		
Ta (181)	0.2	Fe (56)	0.15	100	0.004	86000	0.13
Au (197)	0.02	Fe (56)	0.15	100	0.04		1000

TABLE V
Relative Yields of Some Elements for the Formation of Negative Ions,
 S_{rel}^- , of Positive Ions, S_{rel}^+ , and the ratio $S_{\text{rel}}^-/S_{\text{rel}}^+$

	Al	Fe	Ge	Zr	Cu	Pt	Ag	Pb	Au
S_{rel}^-	4.4	[1]	12	1	6.6	1.4	2.4	0.2	7.4
S_{rel}^+	15.4	[1]	0.9	0.6	0.35	0.13	0.05 (0.5)	0.04	0.02
$S_{\text{rel}}^-/S_{\text{rel}}^+$	0.29	[1]	13.3	1.6	19	10	4.8 (48)	5.5	370

* Reference element: Iron.

ions are defined in the same way as when positive ions are used:

$$\begin{aligned} i_{M, \text{coll}}^- &= i_p (c_M / 10^6) S_M^- n^- \\ S_{\text{rel}}^- &= S_M^- / S_{\text{Fe}}^- = i_{M, \text{coll}}^- / i_{\text{Fe, coll}}^- \\ c_{\min, M} (\text{ppm at}) &= 10^6 \frac{i_{\min, i}^-}{i_{r, \text{coll}}^-} \frac{a_r}{a_i} \frac{1}{S_{\text{rel}}^-} \end{aligned}$$

Table V shows some values of the relative yields of negative ions with respect to Fe. One can see that the relative yields differ by a factor 60 (Ge and Pb) at the most, whereas the yields of the positive ions in the most unfavorable case (Al and Au) differ by as much as a factor of 700.

From the values of $S_{\text{rel}}^-/S_{\text{rel}}^+$ one could conclude that the limit of detection might be considerably improved for Au, e.g., (factor of 370) by using the spectrum of the negative ions. This is not the case, however, as the reference current for the negative ions, $i_r^- = i_{\text{Fe}}^- = 1 \times 10^{-14} \text{ A}$, is a factor of about 100 smaller than the corresponding one for the positive ions, $i_r^+ = i_{\text{Fe}}^+ = 1.4 \times 10^{-12} \text{ A}$. It is a favorable property of the negative-ion yield (which in these preliminary measurements we have determined only for technically-pure samples) that the yields do not differ too much. Should this also apply to the elements in various matrices, it might give a method for semiquantitative, low-selectivity analysis of the elements involved. Moreover the use of the negative-ion spectrum gives us a method of indicating the presence of the strongly electronegative elements F, Cl, O₂, when present only in small concentrations.

Reproducibility

The reproducibility of the ion yield, which is mainly dependent on the vacuum and on the condition of the surface, is rather good. For the absolute

positive-ion yield of Ge single crystals the maximum deviations from a mean value out of seven measurements taken within four months was $\pm 16\%$. Because of the possible influence of oxidation on the ion yield, which will be discussed later, we do not claim that the method is more than a semiquantitative one.

As long as the ion yield cannot be calculated for any element in a given matrix, standard samples have to be used to correct for possible matrix effects and to determine the relative yields, although the use of the negative ions might allow one to do without the determination of the latter.

A big advantage of the ion-bombardment method when using standard samples is that its ion current is the average over a fairly large area of the sample, in our case $3 \times 5 \text{ mm}^2$. Because of this property the requirements of sample homogeneity are not too stringent.

Energy Spread

Figure 4 shows as a preliminary result plots of the ratio (peak width at half-height)/(mass number), which is a measure of the relative energy spread $\Delta V/V_{\text{acc}}$ against mass number.

One can see from these plots that there are three groups of ions:

1. In the top curve we have positive ions with the highest energy spread. They all originate from bulk material.

2. These ions are followed by positive ions like Li^+ , Na^+ , and K^+ . For the negative ions, not shown here, we found an analogous curve with medium energy spread, represented by ions like OH^- , C_2H_2^- , C_2H_2^- , and O_2^- . Besides the energy spread, these ions of the second curve had in common the fact that they disappeared after a relatively short time of bombardment, which means that they originate from contaminations from the surface.

3. Molecules from the gas phase which are ionized by the primary-ion beam have the lowest energy spread (lowest curve).

While this work was being carried out Benninghoven¹⁴ independently found similar criteria for ions of various origin.

The Influence of Oxidation on the Ion Yield

This effect is revealed by measuring the secondary-ion current as a function of time (primary current and source adjustment kept constant).

Figure 5 shows the positive copper-ion current from an OFHC Cu target

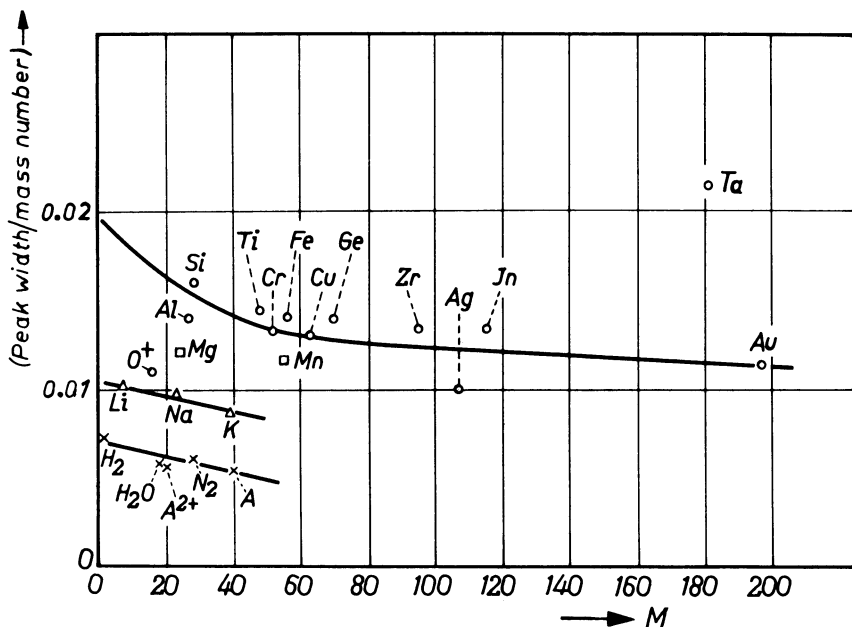


Fig. 4. Energy spread of ions originating from bulk material (top curve), surface layers (middle curve), and from molecules from the gas phase (lowest curve). The peak width at half-height divided by the mass number is plotted against mass number.

as a function of time. Curve 1 is from a heavily-oxidized target. The Cu^+ peak stays constant during the first 2 hr, corresponding to a depth of 2000 Å, under the conditions indicated in the figure. During the next 30 hr it drops gradually to a constant final value about a factor of 30 lower.⁷ The Cu^+ peak in curve 2, from a slightly-oxidized Cu target, starts at a lower value and also drops as a function of time to about the same final value of about 3×10^{-13} Å. Curve 3, from a Cu target filed bright, stays practically constant at 3×10^{-13} Å during the measurement. This behavior can be understood if we observe the spectrum of the negative oxygen ions from the target, which are measured alternatively with the positive copper ions. From the two top curves we can see that complete oxidation of the copper had extended to a depth of about 2000 Å. Within this layer the copper peak as well as the negative oxygen peak is constant. When the primary ions have removed this heavily and completely oxidized layer they successively penetrate into layers with a lower degree of oxidation. The oxygen peak drops accordingly, but the copper peak does so as well. As the concentration of the copper atoms in the technically-pure target may be considered constant, we must conclude from

this that the yield of copper from the oxide layer is greater than from what we may call the "unoxidized" copper target at an oxygen partial pressure of 6×10^{-10} torr in front of our sample. Slodzian¹⁹ and Benninghoven²⁰ came to the same conclusion by varying the oxygen pressure in front of the target or using oxygen ions as the primary ions.

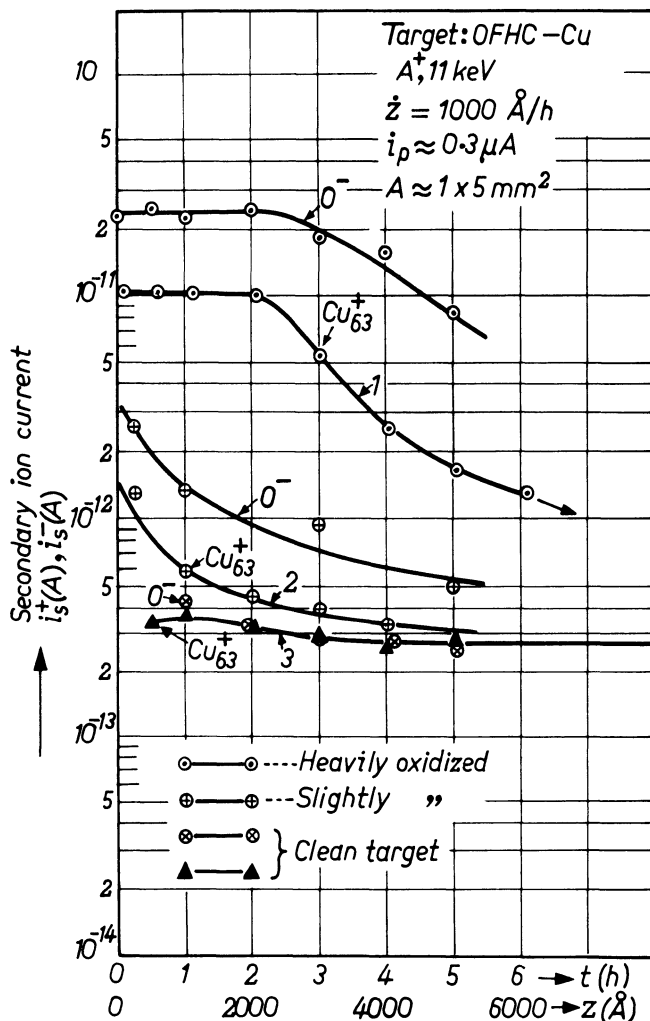


Fig. 5. Secondary-ion currents of Cu^+ and O^- as a function of time from copper targets with various degrees of oxidation.

A simple explanation for this increase in the yield is that the oxide dissociates during the ion bombardment and that the oxygen, which is well known to be strongly electronegative, takes an electron from the copper atom, thus leading to an increased formation of positive copper ions inside the target.

As the ratio of the Cu^+ ions and the O^- ions is roughly constant in time, one might conclude that they originate from the same molecule. The increased rate of formation of copper ions inside the target as described before does not, however, necessarily mean an increased ion yield. This is because the ion yield, which is proportional to the number of secondary ions emitted from the target per impinging ion under given conditions, is the product of (1) the rate of formation of the ions inside the target, and (2) the probability that the ions formed inside the target are not neutralized, i.e., survive. It has been shown^{1,6} that in the case of oxides this chance of survival is increased due to the occurrence of forbidden energy regions.

In conclusion one might say that extrapolating to other metals the use of the positive metal ion and the negative oxygen ion permits the indication of metal oxides in solids.

Moreover, the use of oxygen ions as primary ions or the increase of the oxygen pressure in front of the target might be used to increase the sensitivity in the detection of metals.

Parent Molecules

Figure 6 shows the ion currents of Na^+ and Cl^- as a function of time released from a NiCr layer vacuum-deposited onto glass. Na^+ and Cl^- are found to be roughly proportional to each other as a function of time in the vacuum-deposited layer. It seems logical to assume that these ions originate from a sodium chloride (parent) molecule. This is not the case in the glass substrate, as illustrated by Fig. 6, as the time dependence of sodium is different from that of chloride.

The Determination of Diffusion Profiles

Knowledge of the diffusion profiles of impurities in semiconductors is vital to an understanding of some semiconductor properties. In simple cases the diffusion profiles may be calculated, but calculations for more complex cases soon become difficult. There has for some time been a need for a simple experimental method for the determination of diffusion profiles. By

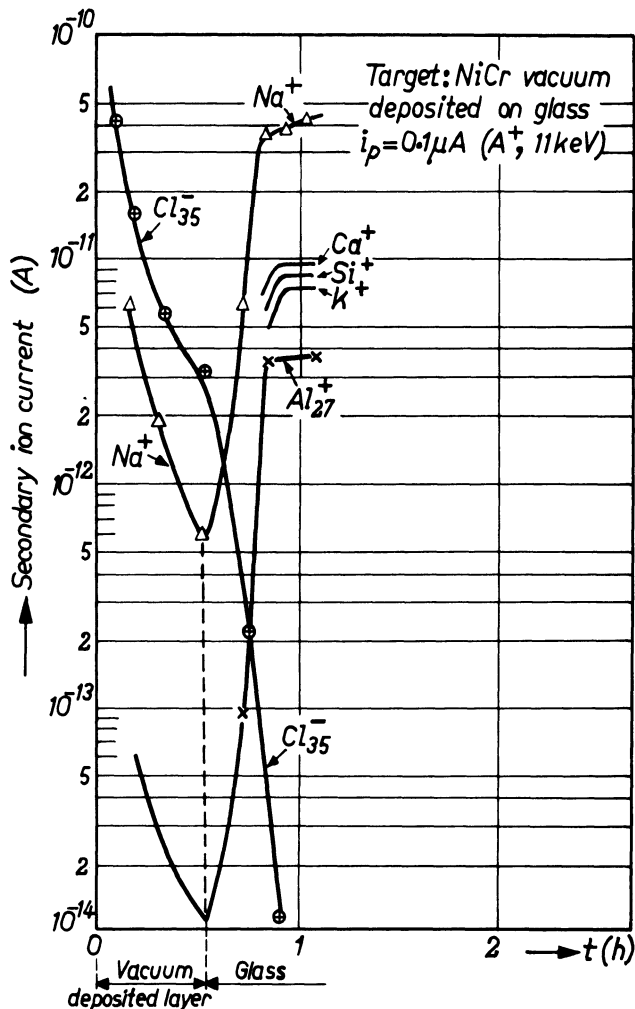


Fig. 6. Secondary-ion currents of Na^+ and Cl^- as a function of time from a NiCr layer vacuum-deposited on glass.

continuously bombarding a solid surface in an ion-bombardment mass spectrometer, layer by layer is sputtered away, and by measuring the secondary ion currents, $i_M^+(t)$ and $i_M^-(t)$, as a function of time one can, if certain requirements are met, find the concentration c_M as a function of depth (see Appendix C).

*Check on the Usefulness of the Ion-Bombardment Method
for the Determination of Shallow Diffusion Profiles*

We have investigated the indium distribution $c_{In}(z)$ in germanium single crystals as a function of depth z . The flat Ge plates ($8 \times 9 \times 1$ mm) were polished, and indium from the gas phase at constant pressure was allowed to diffuse into them at various temperatures T and times t .*

Due to the experimental setup, the concentration of In at the surface $c(0)$ was constant all the time. The solution of Fick's second law in that case gives:

$$c(z) = c(0) \operatorname{erfc} [z/2\sqrt{DT^*}] \operatorname{erfc} u$$

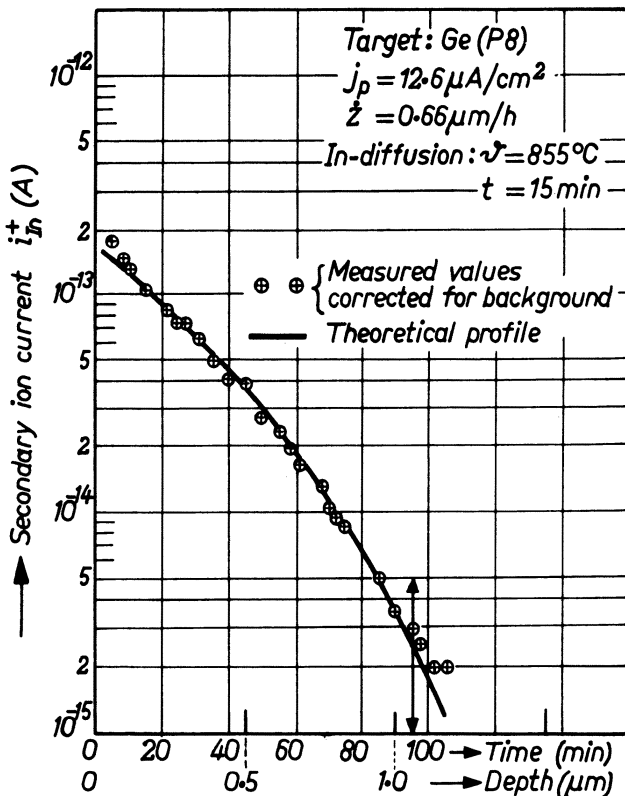


Fig. 7. Indium current from a germanium sample as a function of time. Comparison of experimental values \oplus with theoretical profile (solid line).

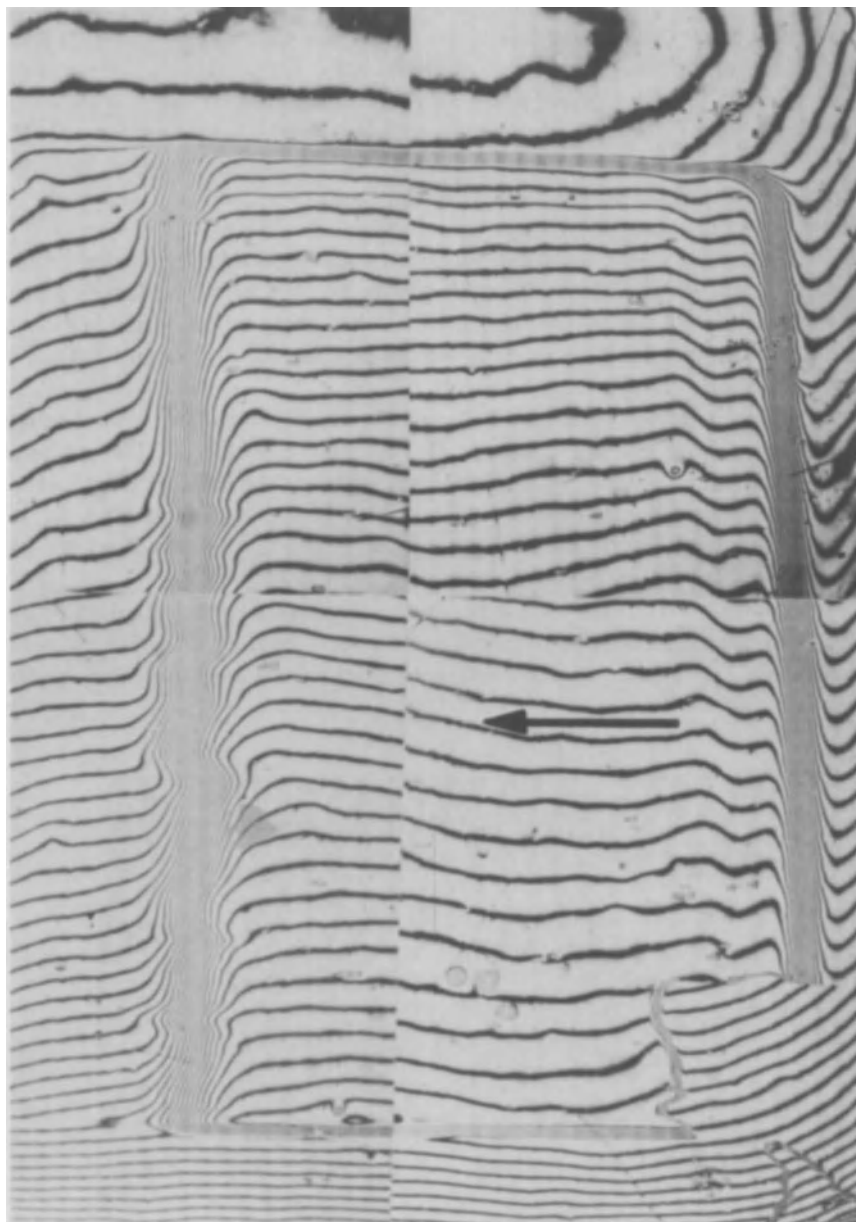


Fig. 8a. Interference micrograph (5890 Å) of a germanium surface after 7½ hr of bombardment. The sample had been held in place by several clamps, one of which extended partially into the bombarded area, thus preventing part of the germanium sample (right lower corner) to be sputtered away. Direction of incidence of the primary ion beam is indicated by an arrow.

where $c(z)$ is the In concentration (at depth z) = f ; $c(0)$ is the In concentration at the surface; $\text{erfc } u = 1 - \text{erf } u = 1 - (2/\sqrt{\pi}) \int_0^u e^{-\eta^2} d\eta$; D is the coefficient of diffusion (cm^2/sec) = $D(T)$, with T the absolute temperature ($^\circ\text{K}$); and t is the time during which In diffused into the Ge (sec).

In Figure 7 we have compared our experimental values (○○○) with the theoretical curve, represented by the full line. Within the limit of error our experimental points fit the erfc function quite well, down to a depth of about 1μ in this case, in other cases only down to 0.75μ .

The spread in the measured values increases quite rapidly toward smaller concentration values due to the overlap with the tail of an unidentified peak at the location of the indium peak. This shows that for the determination of the diffusion profile beneath 1μ our single-focusing instrument has to be replaced by one giving a higher resolution.

Below 1μ we have an additional systematic deviation toward values higher than those given by theory. This is due to a shift of the ion beam across the surface during bombardment, giving the effect described in Appendix C under assumption 2. This shift is due to instabilities in the Penning discharge. Work is being carried out at the moment to eliminate this effect.

Conversion of Time Scale into Depth. To determine the diffusion profile $c(z)$ with depth, as well as to calculate the coefficient of diffusion from the measured $i_{\text{In}}(t)$ values, it is necessary to convert the time scale into depth.

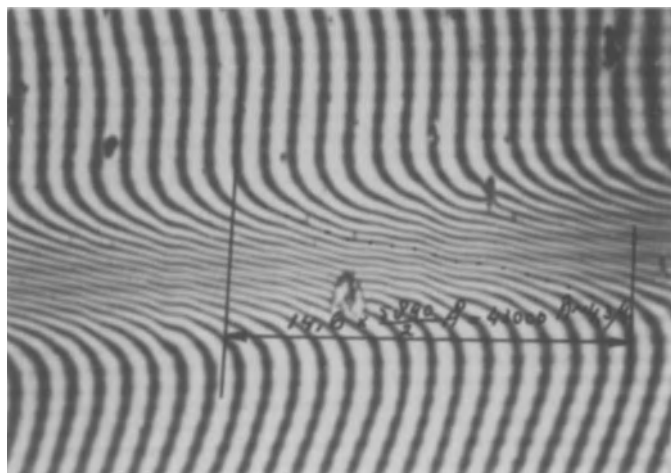


Fig. 8b. Detail of Fig. 8a.

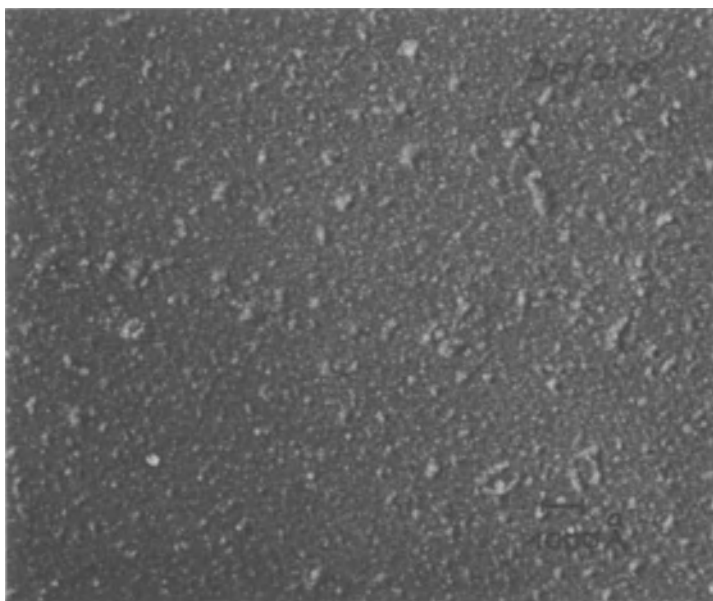


Fig. 9. Electron micrograph of the surface of the germanium sample of Fig. 8 before bombardment.

For this purpose a germanium sample was bombarded with a constant primary-ion current density $j_p = 9.6 \mu\text{A}/\text{cm}^2$ of 11-keV argon ions during 7½ hr. The depth of the pit, flat at the bottom as revealed by an interference microscope (Figs. 8a and 8b), was 4 μ on the average. The rate of removal determined from this is 0.5 μ/hr , corresponding to a sputter rate $S = (\text{number of sputtered neutral particles})/(\text{number of primary ions}) = 10.5$. Electron micrographs of a germanium sample before (Fig. 9) and after (Fig. 10) bombardment show no difference, which means that the germanium had been removed uniformly all over the surface also on a microscale. We may conclude from this that the sputter rate S has been the same across the bombarded area during the bombardment.

Determination of D and $D(T)$

Having converted the time scale into depth, we were able to determine the coefficient of diffusion from our experimental ion-current versus time curves. Figure 11 shows a semi-log plot of D versus $1/T$. From the linear

relationship we find that D may be represented as $D(T) = D_0 \exp(-Q/RT)$, where $D_0 = 300 \text{ cm}^2/\text{sec}$ and $Q = 75.3 \text{ kcal/mole}$. In view of the great uncertainty introduced when extrapolating to $1/T \rightarrow 0$, for the determination of D_0 these values are in good agreement with those given by Bösenberg,²¹ who has determined the diffusion profile by electrical measurements. His values were $D_0 = 20 \text{ cm}^2/\text{sec}$ and $Q = 69.2 \text{ kcal/mole}$. Values of D given by Dunlap²² also fit ours quite well.

For the case of indium diffused into germanium single crystals we were thus able to show (1) that this ion-bombardment method gives diffusion profiles which are in good agreement with the theoretical ones down to a depth of about 1μ , and (2) that the values of the coefficient of diffusion as a function of temperature, as well as the activation energy, are in good agreement with values found by others. It is our aim to use this method for the determination of diffusion profiles in cases where a calculation is impossible.

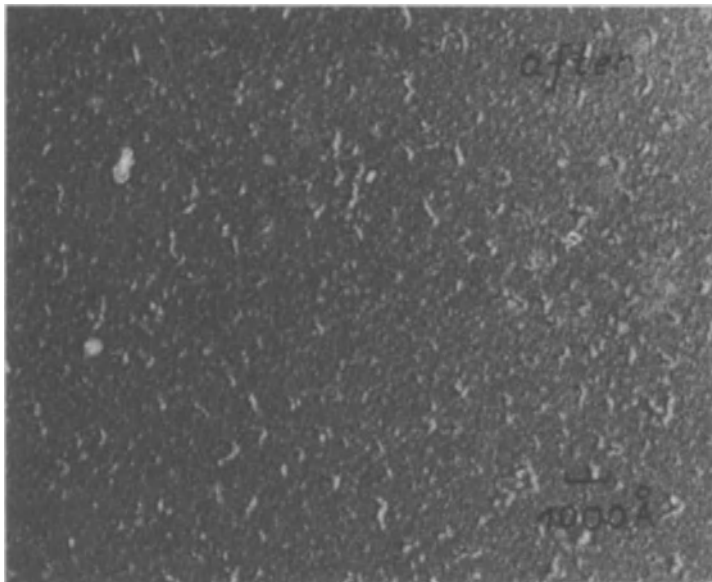


Fig. 10. Electron micrograph of the bottom of the pit from the same germanium sample as in Fig. 9 after $7\frac{3}{4}$ hr of bombardment.

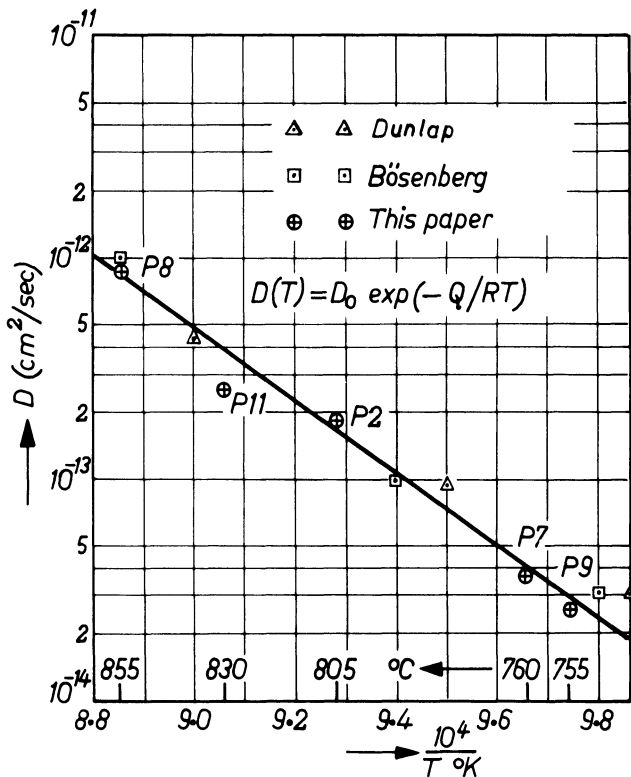


Fig. 11. Semi-log plot of D versus $1/T$.

CONCLUSIONS

The results presented demonstrate the usefulness of the ion-bombardment mass spectrometry for application in bulk analysis and surface analysis and for the determination of diffusion profiles. Our results reported here are preliminary to a certain degree, but we hope to improve the method, particularly with regard to (1) improving the detectable concentration, by using a higher primary-ion current and by using a mass spectrometer with a better resolution, and (2) surface analysis, hoping to get a better understanding of the processes involved when secondary ions are emitted from surface layers or from bulk material.

ACKNOWLEDGMENT

The author wishes to express his thanks to Dr. A. Venema for his continuous interest in this work, to Mr. H. A. M. de Grefte and Mr. J. v.d. Berg for assistance in the experiments, and to Mr. H. A. M. op het Veld and Mrs. J. R. A. Gijsbers for carefully preparing the interference micrograph and the electron micrographs, respectively.*

APPENDIX A

Minimum Detectable Concentration

The minimum detectable concentration $c_{\min, M}$ (ppm at.) of an element with mass M when using the ion current i_i of its isotope i with abundance a_i (%) is found from Eq. (1) as

$$c_{\min, M} = \frac{10^6 i_{\min, i}^+ (100/a_i)}{i_p S_M^+ \eta^+} \quad (A1)$$

where $i_{\min, i}$ means the minimum detectable ion current of the isotope i at the collector.

Taking iron as reference and inserting $S_M^+ = S_{\text{rel}}^+ S_{\text{Fe}}^+$ into (A1), we find, if we also assume $\eta^+(M) = \eta^+(\text{Fe}) = \eta^+$

$$c_{\min, M} = \frac{10^6 i_{\min, i}^+ (100/a_i)}{i_p S_{\text{Fe}}^+ \eta^+ S_{\text{rel}}^+} \quad (A2)$$

Applying (1) to iron and taking $c_{\text{Fe}} = 10^6$ ppm, we find

$$i_{\text{Fe, coll}} = i_p (S_{\text{Fe}}^+ \eta^+) \quad (A3)$$

Inserting (A3) into (A2) and using the relation

$$i_{\text{Fe, coll}}^+ = i_{r, \text{coll}}^+ (100/a_r) \quad (A4)$$

*While the work described in the paper was in progress it came to our attention that diffusion profiles in semiconductors were studied by Bailleul-Langlais²⁵ using the ion-microprobe analyzer described by Castaing.²⁶

gives

$$c_{\min, M} = \frac{10^6 i_{\min, i}^+ (100/a_i)}{i_{r, \text{coll}}^+ (100/a_r) S_{\text{rel}}^+} \quad (\text{A5})$$

where $i_{r, \text{coll}}$ is the ion current of the iron isotope r at the collector and a_r is the abundance (%) of the iron isotope r .

APPENDIX B

Relation between the Minimum Detectable Concentration and the Material Consumed

We have found Eq. (A5) for the minimum detectable concentration of an element M . The total iron current at the collector, Eq. (A4) has been found to be related to the primary ion current i_p as in Eq. (A3). If we let j_p denote the primary current density impinging on the target across an area A , we obtain

$$i_{\text{Fe, coll}}^+ = j_p A S_{\text{Fe}}^+ \eta^+ \quad (\text{B1})$$

As can be seen from (A3) – (A5), an increase of i_p would increase $i_{\text{Fe, coll}}^+$ and therefore improve $c_{\min, M}$, because $i_{\min, i}$ only depends on the choice of the detecting system and not on i_p . As the bombardment area $A = 0.15 \text{ cm}^2$ cannot be enlarged for practical reasons, an increase in i_p means an increase in j_p .

It has been shown⁷ on the other hand that the layer thickness \dot{z} (μ/hr) removed from the Fe matrix per unit of time is given by (j_p in $\mu\text{A}/\text{cm}^2$, ρ in g/cm^3)

$$\dot{z} = (3.6 \times 10^{-4} j_p S) (M/\rho) \quad (\text{B2})$$

$$\dot{z} = j_p S k \quad (\text{B2}')$$

where S is the number of sputtered atoms per impinging primary ion (taken to be five for Fe in our case), M is the molecular weight, and ρ is the density. For $i_p = 1 \mu\text{A}$ we find in this case for iron $\dot{z} = 8.6 \times 10^{-2} \mu/\text{hr}$.

Substituting j_p from (B2') into (B1) gives

$$i_{\text{Fe, coll}}^+ = \dot{z} A (S_{\text{Fe}}^+/S) (\eta^+/k) = \dot{z} A \kappa \quad (\text{B3})$$

where $\kappa = i_{\text{Fe, coll}}/\dot{z}A$ is a constant depending on the element (Fe) under consideration. With $A = 0.15 \text{ cm}^2$ a calculated value of $\dot{z} = 2.4 \times 10^9 \text{ cm/sec}$ and a total iron current $i_{\text{Fe, coll}}$ measured at the collector of $1.4 \times 10^{-12} \text{ A}$, we find $\kappa = 3.9 \times 10^3 \text{ C/cm}^3$. Keeping in mind relation (A4), a substitution of (B3) into (A5) gives

$$c_{\min, M} = \frac{10^6 i_{\min, i} (100/a_i)}{\dot{z} A \kappa S_{\text{rel}}^+} \quad (\text{B4})$$

which is identical to Eq. (5).

APPENDIX C

Requirements with Regard to the Ion Beam When Diffusion Profiles Are to Be Determined

The primary ion current i_p , which has a current density $j_p(x, y)$ depending in principle on x and y , hits the surface across the area A (see Fig. 12.). The current of secondary ions emitted from the target $i_{\text{sec}}^{\text{target}}$ is the sum of all the contributions $\Delta i = j_{\text{sec}} dA$ from small areas dA , where j_{sec} is the current density of the secondary ions emitted from the target: $i_{\text{sec}}^{\text{target}} = \int_A \int j_{\text{sec}} dA$. With $j_{\text{sec}} = j_p(x, y) S_M^+ c(x, y, z) 10^{-6}$ we find for the current of secondary ions emitted from the target

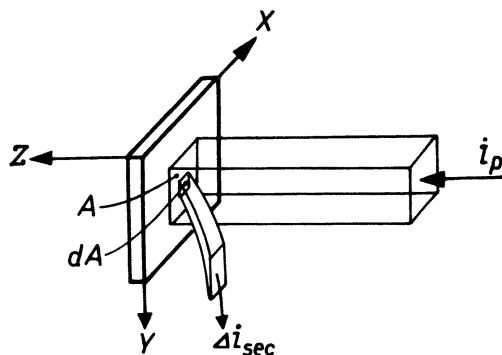


Fig. 12. Schematic representation of primary-ion beam i_p , secondary ions from small surface elements dA , and sample orientation in the mass-spectrometer ion source.

$$i_{\text{sec}}^{\text{target}} = \int_A \int j_p(x,y) S_M^+ c(x,y,z) 10^{-6} dA$$

The ion current at the collector i_{coll} becomes

$$i_{\text{coll}} = \int_A \int j_p(x,y) S_M^+ c(x,y,z) 10^{-6} dA \eta'(x,y) T$$

where S_M^+ is the absolute ion yield; $c(x,y,z)$ is the concentration, which in principle may be a function of x , y , and z ; $\eta'(x,y)$ is the efficiency for extracting the ions emitted from the surface of the target through the extraction slit of the ion source; it may depend on the place of origin (x, y) of the ion; and T is the transmission of the succeeding parts of the mass spectrometer. As can be seen from the definitions of $\eta'(x,y)$, T , and η^+ , $\eta'(x,y)T = \eta^+$.

On the assumptions that (1) the primary-ion current density is constant across the area A ; (2) the concentration varies with depth only: $c(x, y, z) = c(z)$; (3) η' and T do not vary with time; and (4) S_M^+ is also a constant; the ion current at the collector becomes proportional to the concentration, which in turn varies with depth:

$$i_{\text{coll}} = j_p A S_M^+ T c(z) = k_1 c(z)$$

On the further assumption (5) that the rate of removal \dot{z} is constant [see (B2) from Appendix B] the layer thickness $z(t)$ removed after a given time t is proportional to that time

$$z(t) = \int_0^t \dot{z} dt = j_p S K t = k_2 t$$

The time scale may then be calibrated in terms of depth.

Let us next consider the implications of these assumptions in more detail.

Assumption 1. If the primary-ion current density were not constant across the total area, that part with the highest value of the current density would be sputtered most, and after a while the following profile would be obtained (Fig. 13): As the measured secondary-ion current is the sum of the contributions from the areas A_1 and A_2 $i_{\text{sec}} \propto A_1 c_1 + A_2 c_2$, measurements would be made at two points with different concentrations c_1 and c_2 , and an incorrect diffusion profile would be obtained. In order to have the primary-ion current density sufficiently constant across the area A , we have defocused our primary-ion beam, and only a small fraction of the inner part of it was allowed to hit the target. The rest of the ion beam was cut off by a diaphragm of suitable dimensions.

Assumption 2. For the same reason as in assumption 1, the concentration may not vary with x or y . Small dust particles on the surface containing the element under investigation would also falsify the diffusion profile. The

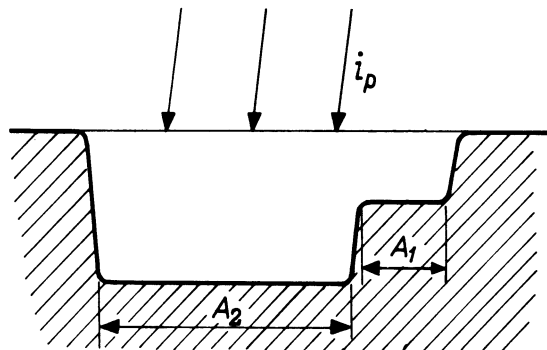


Fig. 13. Cross section (schematic) of the pit of a bombarded sample, illustrating the effect of inhomogeneity in the primary-ion current density.

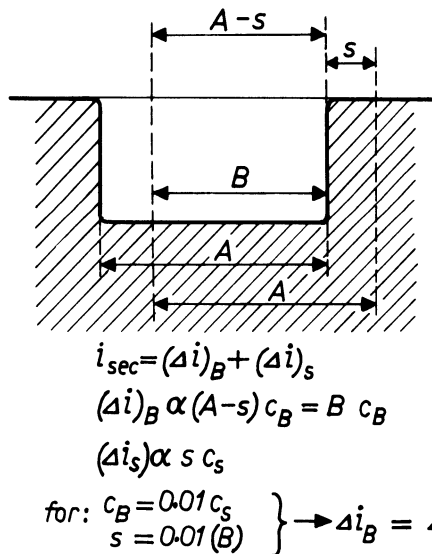


Fig. 14. Cross section (schematic) of the pit of a bombarded sample, illustrating the effect of moving the primary-ion beam across the surface during bombardment.

same result would be obtained if the primary-ion beam moved across the target during bombardment. The secondary-ion current after moving the primary-ion beam is the sum of two contributions (Fig. 14): one from the bottom of the pit i_B and one i_s from a "fresh" surface: $i_{\text{sec}} = i_B + i_s$. Depending on the concentration gradient, the concentration at the bottom c_B

would soon become much smaller than the concentration c_s at the surface. Due to the contribution of the area at the surface, the concentration gradient measured will be higher than the one really present. For the case where $c_B = 0.01 c_s$ and the area at the surface s is only 1% of the area B at the bottom, the two contributions would already be equal.

Assumption 3. The validity of this assumption depends on the stability of the spectrometer.

Assumption 4. The validity of this assumption depends on the surface conditions.

Assumption 5. For a constant removal rate, j_p must be constant and the sputter rate S must be independent of depth.

REFERENCES

1. R. E. Honig, *Advances in Mass Spectrometry*, Elliot, R. M. ed., Vol. 2 Pergamon Press, London (1963), p. 25.
2. H. E. Beske, *Z. Naturforsch.* **19a**, 1627 (1964).
3. A. Benninghoven and F. Kirchner, *Z. Naturforsch.* **18a**, 1008 (1963).
4. H. J. Liebl and R. F. K. Herzog, *J. Appl. Phys.* **34**, 2893 (1963).
5. H. W. Werner, *Philips Tech. Rev.* **27**, 344, (1966).
6. Ya. M. Fogel, *Soviet Phys.-Uspekhi* **10**(1), 17 (1967).
7. H. W. Werner and H. A. M. de Grefte, *Vakuum-Tech.* **17**, 37 (1967).
8. H. W. Werner and H. A. M. de Grefte, *1965 Transactions of the Third International Vacuumcongress*, Stuttgart, Germany, H. Adam, ed., Vol. 2, Part II, Pergamon Press, New York (1965), p. 493.
9. S. Datz and C. Snoek, *Phys. Rev.* **134A**, 347 (1964).
10. A. Benninghoven, *Ann. Physik* **15**, 113 (1965).
11. C. Snoek, W. F. v. d. Weg, R. Geballe, and P. K. Rol, 7th Intern. Conference on Phenomena in Ionized Gases, B. Perović, ed., Građevinska Knjiga, Beograd, 1966.
12. P. Joyes and R. Castaing, *Compt. Rend.* **263**, 384 (1966).
13. W. F. v. d. Weg and P. K. Rol, *Nucl. Instr. Methods*, **38**, 274 (1966).
14. A. Benninghoven, Zum Mechanismus der Ionenbildung und Ionenemission bei der Festkörperstreuung, *Z. Physik*, **220**, 159–180 (1969).
15. P. K. Rol, D. Onderdelinden, and J. Kistemaker, Some Physical Aspects of Sputtering, *1965 Transactions of the Third Intern. Vacuum Congress*, Stuttgart, Germany, Vol. 1.
16. W. F. v. d. Weg, *Nucl. Instr. Methods* **38**, 274 (1966).
17. H. E. Beske, Untersuchung des Ionenbeschusses fester Targets zur Verwendung als Ionenquellen in der analytischen Massenspektroskopie, Paper given at the Spring meeting, Deutsche Physikalische Gesellschaft, Freudenstadt, Germany, 1966, to be published.
18. J. Schelten, Positive Sekundärionenausbeute, gemessen an Standards, Paper given at the Spring meeting, Deutsche Physikalische Gesellschaft, Freudenstadt, Germany, 1967, to be published.

19. G. Slodzian and J. Hennequin, *Compt. Rend.* **263**, 1246 (1966).
20. A. Benninghoven, *Z. Naturforsch.* **22a**, 841 (1967).
21. W. Bösenberg, *Z. Naturforsch.* **10a**, 285 (1955).
22. W. C. Dunlap, *Phys. Rev.* **94**, 1531 (1954)
23. H. Liebl, *J. Appl. Phys.* **38**, 5277 (1967).
24. R. Castaing and G. Slodzian, *Compt. Rend.* **1962**, 1873.
25. J. Bailleul-Langlais, Thesis presented to the Faculty of Science, University of Paris, March 1968
26. R. Castaing, Optique des Rayons X et Microanalyse, IV^e Congrès international sur l'optique des Rayons X et la microanalyse, Orsay, Sept. 1965, Hermann, Paris (1966), p. 48.

Application of Mass Spectrometry to Forensic Toxicology

I. Acidic and Neutral Drugs

Paritosh K. De and Charles J. Umberger

*Department of Forensic Medicine
New York University Medical Center
New York, New York*

and

*Department of Toxicology
Office of Chief Medical Examiner
New York, New York*

The use of mass spectrometry in forensic toxicology to detect acidic and neutral drugs is discussed. The speed and versatility of the mass spectrometer make it suitable for detecting these drugs and their metabolites. The advantages of using this method as an analytical tool include the ability to identify drugs for which good chemical tests are lacking, the use of small samples, and the saving of time by direct determination of acidic and neutral fractions without further purification. The mass spectra of these drugs can be obtained at volatilization temperatures below those necessary for normally-occurring interfering tissue impurities.

INTRODUCTION

In forensic toxicology post mortem examination of the organs, blood, and urine are done to investigate the presence of toxic substances. The organs generally studied are stomach, brain, liver, kidney, and, sometimes, lung. The

nonvolatile acidic and neutral drugs are extracted with an organic solvent after separating tissue materials. In the investigation of acidic and neutral drugs the detection of several kinds of drugs may be required. This can involve not only a large number of drugs, but also their metabolites and various combinations. The use of new drugs and their combinations is becoming increasingly more common. The usage of multiple drugs suggests that the sublethal level of a given drug can be toxic due to potentiation or a simple synergic effect. Greater sensitivity is therefore demanded for the analysis, as the amount of sample is often limited.

Neutral drugs pose the most difficult problems in forensic toxicology because in general they do not give good chemical tests that are applicable in a screening process. Moreover, the interference of chemical tests is more pronounced in tissue extracts.¹

No single method of instrumental analysis can provide as much useful data for the detection of acidic and neutral compounds as the mass spectrometer because of its ability to identify a wide range of organic compounds.^{2,3} Most neutral compounds do not give good ultraviolet spectra. Mixtures of drugs that are present in detectable amounts, particularly with metabolites and normally-occurring impurities, complicate analysis by infrared. The availability of a less-expensive mass spectrometer with a range up to a molecular weight of 800 opened up a new field of application for forensic toxicology.

One of the distinguishing features separating toxicological analysis from chemical analysis is the near impossibility of isolating organic compounds from tissue in a state of purity comparable to the minimum requirements for functional chemical analysis. Controlled temperature allows preferential evaporation or sublimation, with partial separation of interfering tissue components from the drugs and metabolites somewhat analogous to that in fractional vacuum sublimation.¹

EXPERIMENTAL

For the isolation of acidic and neutral drugs from tissue materials the modified Stass-Otto process and subsequent extraction with ether and chloroform at acid pH were used. This is fully described by Umberger.¹ A Bendix time-of-flight mass spectrometer model 12 with 12-107 ion source and 30-12 analogs was used in this study. The mass spectra were recorded in a Honeywell 1508 Visicorder. A heated-crucible direct-inlet system was available for sample introduction. The sample was placed in a quartz crucible which was heated by a tungsten filament at the end of the probe. The probe was provided with a chromel-alumel thermocouple for temperature readout. The

solid materials were directly poured into the crucible in the extracts where there was enough material. In cases of extracts having a small amount of material they were extracted with 95% methyl alcohol, introduced into the crucible with a microsyringe, and then allowed to evaporate under low vacuum to drive off the solvents completely. Special care was taken so that the top and the outside surface of the crucible were free from sample materials. After the crucible was introduced into the mass spectrometer the spectra were taken at room temperature and at two or more different higher temperatures.

Whenever the tissue extract was suspected of having moderate amounts of fats and lipids their extraction with hexane or petroleum ether was performed. The extraction of the residues was carried out at room temperature and then the temperature was lowered. This decreased the slight solubility of some drugs in the solvents and the solution was microsyphoned from the top. The residue was dried under low vacuum.

RESULTS AND DISCUSSION

Table I represents the mass-spectra data for some acidic and neutral drugs. Eight mass peaks above $m/e = 100$ are recorded. The commonly-occurring mass peaks above $m/e = 100$ from the residues extracted from the organs are recorded in Table II. The mass spectra of a normal brain and a liver extract are shown in Figs. 1 and 2.

It is observed from Figs. 1 and 2 that there are various mass peaks below $m/e = 100$ in normal tissue. Therefore in the identification of drugs peaks below $m/e = 100$ are not significant. As there are only a few peaks above 100 from normal tissues, they can be subtracted from the mass spectra in the determination of the acidic and neutral drugs. All other nonvolatile acidic and neutral drugs except urethane (molecular weight 89.09) have molecular weight above 100. With the exception of a few straight chain compounds like acids and substituted ureas, all other compounds give a parent molecular ion peak. Some of the compounds which do not show parent molecular ion peak give $P^+ + 1$ mass peak at higher pressure. With some drugs the parent molecular ion peak is weak in intensity. Of the 100 acidic and neutral compounds investigated, five pairs of barbiturates and two exanthine derivatives have the same molecular weight, and therefore give the same parent molecular ion. They are readily distinguishable from each other by the difference in fragmentation mass peaks.

An examination of the mass spectra of tissue impurities places them in two different groups. The first group of impurities comes at 110°F or below,

TABLE I
Mass Spectra of Some Acidic and Neutral Drugs

Name of compound	Molecular weight	Volatilization temperature	Eight strongest mass peaks, with relative abundance*											
Salicylic Acid	138.12	Room	120 1000	92 600	138 510	121 130	93 72	-	-	-	-	-	-	-
Resorcinol	110.11	Room	110 1000	81 180	82 130	111 80	109 50	83 38	95 25	-	-	-	-	-
Ethinamate	167.2	Room	106 1000	95 549	124 388	96 284	109 279	107 220	105 194	123 82	Paren 8	-	-	-
Phenacetin	179.21	82° - 90°F	108 1000	109 864	179 692	137 488	110 111	180 97	138 96	136 34	-	-	-	-
Doriden	217.26	82° - 90°F	189 1000	132 957	117 762	160 407	217 400	115 320	146 84	202 74	-	-	-	-
Noludar	183.25	82° - 90°F	154 1000	97 572	139 566	125 55	112 53	183 40	168 36	126 30	-	-	-	-
Meprobamate	218.25	82° - 90°F	114 1000	101 732	145 537	144 342	115 160	157 73	116 50	113 45	-	-	-	-
Mebutamate	218	82° - 90°F	115 1000	110 575	157 384	128 238	114 77	116 69	132 56	175 40	-	-	-	-
Pentobarbital	226.26	82° - 90°F	156 1000	141 412	157 265	98 65	142 54	155 51	197 39	112 34	Paren 4	-	-	-
Barbital	184.19	82° - 90°F	155 1000	140 681	97 610	154 231	111 192	156 143	141 88	112 47	Paren 2	-	-	-
Seconal	238.27	82° - 90°F	168 270	167 777	195 277	126 188	196 166	153 105	155 78	182 50	Paren 22	-	-	-
Penthalthal	242.33	82° - 90°F	173 1000	174 578	158 484	242 281	97 169	98 86	129 59	112 48	-	-	-	-
Mephobarbital	246.26	82° - 90°F	217 1000	117 451	118 373	246 360	145 332	103 238	115 207	161 96	-	-	-	-
Phenobarbital	232.23	82° - 90°F	203 1000	232 418	117 379	118 294	103 223	146 200	115 190	161 156	-	-	-	-
Amobarbital	226.27	100° - 105° F	141 1000	156 688	112 435	157 234	168 88	113 79	142 76	197 66	Paren 3	-	-	-
Dilantin	252.26	110° - 113°F	181 1000	105 874	252 847	223 553	209 381	182 367	167 325	208 181	-	-	-	-
Phanadorn	236.26	Above 115°F	150 1000	107 882	207 618	122 326	135 191	105 191	164 161	165 132	Paren 23	-	-	-

**m/e* values above or near 100.

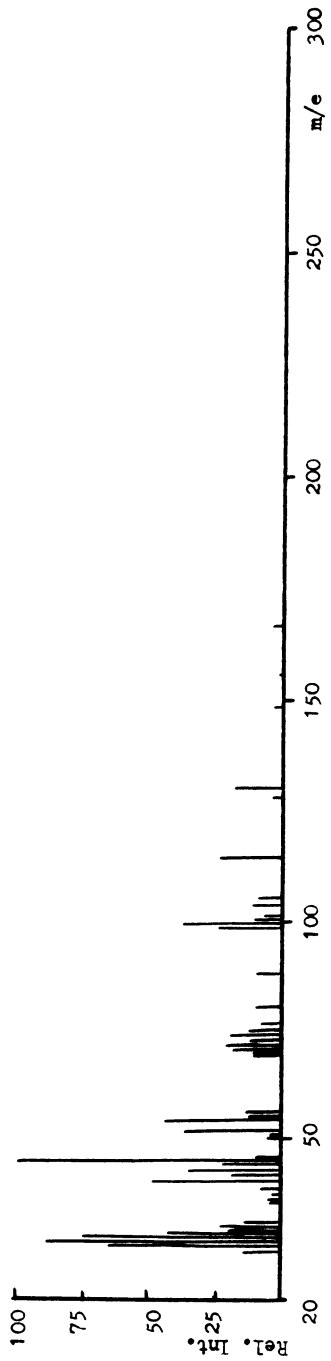


Fig. 1. Mass spectrum of normal brain extract at 105°F.

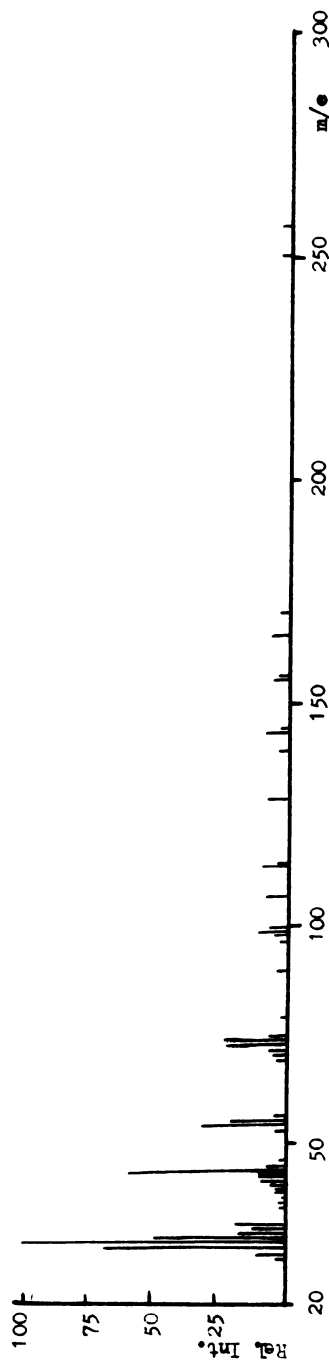


Fig. 2. Mass spectrum of normal liver extract at 110°F.

TABLE II
Mass-Spectral Lines Given by the Impurities
Present in Some Tissue Extracts

<i>m/e</i>	Relative abundance*	<i>m/e</i>	Relative abundance*
100	500	210	2
101	300	224	5
107	260	230	8
114	150	252	16
166	80	257	11
149	33	281	6
150	60	296	10
142	30		
166	14		
171	10		

*Based on 1000 for *m/e* = 43.

and have high vapor pressure. They give *m/e* peaks below or near 100, with the exception of a few impurities not present in all samples. The second group of impurities does not volatilize at 330°F or below under pressure lower than 1×10^{-6} mm.

A few compounds like salicylic acid give mass spectra at room temperature. Some, like pentobarbital, give spectra at temperature around 90°F. Others, such as Dilantin, require higher temperatures of 110–115°F. It is possible to obtain the mass spectra of one component of a mixture at lower temperature, and then elevate the temperature to obtain the mass spectra of the second component and that of the mixture. However, this is influenced by the presence of tissue impurities, metabolites, and other component. The presence of larger amounts of tissue impurities and other components of higher vapor pressure tends to lower the temperature of vaporization of some drugs.

We have been able to identify two compounds in a mixture from tissue elements, and, with little difficulty, as many as three. This is done by linear superposition of the components while taking into account any tissue impurities. With the increase in the scope of drugs included in our study we are working on a computer-based detection by digitizing the mass spectra and storing on tape. Data-processing techniques for low-resolution mass spectra have been described.^{4,5}

In cases of complex spectra involving many compounds the parent molecular ion spectra is plotted at low electron energy and an idea of the number of components derived. Following this survey such purification

methods as solvent extraction, thin-layer chromatography, or gas chromatography are used to separate the compounds, and mass spectra of the separated compounds are compared with the original mass spectra.

REFERENCES

1. C. J. Umberger, in: *Legal Medicine, Pathology and Toxicology*, T. A. Gonzales, M. Vance, M. Helpern, and C. J. Umberger, eds., Appleton-Century-Crofts, New York (1954), pp. 1127, 1153, 1128.
2. K. Biemann, *Mass Spectrometry Organic Chemical Applications*, McGraw-Hill Book Co., New York (1962).
3. H. Budzikiewicz, C. Djerassi, and D. H. Williams, *Interpretation of Mass Spectra of Organic Compounds*, Holden-Day, San Francisco (1964).
4. R. A. Hites and K. Biemann, *Proc. of the International Mass Spectrometry Conference in Berlin* (1967), p. 59.
5. S. Abrahamsson, *Science Tools* 14, 29 (1967).

Identification and Determination of Oxidation Inhibitors in Synthetic Lube Oils by Ultraviolet and Mass Spectrometry

John F. Kinder and James Neel

*Atlantic Richfield Company
Harvey Research Center*

Ultraviolet and mass-spectrometric methods have been developed for the analysis of typical and nonproprietary oxidation inhibitors. These inhibitors are phenothiazine, N-phenyl-alpha-naphthylamine, N-phenyl-beta-naphthylamine, and *p,p'*-diocetyl diphenylamine. The methods are applicable without prior separation of the additives and are valid for concentration ranges of 0.05 or less to 2.4 wt.% of each inhibitor.

Detection and determination of oxidation inhibitors in synthetic lubricants are required in many laboratories for the purpose of quality control. Several methods of analysis are available, and in some cases these methods become rather expensive if prior separation and concentration of the additives are required.

Ultraviolet and mass-spectrometric procedures offer certain advantages to the analyst. In theory, and in actual practice, synthetic lubes are weak ultraviolet absorbers, and a typical aromatic inhibitor which has much stronger absorption should be detected with relative ease. Figure 1 illustrates the ultraviolet absorption of a synthetic lube oil over the range of 400 to 200 m μ in an isoctane solution. In the mass spectrometer the higher-molecular-weight aliphatic esters, such as a synthetic lube base oil, have relatively small parent peaks and large fragment peaks. These parent peaks and fragment peaks can

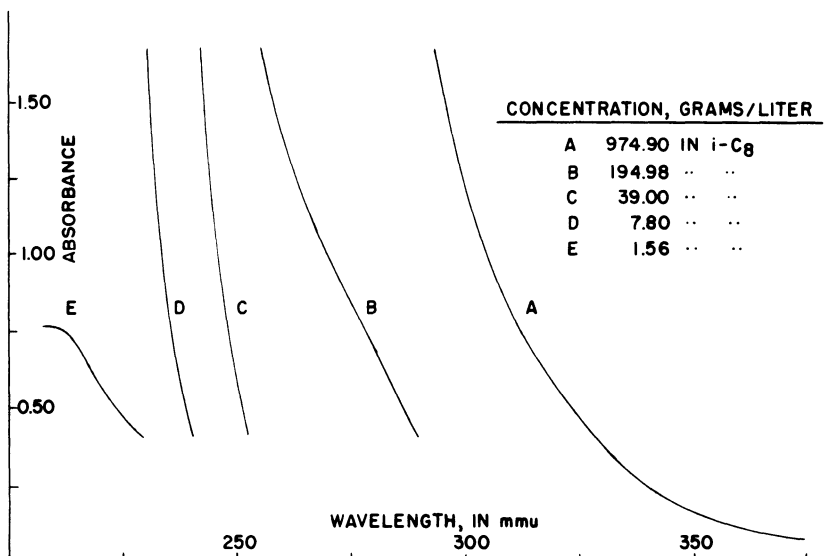


Fig. 1. UV absorption spectrum of base oil.

be reduced to negligible magnitudes by operating at an ionizing voltage which will not fragment the oil molecule but still has enough energy to produce molecular ions from the various species of aromatic inhibitors.

A number of conventional oxidation inhibitors are shown in Fig. 2. Our analytical procedure is designed to detect and determine any combination of these four compounds for a concentration range of 0.00–2.40 wt.%.

Ultraviolet-absorption spectra as obtained in isoctane solution on a Cary Model 14 instrument are presented in Figs. 3–6. The key wavelengths of 252.5, 287, and 336 m μ are rather obvious for the determination, respectively, of phenothiazine (PTZ); *p,p'*-dioctyldiphenylamine (DOPA); and N-phenyl-alpha-naphthylamine (PANA). Two wavelengths, 271 and 307.5 m μ , appear to be usable for the analysis of N-phenyl-beta-naphthylamine (PBNA). Subsequent analysis of synthetic blends will determine if one of these wavelengths is preferable.

Ultraviolet calibration data, in terms of absorptivities, for the four additives are presented in Fig. 7. An underlined value designates the absorptivity of each additive at the key wavelength utilized for analysis. The data in Fig. 7 have been inverted to yield the three inverses shown in Fig. 8.

NAME	STRUCTURE	CODE
p,p'-DIOCTYLPHENYLAMINE	<chem>C8H17-C6H4-N(C6H5)C6H4-C8H17</chem>	DOPA
N-PHENYL- α -NAPHTHYLAMINE	<chem>C1=CC=CC=C1Nc2ccccc2</chem>	PANA
N-PHENYL- β -NAPHTHYLAMINE	<chem>C1=CC=CC=C1Nc2ccccc2</chem>	PBNA
PHENOTHIAZINE	<chem>c1ccsc2cc1[nH]2</chem>	PTZ

Fig. 2. Amine-type antioxidants.

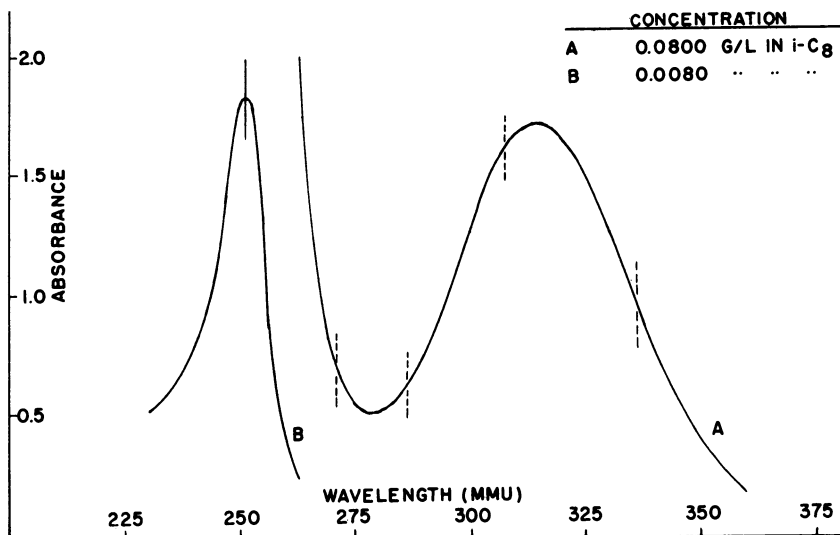
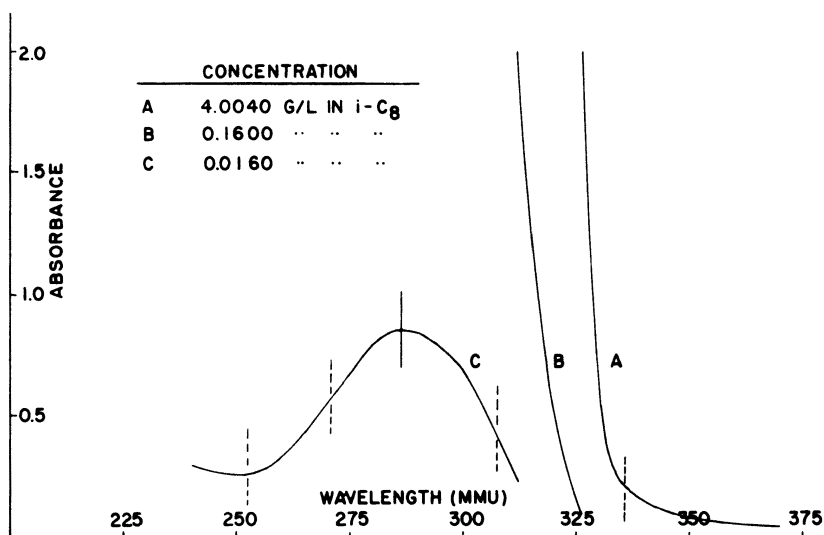
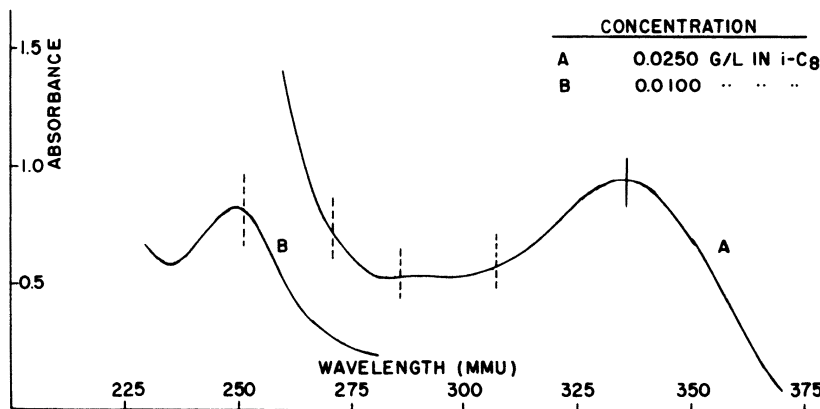
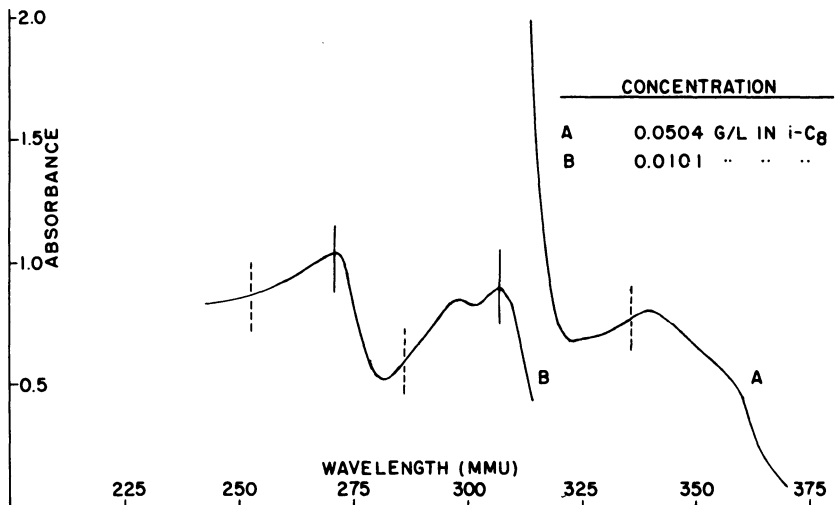


Fig. 3. UV absorption spectrum of phenothiazine.

Fig. 4. UV absorption spectrum of *p,p'*-dioctyldiphenylamineFig. 5. UV absorption spectrum of N-phenyl- α -naphthylamine.

Fig. 6. UV absorption spectrum of N-phenyl- β -naphthylamine.

COMPOUND	ABSORPTIVITY				
	252.5 mmu	271 mmu	287 mmu	307.5 mmu	336 mmu
DOPA	16.563	35.562	54.500	28.439	0.0587
PANA	83.639	28.973	21.648	23.050	38.665
PBNA	84.830	111.401	60.121	88.808	15.129
PTZ	247.929	9.183	8.929	21.504	13.987

Fig. 7. Ultraviolet calibration data.

It will be noted that inverses No. 1 and 2 are used for all inhibitors, but a choice of wavelength for analysis of PBNA can be made at either 271 or 307.5 m μ . Inverse No. 3 presents a simple three-component array for the case in which the less-frequently used PBNA inhibitor has been omitted.

<u>WAVELENGTH, mmu</u>	<u>INVERSE NO. 1 (X100)</u>			
	<u>PTZ</u>	<u>PBNA</u>	<u>DOPA</u>	<u>PANA</u>
252.5	+0.4578	+0.0139	-0.0224	-0.1710
271	-0.2518	+1.4990	-1.4160	-0.4932
287	+0.0261	-0.9815	+2.7660	+0.3704
336	-0.8161	-0.6036	-0.4391	+3.1180

	<u>INVERSE NO. 2 (X100)</u>			
	<u>PTZ</u>	<u>DOPA</u>	<u>PBNA</u>	<u>PANA</u>
252.5	+0.4792	+0.0986	-0.1142	-0.1288
287	+0.0281	+2.7770	-0.9933	+0.3743
307.5	-0.3311	-1.8620	+1.9710	-0.6486
336	-0.8551	-0.6581	-0.3718	+3.0420

	<u>INVERSE NO. 3 (X100)</u>			
	<u>PTZ</u>	<u>DOPA</u>	<u>PANA</u>	
252.5	+0.4601	-0.0093	-0.1664	
287	-0.1388	+1.8390	+0.0474	
336	-0.9176	-1.0090	+2.9200	

Fig. 8. Ultraviolet inverses.

<u>BLEND</u>	<u>COMPONENTS, WEIGHT PER CENT</u>				
	<u>BASE OIL</u>	<u>PTZ</u>	<u>PANA</u>	<u>PBNA</u>	<u>DOPA</u>
A	95.02	0.24	2.37		2.37
B	95.96	0.19	1.93		1.92
C	96.05	0.10	1.93		1.92
D	97.14	0.96	0.95		0.95
E	97.05	0.99		0.99	0.97
F	97.93	0.10	0.98		0.99
G	97.82	0.21	0.99		0.98
H	94.32		1.89	1.90	1.89
J	97.08		0.97	0.98	0.97
K	96.96	0.10	0.98	0.98	0.98

Fig. 9. Composition of synthetic blends.

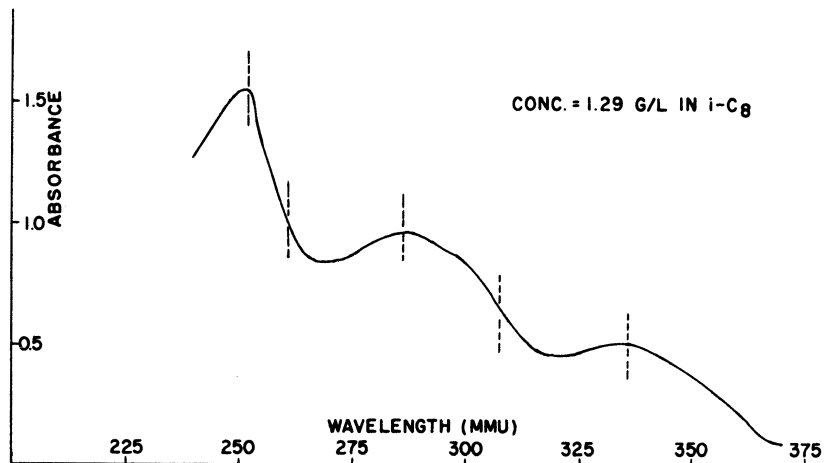


Fig. 10. UV absorption spectrum of base oil with three additives.

Inverses are useful when analyses of one type are made frequently and the calibration data are stable over a long period of time. The concentration of any one component is obtained from the sum of the products of each absorbance times an appropriate constant. For example, using inverse No. 1 of Fig. 8, the concentration of PTZ is obtained by multiplication of observed absorbances at 252.5, 271, and 336 m μ by the constants +0.4578, -0.2518, +0.0261, and -0.8161, respectively. Conversion to weight per cent then follows from C_x/C , where C_x is the calculated concentration of inhibitor x (grams per liter in solvent) and C is the sample concentration (grams per liter in solvent).

The utility and accuracy of the UV method were tested by analyses of ten synthetic blends as shown in Figure 9. Typical UV spectra for blends which contained three and four additives are illustrated by Figs. 10 and 11, respectively. Absorbance measurements were made at those points as indicated on the spectra.

UV analytical data for the ten blends are presented in Figs. 12 and 13. Several conclusions can be drawn, namely, that the UV procedure is accurate, that either 271 or 307.5 m μ can be used for the determination of PBNA, and

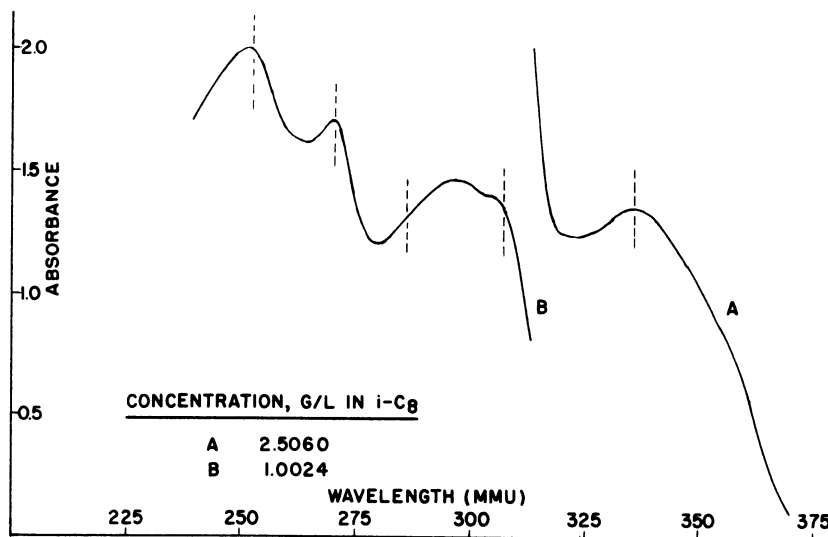


Fig. 11. UV absorption spectrum of base oil with four additives.

<u>BLEND (SYNTHETIC)</u>												
	A			C			D			E		
PTZ	0.24			0.10			0.96			0.99		
PANA	2.37			1.93			0.95					
PBNA										0.99		
DOPA	2.37			1.92			0.95			0.97		
<u>UV ANALYSIS AND INVERSE NO.</u>												
	I	2	3	I	2	3	I	2	3	I	2	3
PTZ	0.20	0.24	0.20	0.09	0.09	0.08	0.86	0.87	0.87	0.91	0.90	-
PANA	2.33	2.35	2.34	1.90	1.89	1.89	0.94	0.94	0.94	0.02	0.02	-
PBNA	0.03	-0.03	-	-0.01	-0.01	-	0.00	0.00	-	0.99	1.01	-
DOPA	2.34	2.39	2.36	1.86	1.86	1.85	0.92	0.93	0.92	0.98	0.96	-

Fig. 12. UV analyses of synthetic blends A, C, D, and E.

	BLEND (SYNTHETIC)							
	F		G		J		K	
PTZ	0.10		0.21		0.00		0.10	
PANA	0.98		0.99		0.97		0.98	
PBNA	0.00		0.00		0.98		0.98	
DOPA	0.99		0.98		0.97		0.98	

	UV ANALYSIS AND INVERSE NO.								
	1	2	3	1	2	3	1	2	3
PTZ	0.08	0.08	0.08	0.18	0.18	0.18	0.00	0.00	-
PANA	0.98	0.98	0.98	0.97	0.97	0.97	0.97	0.97	-
PBNA	0.01	-0.01	-	0.00	0.00	-	0.98	0.99	-
DOPA	0.96	0.98	0.94	0.94	0.94	0.94	0.95	0.94	-

Fig. 13. UV analyses of synthetic blends F, G, J, and K.

	BLEND NUMBER AND COMPOSITION (GRAMS)			
	1	2	3	4
MENAP	3.0000	3.0377	3.0050	3.0056
PTZ	0.1000	0.1014	0.0512	0.0512
PANA	0.1026		0.0502	
PBNA		0.1014		0.0500
DOPA	0.1010	0.1010	0.0519	0.0501

MENAP = 1-METHYLNAPHTHALENE

Fig. 14. Mass-spectrometer low-voltage relative sensitivities.

that the four-way inverse is satisfactory for use with a mixture which contains only three of the above additives.

Low-voltage mass spectrometry provides a complementary confirmation of inhibitor identity and verification of percentage. At an ionizing voltage of 8 V and with an ionizing current of 50 μ A each inhibitor exhibits an appreciable parent peak, whereas the base oil is neither fragmented nor ionized. The parent peaks of PTZ, PANA, and DOPA occur at masses 199, 219, and 393, respectively.

Mass-spectrometer calibration data were obtained from a series of blends

as shown in Fig. 14. The compound 1-methylnaphthalene (MENAP) is an internal standard. Each blend was run on the CEC 21-103C heated-inlet-system mass spectrometer at the standard operating conditions. Results from these runs are shown in Fig. 15, where all sensitivities are based upon divisions per gram and normalized to 500 divisions per gram for the internal standard MENAP. The data for PANA + PBNA is the simple arithmetic average of the sensitivity of each component.

A known amount of MENAP was added to 1 g of each blend, as previously presented in Fig. 9. After thorough mixing each blend containing the internal standard was run on the mass spectrometer. Calculations were carried out based on the equation

$$A \text{ (wt.\%)} = (500/P_M) (P_A/S_A) M,$$

where A is the inhibitor to be determined, P_M is the peak height at mass 142, M is the weight per cent of MENAP in the blend, P_A is the peak height of the parent peak of A , and S_A is the sensitivity of A .

Results of the low-voltage mass-spectrometric analysis of the ten blends are shown in Fig. 16. These data substantiate that the ultraviolet method has a higher degree of accuracy for this analysis. This is to be expected in view of the dependence of the low-voltage method upon a relatively large number of operating parameters.

The sensitivity of the low-voltage procedure is illustrated in Fig. 17, where peak heights corresponding to the parent ions have been tabulated. Detectability of the four additives by this specific method of low-voltage operation is estimated as shown in Table I.

SENSITIVITIES, DIVISIONS PER GRAM, NORMALIZED TO 500 FOR MENAP					
	MENAP	PTZ	PANA	PBNA	DOPA
BLEND 1	500	926	749		368
BLEND 1	500	987	803		399
BLEND 2	500	1025		844	373
BLEND 3	500	960	799		357
BLEND 4	500	970		815	343
AVERAGE	500	974	784	830	368
PANA + PBNA				807	

Fig. 15. Mass spectrometer low-voltage relative sensitivities.

	BLEND									
	A	B	C	D	E	F	G	H	J	K
<u>PTZ</u>										
SYNTHETIC	0.24	0.19	0.10	0.96	0.99	0.10	0.21			0.10
ANALYSIS	0.23	0.16	0.09	0.94	0.94	0.09	0.19			0.09
<u>PANA</u>										
SYNTHETIC	2.37	1.93	1.93	0.95		0.98	0.99	1.89	0.97	0.98
ANALYSIS	2.29	1.76	1.82	0.89		0.94	0.92			
<u>PBNA</u>										
SYNTHETIC					0.99			1.90	0.98	0.98
ANALYSIS					0.91					
<u>PANA + PBNA</u>										
SYNTHETIC								3.79	1.95	1.96
ANALYSIS								3.47	1.77	1.84
<u>DOPA</u>										
SYNTHETIC	2.37	1.92	1.92	0.95	0.97	0.99	0.98	1.89	0.97	0.98
ANALYSIS	2.49	1.87	1.95	0.94	1.01	1.07	1.06	2.01	1.04	1.06

Fig. 16. Mass spectrometer low-voltage analysis of synthetic blends.

	BLEND									
	A	B	C	D	E	F	G	H	J	K
MENAP-142	264	358	280	302	306	266	329	283	313	319
PTZ -199	13	11	5	53	61	5	14	1	1	6
PANA -219	104	98	88	45	51	43	52	172	95	104
PBNA -219										
DOPA -393	53	49	45	22	25	23	28	45	26	27

Fig. 17. Peak heights obtained by low-voltage mass-spectrometric analysis of blends.

TABLE I

Additive	Minimum amount detectable (wt. %)
PTZ	0.02
PANA	0.03
PBNA	0.03
DOPA	0.05

The low-voltage mass spectrum provides a second set of peaks which can be utilized to verify inhibitor identity. These are the parent plus one ($p + 1$) ions, which are due to isotopic contributions. The ratio $(p + 1)/p$ in the mass spectrum will in many cases establish the molecular formula of the molecular species which is ionized.

In summary, the combination of ultraviolet and low-voltage mass spectrometric procedures provides a rapid and accurate analytical technique for the detection and determination of four conventional oxidation inhibitors. Other additives of the heterocyclic aromatic type will, if present, interfere, but should be detectable by the mass-spectrometer run. These interferences should be eliminated or minimized by the inclusion of calibration data for the additional components.

Spectroscopy in Space—An Introduction and Overview

R. E. Ruckman

*Lockheed Electronics Company
Hyattsville, Maryland*

Satellite-borne mass spectrometers of various types, as well as other sophisticated aerospace experiments based on spectroscopy, play an important part in the unmanned scientific satellite programs. Data from these experiments contribute to the growing fund of knowledge about phenomena in space and their mechanisms and interactions. On the assumption that the laboratory spectroscopist is largely unfamiliar with this experimentation, this chapter briefly discusses typical scientific satellites and the experiments they carry, including a short description of a state-of-the-art mass spectrometer.

INTRODUCTION

The field of spectroscopy is divided into different specialties, each with its own instruments and practitioners. In our respective laboratories we use one or more of these instruments and subdisciplines in pursuing our own studies and analyses, but without the necessity for operating the other types of instrument or understanding their uses. Whether one is led by professional curiosity or by necessity to learn about the other branches of spectroscopy, or has become fairly narrowly specialized, he is still able to practice spectroscopy in the laboratory.

Moreover, the cost of newer of different instrumentation is probably the determining factor in its potential acquisition, provided that it is needed. Such considerations as its physical size, its power consumption, and its environmental requirements are met simply by making room for it, plugging another electrical cord into the wall, and wheeling up a tank of dry nitrogen, respectively.

Changes of scale, scan speed, slit width, etc., can be made by the operator, based on real-time judgments performed while monitoring the data outputs. Repairs can be made by the operator, or at the worst, by the manufacturer's service engineer, and the instruments' operation can then resume. When different samples are to be analyzed, the instrument can be set up to accommodate the expected differences in output. In addition, the data are readable by the spectroscopist as soon as the chart or spectrum is completed, whether it comes off in finished form or requires a few minutes of processing.

In the aerospace experimenter's world, all of these operations are subject to the most severe constraints, such that the design and operation of his instrument and the processing of its data are wholly different from the familiar laboratory situation outlined above. Size, weight, and power consumption are only a few of the many variables which must be very carefully worked out during the evolution of a satellite-borne experiment.

Since the aerospace spectroscopist and the laboratory spectroscopist live in different worlds, the question is: to what degree should the latter be interested in the former? since we have already postulated that it is not necessary to be conversant with other branches of spectroscopy in order to work in one's own specialty. One is reminded of the famous one-line book report by a child, who wrote, "This book tells me rather more about tigers than I wish to know." The analogy here is whether or not the spectroscopist wishes to know about aerospace experimentation, and the answer which I propose is: that he should be *personally* interested because he is helping to pay for it, and *professionally* interested because the knowledge gained in the one area may be applicable to progress in the other. In space jargon this is called a "spinoff," a technological gain to the community at large which results from aerospace research and development. Thus it is probable that a study of satellite-borne spectroscopic instruments might result in improvements in the design and data handling of the laboratory instruments.

This chapter is intended to arouse such an interest by discussing briefly some representative satellite programs and some of the spectroscopic experiments they carry, and describing a time-of-flight spectrometer from this group.

UNMANNED SCIENTIFIC SATELLITES

Even the informed layman who follows the nation's space program in the mass media is far better informed about the spectacular manned space flights than about the unmanned scientific satellite programs. The *uninformed* layman probably realizes little except that we are in a "space race" with the Soviet Union to "put a man on the moon," and his feelings as to the necessity or

desirability of that accomplishment vary widely. As spectroscopists, and, therefore, informed, trained scientists, I feel we should be better informed about the scientific aspect, especially as it relates to spectroscopy, of our unmanned satellite programs.

First, a few words about these programs themselves: NASA Goddard has cognizance over a number of such programs, including the OGO, OSO, and IMP satellite families. These stand for, respectively, Orbiting Geophysical Observatories, Orbiting Solar Observatories, and Interplanetary Monitoring Platforms. There are others, of course, including spacecraft flown by other countries, and by other agencies and universities, but I shall limit this discussion to the foregoing three as typical of the general purpose, multiexperiment satellites. These three families were chosen, for the same reason, for an extensive experiment and data-processing study¹ which I have recently completed for NASA-Goddard.

The OGO series began with the launch of OGO-A on 5 September 1964, and will probably conclude with the OGO-F in 1969. These spacecraft carry from 20 to 26 experiments, making them orbiting laboratories able to take simultaneous data on many different phenomena for later correlation. There are two basic orbital configurations, polar and eccentric. OGO-A, B, and E have eccentric or elliptical orbits, which allow data to be taken approximately 135 n.m. (nautical miles) at perigee to approximately 80,000 n.m. at apogee. The EGO's (eccentric OGO's) orbits are inclined approximately 31° from the earth's equatorial plane. OGO-C and F are POGO's or polar-orbiting OGO's, which have a more nearly circular orbit inclined at approximately 85° so that they explore the mechanisms of such polar phenomena as the aurora borealis.

The IMP's began with IMP-A on 26 November 1963, and are currently planned at least through IMP-J, which will run on into the next decade. They are also eccentric orbiters, with wide variations in apogee and perigee, depending on the particular mission, and carry eight or nine experiments each.

The OSO's have provision for pointing some of the experiments at the sun for solar observation and mapping, while others revolve on a "wheel," so that they sight the sun once every 360°. This periodic sighting of the sun, incidentally, is used as a sequence-timing input, and also allows the angle of incidence to be determined for phenomena detected around the remainder of the wheel's rotation. OSO's, which have nearly circular orbits of approximately 300 n.m. altitude, are scheduled at least through OSO-G in 1969.

There are, of course, follow-on programs under construction, one of which is of high interest to many experimenters. It is the S³, or Small Scientific Satellite, which will have standardized modules and a few (about five) compatible experiments on each spacecraft in the series. By compatible, I mean that each S³ will have experiments on board which will not create multiexperiment

interference, will provide data for correlation with the other experiments, and will be selected as a group for the individual spacecraft mission. Being small, the S³ may utilize a cheaper launch vehicle, such as a military rocket. The S³ also has provision for an on-board computer, which will allow some preprocessing of data before telemetry.

In fact, the design of on-board data-processing systems, the complementary design of future experiments *for* on-board data processing, and all of the other interfaces with this technological innovation comprise a broad and important new field in itself. Several investigators²⁻⁴ are working in this field, including the author,¹ which is of potential interest to spectroscopists for two reasons: (1) there is also work being done in data processing on laboratory spectra,⁵ and (2) there may be spinoff applications of new aerospace data-processing techniques to the processing of laboratory data, since both are concerned with identification of spectra.

In any case, in order to develop realistic requirements for future on-board processing of the data outputs of scientific experiments, it is desirable to establish early liaison between the experimenters (who will propose and design the instruments) and those who will design the spacecraft systems and the data-processing systems which interface with those experiments. Consequently, the latter groups should become familiar with the purpose and operation of the experiments so that their outputs will be understood.

For this reason the aforementioned survey¹ was made, including the study of 241 experiments on the OGO, OSO, and IMP families. By choosing only the latest experiment of each of the 72 experimenters in that group, and then applying other selection criteria, detailed descriptions of 53 experiments were collected and programmed for computer analysis.

SPECTROSCOPIC EXPERIMENTS

Many of these experiments use mass spectrometers and other instruments based upon spectroscopy, including: (1) ultraviolet spectrophotometers, (2) x-ray spectrometers, (3) electron and proton spectrometers, and (4) ion mass spectrometers.

For the purpose of this chapter I have confined the discussion to follow to the last category. Satellite-borne mass spectrometers take different forms, depending primarily on the design preference of the experimenter. Variations include the Bennett rf mass spectrometer,⁶ the Faraday cup,⁷ the quadrupole mass spectrometer,⁸ and the time-of-flight type⁹ to be discussed in detail below.

REQUIREMENTS FOR AEROSPACE SPECTROMETERS

The major physical difference between a laboratory spectrometer and one

designed for satellite installation is size. Whether or not the designer is given the maximum inside dimensions of the module for his proposed experiment, he knows that its size may determine its acceptability for a particular satellite. Given a maximum length of 9 in., the designer of the time-of-flight spectrometer specified a path length of 15 cm, compared with its laboratory predecessor's 1-m path length; and, while the 1-m instrument requires pulse- and flight-times in microseconds, the reduction of path length (over which the particle velocities are resolved) entails the corresponding use of nanosecond electronic techniques, which in turn extends the state of the art.

Weight obviously decreases with size, but even so, the weights of each experiment and all other spacecraft systems are carefully minimized, and considered along with each other as they add to the whole. Materials are specified which are stable in the vacuum environment and are nonmagnetic, and/or the experiment must be shielded against producing an exterior magnetic field which would cause interference with other experiments. Electronic components must be potted to ensure electrical insulation and vibrational integrity.

Experiments are extensively tested both in the breadboard and prototype stages to see that they work, and on the actual flight instrument in order to calibrate its outputs and make sure that it passes the many flight-acceptance specifications (thermal/vacuum tests, vibration tests, etc.).

In addition, the fact that the spectrometer has an aperture in the spacecraft, the purpose of which is to admit the particles it *wants* to detect and analyze, does not preclude the simultaneous entry of undesired particles. Therefore the experiment must be designed either to attract the former while blocking the latter, or to discriminate between them.

Furthermore, the data outputs of the satellite spectrometer cannot be removed in readable form by an operator, as is done in the laboratory; nor can adjustments be made, by turning dials, such that the instrument is altered in real time to accommodate different species, or different abundances, in different areas of space. For these reasons, the experiment must be designed with these constraints in mind. The data stream, from the experiments' outputs themselves to the receipt of meaningful data by the experimenter, is one complex problem, and the design of the experiment to make mode changes, changes of scale, and/or changes in data-sampling rates, is another. Both of these major considerations involve the telemetry capability of the specific spacecraft, its ability to accept ground commands (to effect changes in the experiments, among other things), and other criteria which are beyond the scope of this chapter.

The point is, however, that the experimenter may wish to change operational modes of the instrument in order to "tailor" the experiment to the ambient environment, just as the laboratory spectroscopist can set up his instrument for

different samples. The more mode changes, the more complex is the experiment's electronic logic, since these changes must be made by ground command or by previously-set time sequences. Unless and until there is an on-board computer which can make real-time mode changes based on what sensors "see," the flexibility or adaptability of experiments is limited in comparison with the adjustability of their laboratory counterparts. Another suggested solution is to have a scientist astronaut make these real-time judgments while operating some of the experiments himself. Today, however, the experimenter does not, in real time, see his data, which must undergo extensive on-ground processing.

A TIME-OF-FLIGHT MASS SPECTROMETER

A typical example of a state-of-the-art mass spectrometer is the one mentioned earlier, on which I did some developmental analysis in 1966.^{9,10} Proposed both for an earth-orbiting mission and for a Mars fly-by, it consists essentially of a 127° cylindrical electrostatic analyzer, a drift tube of 15 cm path length, and a detector, as shown in Fig. 1. Incident ions are collected and directed into the drift tube by the analyzer.

The spectrometer may operate in three analytical modes: energy per unit charge alone, energy per unit charge and mass per unit charge, and mass per unit

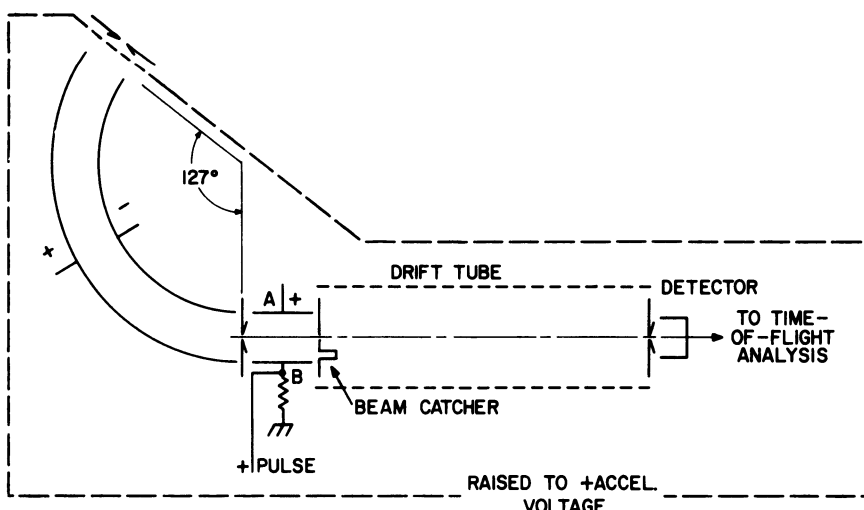


Fig. 1. A state-of-the-art mass spectrometer.

charge alone. The first two modes are automatically sequenced during passage through the interplanetary medium, and the first and third modes are employed in the planet's tail (that of the Earth or of Mars, depending on the mission). In the first mode, the analyzer will be stepped through the E/Z range of 200 eV to 16 keV in 32 steps corresponding to its 32 detector channels, and in turn corresponding to ions having a mass per unit charge up to about 30.

In the second mode, a mass analysis will be performed at each of the 32 steps, and in the third mode the low-energy ions expected in the planet's wake will all be accelerated to 0.5 kV, such that a mass analysis will be performed with the analyzer tuned for 0.5 kV. The combination of these analyses is intended to provide E/Z versus m/Z spectra of the various detectable ion species in the areas of space traversed by the spacecraft. Since one does not get a continuous spectrum, the inputs (counts) from the 32 data channels must be reassembled by the experimenter such that the spectra are reconstructed in his laboratory (referring again to his preflight calibration of the instrument).

In the broader sense, the spectra themselves only provide incidental information, which is then useful in interpreting and confirming theory on phenomena in space, and their interactions and temporal variations. In this case, the relative abundances of ion species in the undisturbed solar wind and in the wake of a planet, while producing spectra of intrinsic interest, are intended to add understanding of the expansion of the solar corona, the interaction of the incident plasma with the planetary atmosphere, and of other larger concepts.

GENERAL EXPERIMENT FEATURES

Experiments are initially designed, in most cases, to investigate the gross features of some phenomenon, in order to prove that it is there, and see what it looks like and what it does. These are called survey-type experiments, and generate further interest in later instrumentation which invariably becomes more sophisticated. Later experiments may simply confirm the measured values of earlier surveys; they may (usually) seek to make measurements with greater accuracy and with more flexibility or coverage. Still others may then investigate predicted interactions between one known phenomenon and another by taking more than one type of measurement, or by correlating their data with data taken simultaneously from other experiments. Once the phenomenon and the methodology for detecting it are understood, experiments may be flown on a series of spacecraft, so that it is "mapped" throughout space, and its long-term temporal variations studied (e.g., over the 11-year solar cycle). Or, an experienced experimenter may go on into another field of investigation, for which he will fly another survey-type instrument, which begins another cycle.

At any rate, each aerospace experimenter has had to start sometime. In fact, quite a few of the experimenters "on" OGO-F are first-timers. My implication is that in the greater spectroscopic community there may be many more experimenters who will conceive future satellite-borne experiments, or at least benefit from the technological spinoffs and from the theoretical knowledge gained from aerospace experimentation in spectroscopy.

REFERENCES

1. R. E. Ruckman, Scientific Satellite Experiment Survey for Evaluation of On-Board Data-Processing Systems, Goddard Space Flight Center Report No. X-563-68-23, Jan. 1968.
2. F. Styles, T. Taylor, T. Trevathan, and M. Tharpe, A General-Purpose On-Board Processor for Scientific Spacecraft, Goddard Space Flight Center Report No. X-562-67-202, July 1967.
3. TRW Systems, A Study to Determine an Efficient Data Format and Data System for a Lightweight Deep Space Probe, Final Report No. 06488-6019-TOOO, Oct. 1966.
4. T. C. Goldsmith and J. H. Trainor, System Design Study for Improved IMP spacecraft, Preliminary Report, Goddard Space Flight Center, Nov. 1966.
5. B. F. Scribner, The Impact of Computer Techniques on Atomic Spectroscopy, Inter. Conf. Spectry. Ottawa, 1967.
6. H. A. Taylor, Jr., H. C. Brinton, and C. R. Smith, *J. Geophys. Res.* **70**, 5769 (1965).
7. H. S. Bridge, A. J. Lazarus, and J. H. Binsack, Plasma Experiment on IMP-H and IMP-J, MIT, Oct. 1966 (unpublished experiment description).
8. R. J. Leite, C. J. Mason, and R. D. Kistler, Instrument Report, Neutral and Ion Mass Spectrometer, University of Michigan, May 1964 (unpublished experiment description).
9. D. L. Lind and K. W. Ogilvie, A Plasma Experiment for the 1969 Mariner Mars Fly-By, Goddard Space Flight Center Report No. X-612-66-115, March 1966.
10. K. W. Ogilvie and R. E. Ruckman, Time of Flight Analysis Applied to Interplanetary Plasma, May 1966 (unpublished draft).

A Computer-Controlled System for Automatically Scanning and Interpreting Photographic Spectra

C. A. Bailey, R. D. Carver, R. A. Thomas,
and R. J. Dupzyk

*Lawrence Radiation Laboratory
University of California
Livermore, California*

In analytical spectrography the most time-consuming portion of an analysis is the scanning and interpreting of the photographically-recorded spectra. A system has been devised to shorten this time considerably by using a small digital computer to control the scanning densitometer and subsequently to calculate abundances from the photographic data. The following description applies specifically to spark-source mass spectrography; however, adaptation to other systems would be relatively straightforward. A typical photoplate from our spectrograph contains several thousand lines from as many as 20 graded exposures, and represents approximately 65 elements. Starting with the most intense exposure, the optical transmission of each line is measured using a Grant microphotometer. These transmissions as well as the position of each line are stored in a PDP-8 computer. The computer initiates and completely controls the scanning, and simultaneously converts each line position to an exact mass number from a calibration performed at the beginning of the scan. The computer is programmed to distinguish between lines and empty areas on the photoplate, and all the graded exposures of each line are recorded before the scanning continues to the next line. Backgrounds are continuously upgraded and recorded along with their adjacent line densities. After the desired area of the photoplate has been scanned an emulsion calibration is calculated from the data stored in the computer. Then all line densities on the linear portion of the calibration curve are converted to ionic abundances. Total time involved in scanning 20 exposures on a 15-in. photoplate is now approximately 5 hr.

The Lawrence Radiation Laboratory has had a CEC 21-110 spark-source mass spectrometer in operation for five years. Two years ago the chemists and electrical engineers started looking for a way to simplify and improve the reduction of the data which is taken on photographic plates.

Several available systems of both plate reader and densitometer were looked into and found to have hard wired programs not applicable to what we wanted to do. We concluded that we had to design the system ourselves.

The Grant Microdensitometer was found to be an excellent plate reader capable of being operated by computer-controlled stepping motors. The densitometer was coupled to a Digital Equipment Corporation PDP-8 computer to construct our present system.

The first component in the system is a spark-source mass spectrograph, CEC 21-110. The ions from a sample are collected on a 2 in. X 15 in. glass photoplate. The mass lines occurring on the plate come from elemental and compound ions, singly and multiply charged. Twenty graded exposures can be collected on a plate. Each exposure is 2 mm in length. For our purposes "exposure" means the number of ions striking the photographic plate; this value is expressed in coulombs. The second component in the system is a Grant Microdensitometer. It has an accuracy of $\pm 1 \mu$ in the *X* and *Y* directions. The densitometer is stepped in 1μ increments in the *X* direction and 5μ increments in the *Y* direction. There are two viewing screens available. One is a projection through a 22-power zoom lens which allows a closeup of the area being scanned. The second screen is an analog signal from the detector displayed on a cathode-ray tube. It is used for adjusting the scanning slits.

The readout is an analog-to-digital converter (ADC) connected to the photomultiplier output. The ADC is capable of 12-bit resolution with a digitizing time of 35 μ sec.

The actual plate-stage drive is accomplished by using 200-steps/revolution digital stepping motors. The *X*-drive incorporates a 5:1 gear reduction, which results in a scale of 1μ per step. No gear reduction is used on the *Y*-drive, and therefore the scale is 5μ per step. Motor speed was selected to allow instant start-stop-reverse response without resorting to controlled speed up to compensate for inertial effects.

The interface from the PDP-8 to the microdensitometer uses only one device selector. The device selector, by program control, puts out any one, or a combination, of three IOT pulses.

IOT-TWO is used to transfer nine status conditions, such as *X* ready, *Y* ready, $+X$ limit, etc., into the accumulator. All but two of the status conditions set the flag. IOT-FOUR actuates any one of nine different control functions, depending on what bit or bits are set in the accumulator. Typical control functions are: step $\pm X$, step $\pm Y$, clear flag, interrupt on, etc.

The interface provides interrupt capability, but it is not being used with the present program.

The third component is the Digital Equipment Corporation PDP-8. It is the 4k version equipped with two Dectape transports and the extended arithmetic element (EAE). The code occupies all of core. The floating-point package-D is used for all the input, output, and most of the calculations. Control and operation of the system is done entirely with software.

The following describes the interaction between the operator and the Grant/PDP-8 system. The emulsion calibration for the plate is made by exposing the plate to the rhenium isotope spectrum at varying intensities, changing the magnet setting between exposures in order to offset the lines. These line-density ratios are fitted into the Hull equation relating plate density to exposure

$$\text{Emissions} = [(T_o - T)/(T - T_{\text{inf}})]^{1/R} \quad (1)$$

where R is calculated to be used later to calculate relative abundances of the ions striking the plate.

The input for this process is through the teletype (TTY). The operator types the number of rhenium lines to be read and a value for the transmission at infinite exposure (T_{inf}).

When the specified number of lines has been read the computer waits for the operator to realign the stage to read from low mass to high mass over the range he desires. When alignment is complete the operator types in a starting and a final location in microns, four mass numbers, and their locations on the plate. These masses are carefully-chosen prominent lines distributed across the range of interest and are fitted into a mass-number calibration equation,

$$\text{Mass} = [(\text{Location} - A)/B]^2$$

where A and B are determined and used later to calculate the mass number of each unknown line from its location on the plate. Twenty exposure values are typed in corresponding to the number of coulombs each line was exposed. At this point the computer is put in complete control, and the operator is no longer needed.

The following is a description of the peaks encountered on a typical photographic plate and the way in which the computer code handles them.

The first peak is a singlet in a clean portion of the plate. The peak-reading process always starts with the most intense exposure. The code calculates a peak detection threshold value. This value is an arbitrary decrease in the transmission calculated from the background values,

$$\text{Threshold} = \text{Average background} - X \% \text{ Average background.}$$

This value is undated every one-ninth of a mass unit if a peak has not

been detected. A peak is determined by testing to see if the incoming transmission value is below the peak detection threshold. If a peak is detected, it is checked to see if it is an honest peak. This check is necessary because of nonuniformity in the emulsion. If it is an honest peak, its peak top is determined and two background values one-ninth of a mass unit on either side of the peak top are taken. One-ninth of a mass unit is an arbitrary distance selected to reach over the very dense lines and yet not encounter other mass lines from multiply-charged ions. There are not a constant number of exposures for each mass line, so the following method is used to determine when all the lines for a individual mass have been read. Two questions are asked of the PDP-8: (1) Have twenty exposures been racked? If yes, then it does not look for more information; if no, the second question is asked. (2) Is the transmission of this peak top below a threshold value calculated from the background values of the previous exposure? If yes, then the stage is racked one exposure in the positive Y direction, the direction of lesser exposure, and the data are stored in a buffer in core. If no, then all the data from that line have been measured and the code racks back to the most intense exposure and continues to look for a new mass.

The second peak is a doublet. The first mass line encountered in a doublet is read in the same manner as a singlet except that the background values are now taken at one-ninth mass unit on one side and at the minimum in the valley between the peaks. The computer is "aware" that there is a mass on its high-mass side. When it has finished the first mass line it then scans the high-mass line. Because the various exposures are not perfectly perpendicular to each other it was necessary to make sure that the stage returned to the peak top of the most intense exposure of each mass line encountered before starting to look for a new mass line. This was especially necessary in the case of doublets.

The third peak is one that lies in fog. Fog is caused by the ions from a very abundant element scattering due to residual charge build up. Fog on plates may have a transmission value as small as 5%. The process of updating the peak threshold detection value every one ninth of a mass unit described earlier allows very light lines to be found in the very dark fog. The process of checking to see if the peak-top value is darker than the threshold calculated from the previous exposure allows all the exposures for a mass line to be read.

The entire plate is read and the data are stored on the Decertapes in two-block segments. The following information is stored: The mass number from Eq. (1), the transmission at the peak top, the transmission at the two background positions, and the exposure value.

The teletype output is shown in Fig. 1: (1) The per cent transmission of the Re-185 and Re-187, (2) the R values for each Re ratio, calculated from the Hull equation, (3) and the average R value.

Following this are the data for all detected masses on the plate, which are

ZT RE 185 & RE 187

+0.4749693E+02	+0.3592184E+02
+0.4901098E+02	+0.3636140E+02
+0.5264959E+02	+0.3936508E+02
+0.5235654E+02	+0.4119656E+02
+0.5601952E+02	+0.4483516E+02
+0.6485960E+02	+0.5196582E+02
+0.6923075E+02	+0.5604394E+02
+0.6910865E+02	+0.5633699E+02
+0.8329668E+02	+0.7479852E+02
+0.7802197E+02	+0.6656897E+02

R VALUES

+0.9467302E+00
+0.1028460E+01
+0.1062021E+01
+0.8881528E+00
+0.8849648E+00
+0.1049275E+01
+0.1114296E+01
+0.1079682E+01
+0.1014555E+01
+0.1131831E+01

$R = \log \left[\frac{\frac{T_o - T_{187}}{T_{187} - T_{\text{inf}}}}{\frac{T_o - T_{185}}{T_{185} - T_{\text{inf}}}} \right] \div \log (1.67)$

AVE R VALUE +0.9789795E+00
1/R VALUE +0.1021472E+01

Fig. 1. Rhenium data and R values.

MASS +0.3127783E+02

ZT	ZB1	ZB2
+0.1582418E+02	+0.2749695E+02	+0.2420024E+02
+0.2061050E+02	+0.3262516E+02	+0.3006104E+02
+0.2703295E+02	+0.4163136E+02	+0.3748472E+02

A(T) A(B) A(B) A(NET)

+0.3143612E-04	+0.1491300E-04	+0.1787448E-04	+0.1504238E-04
+0.4450017E-04	+0.2309754E-04	+0.2616048E-04	+0.1987115E-04
+0.6113529E-04	+0.3088063E-04	+0.3698068E-04	+0.2720463E-04

AVE ABND +0.2337621E-04 PCT ERROR +0.1008904E+02

1/R

$E_{\text{rel}} = \left[\frac{T_o - T}{T_o - T_{\text{inf}}} \right]$

Aburd = $E_{\text{rel}} * \sqrt{\text{Mass}} \div \text{Exposure}$

Fig. 2. Data output. Mass, per cent transmission for mass, and relative abundance for mass.

typed in the following fashion (Fig. 2): (1) The mass number, (2) the per cent transmission of the peak top and the two background values, (3) the abundance of the peak top and the two backgrounds and a net abundance, and (4) the average abundance and the per cent error.

The average abundance is a weighted average, so that all exposure values could be used in the calculation. The weighting function is parabolic.

It was found that the numbers from the Grant/PDP-8 system agreed with hand calculation to within 5%. This is very good agreement, as spark source work is usually quoted to a factor of two. There is no reason to believe that the Grant/PDP-8 numbers are not better. Standard samples are difficult to prepare.

To conclude, let us compare the time spent in reading and reducing the data from one plate. Starting from the time that the plate is developed, dried, and ready for reading until relative abundances are in hand:

1. The Grant/PDP-8 system takes $\frac{1}{2}$ hr of operator time, and for a typical geological sample about 11 hr of system time, approximately 5 hr for reading the plate and 6 hr for typing the data. It can be set up before closing time, and answers are ready at opening time the next morning.

2. With the standard system an operator is almost always required to put the data out on chart paper, convert it to IBM cards, and run a short code on a CDC 3600, taking a total time of three or four days.

The Grant PDP-8 system is a great improvement over the old system. It should be adapted readily to other plate or film-reading systems.

ACKNOWLEDGMENTS

We would like to thank Dr. G. W. Barton for his help in deriving the equations for weighting the average abundance and for calculating a per cent error for the average abundance.

This work was performed under the auspices of the U.S. Atomic Energy Commission.

Nuclear-Particle Spectroscopy

Nuclear Applications of Liquid Scintillation Systems

Donald L. Horrocks

*Chemistry Division, Argonne National Laboratory
Argonne, Illinois*

The use of liquid scintillation systems to study such nuclear properties as disintegration rates and energy spectra and for making particle determinations is discussed. The use of pulse-shape discrimination as a method for counting particles with a high specific ionization over a background of particles with low specific ionization is described.

INTRODUCTION

Most frequently liquid scintillation detectors and counting systems are used in studies calling for measurement of ^3H and/or ^{14}C in biological or similar types of samples. Liquid scintillators are often the ideal, if not the only, way of counting ^3H and ^{14}C in a large number of types of samples. However, it is often overlooked that liquid scintillation systems are very useful as a tool in the study of nuclear properties. They can be used for the determination of disintegration rates, energy spectra, different types of particles, and for studying many other nuclear problems. The fact that many scintillator solutes are extremely fast (decay time < 1.5 nsec) makes them useful for measuring high counting rates, fast coincidences, and short lifetimes.

In this chapter a few applications to nuclear studies will be discussed. There are four main parts, according to the type of particle which excites the liquid scintillation system: (1) electrons, (2) alpha particles (3) neutrons (scattered protons), and (4) fission fragments. In the last two sections special emphasis will be given to the use of pulse-shape discrimination as a method for counting particles with a high specific ionization over a background of particles

with a low specific ionization, such as the measurement of neutrons in the presence of a gamma background.

ELECTRONS

Beta Emitters (Negatrons and Positrons)

Disintegration-Rate Determination

The disintegration rate of certain nuclides with the appropriate mode of decay can be obtained by $\beta-\gamma$ coincidence counting where the beta detector is a liquid scintillator with the nuclide dissolved in it. The betas are absorbed by the liquid scintillator, and a part of the gammas by a NaI(Tl) crystal placed nearby. Figure 1 shows a simple $\beta-\gamma$ coincidence system.

In this type of system the betas are counted with close to 100% efficiency if the E_{\max} of the beta decay is > 200 keV. The efficiency of the gamma-ray counter will depend upon the size of the crystal, the geometry of the sample-crystal pair, and the energy of the gamma ray. There is a correction for scattered gamma rays which give a coincident count. The near 100% efficiency for beta particles makes necessary a correction for the high chance of random coincidence events. Review papers covering this method have been published.^{1,2}

This method has also been applied to $\alpha-\gamma$ coincidence counting. Decay scheme studies have also been made using the determination of beta-gamma coincidence pairs.

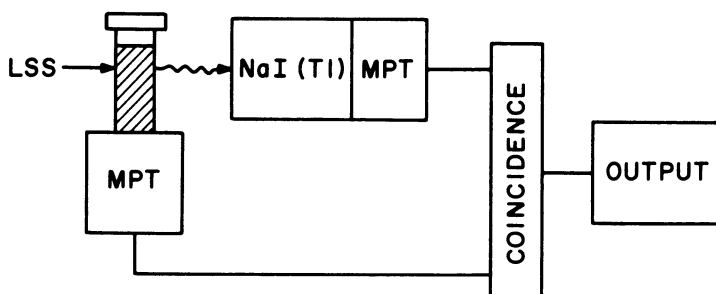


Fig. 1. A type of beta-gamma coincidence counter where the beta detector is a liquid scintillator system.

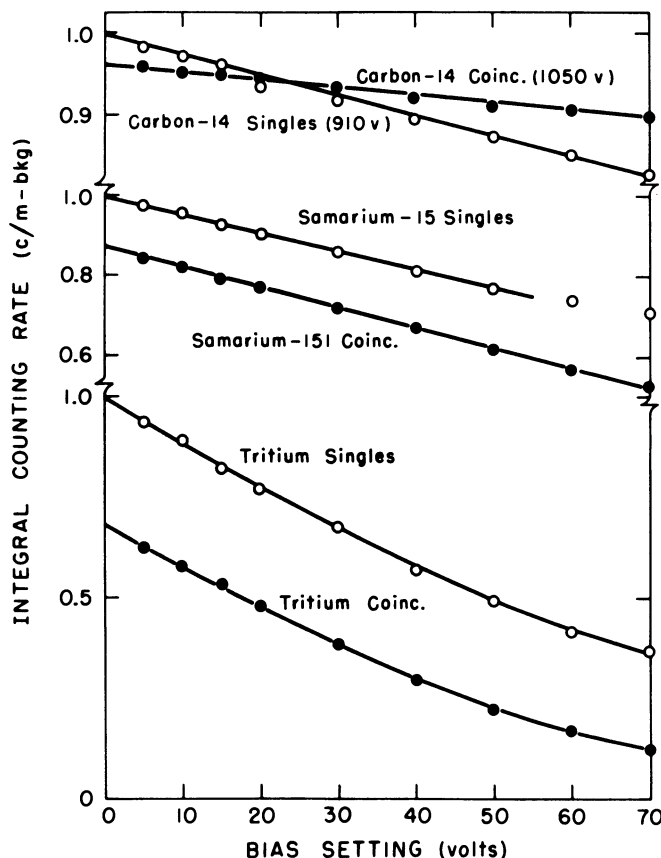


Fig. 2. An integral counting rate plot showing the extrapolation to zero bias to obtain the sample counting rate.

A second method for obtaining the disintegration rate of a sample is the extrapolated integral counting rate method.³ In this method the counting rate is measured for all events above a certain energy (bias) as a function of the successively lowered energy setting. The plot of integral counting rate as a function of bias setting is extrapolated to zero bias, which gives the counting rate of the sample. It is not possible to just set the bias at zero, because of the high noise encountered. Figure 2 shows a typical plot. If each beta particle has enough energy to produce a measurable pulse, then the extrapolated counting rate will equal the disintegration rate (100% counting efficiency). With most beta-emitting nuclides which have an $E_{\max} > 200$ keV the disintegration rate can be obtained in this manner with about a 1–2% uncertainty. For

TABLE I
Comparison of Theoretical and Experimental Counting
Efficiencies for a Liquid Scintillation System (LSS)
with a Figure of Merit of 1.5 keV
per Photoelectron^{4,8}

Nuclide	E_{\max} (keV)	Calculated efficiency for single MPT	Measured efficiency	counts/min LSS	counts/min $4\pi \beta$ -counter
³ H	18	86	86	-	-
²⁴¹ Pu	21	82	82	-	-
⁶³ Ni	67	93	93	-	-
³⁵ S	167	99	99	64,500	64,880
¹⁴⁷ Pm	220	100	100	126,000	125,500
¹³⁷ Cs	510	100	100	40,100	40,500
³² P	1700	100	100	46,800	47,400

beta-emitting nuclides of $E_{\max} < 200$ keV there are a certain fraction of the beta particles (those of low energy) which will have a finite probability of producing too few photons to produce a measurable pulse. In these cases the zero-bias extrapolated counting rate will be less than the disintegration rate.

If the average energy required to produce a measurable count is known, the counting efficiency can be calculated from the known distribution of beta particles from a given nuclide. The disintegration rate can be calculated from the zero-bias counting rate and the theoretically-obtained counting efficiency. This technique has been checked for several low-energy beta emitters^{4,5} and shown to be reliable to an accuracy of $\pm 2\%$. The critical part of this method is to obtain a value for k , the average energy necessary to produce a measurable pulse, which is called the figure of merit. Table I shows results obtained with a system having a k of 1.5 keV/photoelectron. Nuclides which had been standardized by other methods were used to check calculated efficiencies.

Half-Life Measurements

The ability to determine disintegration rates makes liquid scintillation systems ideal for the determination of half-lives by the specific-activity method. Both specific-activity and decay techniques have been used with liquid scintillation systems to obtain half-lives. Table II lists a few of the nuclides for which half-lives have been measured in liquid scintillation systems.

Energy Determinations

The number of photons emitted by a scintillator solution excited by an electron (or other ionizing particles) is a function of the energy of the electron. The measure of the relationship between the relative number of photons (pulse height) and energy of electron has been determined by Flynn *et al.*¹¹ and Horrocks¹² as shown in Figs. 3 and 4. Above about 80 keV the relationship is linear and follows the equation: Energy (MeV) = k (pulse height) + 0.018, where

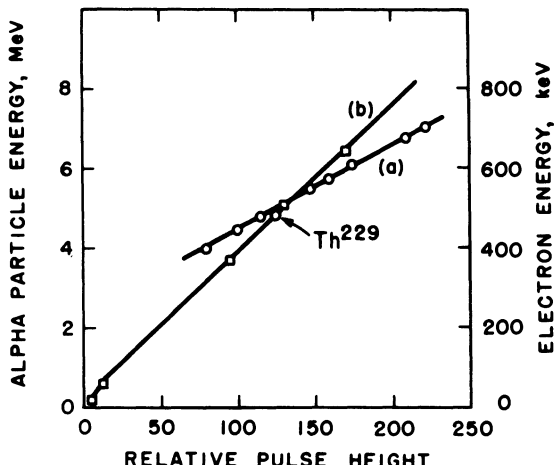


Fig. 3. The pulse height-energy relationship for a liquid scintillation system excited with (a) alpha particles and (b) electrons.

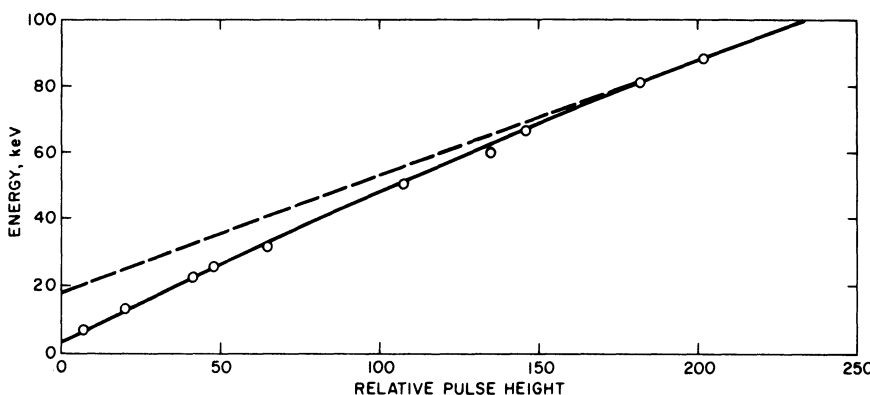


Fig. 4. The pulse height-energy relationship for a liquid scintillation system excited with electrons of low-energy, less than 100 keV.

TABLE II
Some Half-Lives Determined with Liquid Scintillation Systems

Nuclide	Type of particle, energy (MeV)	Technique	Measured half-life	Ref.
^{63}Ni	β^- , $E_{\text{max}} = 0.067$	Specific activity	91.6 ± 3.1 years	6
^{147}Sm	α , 2.2	Specific activity	$(1.05 \pm .02) \times 10^{11}$ years	7
^{87}Rb	β^- , $E_{\text{max}} = 0.272$	Specific activity	$(47.0 \pm 1.0) \times 10^9$ years	8
^{35}S	β^- , $E_{\text{max}} = 0.167$	Decay	$87.17 \pm .03$ days	9
^{45}Ca	β^- , $E_{\text{max}} = 0.255$	Decay	163 ± 1 days	9
^{137}Cs	β^- , $E_{\text{max}} = 1.2, 0.51$	Specific	30.1 ± 0.7 years	10

TABLE III
Values of E_{max} determined with Liquid Scintillation Systems

Nuclide	Accepted energy*		Measure with LSS	Ref.
Nuclide	Decay	(keV)	(keV)	Ref.
^{87}Rb	β^-	275	272 ± 3	8
^{22}Na	β^+	541	533 ± 7	14
^{45}Ca	β^-	254	253 ± 3	8
^{63}Ni	β^-	67	67 ± 2	6
^{32}Si	β^-	210	213 ± 7	15
^{14}C	β^-	156	154 ± 5	15
^{32}P	β^-	1707	1690 ± 30	16

*From Lederer *et al.*³⁰

k is the calibration factor for the particular systems. Below 80 keV the relationship is a smooth curve. This is contrasted with the sharp fluctuations observed with inorganic scintillating crystals.¹³

The maximum energy of the beta (negatron or positron) spectrum is important in characterizing a nuclide. Liquid scintillation systems have been used to measure E_{max} for several nuclides. Table III lists a few nuclides and the values of E_{max} obtained with a liquid scintillation system.

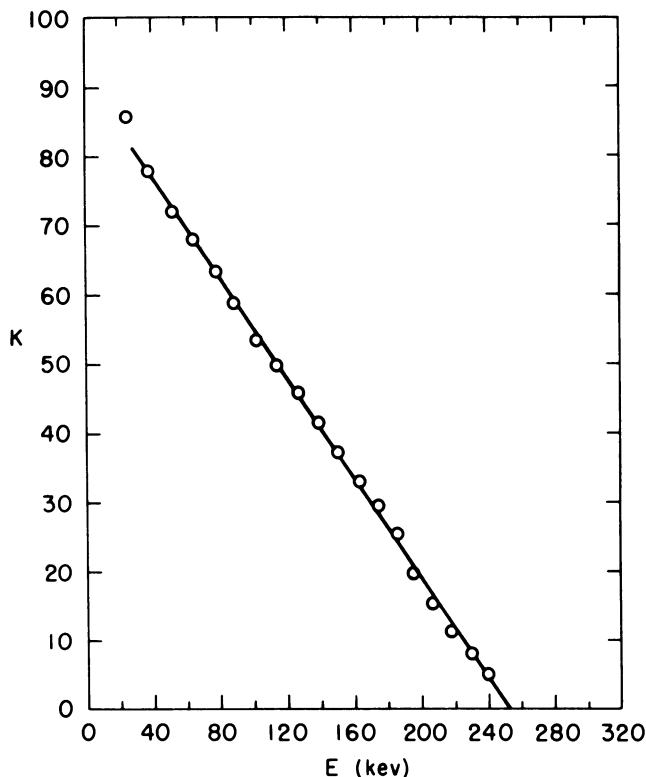


Fig. 5. A Kurie plot for ^{45}Ca obtained with data from a liquid scintillation system showing the extrapolation to obtain E_{\max} of the beta spectrum.

To obtain values of E_{\max} it is necessary to convert the pulse-height spectrum to an energy spectrum by use of the relationship shown in Figs. 3 and 4. In some cases it was shown that a Kurie plot¹⁷ could be made directly from the energy spectrum. In other cases Steinberg and Glendenin¹⁸ showed that the second-derivative correction formula of Owen and Primakoff¹⁹ was applicable to the liquid scintillation system. The extrapolation of the Kurie plot will give the value of E_{\max} . Figure 5 shows the Kurie plot obtained for ^{45}Ca using the second-derivative corrective term.

Conversion Electrons

Nuclides which decay by the emission of conversion electrons have also been counted in a liquid scintillation system.²⁰ Figure 6 shows the differential

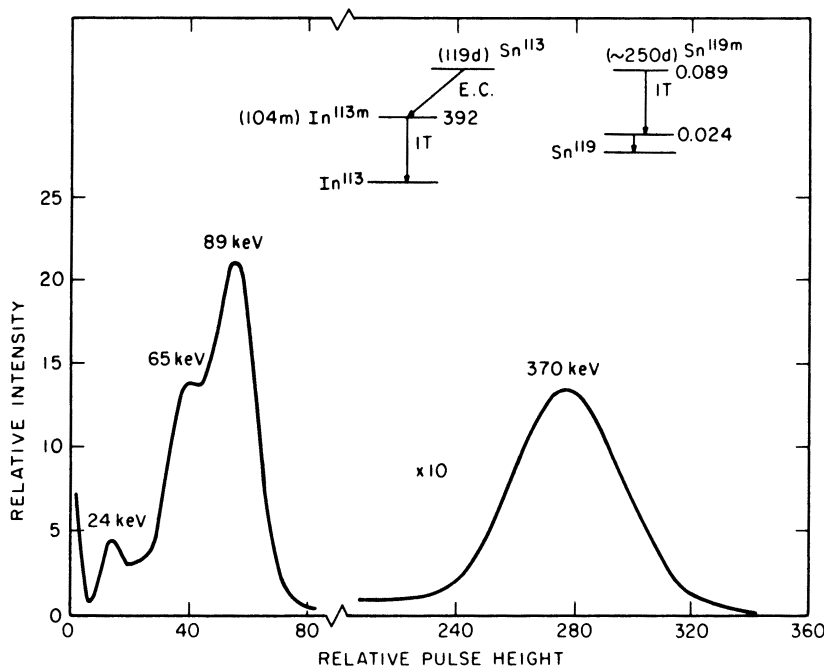


Fig. 6. The differential pulse-height spectrum for a sample containing ^{113}Sn and ^{119m}Sn dissolved in a liquid scintillator solution.

pulse-height spectrum obtained from a sample containing the dissolved nuclides ^{113}Sn and ^{119m}Sn . Figure 7 shows the spectrum obtained for dissolved sample of 5.3-day, β^- -emitting nuclide ^{133}Xe and the 12-day, conversion-electron-emitting nuclide ^{131m}Xe . Figure 7a shows the distribution shortly after preparation, when the sample activity is mostly the beta emitter. Figure 7b shows the same sample at a later date, when the 5-day activity has decayed away with respect to the 12-day activity and both spectra are observed. Figure 7c shows the same sample much later when essentially only the 12-day activity remains. The specific activity of the sample to conversion electron decay is obtained by summing the counts under the peak in the spectrum. The conversion efficiency of the gamma ray which produces the conversion electron can then be used to calculate the disintegration rate of the sample.

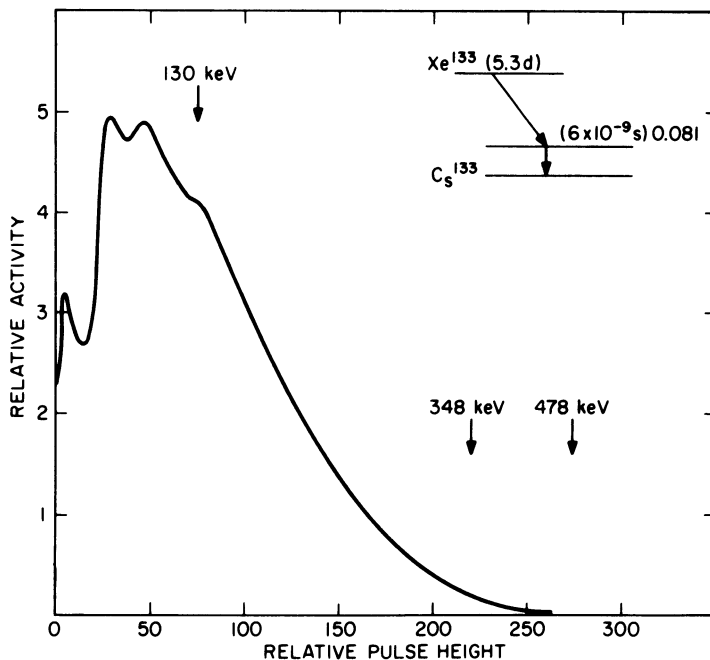


Fig. 7a. The differential pulse-height spectrum of a sample containing the two isotopes ^{133}Xe and ^{131m}Xe immediately after preparation.

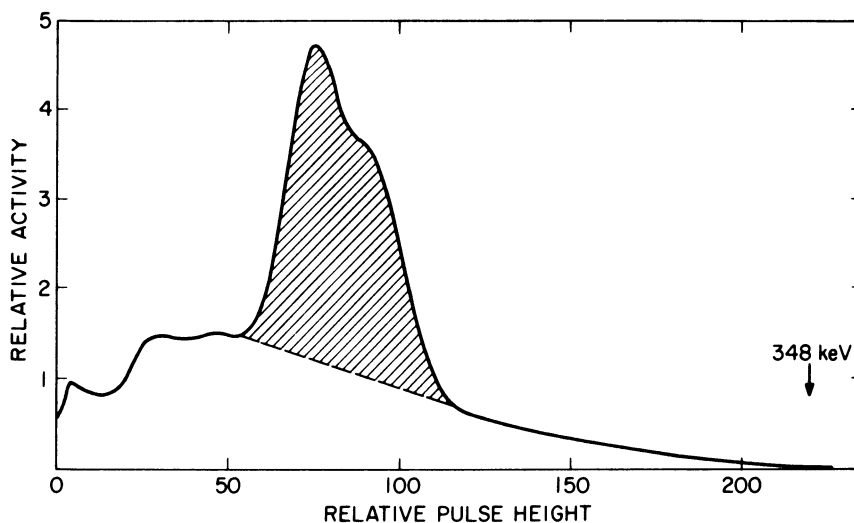


Fig. 7b. The spectrum of the sample in Fig. 7a about 1 month after preparation.

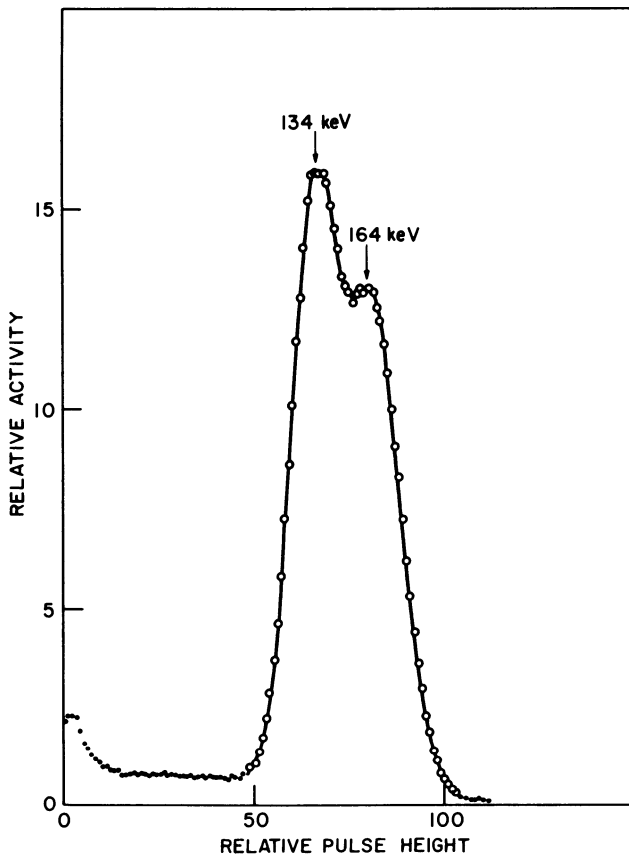


Fig. 7c. The spectrum of the sample in Fig. 7a about 4 months after preparation.

Gamma Rays and X-Rays

Gamma rays and x-rays are measured by the electrons they produce upon their scattering and/or absorption in the liquid scintillator solution. If the energy is low and/or the volume of the scintillator solution is large, the total gamma ray or x-ray will be absorbed and a photopeak will be measured. Figure 8 shows photopeaks obtained for excitation of 0.25 ml of a liquid scintillator solution with 22.5-keV Ag K x-rays and 60-keV gamma rays of ^{241}Am .²¹ It should be remembered that the efficiency for absorption is small and only a small fraction of the 60-keV gamma rays are totally absorbed by the 0.25-ml scintillation system. Most pass through the solution with no energy loss or with a loss less than total energy through scattering.

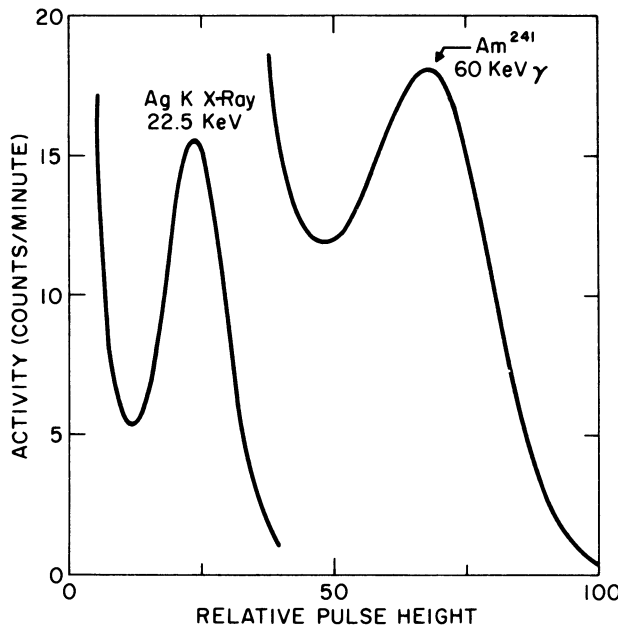


Fig. 8. Differential pulse-height spectra showing photopeaks for external excitation of a liquid scintillator solution with Ag K x-rays (from a ^{109}Cd source) and 60-keV gamma rays (from a ^{241}Am source).

Higher-energy gamma rays can be measured by the Compton-scattering process. When only single scattering events occur, as is most probable in small-volume scintillator solutions, the distribution of scattered electrons will have a predictable shape which depends only upon the energy of the incident gamma rays. The relationship is given by the Compton scatter equation:

$$E_{\max} = 2E_{\gamma}^2 / (2E_{\gamma} + 0.51)$$

where all energies are given in MeV, E_{γ} is the energy of the original gamma ray, 0.51 is the rest mass of an electron, and E_{\max} is the maximum energy that a scattered electron can have. For some common gamma rays the value of E_{\max} is calculated in Table IV. A continuum of scattered electrons is produced up to the value of E_{\max} . Figure 9 shows some typical Compton spectra.

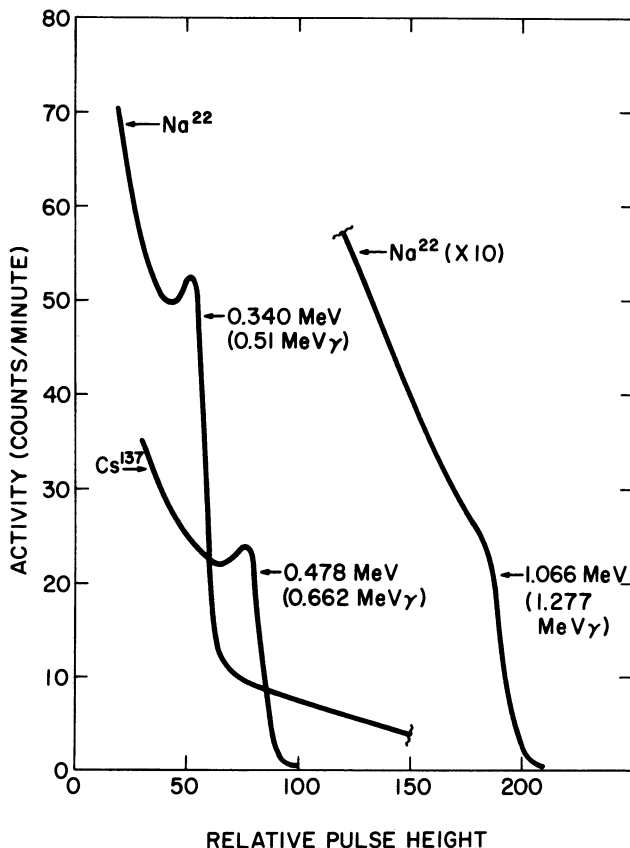


Fig. 9. Differential pulse-height spectra of electrons produced in a liquid scintillator solution by the Compton scattering of high-energy gamma rays.

TABLE IV.
Relation between E_{γ} and E_{\max} for Some
Compton-Scattered Spectra

Nuclide	E_{γ} (MeV)	E_{\max} (MeV)
^{137m} Ba	0.662	0.478
²² Na	0.510	0.340
	1.280	1.066
²⁰³ Hg	0.280	0.147

ALPHA PARTICLES

Liquid scintillation systems have proven very useful for the measurement of alpha-emitting nuclides. The alpha particles can be counted with 100% efficiency. Moderate energy resolution can also be obtained.²² Figure 10 shows the differential and integral pulse-height spectra obtained for a ^{238}Pu sample dissolved in a liquid scintillator solution. All of the alpha counts are under the peak of the distribution, and there is no measurable low-energy tailing. The disintegration rate can be obtained (1) by integrating the number of counts under the peak, or (2) by setting the bias at a value below the peak and measuring the number of counts above that bias.

Very small amounts of alpha-emitting nuclides can be determined in a liquid scintillation system.²³ Figure 11 shows the data for determination of samples with less than 2.6×10^{-14} g of ^{238}Pu . It has been reported²³ that as little as 0.1 disintegration per minute of an alpha-emitting nuclide can be measured.

The energy-pulse height relationship for alpha particles is shown in Fig. 3. Over the energy range 4–8 MeV (which includes most naturally-occurring alpha emitters) the response is linear but not proportional to the energy. For the liquid scintillation system for which this curve was determined the relationship between 4 and 8 MeV is given by the equation: E (MeV) = k (pulse height) + 2.3, where k is the calibration factor.

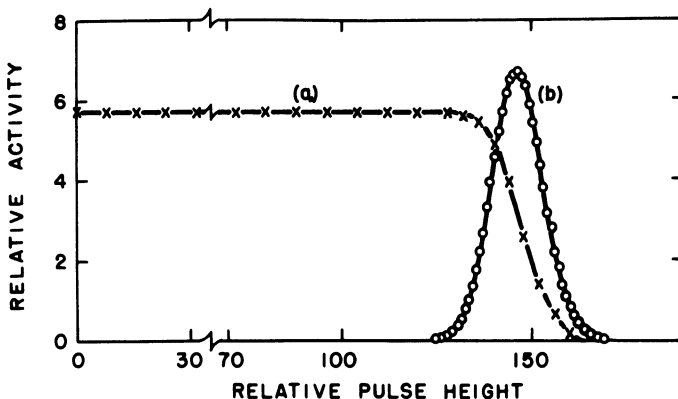


Fig. 10. The (a) integral and (b) differential pulse-height spectra of the alpha particles from a ^{238}Pu sample dissolved in a liquid scintillator solution.

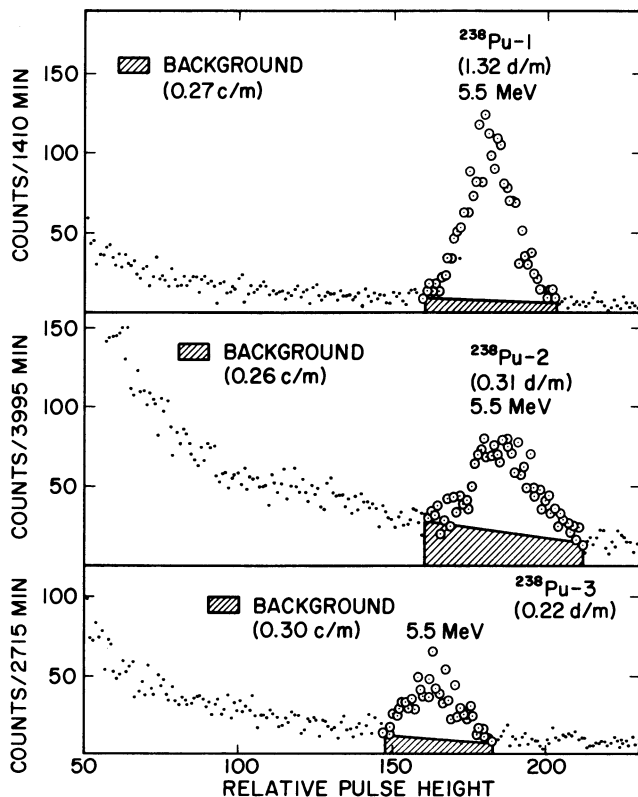


Fig. 11. The differential pulse height spectra obtained from samples containing low counting rates of ^{238}Pu .

The energy resolution of a liquid scintillation system for alpha particles will vary with many variables of the system; optical properties of the system (light guide, MPT, etc.), type of scintillator solution (solutes, solvent), and type of sample (amount of quenching introduced). Under very ideal conditions²² an energy resolution of 5.8% has been obtained. Figure 12 shows the resolving of the alpha particles of ^{233}U (4.8 MeV) and ^{238}Pu (5.5 MeV). Figure 13 shows the spectrum obtained from a sample of ^{232}Th and daughters dissolved in a liquid scintillator solution.

NEUTRONS

Neutrons are detected in the liquid scintillation systems by two methods. Fast neutrons are measured by the protons they produce in the

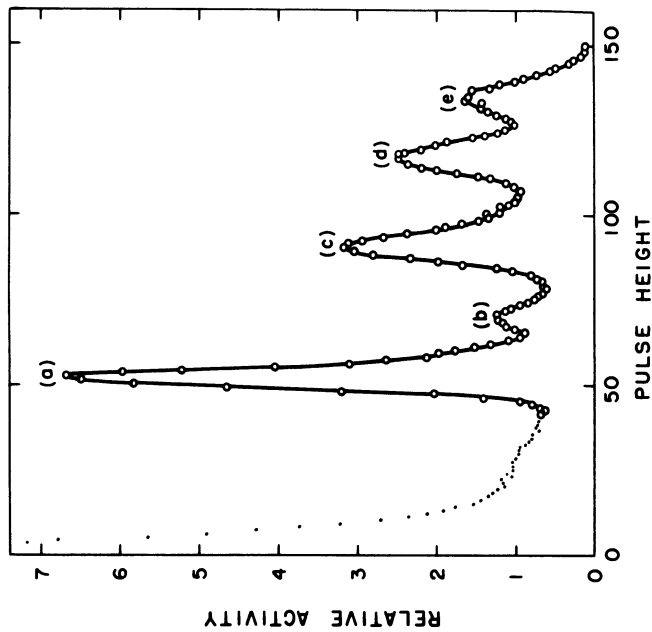


Fig. 13. Differential pulse-height spectrum of a sample of Th showing the various Th isotopes and α -emitting daughters present in the sample (a) 4.0-MeV α -particles of ^{232}Th . (b) 4.7-MeV α -particles of ^{230}Th . (c) 4.0-MeV α -particles of ^{228}Th plus 5.7-MeV α -particles of ^{224}Ra (unresolved). (d) 6.3-MeV α -particles of ^{220}Rn . (e) 6.8-MeV α -particles of ^{216}Po .

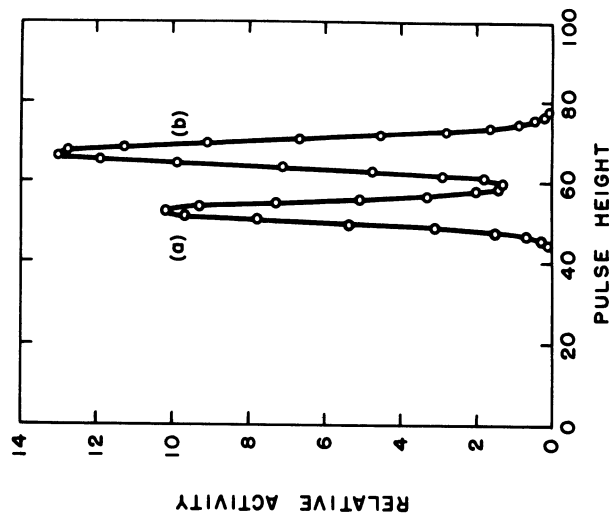
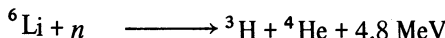
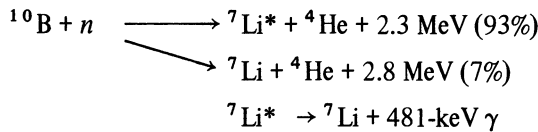


Fig. 12. Differential pulse-height spectrum showing the resolution of two alpha energies in a liquid scintillation system. (a) 4.8-MeV alphas from ^{238}Pu . (b) 5.5-MeV alphas from ^{238}Ra .

solution by the recoil scattering of the H atoms in the organic material. Slow neutrons can be measured by charged particles produced by the capture of the neutron by certain nuclides which have very high cross sections for thermal neutron capture. The two most commonly used capture reactions are



In both cases the resulting energetic particles are measured. Figure 14 shows a typical spectrum obtained with fast neutrons. Figure 15 shows the typical spectrum obtained with thermal neutrons absorbed by a ${}^{10}\text{B}$ -loaded scintillation system.

The very high cross section of ${}^{10}\text{B}$ and ${}^6\text{Li}$ for thermal neutrons gives 100% absorption of those which enter the solution, and thus 100% counting efficiency. To count fast neutrons, only scattering, not absorption, is necessary. According to reported data²⁴ a 2 X 2½ in. liquid scintillator solution has a 74% and 25% efficiency for 0.7 and 14-MeV neutrons, respectively.

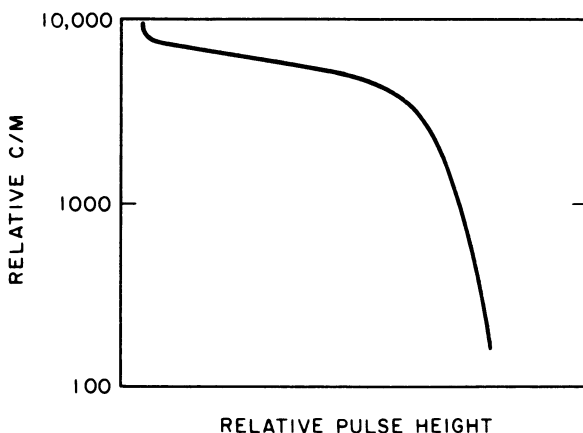


Fig. 14. Differential pulse-height spectrum showing the distribution of proton energies produced by the scattering of neutrons incident upon a liquid scintillator solution.

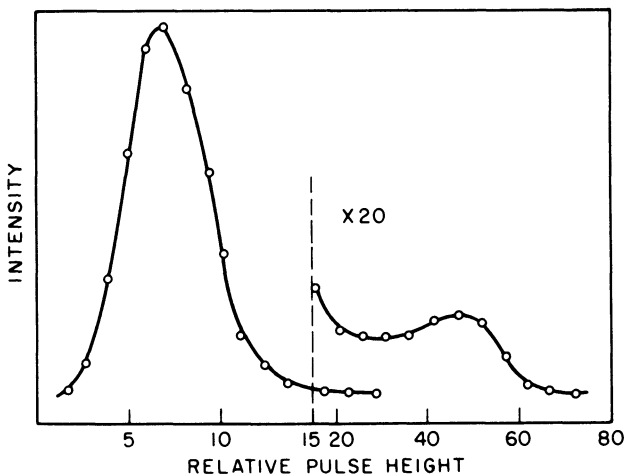
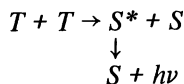


Fig. 15. Differential pulse-height spectrum showing distribution of alpha-particle energies produced by absorption of thermal neutrons in a ^{10}B -loaded liquid scintillator solution. The tail at high energy is due to Compton-scattered electrons produced by the 481-keV gamma ray, which is emitted 93% of the time in the $^{10}\text{B} + n$ reaction.

Pulse-Shape Discrimination

A technique used to enable an experimenter to count neutrons in the presence of a background of gamma rays is called pulse-shape discrimination. The decay time of the light pulse from an organic scintillator is composed of two components: a prompt decay with $\tau \approx 1 - 2.5$ nsec (dependent on solute), and a slow decay with $\tau \approx 250$ nsec. The fraction of the total pulse which decays with the slow decay varies with the type of particle which excites the solution. Figure 16 shows the measure of the intensity distribution with time for excitation with fast neutrons (recoil protons), alpha particles, and gamma rays (scattered electrons). All curves have been normalized at the peak of the intensity.

It is now believed that the slow component is the result of two excited molecules in the triplet state reacting with each other.²⁵ As a result one of the molecules is left in an excited singlet state which decays by fluorescence:



The diffusion of two triplet excited molecules to a point where they can interact is the time-controlling process. The relative intensity of the slow

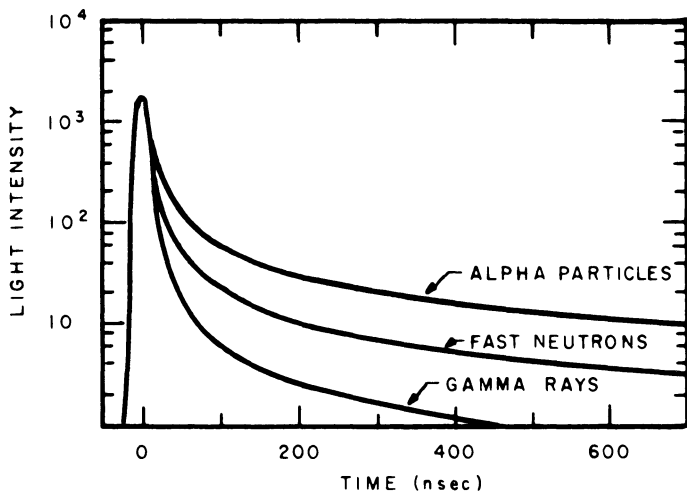


Fig. 16. Time dependence of scintillation intensity for different types of particle excitation.

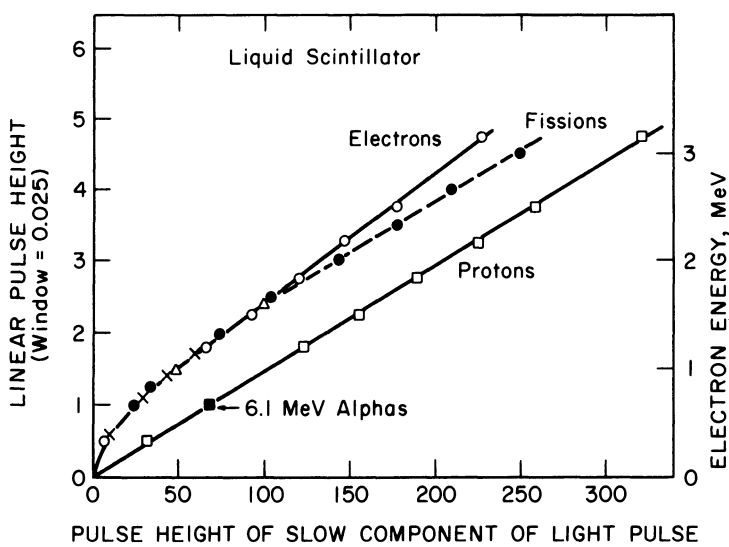
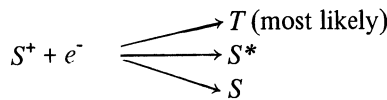


Fig. 17. Amplitude of intensity of slow component coincident with selected intensity of total scintillation.

component increase as the specific ionization of the exciting particle increases. It is believed that the triplet states are preferentially produced by ion recombination:



There are electronic circuits available which utilize the difference in the amount of light in the slow component to separate pulses arising from certain types of particles.²⁶ The use of coincidence techniques makes possible the rejection of all pulses which do not have a certain fraction of the pulse in the slow component. In this manner neutrons (which produce protons) can be counted in the presence of gamma rays (which produce electrons). It is impossible to discriminate between very-low-energy pulses. The lower limit is about 200 keV at present for discrimination between neutrons and gamma rays.

Using proper electronic circuits it is possible to measure the relative

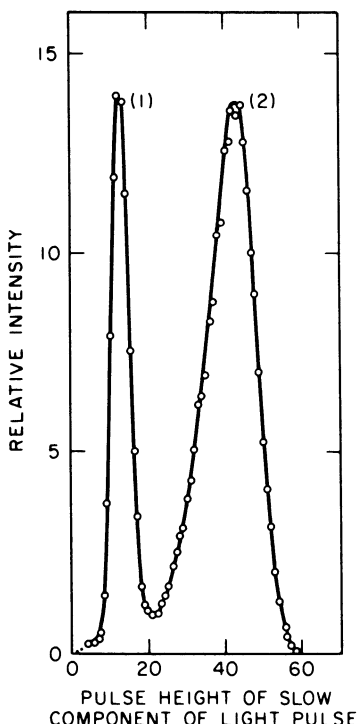


Fig. 18. Differential pulse-height distribution of the intensity of slow pulses which are coincident with a selected intensity of total scintillation

amount of the light pulse in the slow component as a function of energy and type of particle.²⁷ Figure 17 shows the amplitude of the slow component as a function of the total intensity of the light pulse.²⁸ For the same total amount of light, protons have about two times as much intensity in the slow component as electrons. This factor will vary somewhat with the type of scintillator. The presence of oxygen or quenchers preferentially removes the triplet excited molecules. This removes the slow component of the light pulse and thus the source of pulse-shape discrimination.

Figure 18 shows a typical spectrum obtained for the slow component which is coincident with a selected total light intensity from a liquid scintillator solution excited by neutrons and gamma rays. The lower pulse-height distribution is due to electrons (from gamma rays) and the higher pulse-height distribution is due to protons (from neutrons). By selection of a greater total light intensity the two peaks of the distribution of slow pulses will be further

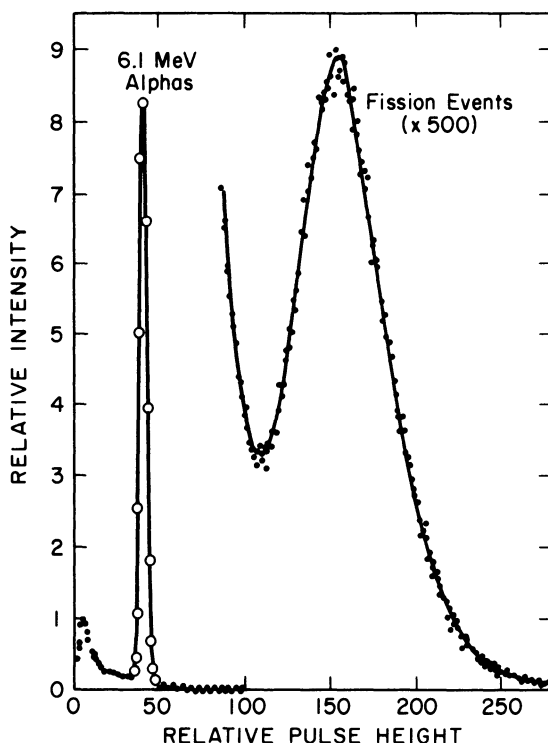


Fig. 19. Differential pulse-height spectrum for sample of ^{252}Cf dissolved in a liquid scintillator solution, showing beta and alpha particles and fission fragments.

apart. By selection of a smaller total light intensity the two peaks will be closer together. At very low total intensity (about equivalent to 200 keV energy) the two peaks will overlap and discrimination will become difficult.

FISSION FRAGMENTS

It was demonstrated²⁸ that fission fragments from the spontaneous fission of ^{252}Cf could be measured for a sample dissolved in a liquid scintil-

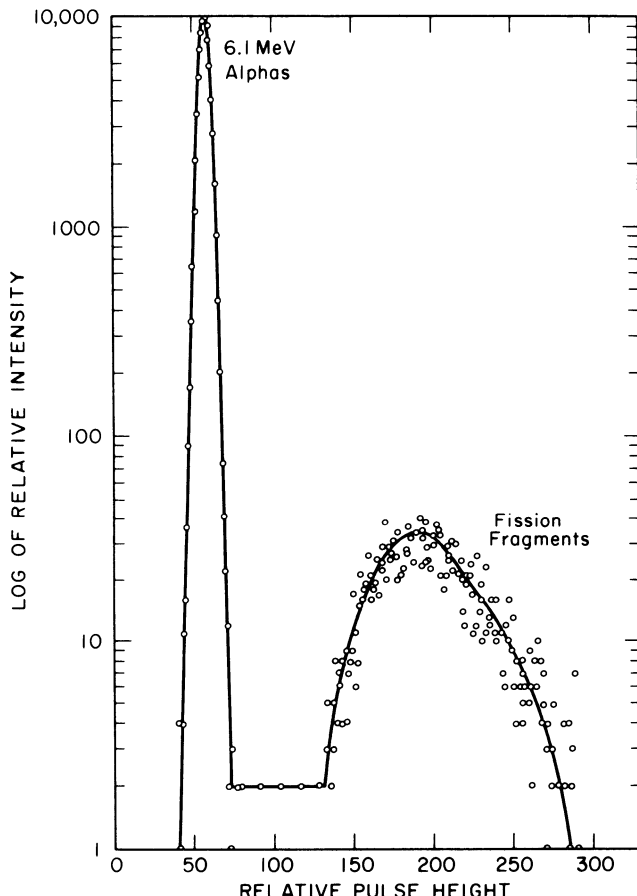


Fig. 20. Differential pulse-height spectrum for sample of ^{252}Cf dissolved in a liquid scintillator solution, showing those pulses remaining after the pulse shape-discriminator circuit was set to eliminate all pulses due to electrons.

lator solution. Figure 19 shows the pulse-height distribution obtained from a ^{252}Cf sample. Present are the distributions for the fission fragments, alpha particles, and beta particles (from decay of radioactive fission products). Using the pulse-shape discrimination technique it is possible to eliminate all pulses from gamma rays and beta particles and count only pulses from alpha particles and fission fragments. Figure 20 shows the pulse-height distribution coincident with the output of a pulse-shape discriminator. From these data the disintegration rate for alpha decay and spontaneous fission decay can be obtained by summing the counts under each peak. In this way the alpha-to-fission disintegration ratio can be obtained. The value obtained was 31.0 ± 0.5 alphas/fission, compared to the literature value of 31.2 ± 0.3 .²⁹

CONCLUSIONS

The liquid scintillation system can be used in many studies of nuclear problems. In this chapter only a few of the many applications have been mentioned and only in a brief way. It is very likely that as the usefulness of liquid scintillation systems becomes better understood and more widely accepted there will be many more applications developed.

ACKNOWLEDGMENTS

This chapter is based on work performed under the auspices of the U.S. Atomic Energy Commission.

REFERENCES

1. J. Steyn and F. J. Haasbroek, *Proc. Intern. Conf. Peaceful Uses of Atomic Energy, Geneva*, Vol. 21, United Nations, New York, (1958), p. 95.
2. G. A. Brinkmann, Doctoral dissertation, University of Amsterdam, 1961.
3. J. Steyn, *Proc. Phys. Soc. A69*, 865 (1956).
4. D. L. Horrocks and M. H. Studier, *Anal. Chem.* 33, 615 (1961).
5. J. A. B. Gibson and H. J. Gale, *J. Sci. Instr. (J. Phys. E)* Ser. 2, 1, 99 (1968).
6. D. L. Horrocks and A. L. Harkness, *Phys. Rev.* 125, 1619 (1962).
7. P. M. Wright, E. P. Steinberg and L. E. Glendenin, *Phys. Rev.* 123, 205 (1961).
8. K. F. Flynn and L. E. Glendenin, *Phys. Rev.* 116, 744 (1960).
9. R. Vaninbroukx and A. Spernol, *Intern. J. Appl. Radiation Isotopes* 16, 289 (1965).
10. D. G. Fleishman, I. V. Burovina, and V. P. Nesterov, *Soviet. J. At. Energy* 13, 1224 (1963). [Translated from *Atomnaya Energiya* 13(6), 592 (1962)].
11. K. F. Flynn, L. E. Glendenin, E. P. Steinberg, and P. M. Wright, *Nucl. Instr. Methods* 27, 13 (1964).

12. D. L. Horrocks *Nucl. Instr. Methods* **30**, 157 (1964).
13. D. Engelkemier, *Rev. Sci. Instr.* **27**, 589 (1956).
14. D. W. Engelkemier, K. F. Flynn, and L. E. Glendenin, *Phys. Rev.* **126**, 1818 (1962).
15. R. L. Brozbinski, J. R. Finkel, and D. C. Conway, *J. Inorg. Nucl. Chem.* **26**, 677 (1964).
16. T. Cless-Bernert, K. E. Duftschmid, and H. Vonach, *Nukleonik* **4**, 162 (1962).
17. Tables for the Analysis of Beta Spectra, National Bureau of Standards Applied Mathematics Series, Report No. 13, U.S. Government Printing Office, Washington, D.C., 1952.
18. E. P. Steinberg and L. E. Glendenin, Argonne National Laboratory, unpublished results, (1960).
19. G. E. Owen and H. Primakoff, *Phys. Rev.* **74**, 1406 (1948).
20. D. L. Horrocks and M. H. Studier, *Anal. Chem.* **36**, 2077 (1964).
21. D. L. Horrocks, *Nucl. Instr. Methods* **27**, 253 (1964).
22. D. L. Horrocks, *Rev. Sci. Instr.* **35**, 334 (1964).
23. D. L. Horrocks, *Intern. J. Appl. Radiation Isotopes* **17**, 441 (1966).
24. R. Batchelor, W. B. Gilboy, J. B. Parker, and J. H. Towle, *Nucl. Instr. Meth.* **13**, 70 (1961).
25. R. Voltz, Thesis, Strasbourg, 1965; T. A. King and R. Voltz, *Proc. Roy. Soc. A* **289**, 424 (1966).
26. W. Daehnick and R. Sherr, *Rev. Sci. Instr.* **32**, 666 (1961).
27. F. D. Brooks, *Nucl. Instr. Meth.* **4**, 151 (1959).
28. D. L. Horrocks, *Rev. Sci. Instr.* **34**, 1035 (1963).
29. D. Metta, H. Diamond, R. F. Barnes, J. Milsted, J. Gray, Jr., D. J. Henderson, and C. M. Stevens, *J. Inorg. Nucl. Chem.* **27**, 33 (1965).
30. C. M. Lederer, J. M. Hollander, and I. Perlman, *Table of Isotopes*, 6th Ed., John Wiley & Sons, New York, (1967).

Instrument Parameters

A Comparison of the Function of the Slit in Light-Absorption Studies Using Tungsten and Laser Sources

Martin J. Houle, Marvin O. Fretwell,
and William J. Romig

*Dugway Proving Ground,
Dugway, Utah*

Recent studies have shown that the laser is an extremely useful substitute for the tungsten lamp in light absorption studies with commercial spectrophotometers. A closer conformity to the Beer-Lambert absorption law and an increase in the useful concentration range are among the advantages of the laser in this application. However, the function of the slit is different for the two types of source. With the laser the slit control acts to regulate the power incident upon the sample and detector, but due to the Gaussian distribution of intensity across the laser beam, it is not a linear relationship with slit width. For the tungsten lamp the slit determines the radiation frequency bandwidth as well as controlling the incident power. The function of the slit is described in detail for the two sources and the difference is discussed in terms of the applicability of the absorption law. Experimental data are also presented which demonstrate this difference. It is suggested that employing neutral density filters or reducing the plasma-tube excitation power may be more desirable than using a slit to attenuate the laser light incident upon a sample.

INTRODUCTION

During the last few years it has become apparent that the laser is potentially a very useful light source in chemical absorption studies. In a recent paper¹ experimental data was presented which demonstrated some of the advantages to be gained from substituting a laser for the tungsten lamp in light-absorption

experiments. Among the advantages reported were an apparent increase in absorptivity, exact conformity to Beer's law within the limits of the intensity of the laser light, and an increase in the usable concentration range. However, the investigations were limited to an absorbing species whose maximum coincided with the 632.8-nm transition of the laser. It was pointed out that due to the relatively few transitions available from any one specific type of laser, applications of this type were limited unless reliable off-peak absorbance measurements could be made. In a subsequent paper² the applicability and reliability of the laser for off-peak light-absorbance measurements were investigated. It was found that even if the wavelength of the absorption maximum of a compound was removed from an available laser transition to the extent that the absorbance of the laser beam was only 20% of that obtained on-peak with a tungsten lamp, the accuracy and the precision of the laser measurements were at least as good as the tungsten lamp used on-peak. The laser also allowed a many-fold increase in the concentration range that could be investigated compared to the tungsten lamp used off-peak. To obtain the desired comparison in both investigations, the path normally traversed by the tungsten light through the spectrophotometer was also used for the laser beam. This placed the laser at a distinct disadvantage by unnecessarily passing the light through collimating lenses and monochromators, but was done to gain the desired comparisons.

The slit mechanism is one element of the spectrophotometer whose function is different in laser and in tungsten-lamp applications. When used with the tungsten lamp the slit not only limits the total power reaching the detector, but also limits the band-pass width of the light incident upon the sample. With the laser its function is simply to limit the total power. In the current investigation the results obtained from laser and tungsten lamp-experiments are described in terms of the Beer-Lambert absorption law, emphasizing the difference in function of the slit mechanism between the two light sources.

A light source-monochromator-detector configuration was employed in this study. A simple chemical system consisting of a commercial dye dissolved in an appropriate solvent was used to demonstrate the differences.

THEORETICAL

The classical form of the Beer-Lambert absorption law is valid only when monochromatic radiation is used. This has been discussed in detail by a number of other investigators and the results apply directly to the current study.³⁻⁵ In actual practice monochromaticity can be approached, but is

never quite attained. Even laser transitions have a finite width. When conventional light sources are used the purity of the light incident upon the samples varies with the sophistication of the instrumentation. The purity of the incident light obtained from high-quality spectrophotometers is dependent upon the intensity of the light source, the sensitivity of the detector, the signal-to-noise ratio of the associated amplifier circuitry, and the optical-dispersion characteristics of the monochromator. In regard to this last factor, the function of the slit mechanism in the spectrophotometer is an indispensable part of the monochromator unit. The slit directly governs the bandwidth of light emerging from the monochromator compartment to impinge onto the sample. This band of light emerging through the exit slit contains a distribution of wavelengths. In the following discussion the bandwidth is defined by the interval between λ_1 and λ^2 . The distribution of radiant power within this bandwidth is described by a distribution function $P_0(\lambda)$. The amount of radiant power carried by all wavelengths in the vanishingly small interval of pass band $d\lambda$ is $P_0(\lambda) d\lambda$. The relation between these two quantities is given by

$$dP_0 = P_0(\lambda) d\lambda \quad (1)$$

The total radiant power P of the band of light passing through the slit from the monochromator is obtained by summing the power from all the wavelength intervals within the distribution:

$$P_0 = \int_{\lambda_2}^{\lambda_1} P_0(\lambda) d\lambda \quad (2)$$

Monochromatic radiation of radiant power P_0 incident upon an absorbing solution of concentration c is attenuated as it passes through the solution of a given path length b according to the equation

$$P = P_0 e^{-abc} \quad (3)$$

However, in order to apply this expression to studies made using light with a finite bandwidth, we must first divide the finite band into monochromatic increments:

$$dP_T = dP_0 e^{-abc} = P_0(\lambda) d\lambda e^{-a\lambda bc} \quad (4)$$

Each of these vanishingly small distributions carry an increment of radiant power $P_0(\lambda) d\lambda$ which behaves as though it was monochromatic. The dependence of the absorptivity constant a on wavelength is indicated in this

equation by a_λ . Thus dP_T is the incremental contribution to the total transmitted power by each of the wavelength intervals $d\lambda$. The total transmitted power P_T is obtained by integrating each of the increments of power over the band interval passing through the slit:

$$P_T = \int_{\lambda_1}^{\lambda_2} P_0(\lambda) e^{-a_\lambda b c} d\lambda \quad (5)$$

By substituting Eqs. (2) and (5) for P_0 and P_T into the usual expression of the Beer-Lambert Law,

$$A = \log(P_0/P_T) \quad (6)$$

we obtain the following correct form for use with finite bandwidths:

$$A = \log \left\{ \left[\int_{\lambda_1}^{\lambda_2} P_0(\lambda) d\lambda \right] / \left[\int_{\lambda_1}^{\lambda_2} P_0(\lambda) e^{-a_\lambda b c} d\lambda \right] \right\} \quad (7)$$

This equation makes it readily apparent why deviations from Beer's law are often seen in chemical absorption data. Deviations are especially obvious when differential analyses are performed because quite wide slit settings are normally required to re-zero the equipment.

In contrast, laser radiation is considered to be monochromatic. Although the laser radiation does have the finite linewidth, this is normally many times below the resolving power of the monochromator used in commercial spectrophotometers, so for practical purposes is considered to contain only one wavelength of light. Therefore the usual expression of the Beer-Lambert law can be considered valid for light-absorption studies in which lasers are used as the light source.

A further consideration when comparing conventional radiators with a laser is the difference in distribution of power across the beam. A uniformly-illuminated slit, such as obtained with a narrow band of dispersed light from the tungsten lamp, passes radiant power as described by the equation

$$P_s = \int_{x_1, y_1}^{x_2, y_2} P dx dy \quad (8)$$

P_s is the total radiant power passing through the slit and x and y are the dimensions of the illuminated slit. However, it has been shown that for a laser the power across the beam is not uniform, but closely approximates a Gaussian distribution as described by

$$I(r) = (2P_0/\pi a^2) [\exp -2(x^2 + y^2)]/a^2 \quad (9)$$

In this equation $I(r)$ is the intensity (watts/cm^2) when P_0 is the total power of the laser beam, and a is the radius from the center of the beam to a point at which the intensity falls to $1/e^2$, or 0.135 times the central intensity. Beyond these limits fluctuations in the beam caused by radiation striking the walls of the plasma tube produce a deviation from the Gaussian equation. However, 86.5% of the total beam power is contained within these limits. Combining Eqs. (8) and (9) gives the laser power passing through a slit,

$$P_s = \int_{-L/2}^{L/2} \int_{-W/2}^{W/2} \frac{2P_0}{\pi a^2} \frac{\exp[-2(x^2 + y^2)]}{a^2} dx dy \quad (10)$$

where W is the slit width and L is the slit length.

EXPERIMENTAL RESULTS

A Spectra-Physics Model 125 helium-neon gas laser was used throughout this study with the wavelength set at the 632.8-nm transition. Maximum radiant power (15 mW) was obtained by fine adjustment of the tuning mechanism. Beam diameter was 2 mm between the $1/e^2$ intensity points, and the beam diversion was 0.7 mrad at 632.8 nm.

A Beckman Model DB-G was selected as the representative spectrophotometer because of its linear dispersion. It was operated as a single-beam instrument by switching to the flame mode. When used with the laser as the light source the laser beam was introduced into the spectrophotometer by removing the light plug on the left side of the DB-G, where light signals are introduced if the equipment is used with an atomic-absorption accessory. The source selector mirror was set in the hydrogen lamp position and the hydrogen lamp removed. By using this configuration the tungsten lamp is not in the path of incoming laser light. The beam impinges on the source selector mirror, from which it is directed into the monochromator compartment, into the sample compartment, and finally to the detector. The laser is oriented to produce maximum meter response with the wavelength dial set at 632.8 nm. Extremely narrow slits were required when the laser was used as the light source to protect the meter and the detector. The tungsten lamp was kept off during these experiments.

The differences in the function of the slit mechanism when used with laser and with tungsten-light sources were demonstrated for light-absorption studies by using Alkali Fast Green A (AFGA) as shown by the spectral scan

given in Fig. 1. The absorption maximum of an ethanolic solution of the dye is located at 633 nm.

AFGA was selected as the dye because its absorption maximum is very close to the 632.8-nm transition of the helium-neon laser. Standard solutions of the dye were prepared in ethanol prior to measuring the absorption of tungsten and the laser light. The resulting concentration-absorbance calibration curves are shown in Fig. 2. When ethanol was used as the zero reference comparable results were obtained from both light sources. However, differential spectrophotometry emphasizes the difference in slit function for the two light sources. In this case standards of the dye were used as the zero reference, which of course required the use of wider slit settings. As a result, a broader band of wavelengths passed through the slit when the tungsten lamp was used. Deviations from Beer's law is apparent in the calibration curves of Fig. 2, and, because of the necessity for increasingly wider slits, become more pronounced as the concentration of the zero reference is raised. Identical experiments with the laser show exact conformity with Beer-Lambert law

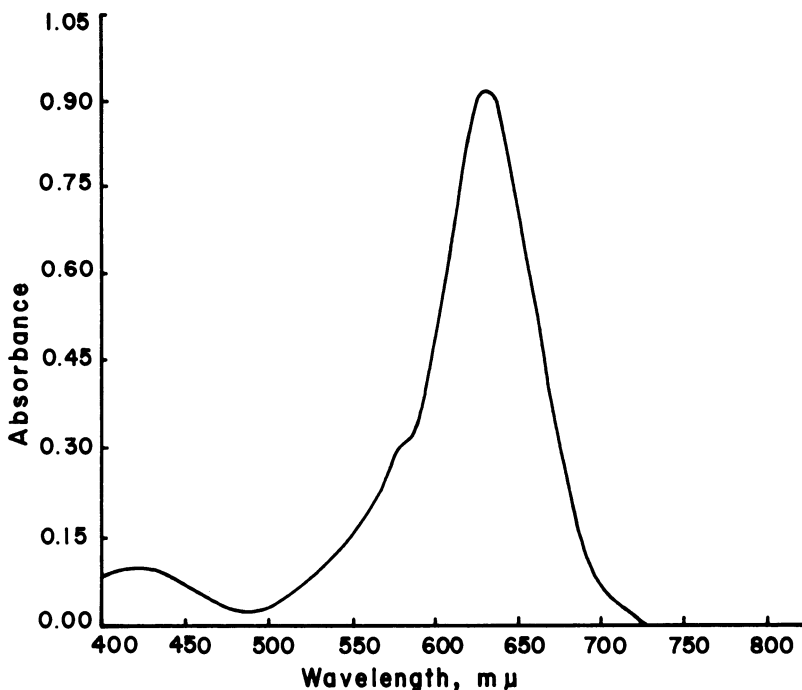


Fig. 1. Spectral scan of Alkali Fast Green A (AFGA).

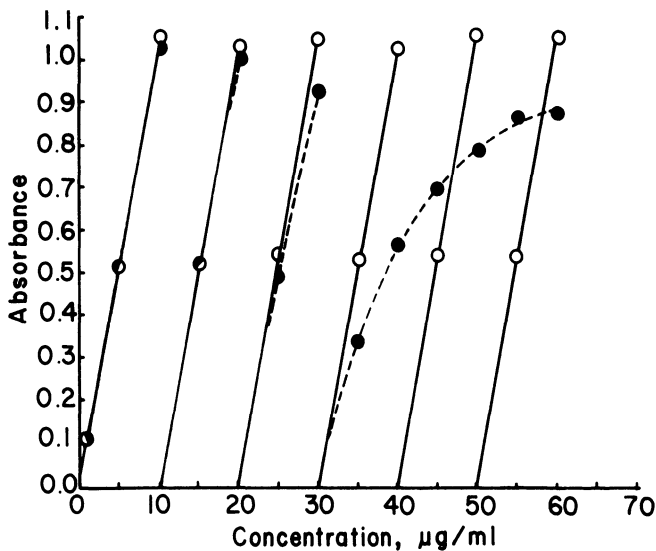


Fig. 2. Concentration-absorbance calibration curves for Alkali Fast Green A (AFGA) using a solvent reference and a differential analysis for the tungsten-lamp (solid circles) and the laser (open circles).

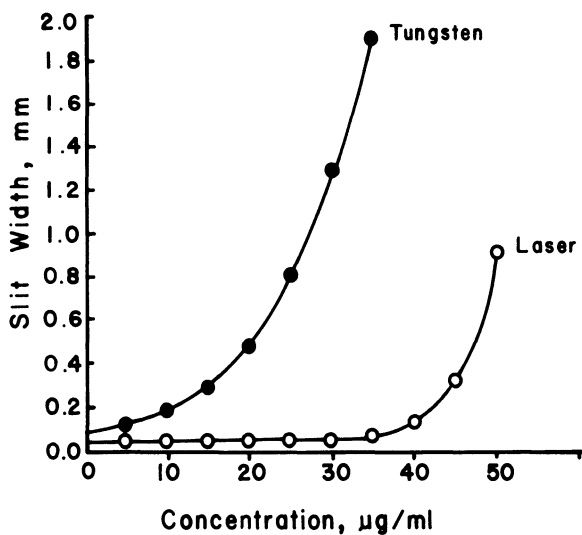


Fig. 3. The effect of concentration on slit width.

regardless of the concentration of the zero reference because the monochromatic character of the light is not affected by changing the slit.

The above experiments adequately demonstrate the effect that variable slit settings produce upon absorption data obtained from each light source. However, they do not show the changes in radiant power for each source as the slit is increased. An experiment was therefore designed in which dye standards were placed in the light path and the slit adjusted to maintain a constant meter reading on the spectrophotometer. An absorbance of 0.43 was selected as reference point because at this absorbance value the photometric error is at a minimum.⁶ Figure 3 illustrates the relationship obtained between concentration and slit width. The tungsten-lamp plot indicates that as the slit increases with an increase in concentration the slope of the line continuously changes. The laser plot shows nearly a constant slope until a point is reached where the power drops off rapidly because of the Gaussian distribution of power across the laser beam. The comparison further demonstrates the effect of using polychromatic radiation in light-absorption studies.

The results of measuring the change in effective bandwidth when changing slit width are given in Table I. The table shows that with a fully open slit (2.0 mm) the effective bandwidth is only 5.20 nm. It is obvious from the spectral scan of AFGA shown in Fig. 1 that a bandwidth of this size could not alone account for the degree of nonlinearity seen in the plots. A portion of the deviation is most probably due to stray light. Stray light can be considered a distribution of wavelengths, and although not a uniform distribution, it would produce an effect upon the absorption data similar to that obtained by increasing the width of the pass band. Regardless of which factor is contributing the most to the deviation from the absorption law, this is a

TABLE I
The Effect of Changing Slit Width
Upon Effective Bandwidth

Slit width (mm)	Effective bandwidth (nm)
0.083	0.22
0.890	0.23
0.120	0.30
0.180	0.47
0.290	0.75
0.480	1.24
0.800	2.10
1.3	3.4
1.9	4.95
2.0	5.20

limitation in commercial spectrophotometers that is eliminated by using a laser as a light source.

CONCLUSION

The use of lasers with spectrophotometers is presently limited. These experiments were conducted primarily to demonstrate the difference in the function of the slit when used with the laser and with the tungsten lamp. However, the results show that a laser photometer is feasible for light-absorption studies. The availability of laser transitions spaced over a wide portion of the spectrum and the development of tunable lasers make the concept of a laser photometer quite practical, especially in view of the applicability even for off-peak measurements.

It can be concluded that other power-limiting devices, such as neutral density filters, changes in plasma-tube power, or electronic attenuating devices in the detector would be better than slits or iris diaphragms for limiting the laser power reaching the detector. This would avoid the problem caused by the Gaussian distribution of power across the laser beam.

REFERENCES

1. M. J. Houle and K. J. Grossaint, *Anal. Chem.* **38**, 786 (1966).
2. M. J. Houle and M. O. Fretwell, N.W. Regional ACS Meeting, June 1967.
3. Frederick C. Strong, *Anal. Chem.* **24**, 338 (1952).
4. G. M. Louden, *J. Chem. Educ.* **41**, 391 (1964).
5. C. F. Hiskey and Irving G. Young, *Anal. Chem.* **23**, 1196 (1951).
6. Gilbert H. Ayres, *Anal. Chem.* **21**, 652 (1949).
7. Laser Techniques Bulletin No. 1, Spectra-Physics, Inc., Mountain View, California.

Index

- Aerospace spectrometers, 289
Analysis, indirect atomic absorption methods, 222
Analysis of plant ash solutions, 152 results, 159
Analysis, stainless steels, 161
Atomic absorption analysis of stainless steel, 161 detection limits in iron-base matrix, 167 difficult working areas in flame photometry, 169 arsenic and selenium, 171 high-temperature flames, 172 limitations of sample composition, 183 low-feed-rate samples, 177 low-sensitivity elements, 179 releasers and protectors, 187 effect of burner, 203-204 experimental considerations, 201 experimental device, 215 indirect methods of analysis, 222 mineral and trace elements in man, 227 reproducibility and error for calcium, magnesium, and zinc, 233 single-element-multielement lamps, mode of operation, 203-204
- Balance, calcium, magnesium, and zinc during low and high intake, 231-232
Betaprobe, 7
 Ca^+ , Ca^0 , Ca^* , CaO , influence on aluminum chloride and aluminum nitrate, 195 phosphate, 193 sulfate, 194
Calcium flame interference, 189
Carbon and clean surfaces, 71
CdS films, 18
CdSe films, 16
CdTe films, 22
Characterization of semiconductor surface layers, 31
Computer-coupled x-ray, 97 correction for instrument parameters, 102 correction for interelement effect, 99
Effect of burner-atomic absorption, 203-204
Electron probe, surface analysis, 80 thin-film studies, 91
Film studies, electron probe, 91
Film thickness, 3 CdS films, 18 CdSe films, 16 CdTe films, 22 HgSe films, 25

- Film thickness, (continued)
 fluorescence method for measuring, 3
- Forensic toxicology, 267
- Fuel flowrate, calcium depression, 196
- Function of slit in light-absorption studies, 329
- Height above burner, calcium depression, 196
- High-energy electron diffraction, analysis of surfaces, 62
- Hollow cathode lamp, mode of operation, 208-209
- Hot gases, 133
 heat flux calculation, 135
- Laser source, 329
- Liquid scintillation systems, 303
- Mass spectra of some acidic and neutral drugs, 270
- Mass spectrometry
 application to forensic toxicology, 267
 determination of oxidation inhibitors, 274
 investigation of solids by means of ion bombardment, 239
 diffusion profile, 252
 influence of oxidation, 249
 interference micrograph of Ge surface, 255
 limit of detection, 245
- Mass spectrum of secondary ions, 242
- Nondispersing x-ray system, 8
- Nuclear application of liquid scintillation systems, 303
 alpha-emitting nuclides, 315
 disintegration rate, 304
 neutrons, 316
- Oxide films, 75
- Plant ash solution
 chemical standards and buffer solutions, 154
- Plant ash solution (continued)
 sample preparation, 155
- Requirements for aerospace spectrometers, 289
- Shift in K wavelength, 122
- Shift in M series of lanthanum, 122, 127
- Solids, study by ion-bombardment mass spectrometer, 239
- Spark-emission spectroscopy
 analysis of plant ash solutions, 152
 analysis of stainless steel, 161
- Spectroscopy
 in space, 286
 study of hot gases, 133
- Surface analysis
 electron probe, 80
 compositional change in sample preparation, 87
 segregation of impurities, 82
 high-energy electron-diffraction and x-ray emission, 61
- Surface-layer defects in silicon crystals, 31
- Surface reflection topography, 36
- Synthetic lube oils, determination of oxidation inhibitors by ultraviolet and mass spectrometry, 274
- Tungsten sources, 329
- Ultrasoft x-rays, total reflection, 108
- Ultraviolet spectrometry, determination of oxidation inhibitors, 274
- Volume absorption coefficient
 for acetone, 139
 for methanol, 140
- Volume emission
 of acetone, 138
 of methanol, 140
- Wavelength shift, x-ray, 121
 K wavelengths, 122

- Wavelength shift (continued)
 M wavelength spectra for lanthanum, 126
- X-ray
 attenuation on reflection topography, 51
 Betaprobe, 7
 computer-coupled, 97
 diffraction topography, 31
 fluorescence analysis of stainless steels, 161
 fluorescence method for measuring film thickness, 3
 comparison of count rate, 26
- X-ray (continued)
 instrument parameters, 102
 interelement effect, 99
 nondispersing system, 8
 possible analysis of light elements, 108
 surface-layer defects in silicon crystals, 31
 extinction-contrast effect, 33, 35
 surface reflection topography, 36
 transmission topography, 34
 wavelength shift with voltage, 121
 M spectra of lanthanum, 126